ON THE MECHANICS OF NON-INTERLOCKING AND INTERLOCKING PATTERNED INTERFACES INSPIRED BY NATURE

by

Maryam Sadat Hosseini

A Dissertation

Submitted to the Faculty of Purdue University

In Partial Fulfillment of the Requirements for the Degree of

Doctor of Philosophy

Lyles School of Civil Engineering

West Lafayette, Indiana

December 2019

THE PURDUE UNIVERSITY GRADUATE SCHOOL
STATEMENT OF COMMITTEE APPROVAL

Prof. Pablo D. Zavattieri, Chair

> Lyle School of Civil Engineering

Prof. John E Haddock

> Lyle School of Civil Engineering

Prof. Marcial Gonzalez

> School of Mechanical Engineering

Prof. Ghadir Haikal

> Lyle School of Civil Engineering

Prof. David Kisailus

> Chemical and Environmental Engineering, UC Riverside

Approved by :

> Dr. Dulcy Abraham

> > Head of the Graduate Program

Dedicated to my parents, husband, and my brother.

ACKNOWLEDGMENTS

First, I would like to thank my advisor, Prof. Pablo D. Zavattieri, for his support, patience and valuable guidance throughout this project. I would also like to thank my thesis committee members: Prof. John E. Haddock, Prof. Marcial Gonzalez, Prof. Ghadir Haikal, and Prof. David Kisailus for their helpful discussions, ideas, and suggestions that encouraged me to widen my research from a different perspective.

I would like to appreciate the help and support from my dear husband, Dr. Masoud Ghavami, my dear brother Dr. Samuel Hosseini, my dearest parents Mohammad Hosseini and Azar Vasefi, and my dear sister Yasmin Ehteshami for their unconditional love and support during my Ph.D. I could not accomplish my work without their encouragement and support.

TABLE OF CONTENTS

LIST OF TABLES

LIST OF FIGURES

ABSTRACT

Author: Hosseini, Maryam Sadat. Ph.D.
Institution: Purdue University
Degree Received: December 2019
Title: On the Mechanics of Non-Interlocking and Interlocking Patterned Interfaces Inspired by Nature
Major Professor: Pablo D. Zavattieri

Nature has been adopted several techniques to survive over the past billion years of evolution. Geometrically patterned interfaces seem to be a common motif in Nature. In particular, architecture plays a crucial role in increasing the strength, toughness, and damage tolerance among different species. For instance, alligator, turtle, armadillo, sea urchin, ammonite, Ironclad beetle, and boxfish are among species included patterned interfaces inside their structure. Here, the role of shape, geometry, and microstructure of both interlocking and non-interlocking patterned interfaces inspired by Nature is investigated in enhancing the mechanical properties under multiaxial loading conditions.

The role of non-interlocking patterned interfaces is studied under remote mode-I loading conditions. In particular, the role of the shape of the opening crack behind the crack tip is investigated as the crack propagates along the interface. The shape of the interface behind the crack tip for different amplitude-to-wavelength aspect ratios is studied by comparing the results from two analytical models with finite element simulations through the J-integral method. Additionally, the role of the material length scale is explored by investigating the relationship between the geometrical characteristic lengths and the emerging material length scale using a finite-element-based cohesive zone model. The results suggest that geometrical toughening is influenced by a size effect, but it is bounded between two extreme conditions.

The role of interlocking patterned interfaces is investigated for both boxfish carapace and Ironclad beetle cuticle. These two species are selected due to their extraordinary performance against attack and compression loads, which are fatal to the other species. The boxfish carapace (Lactoria cornuta) contains hexagonal dermal scutes, a combination of the brittle hexagonal plate (hydroxyapatite) on top of a very compliant (collagen) material. While the mineral plates are separated by patterned sutures (triangular patterns), there is no interphase material connecting

them. Instead, the connection between mineralized plates is done through the collagen base which is different from other naturally occurring sutures (e.g., sutures in turtle, alligator, armadillo). The protective role of the boxfish scute architecture in controlling the crack directions is investigated by employing analytical, numerical, and experimental tools for different geometrical and material parameters. Further analysis revealed that this architecture helps to arrest the cracks inside the sutures area. Additionally, the results confirmed that both architecture and material properties play a key role in controlling the direction of the crack inside the brittle plates.

Beetles are a subclass of arthropod dating back over 300 million years. The complex cuticle microstructure found within the exoskeleton (elytra) of this specially adapted insect results in extremely high compressive resistance, far beyond any other beetle identified to date. Elytra consists of separated parts connected using dovetail-joints blades and contains a hierarchical assembly of alpha-chitin fibers embedded within a proteinaceous matrix that provides both strength and toughness. The architecture of the suture region of the elytra, modified for terrestrial living, has a unique architecture consisting of specially modified interlocking blades, whose elliptical geometry, laminated microstructure, and frictional interfacial features, enhance mechanical properties such as toughness and load resistance. The presence of microstructure inside the interlocking joints results in delamination inside blades and, thus, develops a new competing mechanism that is different from pull out or fractures. By using a combination of finite element analysis, experimental methods (i.e., optical and electron microscopy, computed tomography, and mechanical testing), and 3D printing prototype technique, the unique adaptations, novel architectural design features and interfacial structures are revealed within the exoskeleton of Ironclad beetle. The results from FE simulations and experiments confirmed that the ellipse shape for the blade has priority over the circular shape in terms of mechanical properties. Besides, including laminated architecture inside the blade's geometry can increase the toughness of the system up to three times in comparison to the homogenous blades, and this method is beneficial for the materials with limited ductility. Thus, this model system represents a tough, resistance biological material that exemplifies a departure from other types of beetles and can be inspired for future engineering applications.

CHAPTER 1. INTRODUCTION

1.1 Literature Review

Nature uses patterned interfaces technique to connect the separate parts or segments inside the carapace of various species. This type of connection causes smooth surfaces in connection joints as well as animal movements (increase flexibility and toughness). The geometrically patterned interfaces are widely used in Nature and provoke many outstanding mechanical properties in biological systems (Lin et al., 2014; Chen et al., 2015; Dunlop et al., 2010, and 2011). In recent studies, these geometrically patterned interfaces named sutures (Achrai and Wagner., 2017; Chen et al., 2011). The sutures interface can be seen through the armors of many species in Nature (Naleway et al., 2015). For example, the leatherback sea turtle osteoderm consists of bony plates interconnected by collagen fibers using sutures. Sutures offer both flexural and interlocking behavior for the carapace and prevent crack propagation between the osteoderms (Chen et al., 2015). The sutures in the red-eared slider turtles connect the rigid ribs in the shell and increase the fatigue resistance of the osteoderm (Achrai et al., 2015). In the armadillo's osteoderm, the bony plates are connected by sutures and non-mineralized interphase collagen fibers and result in enhancing the toughness of the osteoderm (Chen et al., 2011). Alligators are also developed arbitrary bony plates in their osteoderms interconnected by sutures and collagen Sharpey's, which offer both flexibility and protection (Sun et al., 2013). The fish carapace such as arapaima, teleost, and boxfish consist of bony rigid elements embedded in a compliant skin. These dermal armors protect species against the attack of predators (Vereney and Barthelat, 2014; Brute et al., 2008; Meyers et al., 2012; Lin et al., 2011). For instance, the carapace of the boxfish contains scutes, and each scute includes a highly mineralized plate and a compliant collagen base. The mineralized plates connected using triangular sutures shape, and unlike most other species in Nature, the collagen sharpy's does not exist between the teeth (Yang et al., 2015). Another remarkable example of Nature is a woodpecker. Woodpeckers are capable of repeated pecking on a tree at remarkably high deceleration (10000 ms $^{-2}$) without any brain injuries (Gibson, 2006). The study on the red-bellied woodpecker beak revealed that the beak develops suture lines in the outer layer (rhamphotheca)and results in increasing the ability to bear the compressive loads (Lee et al., 2014). The examples of patterned interfaces (sutures) in Nature are shown in Figure 1.1
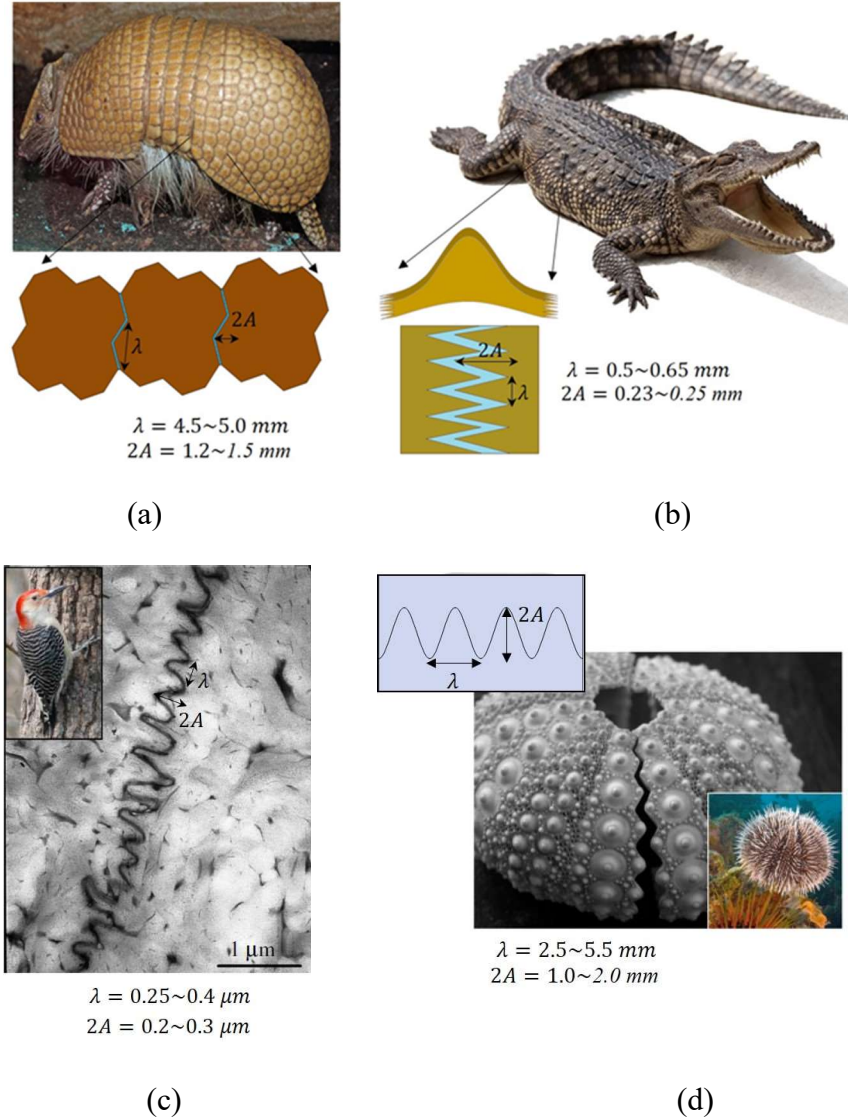
Figure 1.1. Suture structures in Nature: (a) armadillo osteoderm sutures connect by collagen fibers (b) alligator osteoderm contains sutures interconnected by collagen fiber, (c) The cross-sectional view of the woodpecker beak includes sutures (adapted from Lee et al., 2014), (d) sea urchin exhibits an architecture that induces a sinusoidal path (Hosseini et al., 2019).

Sutures interface geometries include broad-ranging in Nature, from flat sutures interface such as infant human skulls (Sun et al., 2004) to complicated, fractal-like designs in ammonite (Saundres et al., 1996). These interfaces not only help to transmit loads and absorb energy but also benefit the systems by increasing mechanical properties such as stiffness and toughness (Li et al., 2012). For instance, role of cranial sutures in the skulls of humans (Miura et al. 2009), dinosaur (Rayfield, 2004), Sus scrofa (Sun et al., 2004; and Popowics et al., 2007), goats (Jaslow et al., 2000), monkey cranium (Wang et al., 2010), Lizard (Moazen et al., 2008) is to protect brain against multiaxial

loadings which occur during impacts or mastication (Wang et al., 2010). For example, the giant theropod dinosaur was capable of producing exceptionally powerful chew forces and resisting multidirectional loadings (Rayfield, 2004). During the loading, the high strain can be distributed through cranial sutures, and thereby, less strain can be experienced in the face (Herring and Ochareon, 2005; Kupczik et al., 2007).

Sutures interlocking behavior have been bioinspired through many numerical analysis (Li et al., 2011, 2012, 2013), finite element analysis (Roth et al., 2007; Rayfield et al., 2007; Jasinoski et al., 2010) and experimental studies (Malik et al., 2016; Mirkhalaf et al.,2014; Porter et al., 2016) . Ortiz and co-workers developed an analytical framework by using the principle of virtual work concept to invest the effect of sutures interface in enhancing the mechanical properties (Li et al., 2011, 2012, 2013). The analytical solutions for stiffness, strength, failure mechanism and toughness were derived for four categories of suture shapes, including different angles (i.e., triangular, trapezoidal, rectangular, and anti-trapezoidal). Among the various sutures geometries, the triangular shape demonstrated the highest stiffness, strength, and fracture toughness in comparison to the other interfacial shapes. It was also shown that the presence of the bound-tip between interfacial layer and tooth geometry or decreasing the tip angle under mode-I loading can increase strain energy and load transfer to the tips and thereby, improve stiffness. Besides, increasing a tip angle can cause more ductile failure of the interface and results in higher toughness. This study suggested that the anti-trapezoidal shape is desired for situations where damage tolerance is required and can increase strain failure due to interlocking mechanical behavior (Lin et al., 2014).

Zavattieri and the co-workers investigated crack propagation along the sinusoidal interface (non-interlocking patterned interfaces) between two identical semi-infinite elastic materials under remote mode-I loading (Zavattieri et al., 2007). The failure consisted of a series of stable and unstable crack propagation under a constant load. The parametric studies stated that the cohesive zone length of the interface, crack tip position, and shape of the initial open crack did not affect effective toughness while it had a significant influence on stable crack propagation behavior between the initiation of crack growth and beginning of unstable fracture. Their results also indicated that for values of the amplitude-to-wavelength aspect ratio (A/λ) larger than 0.5; the effective interface toughness (K_{Ic}/K_0) improved up to three times in comparison to the flat interfaces. Moreover, the authors showed that the Corttel and Rice analytical framework based on

a kinked crack (Cotterell and Rice., 1980) was only valid for small values of aspect ratio ($A/\lambda \leq 0.25$) in the sinusoidal interface (Zavattieri et al., 2007, 2008). In a follow-up study, the fracture toughness between two elastically dissimilar solids under mode-I loading was found to be dependent on the interface aspect ratio, and mismatch in elastic properties (α) (Cordisco et al. 2012). The critical value of α corresponds to the optimized value of K_c / K_0 was varying by changing the values of aspect ratio. Additionally, the authors also observed that the properties of the cohesive interface did not influence its interfacial toughness (Cordisco et al., 2012).

In a subsequent study, the authors accounted for the inelastic behavior of the solid materials around interfacial cracks. This enabled to explore the transition from stable to unstable crack propagation, which causes an increase in the fracture toughness of the interface (Cordisco et al., 2014). In 2016, the failure behavior of patterned interfaces includes two phases of aluminum and polymer was investigated within the computational models by Hirsch and Kästner (Hirsch and K¨astner. 2017). The results stated that, for the constant value of the aspect ratio (i.e., $A/\lambda = 1$), by increasing the length of the RVE, the required nodal force and traction increases under mode-I loading. However, three different failure mechanisms were observed under mode-II depend on the aspect ratios range, which the primary failure mechanism was the transition from adhesive to cohesive failure type(Hirsch and K¨astner. 2017).

Experimental studies on interlocking patterned interfaces noticed a significant improvement in material fracture resistance, especially when fine-tuning considered in the interface topology (Mirkhalaf and Barthelat, 2017). Many researchers have used 3D printing techniques to understand the role of the sutures, such as jigsaw-like suture morphology, which can be found in diatoms and mollusk shells. For instance, in the study by Mirkhalf and Barthelat in 2017, the material toughness of the system was increased up to ten times with respect to the original polymer by using interlocking jigsaw patterns under tensile loading conditions. The idea of using a weaker interface within intricate architectures was also studied by carving weak interfaces using the laser-engraving technique to the aluminum oxide (Malik and Barthelat., 2016).

The process of crack growth in materials is a competition between several dissipation mechanisms. The driving force of a crack is defined by the stress and local crack tip deformation fields and can be presented by the critical energy release rate or fracture toughness. The mechanisms associated with the resulting fracture toughness can be divided into two categories: intrinsic and extrinsic. In the intrinsic mechanisms, toughening is achieved by increasing the inherent microstructural resistance and usually occurs ahead of the crack tip. The extrinsic mechanisms occur wake of the crack tip and work to delay the crack propagation (Ritchie 1988, 1999). The study by Anderson et al. in 1979 presented the effect of fine-tuning the interface topology by performing the experiments such as increasing the surface areas (i.e., intrinsic mechanism) and controlling the roughness parameter at the material interfaces (Anderson et al., 2005). Another study by Evans and Hutchinson (Evans and Hutchinson 1989) stated that the toughening in the patterned interfaces result from the contact interaction and shear locking behind the crack (i.e., extrinsic mechanism). Bridging techniques, also known as an effective way along with plastic deformation to increase interface toughness under large deformations (Oh et al., 1988). A combined experimental and theoretical study of crack propagation along sinusoidal patterned interfaces in a double cantilever beam of different aspect ratios under mode-I revealed that the fracture resistance could increase with the aspect ratio. Besides, the crack initiation and propagation could be significantly delayed by increasing the aspect ratio of the sinusoidal patterned interfaces and results in a significant increase in the values of effective toughness (Cordisco et al., 2016).

1.2 Motivation for this study

As previously discussed in section 1.1, the geometrically patterned interfaces seem to be a common motif in Nature. Under various loading conditions, two types of behavior can be expected for patterned interfaces:

i) Non-interlocking patterned interfaces (e.g., patterned interfaces exist inside the sea urchin, ammonites, and diatoms under tensile loadings)

ii) Interlocking patterned interfaces (e.g., the interlocking interfaces exist in the boxfish carapace, Ironclad beetle cuticle, turtle, and alligator osteoderms under shear and compression loadings).

In the present study, the role of both non-interlocking and interlocking patterned interfaces on enhancing the mechanical properties will be investigated. Therefore, the motivations for this study are summarized as follows:

Motivation 1: To understand the role of the shape of the crack behind the crack tip in non-interlocking sinusoidal pattern interfaces under remote mode-I loading.

The next focus of this study is to understand the role of interlocking patterned interfaces primarily inspired by Lactoria cornuta (boxfish) and Zopherinae Ironcladad beetle. These two species were selected because of their performance against the attack and multiaxial loads, as well as their specific architecture.

Therefore, the second motivation for this study is to understand the role of boxfish architecture. During the shear test between two scutes of boxfish carapace, the damage only occurs around sutures, and therefore, the primary motivation for this part of the study is to understand the effect of architecture inspired by boxfish scute in controlling the crack direction. The boxfish carapace is presented in Figure 1.2 (a). Thus, the second motivation for this study can be expressed as follows;

Motivation 2: To understand the protective role of boxfish scute architecture in controlling the crack direction under shear loading.

Finally, the elytra of the Ironclad beetle (Figure 1.2(b)) adopted an incredibly strong and tough interdigitated set of ellipsoidal shaped blades connection (dovetail joints) that resemble pieces of a puzzle. The role of homogenous jigsaw interlocking blades on enhancing the mechanical properties previously investigated by Mirkhalaf and Barthelat in 2017. Based on this study, two competing mechanisms exist under tensile loading; i) pullout and ii) fracture in the neck. Blades in the Ironclad beetle developed a puzzle-like laminated architecture, and under loading (i.e., compression loads), delamination inside the blades is primary reason for the failure. Thus, I hypothesize that elliptical geometry, the number of blades, and puzzle-like laminated architecture in Ironclad beetle suture incorporate additional interlocking features to resist fracture by uniformly distributing stress and developing delamination. Thereby, the next motivation for this study will be presented as follows;

Motivation 3: To gain insight into the mechanics of the interlocking sutures in Ironclad beetle and understand the benefits of having layered architecture inside the interlocking joints.

<center>(a)   (b)</center>
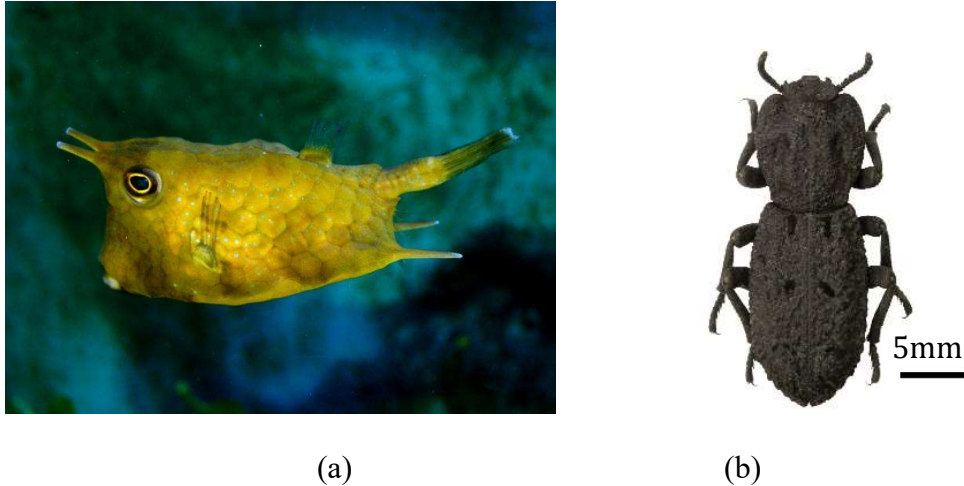
Figure 1.2. (a) Image of Lactoria cornuta (b) Image of Diabolical Ironclad beetle (*P. diabolicus*)

1.3 Goals and objective of this research

The goal of this study is to gain a fundamental understanding and provide new insight into the mechanics of naturally occurring patterned interfaces (interlocking and non-interlocking) in order to achieve similar performance in biomimetic materials and structure.

Therefore, the following objectives are presented for this study

Objectives:

1) To expand our understanding about the mechanics of naturally occurring patterned interfaces and their role in protection against attack and under multiaxial loadings

2) To investigate the role of architecture (geometry and mechanical properties) in preventing catastrophic failure in the bio-inspired system.

3) To develop a guideline to design and fabricate a biomimetic material that can achieve similar performances to this biological material so that it can be translated to engineering, biomedical, and aerospace engineering applications.

To achieve the above goal and objectives, the following tasks are required to get a better insight into the mechanics of interlocking patterns:

- Analytical method

- Numerical approach

- Experimental procedure (3D printing, biomimetic, etc.)

One of the focus of this research is to understand the role of pattern interfaces in the toughening mechanism of the system. The role of the crack shape behind the crack tip in the toughening of the patterned interfaces is studied under remote mode-I loading conditions. For this purpose, the sinusoidal pattern interfaces were evaluated regarding the interface fracture toughness of both low and high asperity aspect ratios. For all the aspect ratios, two identical linear and elastic solids bonded together within a semi-infinite domain using a patterned interface. In addition, the fracture process zone is assumed to be infinitely small in comparison to the size of the pattern, and therefore, the linear elastic fracture mechanics (LEFM) concept was applied along with the numerical *J-integral* to evaluate the role of the shape behind the crack tip. Besides, I studied the ability of LEFM models (i.e., single and double kinked crack models) to estimate the role of the crack shape behind the crack tip for different values of aspect ratios. These models enable us to get a better insight into understanding the effect of patterns shape on the effective toughness in comparison with numerical results. Finally, a relation between the material fracture resistance, mechanical properties, and the characteristic geometrical lengths of the pattern is investigated for the sinusoidal patterned interface of different aspect ratios (fracture process zone is large with respect to the size of the patterns) by considering two approaches; (a) A finite element models of sinusoidal pattern interface using cohesive zone method (CZM) (previously discussed by Coredisco 2016; Hosseini et al., 2019) and (b) Experimental procedure using 3D printed samples of the sinusoidal patterned interface. During the tensile test on 3D printing samples, the Digital Image Correlation (DIC) technique was utilized along with the experiment to get a better insight into the strain distribution as well as crack propagation inside the patterned interfaces. The experimental results are used as an asset to confirm analytical and numerical solutions. The results and more discussions are presented in Chapter 2.

Chapters 3 and 4 present an in-depth study of boxfish carapace architecture. The material characterization of both collagen base and mineralized plate, as well as the role of collagen architecture (bouligand architecture), are investigated in Chapter 3. The role of boxfish carapace architecture in controlling the crack direction under shear loading is discussed in chapter 4.

Boxfishes develop defense mechanisms (carapace architecture) which are different from other types of fish. In particular, four types of scale can be observed in fish which are categorized as; i) overlapping elasmoid scales in teleost, ii) interlocking ganoid scales in gars and bichirs, iii) partially imbricated placoid scales in sharks, iv) tessellating carapace scute in boxfish (Porter et al., 2017). As previously discussed, boxfish scutes contain a thin layer of very brittle mineralized plate (hydroxyapatite) which is placed on top of soft collagen subbase. Also, the mineralized plates develop sutures around its hexagonal plates. Boxfish carapace developed scutes similar to reptiles such as alligator, turtle, armadillo (Chen et al., 2015, Achrai et al., 2015, Chen et al., 2011, Sun et al., 2013) and used sutures for the purpose of connection. In most of the reptiles, the sutures connection are made through collagen sharpy's while in boxfish; there is no connection between sutures. The shear test between two scutes revealed that the cracks are arrested around sutures area and thus, I hypothesize that the presence of sutures in its current combination (thin brittle plates on top of a compliant collagen base) can help to control the crack propagation direction in the mineralized plate under shear loading. To understand the correct behavior of the boxfish armor carapace, various methodologies were employed such as the finite element method, experiment on boxfish carapace, 3D printing, and molding techniques. In Chapter 3, I characterized the material properties of both collagen base and mineralized plate through reverse engineering techniques by using the FE models and in-situ experiment. In addition, the role of bouligand architecture inside the collagen subbase was investigated through FE model to understand the effect of the orientation of the layers in increasing toughness inside the collagen.

Chapter 4 mainly focuses on the effect of scute architecture inspired by boxfish carapace in controlling the crack direction under shear loading conditions. For this purpose, the biomimetic samples are created using gypsum (brittle plate) and silicone (soft substrate). The gypsum samples were created by using the silicon molding technique. Finally, the assembly of gypsum, silicone with a variety of sutures angle were tested in shear using the universal tensile testing machine (MTS). The DIC method accompanied during the experiments to capture the crack propagation and strain distribution. In addition, the FE models similar to biomimetic samples were developed through FE software ABAQUS for the purpose of comparison with experiments and better insight into the crack propagation process. This chapter continues by deriving the simplified analytical models based on LEFM approach along with finite element solutions to predict the role composites

(the modulus and strength aspect ratio of the soft sub base to brittle plate) with an inclined crack and its effect in controlling the crack propagation direction.

The compression resistance nature of Ironclad beetle is presented in Chapter 5. This chapter focuses on the abdominal portion of the Ironclad beetle exoskeleton, consisting of the elytra and ventral cuticle. The ordered arrangement and complex architectures found within the exoskeleton (elytra) of this specially adapted insect result in extremely high compressive resistance, far beyond any other beetle identified to date. More specifically, I wanted to understand the role of sutures connecting elytra parts in the Ironclad beetle. To date, structure-mechanical property relationships of blades have not yet been fully realized for the ironclad beetle's exoskeleton. Here, by using a combination of optical and electron microscopy, computed tomography and mechanical testing, 3D printing prototype, and finite element analysis, the unique adaptations, novel architectural design features and interfacial structures have been revealed within the exoskeleton of *P. diabolicus* and their divergence from terrestrial Coleoptera.

The role of laminated architecture inside the interlocking blades bio-inspired by Ironclad beetle is studied in Chapter 6. In the Ironclad beetle blades, the arrangement of ultra and microstructural features associated with enhanced mechanical performance. Previous studies by Barthelat and Ortiz groups (Malik et al., 2017, Mirkhalaf and Barthelat, 2017, Porter et al., 2017, Li et al., 2011, 2012) revealed the presence of two competing mechanisms inside the homogenous interlocking patterns such as pullout and fracture. However, the blades in Ironclad beetle consist of laminated architecture and result in delamination which is a dominant failure mode. Therefore, the architecture inside the Ironclad beetle adds a new competing mechanism to the system, which is required to be studied. This chapter mainly focuses on the failure mechanism of sutures, specifically, blades architecture with focusing on three competing mechanisms such as; pullout, delamination, and fracture. It is essential to understand why Nature follows this design and what are the benefits of having delamination over two other competing mechanisms. Both finite element analysis and 3D printing experiments are used to derive a better understanding of these new interlocking joints mechanisms. Finally, studying a single multi-layered blade enabled us to design multilayered composites by avoiding damage localization and increasing the toughness.

The conclusions and findings of this study, along with future recommendations are presented in Chapter7.

1.4 Justification for this research

Nature uses sutures or blades as a technique to connect separate parts. It causes smooth surface in connection joints and helps the animal movements (e.g., increase flexibility and toughness). In real life, many applications use interlocking interfaces or joints to connect separate parts, for instance, hull panels in rowboats, sectional kayaks, and interlocking panels in construction fields to reduce earthquake loads(Ali et al., 2012; Ghaffary and Karami, 2018 and 2019; Hosseini., 2013). The new Samsung's foldable phone-tablet uses the interlocking joint connections to provides a customer with a large screen and the ability to fold the instruments. Dovetail joints in the gas turbines are another example of interlocking joints. In aero-engine rotating discs (i.e., gas turbines), the connection between the blades and disc provided using dovetail joints (Ruiz et al., 1984). In addition, connecting various materials (i.e., polymer, ceramic, steel, and aluminum) in composites always being a significant challenge in various industries such as aerospace and construction; as a result, there is a need for a proper connection techniques such as patterned interfaces between various materials (Kim et al., 2010; Ghavami et al., 2019; Ghavami, 2014). Here, I suggest the interlocking joints as a technique to connect various materials in order to increase bonding and avoid the present challenges. In general, this application is useful in any connection that smooth surfaces were required or bolts and nuts techniques are not desired. Studying Nature is a key that provides us an insight into the mechanism of patterned interfaces and eventually helps us to develop and improve design and guidelines for biomimetics materials.

CHAPTER 2. INVESTIGATING THE ROLE OF NON-INTERLOCKING SINUSOIDAL PATTERENED INTERFACES ON THE EFFECTIVE TOUGHNESS UNDER REMOTE MODE-I LOADING

2.1 Introduction

Non-interlocking patterned interfaces seem to be a common motif in Nature. In particular, geometry seems to play an essential role in increasing the strength, toughness, and damage tolerance among different species. Here, the role of the shape of the opening crack behind the crack tip is investigated for the sinusoidal patterned interfaces as the crack propagates along the interface. In particular, I studied the shape of the interface behind the crack tip for different amplitude-to-wavelength aspect ratios with two analytical models and compared the results with finite element simulations through the J-integral. Additionally, I studied the role of material length scale by investigating the relationship between the geometrical characteristic lengths and the emerging material length scale using a finite element-based cohesive zone model and 3D printing prototyping technique. The results suggest that geometrical toughening is influenced by a size effect, but it is bounded between two extreme conditions.

2.2 Problem Formulation

Two semi-infinite, identical elastic materials with Young's modulus E and Poisson's ratio ν are bonded along with an interface for a periodic sinusoidal pattern morphology. The sinusoidal morphology is presented as follows.

$$y(x) = A[1 + sin\ (2\pi\{x - \frac{\lambda}{4}\}/\lambda)] \tag{2.1}$$

Where 2A is a peak to valley amplitude of the interface and λ is a wavelength where the ratio of A/λ is defined as an asperity aspect ratio. The value of kink angle γ has different values through the period of sinusoidal pattern and is defined as an angle between the horizontal line and tangent to the sinusoidal pattern. The solid is assumed to be sufficiently strong and tough with respect to the interface for all the cases. As such, the crack is constrained to growth along with the interface. Before the initial loading is applied, the crack tip is placed at $(x, y) = (0, 0)$ (coincident with the center of coordinates). The open crack is represented by the region $x < 0$; whereas the interface is initially defined for $x \geq 0$. The valleys are presented by the positions $x=n.\ \lambda$, and the peaks by the

positions *x=n (λ /2)*, where *n=1, 2, ...* represents the period number from the original crack tip position. The model domain is assumed to be in-plane strain, and the load is applied through a monotonically increasing mode-I stress intensity factor, K_I. Since the materials are in linear elastic regime, the thickness near the crack tip does not affect the results and the K field results are valid and not dependent on the thickness. However, in an elastic-plastic material, thickness plays an important role, especially near the crack front and, therefore, influences the response of the material (i.e. deriving force) (Kotousov and Wang, 2002; Kotousov et al., 2013; Zavattieri 2006).

An asymptotic K-field is applied as displacements at the boundary of the domain at a distance R_0 from the initial crack tip, assuming LEFM conditions hold in the entire domain, except near the crack tip where details of the interface become important. Equations 2 and 3 represent the applied displacement at the boundary for a given value of K_I.

$$u_x = \frac{2(1+v)K_I}{E}\sqrt{\frac{R}{2\pi}}\cos\frac{\theta}{2}\left(2 - 2v + sin^2\frac{\theta}{2}\right) \tag{2.2}$$

$$u_y = \frac{2(1+v)K_I}{E}\sqrt{\frac{R}{2\pi}}\sin\frac{\theta}{2}\left(2 - 2v + cos^2\frac{\theta}{2}\right) \tag{2.3}$$

Where $R = \sqrt{x^2 + y^2} \gg A$, $\theta = tan^{-1}(y/x)$. The crack will begin to propagate when K_I reaches its critical value. Moreover, Interface assumed to be weaker than the elastic solids, so the crack always propagates along the interface.

(a)

(b)

(c)
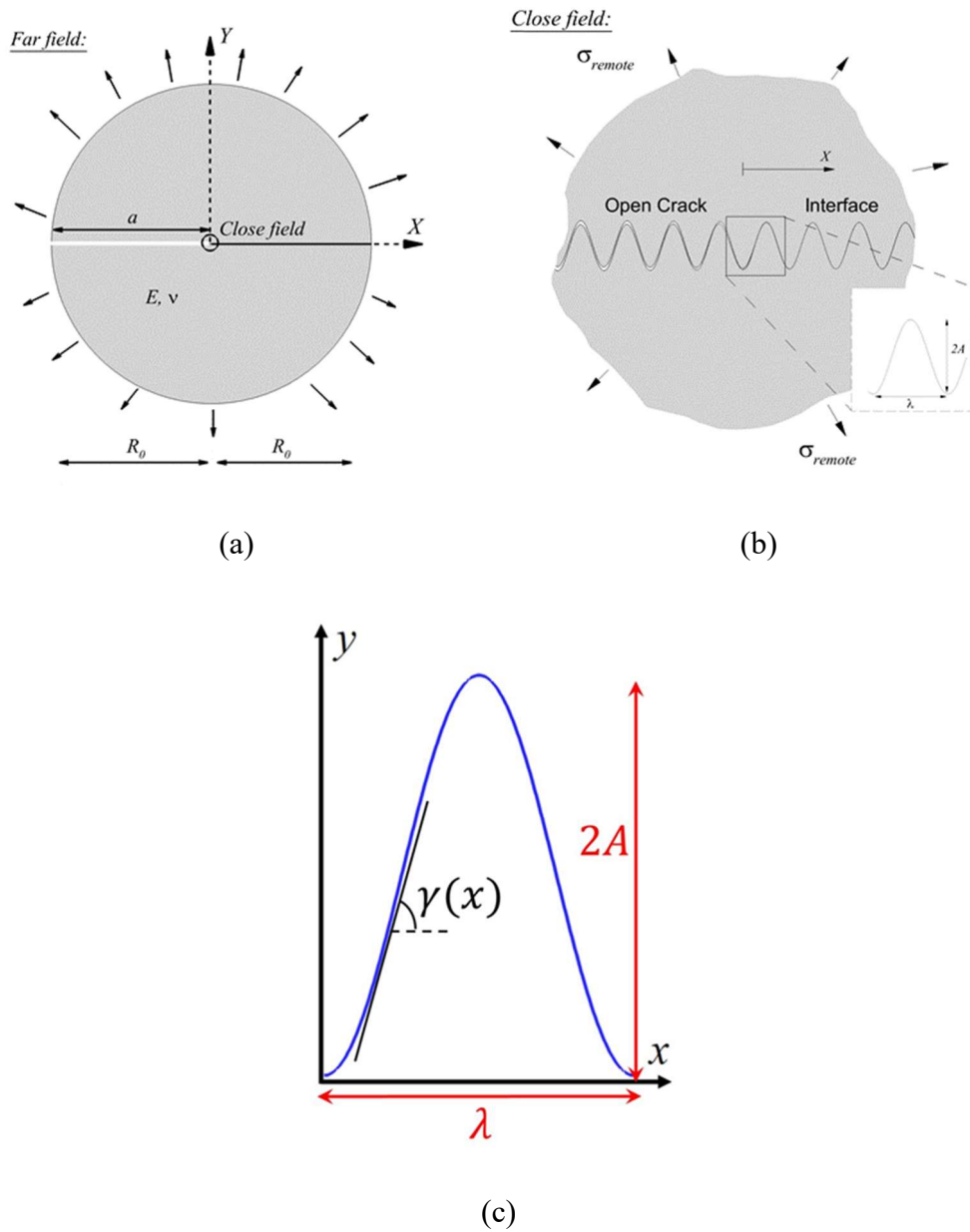
Figure 2.1. a) Schematic of the semi-infinite crack growing along a sinusoidal patterned interface. (b) Details near the crack tip. The interface has a sinusoidal profile with amplitude A and wavelength λ as denoted in the inset figure. Schematics of one period of (c) the sinusoidal pattern where kink angle ($\gamma(x)$) is for different patterns Linear Elastic Fracture Mechanics (LEFM)

According to LEFM, there exists a remote critical interface toughness, K_{Ic}, which corresponds to the unstable crack tip growth without an increase in the applied K_I. We are interested in the determinating the relationship between K_{Ic} and fracture toughness of a reference interface, K_0. In this study, the size of fracture process zone, l_{fp}, is much smaller in comparison to the patterns length (i.e. A, λ), $l_{fp} << A$, λ, the crack tip energy release rate for the flat interfaces can be approximated by Irwin's expression shown in Equation 2.4 (Anderson et.al., 1995).

$$G = \frac{(1 - v^2)}{E}(k_1^2 + k_2^2), \qquad \psi = tan^{-1}\left(\frac{k_2}{k_1}\right) \tag{2.4}$$

Where k_1, k_2 are the asymptotic local stress intensity factors and ψ is the phase angle between the shear and normal stresses. Inorder for crack to growth in an interface subjected to remote loading conditions the following equation should be satisfied

$$G = G_c(\psi) \tag{2.5}$$

Where $G_c(\psi)$ is the phase-dependent critical energy release rate of the interface. In the case of the flat interface, the critical condition is $G_0 = G_c(\psi = 0)$, and Equation 2.6 takes the form as follows

$$K_{Ic} = K_0 = \sqrt{E \cdot G_0/(1 - v^2)} \tag{2.6}$$

In Equation 2.6, K_0 represents the maximum remote stress intensity factor needed to break the flat interface. To obtain the K_{Ic} in the triangular pattern field, the local stress intensity factors need to be measured by the numerical *J-integrals* around the crack tip, and this is accomplished by using the virtual crack extension domain integral method implemented in ABAQUS (Parks., 1977 and Shih et al., 1986). In our model, the critical energy release rate is assumed to be independent of the phase angle at any crack tip position of the triangular interface, i.e., $J = G_c(\psi) = G_0$. Thereby, one can obtain the normalized fracture criterion for crack growth in a pattern interface as follows (Equation 2.7),

$$\frac{K_I}{K_0} = \frac{1}{\sqrt{E \cdot J/(1 - v^2)K_I^2}} \tag{2.7}$$

Assuming the resistance to crack growth is independent of the intrinsic interface work of fracture($\Gamma_c = \Gamma_0$), following the Griffith criterion (Anderson, 1995) we have,

$$\frac{G_{Ic}}{G_0} = \frac{A_0}{A_s} \tag{2.8}$$

In Equation 2.8, G_{Ic} and G_0 represent the remote critical energy release rate needed to extend the crack along the sinusoidal and flat interfaces, respectively. The characteristic area for the sinusoidal interface is represented by A_s (the projection of sinusoidal pattern area into the horizontal direction) while the equivalent flat area is presented by A_0. Equation 2.8 indicates the interface toughening results from the increase in the area in a pattern interface adds to an equivalent flat interface. Following Irwin equation (Anderson, 1995), Equation 2.8 can be expressed in a new form as Equation 2.9 regarding the normalized stress intensity factor,

$$\frac{K_{Ic}}{K_0} = \sqrt{\frac{A_0}{A_s}} \tag{2.9}$$

2.2.1 The single and double kinked crack models

In this section, we present analytical approaches that can be used to explain the role of the shape of the crack behind the crack tip as the crack grows along the interface. The concept of the kinked crack tip in an infinite domain using a LEFM was first developed by Bilby and Cardew (1975). A solution for kinked crack has been proposed for the local elastic stress intensities at the crack tip (Bilby and Cardew, 1975; Cotterell and Rice, 1980). Similarly, in 1983, Sures developed an analytical model for a double kinked crack case based on the models developed by Cotterell and Rice (1980) (Suresh., 1983). The schematic of the single and double kinked crack models is shown in Figure 2.2(a) and (b), respectively. The local stress intensity factors at the crack tip can be represented by Equation 2.10 (Bilby and Cardew, 1975).

$$k_1 = c_{11}(\alpha) \cdot K_I + c_{12}(\alpha) \cdot K_{II} = c_{11}(\alpha). K_I \tag{2.10}$$

$$k_2 = c_{21}(\alpha) \cdot K_I + c_{22}(\alpha) \cdot K_{II} = c_{21}(\alpha) \cdot K_I$$

Where k_1, k_2 are local stress intensity factors at the crack, and K_I, K_{II} are the global stress intensity factors for mode I and II, respectively. Also, α denotes the angle between the crack and the x-direction. A single kinked crack model assumes that the length of the kinked crack is much smaller

than the length of the main crack, $a >> b$ (see Figure 2.2(a)). Since the crack tip stress intensities are for mode I loading, thereby, $K_{II} = 0$. The first order solutions for the angular functions can be expressed as (Cotterell and Rice, 1980)

$$c_{11}(\alpha) = cos^3\left(\frac{\alpha}{2}\right) \tag{2.11}$$

$$c_{12}(\alpha) = -3 \sin\left(\frac{\alpha}{2}\right) cos^2\left(\frac{\alpha}{2}\right)$$

$$c_{21}(\alpha) = \sin\left(\frac{\alpha}{2}\right) cos^2\left(\frac{\alpha}{2}\right)$$

$$c_{22}(\alpha) = \cos\left(\frac{\alpha}{2}\right)\left[1 - 3\sin^2\left(\frac{\alpha}{2}\right)\right]$$

For the double kinked crack model, *a, b, b'* represents the length of the crack segments, and it assumes that $a>>b>>b'$. The local stress intensity factors for a double kinked crack case subjected to a remote mode I K_I field can be calculated using Equation 2.10. As the second kink (*b'*) develops, the stress intensity factors at the tip of the second kinked can be obtained by substituting the stress intensities of the first kink in Equation 8 for K_I and K_{II}, respectively, and by setting $\alpha = \alpha'$. This leads to the angular functions for the double kinked crack model (Suresh, 1983):

$$c_{11}(\alpha) = cos^3(\alpha/2)\,cos^3(\alpha'/2) + 3\,sin(\alpha/2)\,cos^2(\alpha/2)\,sin(\alpha'/2)\,cos^2(\alpha'/2)$$

$$c_{21}(\alpha) = cos^3(\alpha/2)\,sin(\alpha'/2)\,cos^2(\alpha'/2) - sin(\alpha/2)\,cos^2(\alpha/2)\,cos(\alpha'/2)\,[1 - 3\,sin^2(\alpha'/2)] \tag{2.12}$$
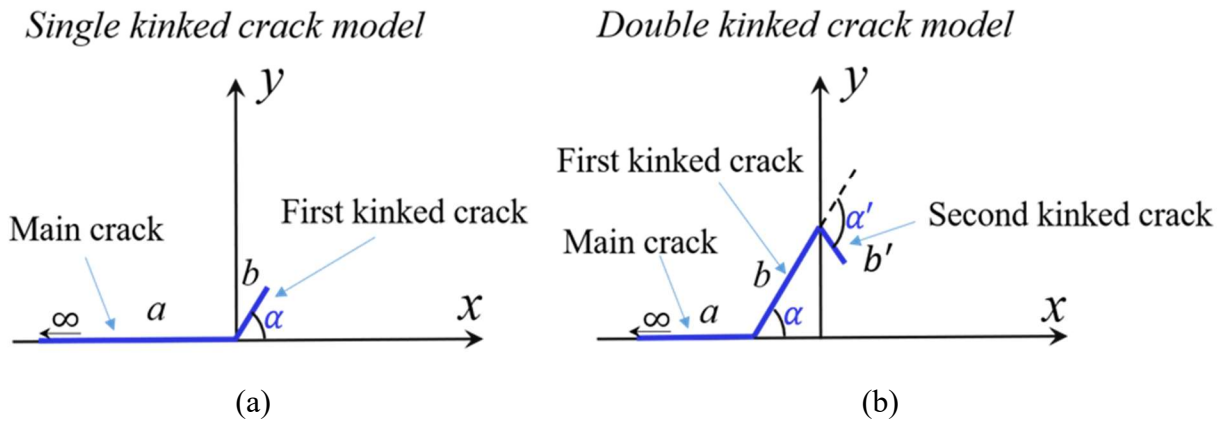
Figure 2.2. (a) The single and (b) double kinked crack models. The values a, b, b' represent the length of the crack segments (a>>b>>b').

In Equation 2.7, K_I/K_0 represents the maximum normalized global stress intensity factor needed to propagate the crack an infinitesimal distance along a patterned interface normalized with respect to the one needed for a flat growing crack. By assuming $G_0 = G_c(\psi = 0)$ and replacing Equation 2.10 into Equation 2.7, the analytical solution for K_{Ic}/K_0 can be achieved in terms of the angular functions.

$$\frac{K_{Ic}}{K_0} = \frac{1}{\sqrt{c_{11}^2 + c_{21}^2}} \tag{2.13}$$

2.2.2 Cohesive Zone Model

A cohesive zone model, CZM, is employed here to represent the interfacial decohesion at the bonded interface The CZM can be defined as a fracture process zone ahead of the crack tip which usually occurs due to the plasticity or microcracking, and it can be used to predict the uncracked region especially for the inelastic materials. In the LEFM approach, the fracture process zone ahead of the crack tip is negligible and can be ignored, while for the inelastic materials the size of the nonlinear fracture process zone is significant in comparison to the size of the crack geometry (Elices et al., 2001). As a result, the CZM introduces a new material length scale to the system considering that the crack develops a fracture process zone ahead of the crack tip. When the length of this fracture process zone, l_{cz}, is much larger than any other geometrical features of the patterned interface, no closed-form solution can be obtained, and LEFM is no longer valid. As such, a numerical solution is needed, and results can be compared with the LEFM predictions which represent the extreme case when l_{cz} is much smaller than any other characteristic length scale. This will enable us to get an insight into a relationship between the material fracture resistance, mechanical properties, and emerging characteristic lengths scales.

In this model, the gradual degradation of the mechanical behavior in the fracture process zone is modeled using the cohesive traction-separation law which characterizes the inelastic contribution to the problem of interfacial debonding. Several cohesive constitutive models detailed in literature can be used to describe the CZM and fracture process zone ahead of the crack tip (Camacho and Ortiz, 1996; Espinosa and Zavattieri, 2003; Li et al., 2006; Tvergaard and Hutchinson, 1993; Xu and Needleman, 1994). In this section, a Tvergard-Hutchinson traction-separation law (Tvergaard & Hutchinson, 1993) is adopted. The Tvegard-Hutchinson traction-separation law relates the normal (Δ_n) and tangential (Δ_t) displacement discontinuities with the normal (T_n) and tangential

(T_t) tractions and has been successfully applied to describe single and mixed mode decohesion in adhesive joints in composites (Li et al., 2006) and metals.

Viscosity parameters introduced to regularize instabilities during the initial crack propagation process. The strength of the cohesive interface in mode I and II (σ_{max}, τ_{max}, respectively) are defined as the peak stress of the traction-separation law for normal and shear modes and the work of separation as the energy dissipated by separation interfaces. Previous studies found that the ratio between the normal work of separation and the tangential work of separation has negligible effects in the effective toughness of the sinusoidal interfaces between similar elastic bodies when compared to flat interfaces (Zavattieri et al., 2007) for $A/\lambda < 2.0$. Consequently, the values of normal and shear separation is chosen to be equal ($\delta_n = \delta_t$) in such that the cohesive strength of the sinusoidal interface in both Modes I and II is the same, $\sigma_{max} = \tau_{max}$ and the work of separation is $\Gamma_{Ic} = \Gamma_{IIc} = \Gamma_c$. Finally, for purposes of comparison between the cohesive work of separation for flat (Γ_0) and patterned interfaces is chosen such that $\Gamma_c = \Gamma_0$.

Similarly, for a semi-infinite flat crack under a remote K_I field, $\Gamma_0 = G_0$ (Cotterell and Rice, 1980). Under these assumptions, the CZM traction separation law is characterized by two intrinsic interfacial mechanical properties, σ_{max} and G_0. Both can be used to estimate the size of the fracture process zone, l_{cz} (Rice, 1980)

$$l_{cz} = \frac{9\pi}{32} \cdot \frac{E}{(1-v)} \cdot \frac{\Gamma_0}{\sigma_{max}^2} \qquad (2.14)$$

2.3 Dimensionless analysis for a patterned interface

In general, within the CZM framework, the stress singularity obtained at the crack tip in the LEFM solution is substituted with a finite non-linear traction-separation law along l_{cz}. For the case of flat crack, $l_{cz} << R_0$, and therefore, the CZM solution converges to LEFM. However, when l_{cz} is comparable with respect to the pattern interface characteristic lengths (i.e., A, λ), the effect of l_{cz} needs to be considered (Cordisco et al.,2016).

As such, K_{Ic} is expected to be a function of the geometrical parameters (A, λ), material properties (E, v, l_{cz}), and the cohesive law parameters ($\sigma_{max}, \tau_{max}, \delta_n, \delta_t$). Based on the assumptions discussed

before for CZM, some parameters such as δ_n, δ_t are assumed to be constant and removed from the analysis. We also assumed that $\sigma_{max}/\tau_{max} = 1.0$, and it could be removed. Therefore, the dimensionless groups can then be expressed as follows,

$$\frac{K_{Ic}}{K_0} = \Gamma\left(\frac{A}{\lambda}, \frac{\sigma_m}{E}, \frac{l_{cz}}{\lambda}, v\right) \tag{2.15}$$

The pattern normalized characteristic length is defined as the asperity aspect ratio, A/λ, and the material normalized characteristic length scale is defined by l_{cz}/λ. For $l_{cz}/\lambda > 1.0$, the cohesive zone length is significantly larger than one sinusoidal asperity. In a larger area, the normal traction should also depend on the stress distribution along the sinusoidal morphology. A schematic of the cases with small and large cohesive zone length with respect to the geometrical length scale is shown in Figure 2.3.

Presumably when $l_{cz}/\lambda > 1.0$, the fracture process zone is much larger than the geometrical features of the interface that the effect on the fracture energy could be in principle considered as an increase in effective area where the actual decohesion process takes place. As such, and following the Griffith criterion on the crack growth, we will have

$$\frac{G_{Ic}}{G_0} = \frac{A_0}{A_s} \tag{2.16}$$

In Equation 2.16, G_{Ic} and G_0 represent the critical energy release rate needed to extend the crack along the sinusoidal and flat interfaces respectively. A_s represent the characteristic area for the sinusoidal interface, while the equivalent projected flat area is presented by A_0 (Figure 4(b)). Equation 2.16 describes the interface toughening results from the increase in the area in a pattern interface that adds to an equivalent flat interface. Following Irwin equation (Anderson, 1995), Equation 2.16 can be expressed regarding the normalized stress intensity factor,

$$\frac{K_{Ic}}{K_0} = \sqrt{\frac{A_0}{A_s}} \tag{2.17}$$
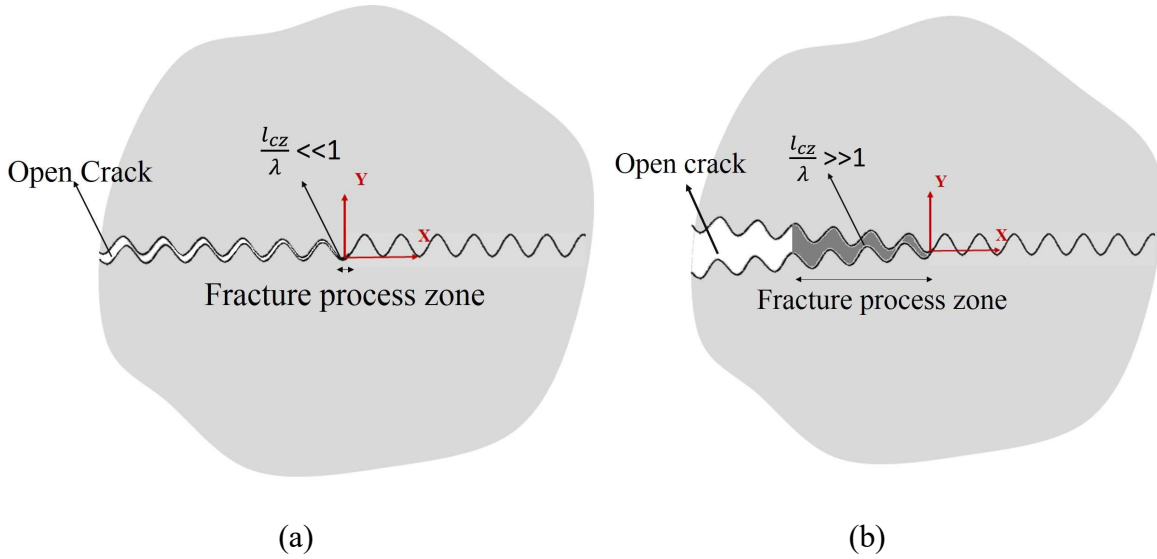
Figure 2.3. (a) The cohesive zone length is very small compared to the length of the pattern ($\frac{l_{cz}}{\lambda} \ll 1$), (b) the cohesive zone length is larger than sinusoidal asperity ($\frac{l_{cz}}{\lambda} \gg 1$)

2.4 Analytical and Numerical role of sinusoidal patterned interfaces on the toughness

In this section, the effect of sinusoidal non-interlocking patterned interfaces on the effective toughness is investigated using both analytical models (single and double kinked cracks) and numerical *J*-integral method. The effective toughness is calculated for different values of the aspect ratio for the sinusoidal non-interlocking patterned interface. At the end of this section, the results from the sinusoidal non-interlocking pattern will be compared to the non-interlocking triangular and arbitrary patterns that discussed previously by Hosseini et al., 2019.

2.4.1 Sinusoidal non-interlocking patterned interfaces

In this section, several sinusoidal pattern interfaces with aspect ratios ranging between *0.0 < A/λ ≤ 2.0* were studied. The fracture process zone is assumed to be infinitely small with respect to the size of the pattern, and therefore, the single and double kinked crack approaches can be utilized along with a numerical *J*-integral method to study the effect of shape behind the crack tip. Cases with larger fracture process zone will be investigated in section 2.4.

The role of the shape of the crack behind the initial crack tip in the sinusoidal pattern was investigated by Zavattieri et al., 2007. In that study the authors considered two different shapes for the initial crack path; i) half sinusoid interface (an initial straight crack with the crack tip located

at the transition from straight to sinusoid), ii) full sinusoid interface, where the crack tip placed within the sinusoidal path (see Figure 2.4(a)). For the case of the half-sinusoidal interface, the first and second instabilities occur at $x/\lambda = 1/3$ and $x/\lambda = 1/2$ respectively. It is also observed that the value of K_I/K_0 for a second instability in the half-sinusoidal case is equal to K_{IC}/K_0 of the full-sinusoidal case. From the second instability, the crack grows indefinitely at constant load and, as such, that point was selected as the effective toughness of the half-sinusoidal interface (Figure 2.4(b)). For the half-sinusoid case, the first instability of the interface path follows exactly the LEFM results predicted by single kinked crack approximation while the second instability falls exactly on the effective interface toughness (K_{IC}/K_0) calculated from the numerical J-integral as presented in Figure 2.4(c). This results lead to two important observations : (1) It pattern needed a lower load (lower K_I/K_0) to trigger unstable crack propagation when the shape of the open crack behind the crack tip is flat in comparison to the sinusoidal pattern. Figure 2.4(a) shows the difference in the stress distribution surrounding the crack tip suggesting that the sinusoidal shape of the crack behind the crack tip may shield the crack tip and therefore delaying the unstable crack propagation, (2) The single kinked crack approximation is better suited for predicting the first instability in the half-sinusoidal case. This occurs because the shape of the open crack in the single kinked crack is indeed flat and matches the general shape of the single kinked crack model as shown in Figure 2.2(a). In order to predict the second instability in the half-sinusoidal case (or the first instability in the full-sinusoidal case), which corresponds to the effective toughness of the sinusoidal interface, a more complex description of the sinusoidal geometry of the open crack behind the crack tip is may be required. As a result, the two conditions with the analytical models (single and double kinked crack models) were utilized to understand the role of the shape behind the crack tip.

The single kinked crack approach is adopted such that, for each point along the sinusoidal path, the crack tip is defined as a tangent to the sinusoidal path and the kinked angle is defined by the angle between the tangent and the horizontal line. By using this method, Zavattieri et al. (2007) demonstrated that the effective toughness of the interface, K_{IC}/K_0, can be reasonably estimated with the single kinked crack approach for $A/\lambda < 0.25$. However, it becomes less accurate for $A/\lambda > 0.25$. Although the results stated that the angle at the crack tip plays an important role in the value of K_{IC}/K_0 for the $A/\lambda < 0.25$, some geometrical aspect of the sinusoidal crack behind the crack tip seems to be missing for larger aspect ratios. Therefore, we aim to employ the double

kinked crack model to determine if more information about the shape of the crack behind the crack tip plays an essential role on the effective toughness, especially for the higher values of the aspect ratio. Figure 2.4(d) shows the effect of shape on K_{IC}/K_0 for $A/\lambda = 0.5$ by changing the angle α (see Figure 2.2(b)) in the double kinked crack model definition and placing a crack tip at $x/\lambda = 0.25$ (From the single kinked crack approach, for $A/\lambda = 0.5$, the K_{IC}/K_0 occurs at $x/\lambda = 0.25$). The comparison between single kinked, the double kinked crack and numerical J-integral method for different values of α (Figure 2.4(d)) suggest that, as the angle α increases, the double kinked crack solution converges to the numerical J-integral method.
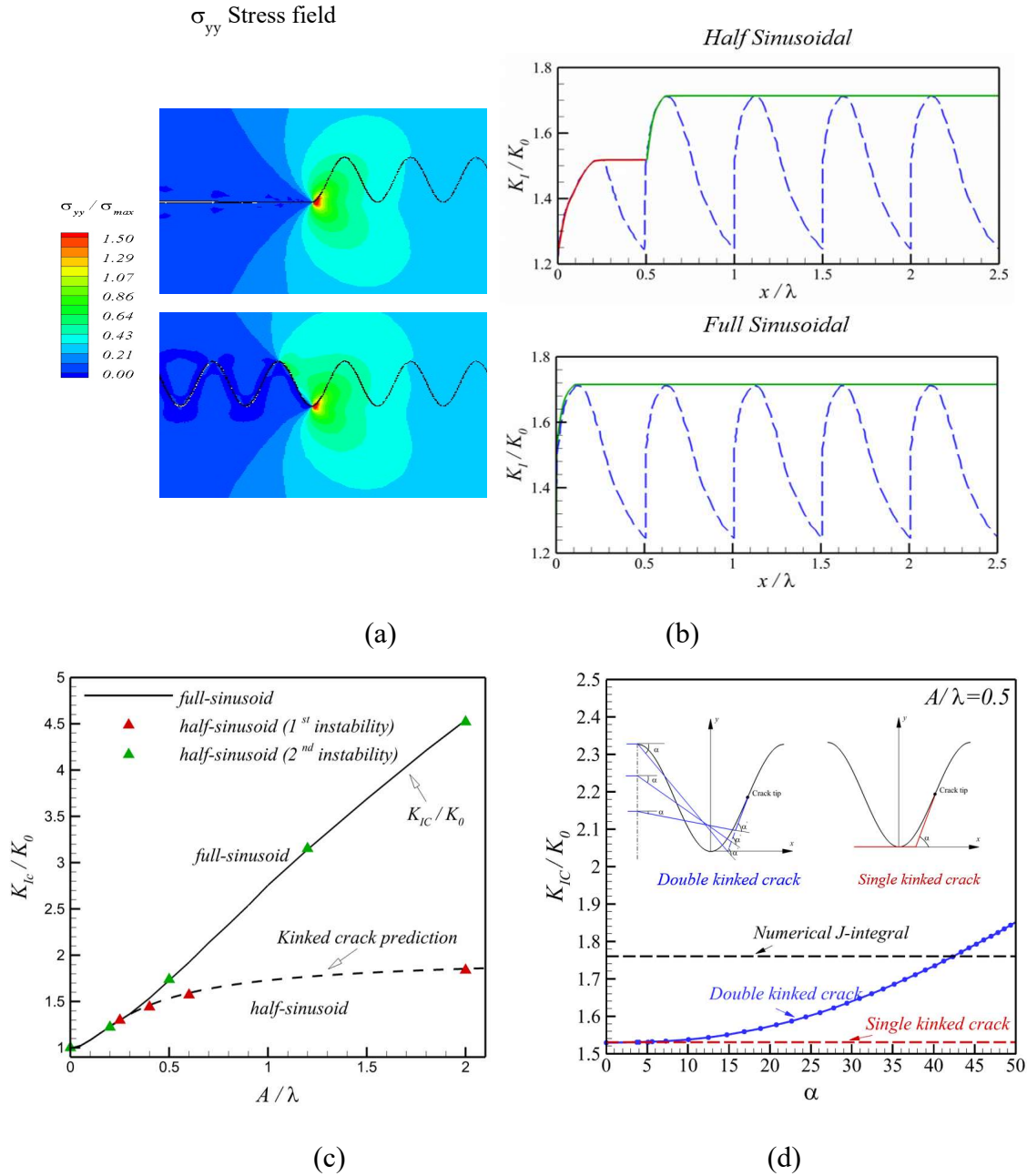
Figure 2.4. (a) The normalized stress field contour near the crack tip for the half and full sinusoidal pattern interfaces for $A / \lambda = 0.5$, (b) The numerical results for K_I / K_0 along the sinusoidal path for both half and full sinusoidal pattern interface, (c) Value of the critical load at which the first and the second instability occurs. The second instability corresponds to the calculated apparent interface toughness (Figure adapted from Zavattieri et al., 2007), (d) the effect of angle α on the value of K_{IC}/K_0 for $A/\lambda = 0.5$.

The direct application of the single and double kinked crack models on sinusoidal patterned interfaces is challenging due to the shape of the sinusoid. The schematic of single kinked approach which used by Zavattieri et al., 2007 to determine the fracture toughness is shown in Figure 2.6(a). Using both single and double kinked crack models on the sinusoidal patterned interfaces are challenging due to the shape of the sinusoid, especially, for the double kinked crack, since the two kink cracks should be able to capture the shape of the sinusoidal pattern. Nonetheless, if successful, the double kinked crack model could become a valuable tool to understand the shape of the crack behind the crack tip and to develop design guidelines for patterned interfaces. As presented in Figure 2.2(b), the double kinked crack model represented by two kinked cracks followed by one main horizontal crack. For each point along the sinusoidal path, the crack tip is defined as a tangent to the sinusoidal path similar to the single kinked crack model that used by Zavattieri et al., 2007. Previously, Zavattieri et al. in 2007 investigated the effect of the shape of the initial crack path on the effective toughness of the sinusoidal patterns interface based on the above information, in order to account for the shape of the initial crack path behind the crack tip using double kinked crack approach, at least a wavelength is considered. In following, the step-by-step procedure of developing the double kinked crack model on the sinusoidal interface will be explained along a half period of the sinusoidal interface (see Figure 2.5(b)).

1) Point A represents the peak of the previous sinusoidal period and it is placed at $(-\frac{\lambda}{2},2A)$. The shape of the crack on the left of A is represented by the segment a (as shown in Figure 2.2 (b) and Figure 2.5(b)), assuming that this portion of the crack is sufficiently far from the crack tip, and therefore, we neglect its influence. As such the horizontal crack a is defined by $y = 2A$.

2) The position of the evolving crack tip, defined by point B, is defined by the tangent along the sinusoidal interface at such point. The tangent also defines the line b'. The crack tip position varies along the repeating segment $(0,0)$ to $(\frac{\lambda}{2},2A)$. The evolution of K_I/K_0 is considered to repeat along similar periods.

3) I defined the interval AB $[X_A - X_B]$, selected between points A and B as shown between green brackets in Figure 2.5 (b).

4) The segment b (line AO') is defined by linear regression of all the points along the sinusoid between points A and B (interval $[X_A - X_B]$).

5) Point *O* is defined as an intersection between lines *b* and *b'*.

A MATLAB code was developed to calculate the linear regression of the sinusoidal path up to the point of the crack tip. Due to the periodicity, only one wavelength for each sinusoidal pattern is presented for the results.

Figure 2.5. (a) A schematic of using the single kinked crack model in the sinusoidal patterned interface. (b) The definition for double kinked crack used for sinusoidal pattern interface

The comparison between three different methods (i.e. analytical approaches and the numerical *J*-integral) for the sinusoidal pattern interfaces with different values of aspect ratio ($0 < A/\lambda < 2.0$) are presented in Figure 2.6(a)-(e). These results reveal that, for the small values of aspect ratio ($e.g., A/\lambda = 0.1$), the single kinked crack model follows closely the numerical *J*-integral results and even shows a better response in comparison to the double kinked crack (Figure 2.6(a)). This can be explained by the fact for the small values of aspect ratios (*A/λ<0.25*), the shape behind the crack tip is not wavy enough (close to the straight line). Moreover, Zavattieri et al., 2007, found that for *A/λ<0.25,* the results from the flat-half sinusoid was very similar to the full-sinusoid case. Therefore, for small values of aspect ratio, the shape behind the crack tip can be ignored, and as a result, the single kinked crack analytical model would be a good option. As the aspect ratio increases, the single kinked crack model is not able to predict the correct value for the sinusoidal interface, while, the double kinked crack model shows higher values for effective toughness in comparison with the single kinked crack, it shows lower values in compare with the numerical *J*-integral. These results confirm the role of shape behind the crack tip and these finding are in accordance with Zavattieri et al., 2007. Finally, the effective fracture toughness for all three

different methods for different values of the aspect ratios are presented in Figure 2.5 (f). Finally, an accurate value of K_I / K_0 along the interface is obtained by solving the numerical *J*-integral method.

Figure 2.6. A comparison between single and double kinked crack model with numerical J-integral over the sinusoidal path for different values of aspect ratio (a) $A/\lambda = 0.1$, (b) $A/\lambda = 0.5$, (c) $A/\lambda = 1.0$, (d) $A/\lambda = 1.5$, (e) 2.0. (f) The predicted effective toughness on sinusoidal interfaces for low and high asperity aspect ratios

When the aspect ratio is small enough $(A/\lambda < 0.25)$, the interfacial shape is very close to the straight line. Thus, one can use the single kinked crack approximation to predict the correct value for the effective interface toughness and ignore the effect of shape behind the crack tip. The single kinked crack approximation is suitable for the cases where the shape behind the crack tip is not important or can be ignored. However, For the larger values of the aspect ratios $(A/\lambda > 0.25)$, the shape behind the crack tip plays an important role and cannot be ignored anymore.

2.5 Comparison between triangular, arbitrary, and sinusoidal patterned interface under remote mode-I loading

In this section, a comparison between triangular, arbitrary, and sinusoidal patterned interfaces is performed for the representative aspect ratio of 0.3. Previously, the role of other non-interlocking patterned interfaces (i.e. triangular and arbitrary pattern interfaces) discussed (Cordisco et al., 2014; Hosseini et al., 2019). In Figure 2.7, the resistant curve for the triangular, arbitrary, and sinusoidal pattern interface is shown in solid green, blue, and red curves, respectively. Based on Figure 2.7, the triangular and arbitrary pattern interfaces show equal value for the effective toughness ($K_{Ic}/K_0=1.46$) which is higher than the effective toughness for the sinusoidal pattern interface ($K_{Ic}/K_0=1.37$). It is also interesting to notice that K_{Ic}/K_0 in an arbitrary interface occurs at the segment with a maximum kink angle ($\gamma = 70°$). Where this value is equal to the effective toughness of the triangular pattern with kink angle equal to $\gamma = 50°$ and this can be explained because the effective toughness depends on the shape of the crack behind the crack tip. However, both the triangular and arbitrary pattern interfaces develop sharp angles in their tips, which might cause stress concentration in those areas. In actual materials, these stress concentrations might cause crack branching into the solid part and therefore not constrained the crack to growth along the interface path (Liu and Li., 2018).). Such condition is not considered in our models, and it is beyond the scope of this work. As a result, one can conclude that the sinusoidal interface path might be more desirable pattern in comparison to the two other pattern shapes. Although it gives a little bit lower value of fracture toughness in comparison to the two other cases, we can make sure that the crack constrained to propagate through the sinusoidal path.
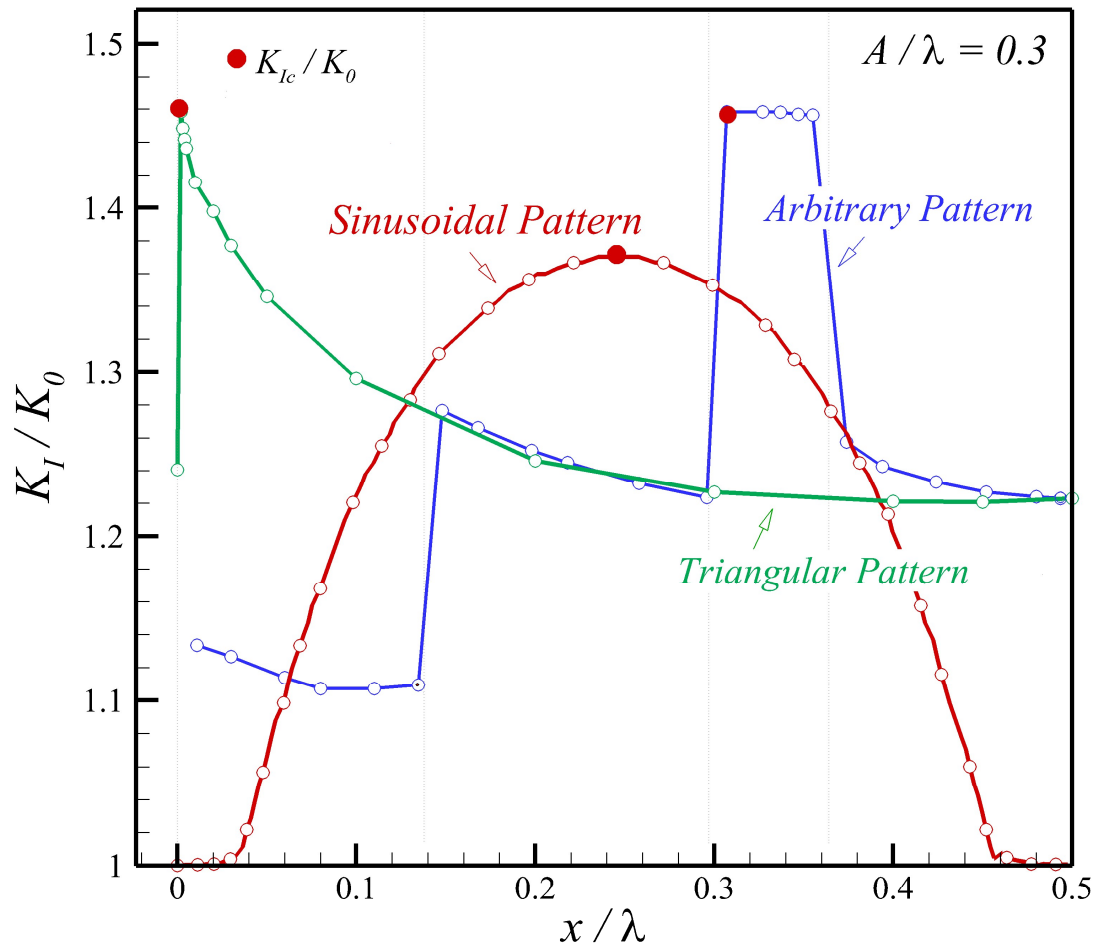
Figure 2.7. Crack propagation paths for the triangular, arbitrary, and sinusoidal patterned interfaces of $A/\lambda = 0.3$.

2.6 Effect of materials and geometrical length scales in the sinusoidal pattern interfaces

2.6.1 Background

In section 2.3, we found that when the fracture process zone is significantly small compared to the size of the pattern, the increase in the normalized macroscopic fracture toughness could be associated to the shape of the crack behind the crack tip and the crack kink direction with respect to the remote loading conditions. It was shown that the shape of the pattern could be used to maximize the normalized macroscopic fracture toughness, it has also been demonstrated that for sinusoidal patterned interfaces between two identical elastic materials, the A/λ ratio is a key parameter in characterizing interface toughening with respect to flat interfaces (Zavattieri et al., 2007, 2008). However, specifying the interface, A/λ or the shape are not adequate criteria to explain the A, λ geometric length scales magnitudes that maximize toughness. Additional considerations regarding the size scale at which the interface pattern is designed should also be evaluated. In order to design materials and benefits from patterned interfaces (i.e., improve crack propagation resistance at multiple scales similar to Nature), a relation between the material fracture resistance mechanical properties and the characteristic geometrical lengths of the pattern is required (Barthelat et al., 2007; Krauss et al., 2009),. The pattern adds a new geometric length scale to the crack propagation problem, and the relation to material length scales in the damage zone (Anderson, 1995; Bazant and Planas, 1997; Cavalli and Thouless, 2001) have to be considered. In this section, we seek for a relationship between the patterned geometrical characteristic lengths and the material length scale, which allows the construction of design guidelines for fracture-resistant materials at multiple scales following the concept of interface patterning. To generalize the problem of crack propagation along patterned interfaces, the semi-infinite theoretical model proposed in section 2.3 for the sinusoidal pattern (asymptotic field solution for the K-field between two identical elastic materials) is used to find fundamental relations between the pattern and material lengths scales independent to additional characteristic length scales such as the material structural size or boundary conditions. A cohesive zone model (Barenblatt, 1959; Dugdale, 1959; Espinosa and Zavattieri, 2003; Xu and Needleman, 1994) is used to characterize the interface de-cohesion and introduce the fracture process zone as an additional material length scale associated to the damage ahead of the crack tip (Bazant and Planas, 1997; Cavalli and Thouless, 2001; Li et al., 2004).
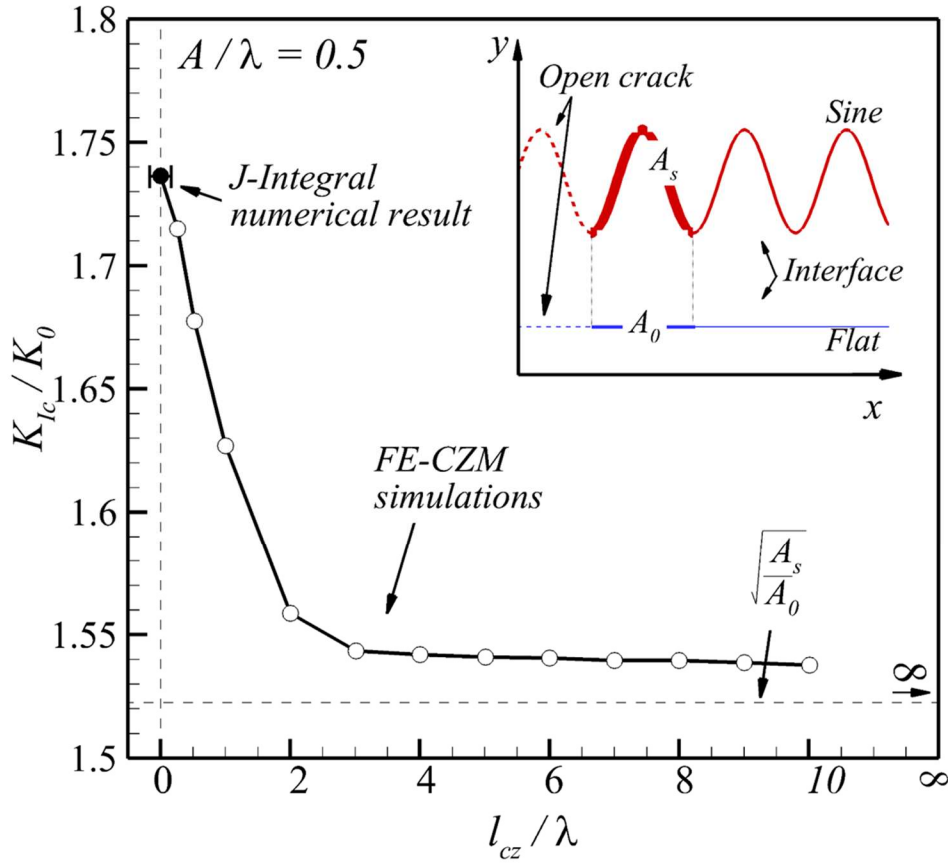
Figure 2.8. Normalized macroscopic fracture toughness against the normalized fracture process zone size (adopted from Cordisco, 2014).

2.6.2 Experimental Investigation

As previously discussed, patterned interfaces add an interesting interplay between the geometrical and material characteristic length scale to the design. In this section, the effect of the characteristic length scale is investigated experimentally using 3D printed specimens. Therefore, the samples with a sinusoidal patterned interface considering for different aspect ratios ($A/\lambda = 0.0, 0.25, 0.5, 1.0$) are printed with a Connex 350 3D Printer using a combination of stiff and soft/weak polymers. All the samples were designed with $\lambda = 20$ mm, and varying amplitude, $A = 0$ mm, 5.0 mm, 10.0 mm, and 20.0 mm, with a total sample width of 40 mm. The out of plane thickness was 2.0 mm for all the samples. The midline of the wavy layer follows the sinusoidal function presented in Equation 1. Then the top and bottom parts of the interfaces are connected using Tango Black Polymer. The 3D print samples are shown in Figure 2.9 (a). The experimental

tests were performed under Quasi-Static Mode-I loading conditions using a tensile test machine. Digital Image Correlation method (DIC) is also utilized during the experiments in order to get a better insight into the interfacial separation between two parts in the sinusoidal patterned interfaces. The Lagrangian strain distribution along the sinusoidal pattern interface of different aspect ratios is shown in Figure 2.9 (b) followed by the stress-strain curves from the sinusoidal patterned interfaces presented in Figure 2.9 (c). The DIC results confirm higher strain distribution along the sinusoidal path for larger aspect ratios. Also, results confirm more uniform strain which means no crack propagation. These results confirm that multiple nucleation sites show up randomly along the sinusoidal and spread almost simultaneously along the width of the sample suggesting that crack propagation is not the main separation mechanism. As a result, by changing the aspect ratios of the sinusoidal interface and inducing an effective change of the area of the interfaces, the effective toughness from these tests eventually can be compared with those obtained for large $l_{cz}/\lambda \gg 1$.

The results state that, by increasing the aspect ratios, the maximum force under tension increases. Since the area under stress-strain curves can be defined as the energy release rate, thus the energy release rate increases by increasing the aspect ratio. Since the value of the lcz is bigger than the geometrical length scale of each sample, the effective toughness for these samples can be estimated according to Equations 2.10 &11. The effective toughness for different values of aspect ratio using different methods (numerical J-integral, CZM method for different ratios of lcz/ λ, and experimental approach using 3D print samples) are presented in Figure 2.10. The results from the numerical J-integral and Irwine equation (Equation 2.9) are presented in solid black lines. The simulations for different lcz/ λ ratios using numerical CZM shown in thin dashed lines (adopted from Cordisco, 2014) and experimental results are presented in solid red line.
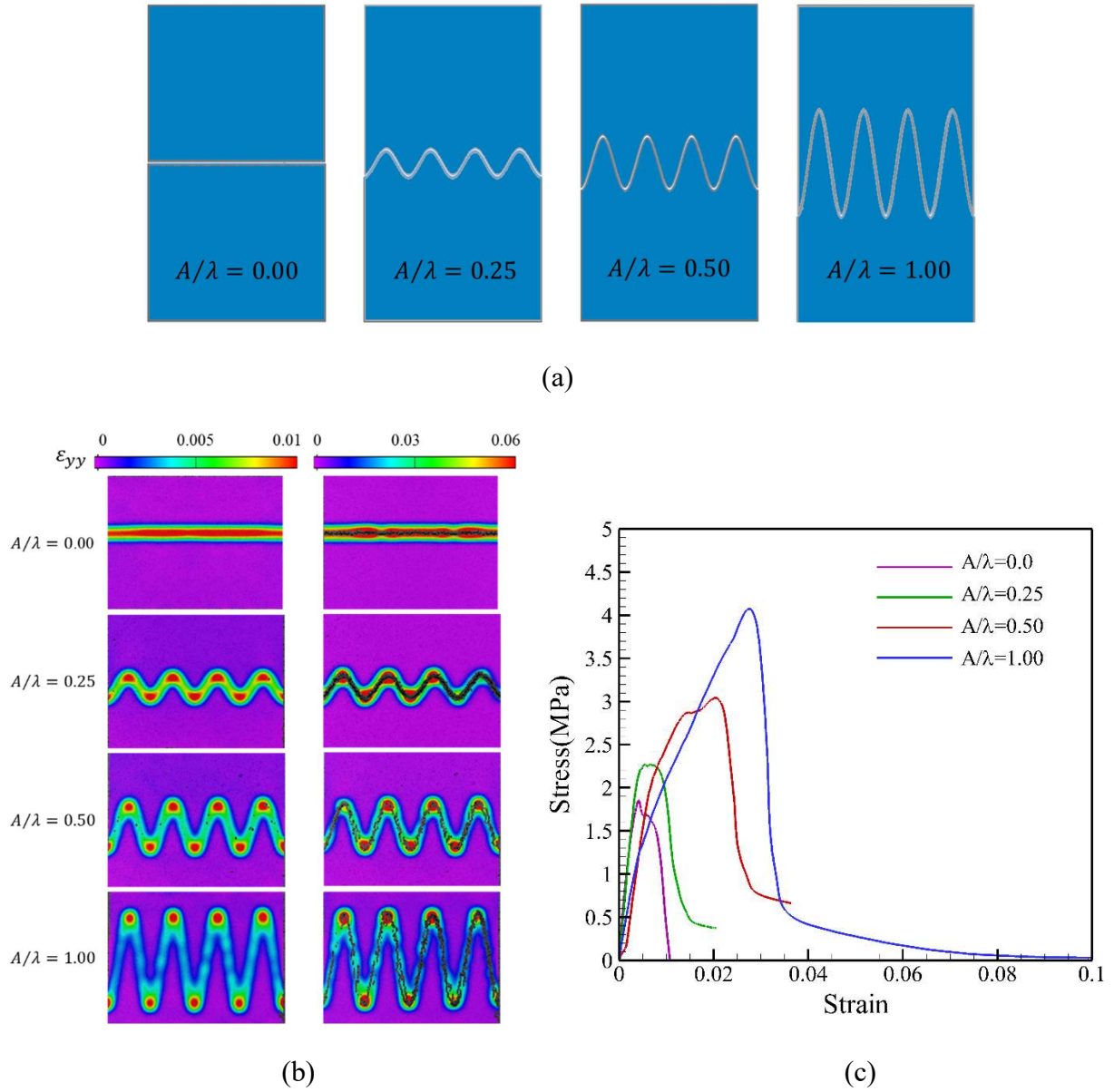
Figure 2.9. (a) 3D printing samples with the sinusoidal interface of aspect ratios of 0, 0.25, 0.5, 1.0. (b) Strain distribution around sinusoidal pattern interfaces of different aspect ratios. (c) Stress-strain curve for sinusoidal patterned interfaces of different aspect ratios under remote mode-I loading.

The CZM results are in excellent accordance to the limiting cases shown by thick solid lines when the CZM is set such that l_{cz}/λ tends to zero, the results converge to the numerical *J*-integral solution, and when l_{cz}/λ tends to infinity, the results converge to Irwine equation (Equation 2.9). The results from the 3D prints experiments for three different aspect ratios are also very close to the case where l_{cz}/λ tends to infinity, and this is due to the fact that the cohesive zone length is bigger than geometric length scales for the sinusoidal patterns. The results in Figure 2.10 also indicated that by increasing aspect ratio (A/λ) values, l_{cz}/λ controls the interface toughening. Developing sinusoidal material interfaces by maximizing A/λ and minimizing l_{cz}/λ at a pre-defined material length scale, results in material resistance to crack propagation. Therefore, both A/λ and l_{cz}/λ must be considered as two primary characteristic dimensionless groups in defining interface toughnessof patterned interfaces.
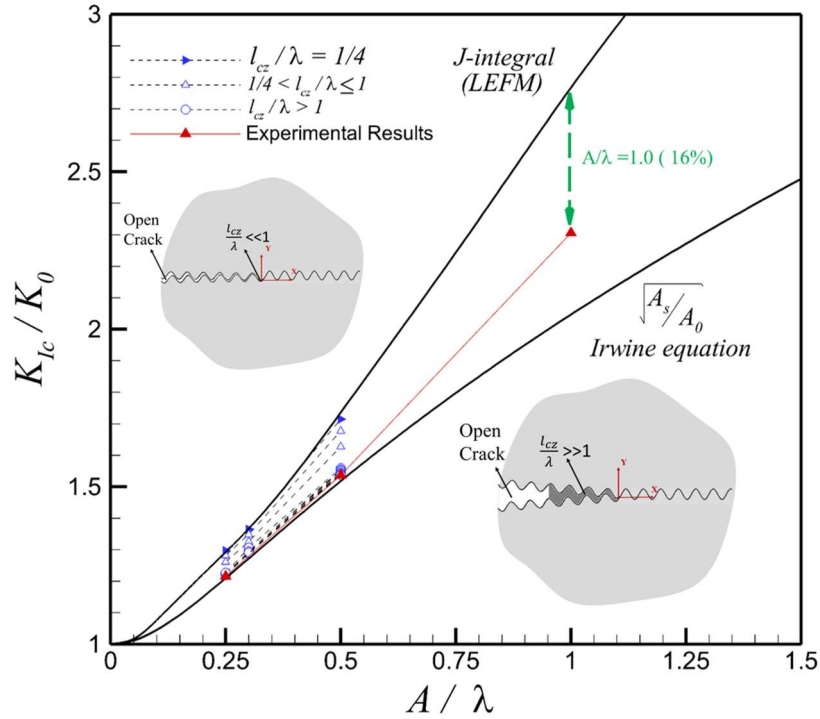
Figure 2.10. Crack propagation resistance vs. interface aspect ratios A/λ for various values of l_{cz}/λ

2.7 Summary and Conclusions

The effect of the sinusoidal patterned interface on effective toughness is investigated using both numerical and analytical methods. For the sinusoidal patterned interfaces, for the aspect ratios of $A/\lambda < 0.25$, the effective toughness of the interface could be estimated using a single kinked crack formula, and single kinked crack model presents better performance in predicting the effective toughness in compare to the double kinked crack approach. A double kinked crack model over the sinusoidal interface shows higher values of the effective toughness in comparison to the single kinked crack approach, notably, for the cases with higher values of aspect ratios. This confirms the importance of considering the shape of the crack behind the crack tip. However, the correct results still need to be calculated using numerical methods.

The idea of using both single and double kinked crack models, confirm that one can use the single kinked crack model to estimate the effective toughness when the shape behind the crack tip is not important, or the pattern is flattened enough that shape behind the crack tip can be ignored. However, for the higher values of aspect ratio, the shape behind the crack tip shown a great influence on the effective toughness and cannot be ignored.

Finally, the relationship between the interface geometric characteristic lengths (A,λ) and the interface material length scale (l_{cz}/λ) suggested that when l_{cz}/λ tends to zero, the shape of the crack behind the crack tip, and the crack kinking direction with respect to the remote loading conditions significantly contributes to the interface toughening mechanics. While in cases where $l_{cz}/\lambda \gg 1$, the contribution is mainly obtained by the increase in the crack propagation length or area and, thus, one can easily confirm that l_{cz}/λ represents another key role for developing design guidelines, which can be used to improve the resistance to crack propagation at multiple material length scales in the sinusoidal pattern interfaces.

Also, in the presented research, the 3D printing samples with sinusoidal pattern interfaces were tested under remote tensile loading conditions. In these tests, by increasing the aspect ratio of the sinusoidal pattern, the interface area increases and since the separation between surfaces is governed by the instantaneous forces, the effective toughness from these tests can be compared with results of the large fracture process zone. The DIC results also confirm more uniform strain along the sinusoidal pattern and no crack tip along the sinusoidal path interface and separation in the interface occurs in random locations (similar to the trend that expected in interface with large fracture process zone). The results of the experiment using 3D printing prototype, with three different aspect ratios are also validated the idea that when l_{cz}/λ tends to large values, the effective toughness depends on the interface area. Therefore, higher values for K_{Ic}/K_0 can be obtained by selecting $l_{cz}/\lambda < 1.0$ and the largest possible value of the aspect ratio (A/λ).

CHAPTER 3. BOXFISH SCUTE MATERIAL CHARACTERIZATION

3.1 Introduction

Biological systems provide a great source of inspiration for mechanical applications due to resistance and extraordinary performance against attack in billions of years of evolution. In engineering applications, there is always a tradeoff between stiffness, strength, and toughness. However, biological systems overcome this issue by developing specific architectures (Naleway et al., 2015). Different species develop various defending mechanisms to protect themselves. Previously, scientists have been exploring the role of architecture in dermal armors of various fish due to their ability to defend against predators attack while maintaining enough flexibility to maneuver efficiently (Porter et al., 2017). For example, the teleost fish develops overlapping elasmoid scales, while gars develop interlocking scales in their carapace. These scales protect arrays of tough bony plates and usually contribute to less than 20% of the weight of the fish (Meyers et al., 2012; Lin et al., 2011; Vernerey and Barthelat 2014). Sharks carapace contains imbricated placoid scales, and these scales responsible for anti-biofouling and reduction in drag forces (Porter et al., 2017). Boxfish carapace includes hexagonal scutes tessellations and shows high resistance against the attack of other predators such as shark (Yang et al., 2015). Boxfishes belong to the Tetraodontiforms order, which also includes triggerfish, pufferfish, trunkfish, and ocean fish, as well as 37 other species among the Ostracidae and Aracandiae families (Santini et al., 2013). Boxfishes (the family of Ostraciidae) has a rigid armor-like carapace (Besseau and Bouligand 1998) and characterized by their boxy shape with a carapace consisted of hexagonal bony plates. This boxy structure results in several vortices around the carapace and provides a self-correcting swimming motion (Bartol et al., 2005; Gharib et al., 2002). Due to the boxy structure of the carapace, the boxfish is only capable of low-speed swimming (about 5-6 body length per second) in comparison to other types of fish. Thus, this armor carapace is responsible for protecting these species against attack or penetration. The scute of the boxfish composed of two primary components: i) a thin layer of the mineralized plate and ii) the protein sub-base. The mineralized plates mostly contain hydroxyapatite $(Ca_{10}(PO_4)_6(OH)_2)$ and soft sub-base is primarily made of typed-I collagen (Yang et al., 2015).

The carapace or osteoderm of various species in Nature develops several connection techniques not only to advance the movement and flexibility but also, provide a defense mechanism similar to the biological systems. In Nature, patterned (non-interlocking and interlocking) interfaces are one of the most common techniques for connection. Role of non-interlocking pattern interfaces previously discussed in Chapter 2. In the current study, the geometry of the interlocking patterned interfaces is referred to as sutures. Sutures can be seen in a variety of species ranging from very smooth sutures interface (those found in infant human skulls) to more complex geometries as those found in ammonite (Sun et al., 2004; Saundres and Work, 2004). The other examples from Nature are Armadillo, Alligator, leatherback sea turtle, and woodpecker. In Armadillo osteoderm, sutures connect the bony plates using non-mineralized collagen fibers and result in increasing osteoderm toughness (Chen et al., 2011). Alligators have also developed arbitrary bony plates in their osteoderms, which are interconnected by 3D-shape zigzag sutures and collagen Sharpey's fiber that offer flexibility to the system(Sun et al., 2013). The sutures in leatherback sea turtle also increase the strength of the carapace and prevent crack propagation inside bony plates (Chen et al., 2015). Another remarkable example in nature is the skull of woodpeckers, which are capable of repeated pecking on a tree at remarkably high deceleration ($10000 m/s^2$) without any apparent brain injury (Gibson, 2006; Jung et al. 2019).

In this chapter, I firstly characterized the material properties of the boxfish scute (both hydroxyapatite and collagen type I sub-base) using literature, in-situ test, and FE models. Previous studies on the boxfish collagen type I using *in-situ* SAX analysis reveals the existence of bouligand microstructure (Besseau and Bouligand 1998) in increasing the toughness of the system. Here, I investigate the role of bouligand architecture inside collagen type-I numerically under shear loading conditions.

The followings are the objective for this chapter:

Objective 1: Material characterization for boxfish scute using (both hydroxyapatite and collagen type I sub-base) using literature, in-situ experiments, and FE models

Objective 2: To understand the role bouligand architecture inside collagen type-I under shear loading

3.2 Scute structure

Boxfish carapace contains hexagonal dermal scutes, a combination of the brittle hexagonal plate (hydroxyapatite) on top of a very compliant (collagen) material. This offers a flexible armor that protects the boxfish against predators. The mineralized plates are separated by patterned (zigzag) sutures; there is no interphase material connecting them. Instead, the connection between mineralized plates is done through the collagen base (see Fig. 3.1). This is different from other naturally occurring sutures (e.g., sutures in turtle, alligator, and armadillo). The microcomputed tomography images of the boxfish carapace (In this study, *Lactoria cornuta*) is presented in Figure 3.1 (a) & (b). The sutures of the boxfish carapace are presented in Figure 3.1(c).

(a)   (b)   (c)
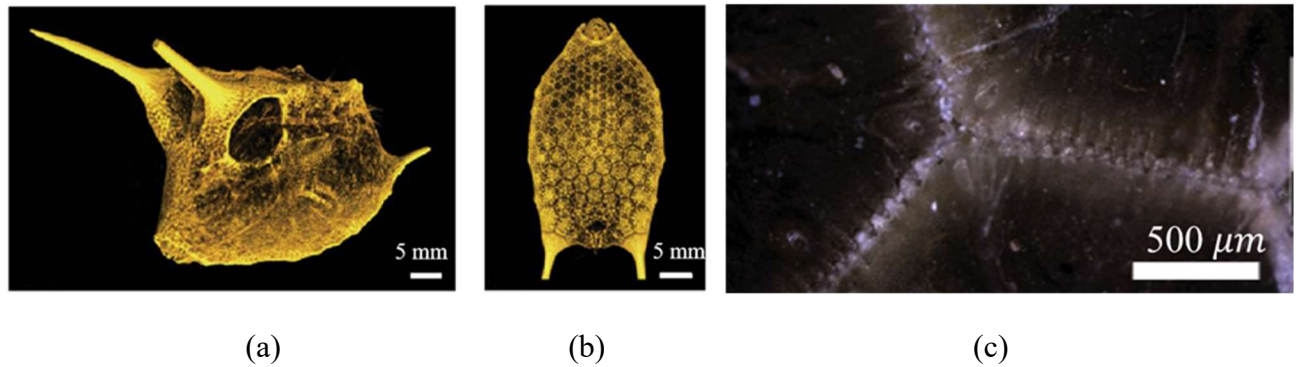
Figure 3.1. Micro-computed tomography image of boxfish (Lactoria cornuta) (a) perspective view,(b) ventral view, (c) zigzag sutures in the mineralized plate (Figure adapted from Yang et al., 2015).

3.3 Boxfish scute material characterization

In this section, the material properties for both mineralized plate and type-I collagen sub-base is characterized using both numerical modeling and *in-situ* experimental tests. The primary purpose of this characterization is to get insight through the composite properties of each scute. Also, it enables us to use this material property for further analysis, such as shear tests (a detailed discussion will be presented in Chapter 4).

3.3.1 Characterization for collagen type-I

Collagen type-I exists in the body of many animals in Nature; for example, rat-tail, rabbit skin, human skin, human tendons, and bone (Gentelaman et al., 2003; Haut., 1986; Miyazaki and Hayashi, 1999; Yang et al., 2015; Rigby et al., 1959; Freed and Doehring, 2005). Collagen type-I in Nature behaves as a hyperelastic material with an average elastic modulus ranging between 0.1-1.1 GPa (see Table3.1). Besides, the stress-strain curves for collagen type-I demonstrate significant variations in different species as the rabbit skin represents more ductile behavior (lower tensile strength and stiffness) in comparison to rat tail and teleost fish, which demonstrate higher stiffness and more brittle-like behavior (see Figure 3.2). Due to significant variations in collagen material in Nature, there is a need to characterize the collagen type-I, which exists in boxfish scute.

The schematic of the geometry and dimension of single hexagonal scute from boxfish carapace is presented in Figure 3.3. As presented in Figure 3.3, the geometry of each scute is very small, and therefore, it is physically impossible to perform tensile tests using coupon (dog bone) samples.

Table 3.1. Collagen type I in different animals

Animal	Elastic modulus
Crosslinked rat tail tendon (Gentleman et al., 2003)	1.10 GPa
Non-crosslinked rat tail tendon (Gentleman et al.,2003)	50–250 MPa
Rattail tendon (Haut 1986)	960–1570 MPa
Rat tail tendon (Kato et al., 1989)	480–540 MPa
Rabbit patellar tendon (Miyazaki and Hayashi, 1999)	30–80 MPa
Skin (Yang et al., 2015)	0-50 MPa
Tendon(Rigby et al., 1959)	1 GPa
Mitral Valve (Freed and Doehring, 2005)	10-50 MPa
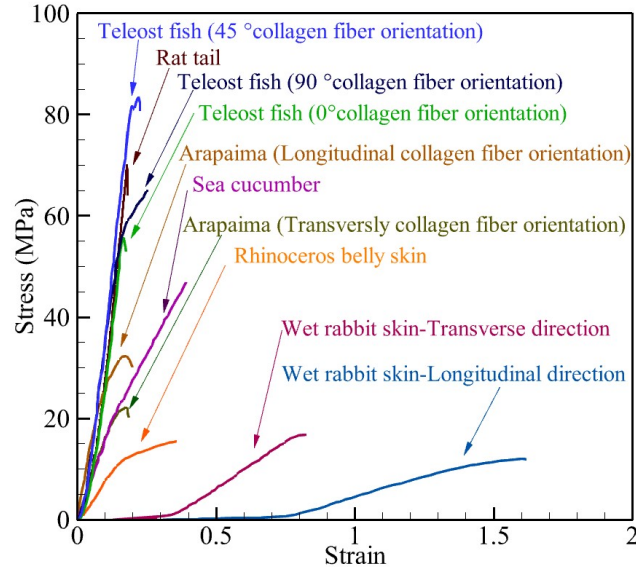
Figure 3.2. Stress-strain curves for collagen type-I in Nature

As a result, a reverse engineering technique was employed in order to characterize the mechanical properties of the collagen in the sub-base. As previously discussed, each scute in the boxfish carapace connected only through the collagen interface, and there is no connection between sutures in mineralized plates. The schematic of two scutes of boxfish carapace when the mineralized plates removed from the top part is presented in Figure 3.3(b).

(a)   (b)
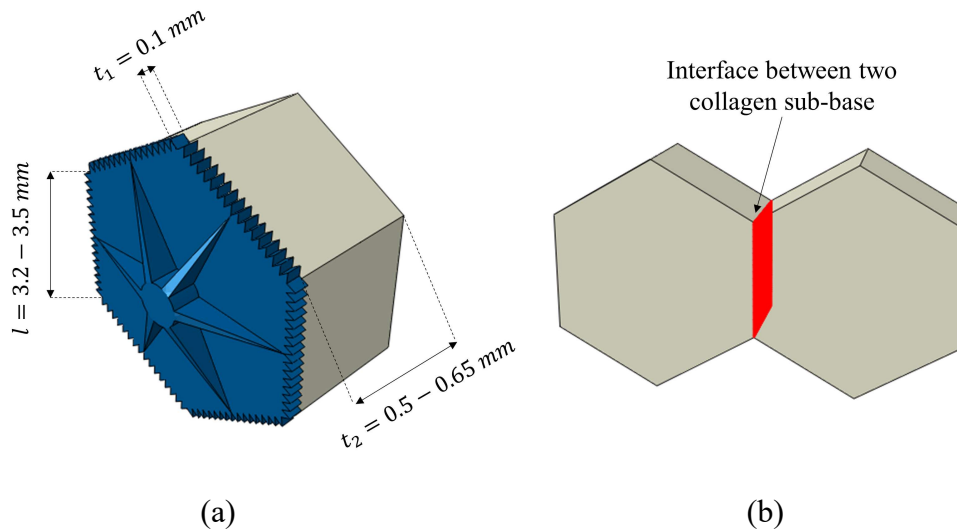
Figure 3.3. (a) The schematic of single scute of boxfish (Lactoria cornuta) carapace, (b) the schematic of two collagen sub-base used for both in-situ experiments and FE models.

3.3.2 In-situ experimental tests between two scutes without mineralized plates

Several *in-situ* tensile tests were conducted between two scutes without mineral plates to determine the stress-strain curves. The average geometrical lengths scale (i.e., width, average thickness, and initial length) of each scute were shown in Table 3.2. The lower and higher values of stress-strain curves from the tests are selected and named as a lower and upper bound, respectively. Therefore two sets of finite element results were developed with respect to these bounds.

Table 3.2. The initial geometry of the scutes used for the tensile test

Test numbers	Average width (mm)	Average thickness (mm)	Initial length L_0 (mm)
Test1	3.76	0.54	2.68
Test2	3.38	0.64	2.94

3.3.3 Finite element modeling

In order to gain the correct behavior of the collagen base, the reverse engineering technique was used in this section followed by several FE simulations in order to predict the correct behavior of both collagen base and interface (see Figure 3.3(b)). Several cases were needed to run to obtain the correct behavior of both collagen and cohesive interface between scutes. Collagen material is defined as a hyperelastic material, and traction-separation law was utilized to model the cohesive interface between the collagen. Once the correct initial stiffness of the collagen was determined, the next step is to develop an accurate model for the cohesive interface. The traction separation law in ABAQUS assumes initially linear elastic followed by initiation and damage evolution (see Figure 3.4). Therefore, the cohesive surface defines by two parameters, maximum strength, and fracture energy. Finally, for the purpose of validation, two sets of parametric studies were developed.
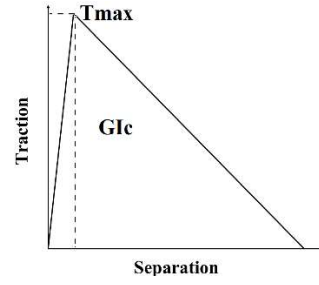
Figure 3.4. Traction-Separation Law used in ABAQUS for cohesive Interface

For case 1, the maximum stress T_{max} in the traction-separation was kept constant, and the fracture energy varies between 2N/mm to 6N/mm while for case 2, the fracture energy kept constant and equal to 5N/mm and maximum stress varying between 10-15 MPa. The result from both cases 1 and 2 are presented in Figure 3.5 (a) and (b), respectively. The primary purpose of this parametric study is to make sure that we are consistent in the characterization.

(a)   (b)
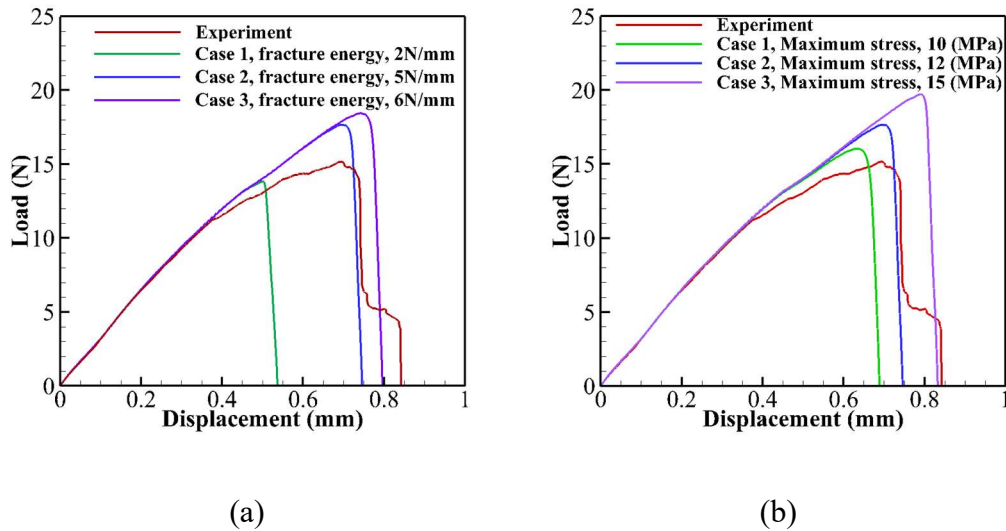
Figure 3.5. Validation of characterization technique. (a) Constant fracture energy (5 N/mm) for all the cases for the maximum stress ranging between 10-15 MPa. (b) Constantan maximum stress of 12 MPa and fracture energy ranging between 2-6 N/mm.

The summary of cohesive interface characterization is presented in Table 3.3 for the lower and upper bounds.

Table 3.3. Cohesive interface characterization using ABAQUS for the lower and upper bound

	Maximum Nominal Stress (MPa)	Fracture Energy (N/mm)
Lower bound	12	5
Upper bound	15	8

The finite element results for collagen type-I material characterization for lower and upper bounds are presented in Fig 3.6 (a). The comparison between FE simulations and *in-situ* experiments for two scutes of boxfish without mineral plates shows a good consistency between experiments and FE results (Fig 3.6 (b)). The schematic of FE simulations between two collagen subbases is presented in Fig 3.6 (c). Finally, the maximum principal stress distribution contour on bulk collagen during the tension test is presented in Fig 3.6(d).

(a)

(b)

(c)

(d)
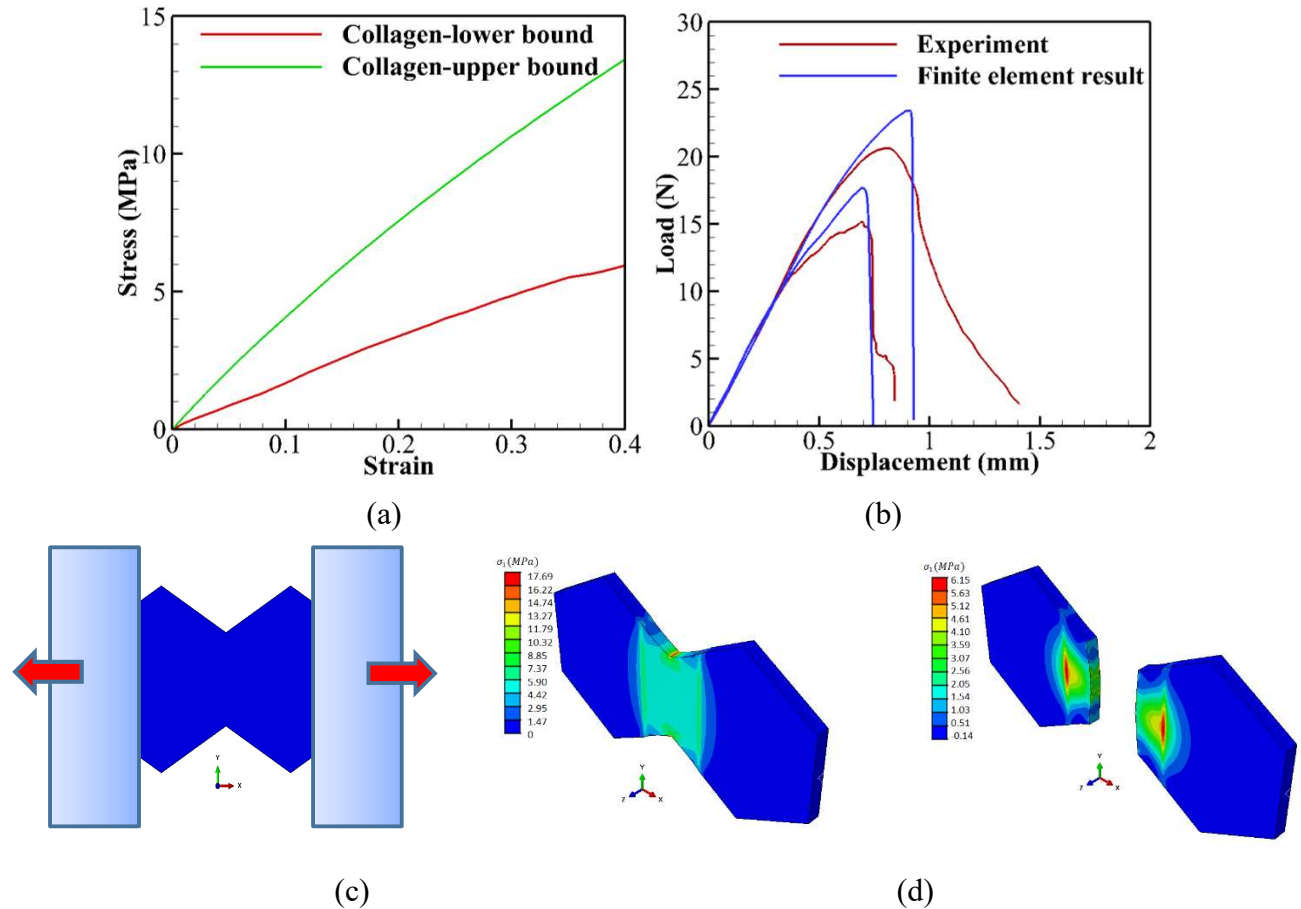
Figure 3.6. (a) The upper and lower bounds for the collagen material used in FE analysis. (b) Comparison between experiments FE simulations (c) Schematics of the tensile test (d) Maximum Principle stress contour on bulk collagen during the tension test.

3.4 Mineralized plate characterization (Hydroxyapatite)

The mineralized plates are mainly made of Hydroxyapatite (HA), $Ca_5(PO_4)_3(OH)$ (Yang et al.,2015; B. The fracture toughness of hydroxyapatite can be found in literature as shown in Table 3.4.

Table 3.4. Fracture toughness of the hydroxyapatite in literature

Fracture toughness MPa$\sqrt{m}$		Literatures
Temperature (℃)		
1000°	0.82	Mobasherpour, I., et al, 2009
1200°	0.78	
1.2		Halouani, R., et al. 1994
1		Van Dijk et al., 1981

Based on the literature, the average value of fracture toughness of hydroxyapatite is assumed to be 1 MPa$\sqrt{m}$. Moreover, the maximum strength of the hydroxyapatite is adopted from Woodard et al., 2007, and it is equal to 26 MPa (Woodard et al., 2007).

The finite element models of two scutes (similar to the test developed by Yang et al., 2015) under tensile loading is developed using the material characterized in sections 3.3 and 3.4. Both FE simulations and the experiments show a good agreement with each other, as shown in Figure 3.7.
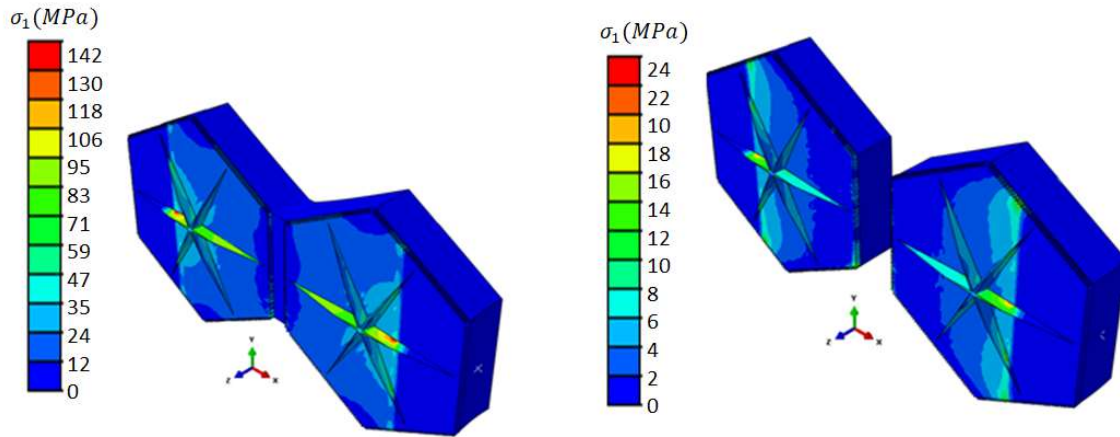
(a)
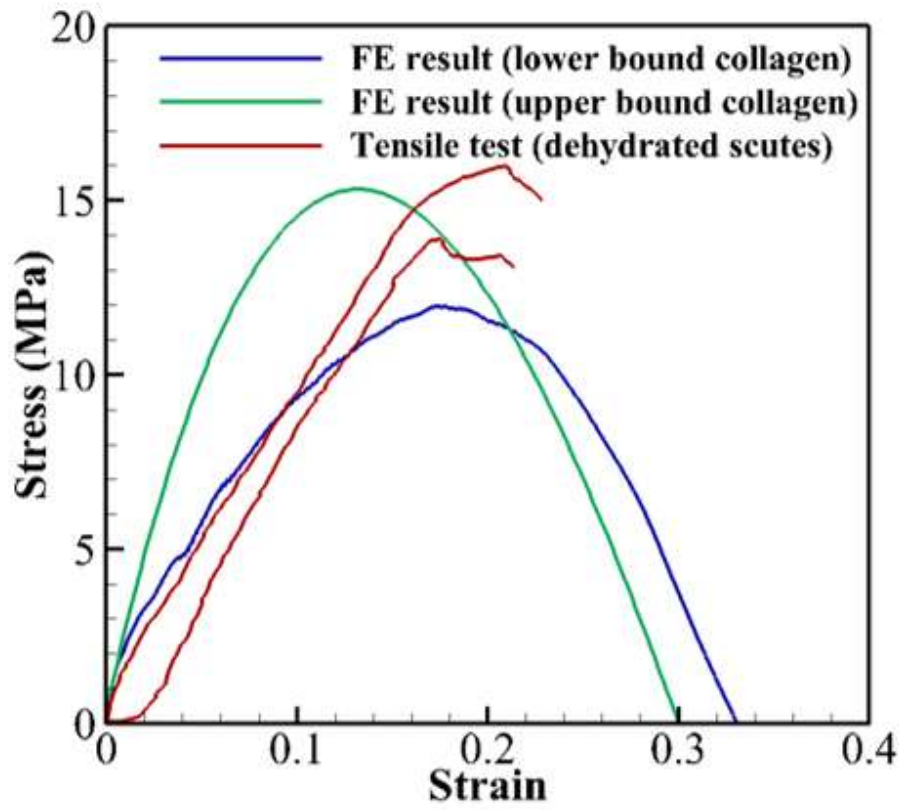
(b)

Figure 3.7. (a) The maximum principal stress in the beginning and after the separation between two scutes. (b) a comparison between stress-strain curves from finite element results and the experiments using lower and upper bounds. Finally, the comparison between stress-strain curves for collagen type-I that characterized for boxfish scute using reverse engineering technique and collagen type-I in other species is shown in Figure 3.8.
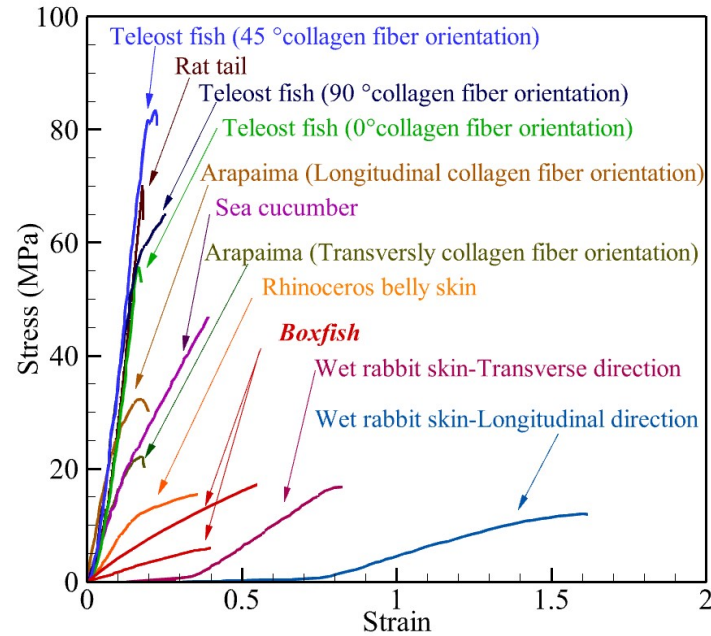
Figure 3.8. Comparison between collagen type-I found in boxfish scute and other species

3.5 Collagen type-I microstructure (role of bouligand microstructure)

Although the scale geometry and entire structural layout of the carapace/osteoderms play an essential role in the overall performance of the biological system, recent studies state that microstructure of each scale is another essential factor (Rivera et al., 2019; Salinas et al.; 2017; Suksangpanya et al., 2017). Specific attention goes to boxfish collagen type I. The ladder-like micro-structures of collagen within the scute interior can be seen (Fig. 3.9 (a)). However, during in situ SEM mechanical loading, it can be seen that these collagen planes deform in a much more complex way that would be expected from a ladder-like structure consisting of bidirectional/orthogonal collagen fibrils and forms this unique S-shape structure (Fig. 3.9 (b)). It is hypothesized that this S-shape is due to bouligand microstructure between each ladder. Similar behavior was observed throughout the interior of the scute's collagen base. It is proposed that this structure allows for the collagen planes to realign with applied stress; therefore, increasing the deformation resistance of the scute interior, which is similar to previous literature on the deformation response of Bouligand structures found in nature (Garner et al., 2019).

(a)   (b)
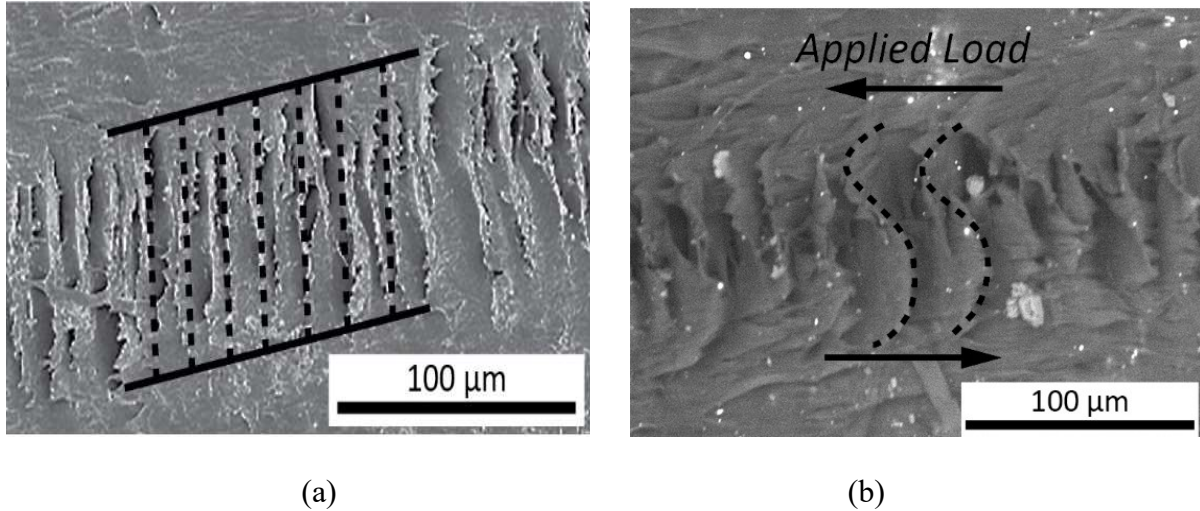
Figure 3.9. (a) Collagen base in boxfish scute contains ladder-like bouligand structure, (b) Presence of "S" shape after applying shear test between two scutes (Figure adapted from Garner et al., 2019).

To understand the reason why the S-shape developed in collagen after shear test, a 3D finite element (FE) model of material element unit cell was developed by employing N (N = 20) stacked layers of continuum shell elements of thickness d and a pitch distance of D as presented in Figure 3.10 (a) and (b). Such a unit cell represents the behavior of bouligand structure inside the collagen scute, showing the material element cell in the forms of N helicoidally stacked layers with different orientations. The material property is adopted from a nacre (Barthelat et al.,2006) due to the anisotropic nature of the material. The layers were completely bonded together, and shear displacement control applied on the top and bottom surfaces of the model. The results from FE models of both homogenized material and bouligand architecture are compared and presented in Figure 3.10 (c), respectively. The comparison between the normalized horizontal displacements of these two microstructures reveals that the S-shape could be explained due to the nonlinearity in geometry caused by anisotropic material orientation in the bouligand architecture.

(a)

(b)

(c)
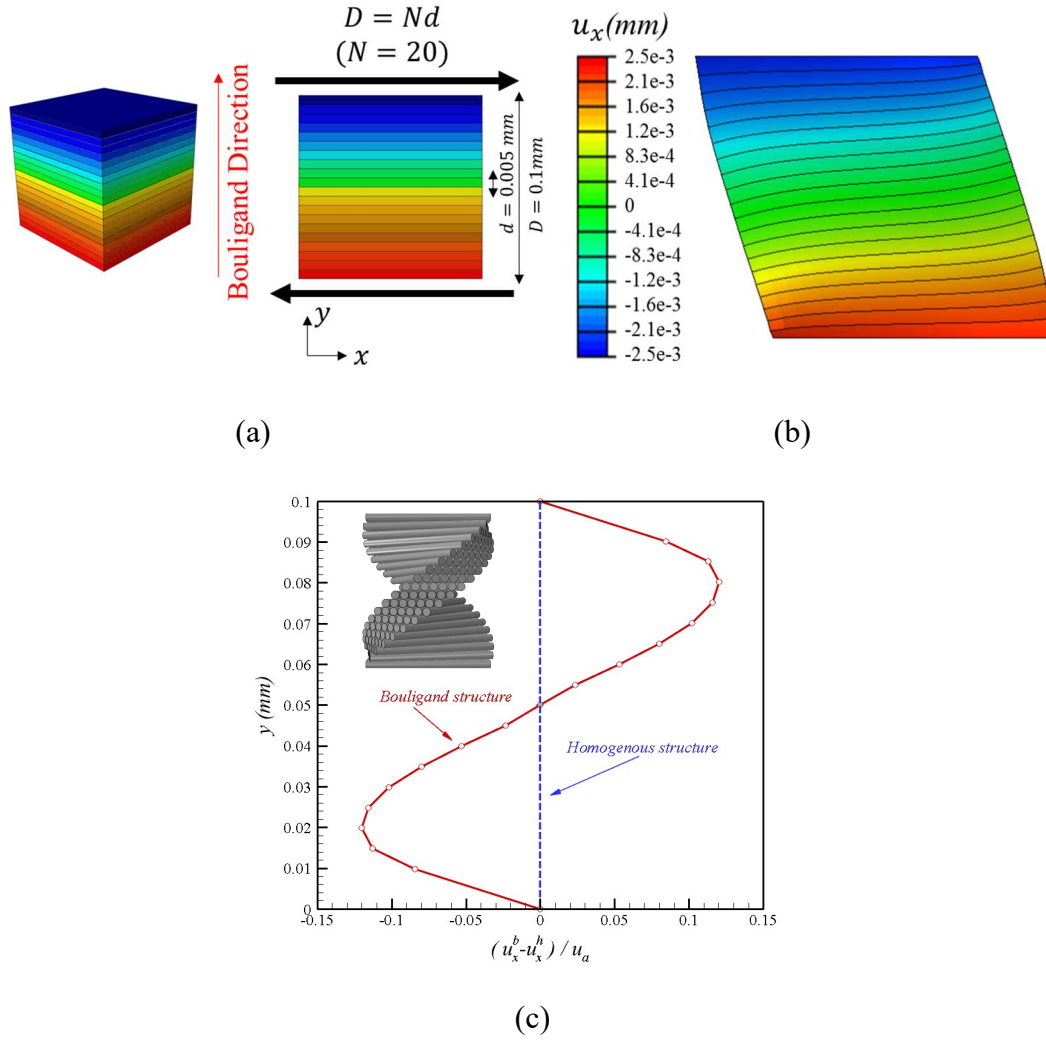
Figure 3.10. (a) Schematic diagram of the layered model for finite element model where, D defines pitch distance, d accounts for the layer thickness, and the total number of layers are equal to 20 (N=20) (b) horizontal displacement of element unit cell for Bouligand cells, (c) the normalized horizontal displacements of Bouligand structure and homogenous material along vertical (y) direction (pitch angle direction (D)).

In addition to the above results, the role of plate orientation was also studied for four different orientations: i) +45/-45, ii) 0/90, iii) bouligand microstructure (similar to what we observed in boxfish), iv) 0/0 orientations. Both loading and boundary conditions were similar to the previous paragraph. The results from this parametric case studies are presented in Figure 3.11(a)-(d).
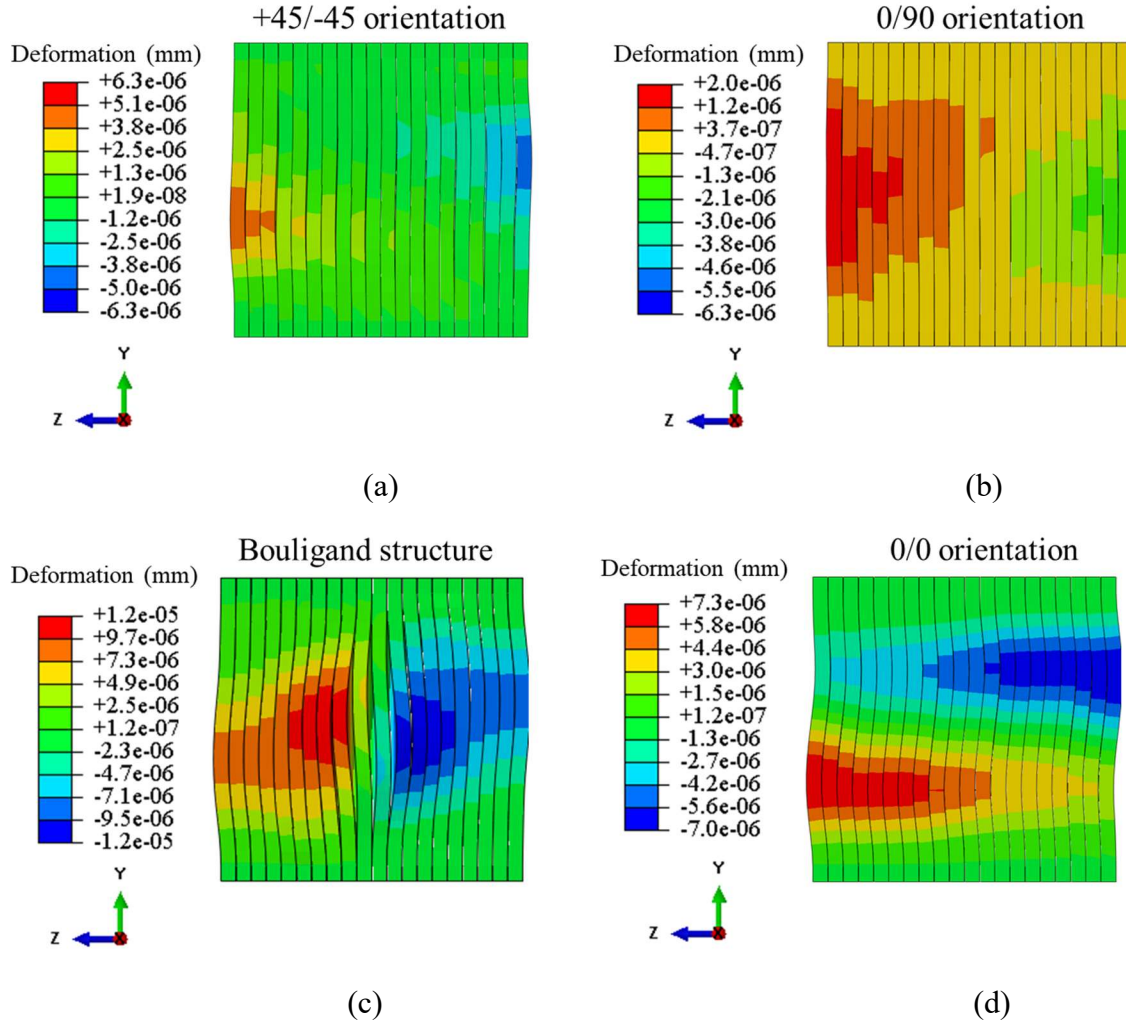
Figure 3.11. Horizontal deformation under simple shear for different orientation after fifty cycles of loading and unloading, (a) +45/-45 orientation, (b) 0/90 orientation, (c) bouligand structure, (d) 0/0 orientation

Figure 3.11 shows the horizontal displacement after one cycle of loading and unloading for all four different orientations. Based on comparison, the bouligand structure shows higher horizontal displacements in comparison to the other three orientations. The normalized values of peak load, stiffness, toughness, and maximum horizontal displacements for all four orientations are presented in Fig 3.12. All the values in Fig 3.12 were normalized with respect to the 0/0 orientation model. The results state that the bouligand orientation presents a better performance in comparison to the other orientations in terms of stiffness and maximum horizontal displacements. However, the peak load and toughness are the highest for 0/90 orientation. As expected, the lowest values for all the mechanical properties occur at 0/0 orientation. These results also confirm that the loading direction

is important, and one should also consider the material orientations with respect to the applied loading conditions.
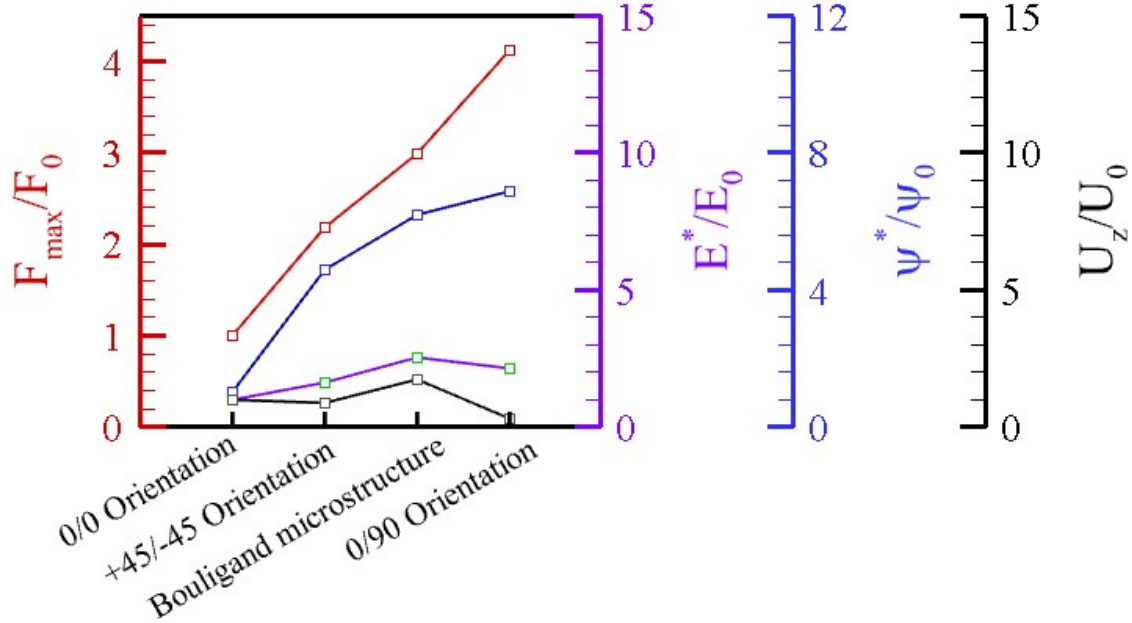
Figure 3.12. Comparison between normalized peak load (red), normalized stiffness (purple), normalized toughness (blue), and normalized maximum horizontal displacement (black) for all four types of orientations (+45/-45, 0/90, bouligand, and 0/0 orientations) in this study. All the values are normalized with respect to 0/0 orientation.

3.6 Summary and conclusions

In this chapter, materials used in each scute of boxfish carapace were characterized using in-situ experiments, FE simulations (reverse engineering technique), and literature. The results from the FE simulations of collagen type-I show a good agreement with the experiments. Finally, the role of bouligand architecture inside the collagen base was investigated using 3D unit cell in forms of N helicoidally stack layers with different orientations for a single pitch similar to the boxfish microstructure. The results stated that the nonlinearity which we observed during SEM mechanical testing can be explained due to the anisotropic nature of the bouligand orientation.

CHAPTER 4. ROLE OF BOXFISH SCUTE ARCHITECTURE IN CONTROLLING THE CRACK DIRECTION

4.1 Introduction

Over billions of years of evolution, biological systems develop various sophisticated mechanisms to protect against attack or adapt into habitat to survive. Studying these mechanisms enable us to understand the mechanics and provide insight to develop or improve future engineering applications. Biological systems overcome the tradeoff between stiffness, strength, and toughness by means of specific microstructure or architectures. For instance, many arthropods such as beetle's family (Cheng et al., 2019; Libby et al., 2014; Jewell et al.,2007; Yang et al., 2017; Rivera et al., 2019), mantis shrimp (Suksangpanya et al., 2018), and crabs (Cheng et al., 2008) have been evolved bouligand microstructure inside their bodies. The existence of this architecture helps to increase toughness as well as damage tolerant properties. Patterned interfaces, including both non-interlocking and interlocking patterns, are another common motif in Nature to enhance mechanical properties such as toughness (Hosseini et al., 2018 and 2019; Cordisco et al., 2012, 2016 and 2017; Rivera et al., 2019).

Marins are also developed various dermal armors as a defense mechanism approach. The overlapping elasmoid scales in teleost fish, interlocking ganoid scale in gars, imbricated placoid scales in sharks, and interlocking hexagonal scutes in boxfish are all examples of armors developed in order to protect these fish against attack or penetration. Moreover, these microstructures help to maintain flexibility in order to maneuver in the water as well as reducing the drag force (Porter et al., 2017). Although both dermal armor and scale geometry play an essential role in the performance of the marine species, an individual scale architecture is another key in increasing the mechanical properties. For instance, elasmoid scales in teleost fish have been developed a gradient of mineralization through the scales thickness to resist against penetration and increase bending stiffness (Dastjerdi et al., 2015). Similarly, arapaima gigas carapace contains elasmoid scales and further analysis through the microstructure of these scales reveals the presence of the inner lamellar layer, which consists of uniaxial mineralized collagen fibrils. In each layer, the fibrils alignment changes periodically and create bouligand type structure (Zimmermann et al., 2013).

Boxfishes (superfamily Ostraciodea) belong to the Tetraodontiforms order and developed flexible dermal armor which differs from other families of fish (Santini et al., 2013; Yang et al., 2015). Boxfishes can reach speeds higher than six body lengths per second to achieve minimal turning radius as well as control of their position (Bartol et al., 2005; Van Wassenbergh et al., 2014). Also, boxfishes are capable of producing destabilizing vortices which help to enhance maneuverability in high turbulent waters, and as a result, these species can efficiently navigate in coral reef habitat (Bartol et al., 2005). Since the speed of boxfishes is slow in comparison with other types of fish, the specific carapace architecture is responsible for providing defense mechanisms against attack. The in-situ experiments on the two scutes of the boxfish reveal that specific boxfish scute architecture can help in controlling the crack direction in the hard(brittle) mineralized plates (more explanation will be provided through the manuscript). Therefore, the primary purpose of this study is to understand the role of boxfish scute and its architecture in protecting the carapace and if this architecture can provide us insight into the mechanics of controlling cracks propagation direction. To this aim, this study explains the role of architecture such as sutures geometry (sutures angle) and material properties (role of bi-layered material, a combination of brittle and soft substrate) by using analytical, numerical and experimental models.

4.1.1 Boxfish scute geometry

Boxfishes are mostly recognized by their boxy-shape carapace and non-overlapping hexagonal scutes, which make them different from other types of fish, as can be seen in Fig4.1 (a). The study by Yang et al., 2015 on boxfish carapace (Lactoria cornuta) revealed that each hexagonal scutes contain two distinct parts, i) a thin layer of mineralized plates which mostly contains hydroxyapatite (brittle materials), and ii) a thick layer of soft material which is type-I collagen (Yang et al., 2015). Also, sutures (triangular-like) microstructure evolved around mineralized plates, and unlike other species such as turtle, alligator, and armadillo (Chen et al., 2013; Chen et al., 2015; Yang et al., 2013) no interface connection exists between sutures. As a result, the connection only occurs through the collagen base. The experimental results between two scutes under tensile tests reveal that the collagen base is mainly responsible for the separation, and suture interfaces do not play a role. Under shear loading between two scutes, cracks arrested around sutures areas, and as a result, the collagen base was responsible for the rest of the separation. Since the mineralized plate mainly consists of hydroxyapatite (a biological ceramic/ brittle behavior), it

is expected to see at least one main dominant crack propagates through the entire plates under shear loading when sutures presence. However, based on *in-situ* shear test results, multiple cracks developed around sutures areas without any damage in the mineralized plates, and thereby, it is hypothesized that collagen beneath should play a role in controlling the crack direction as shown in Figure 4.1 (b) and (c). The carapace of the boxfish represents excellent resistance against punch, bending, and shear loadings (Yang et al., 2015). The presence of brittle plates on top of the soft substrate and its damage mechanisms have been investigated through many studies. A quick summary of previous works regarding the brittle plates and soft subbase laminates (see section 4.1.2) can give us more insight through the mechanics of boxfish scute.

(a)

(b)   (c)
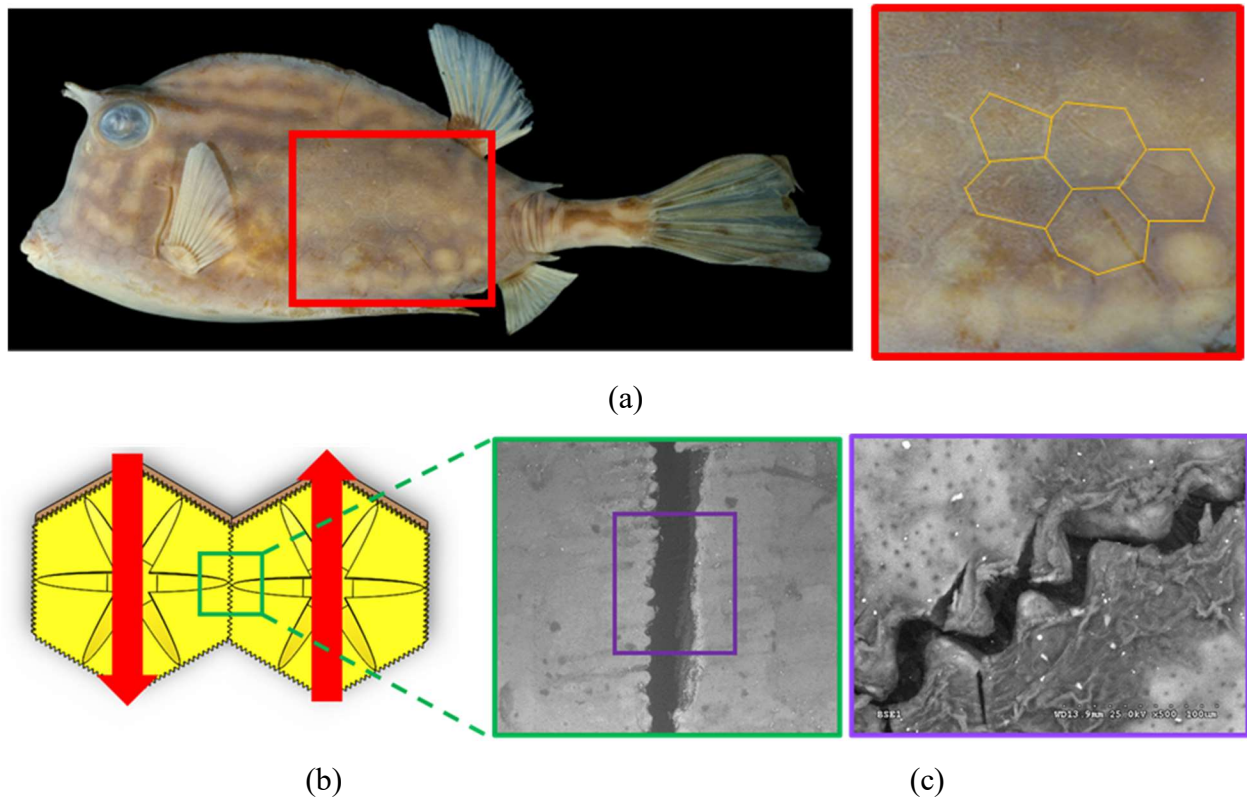
Figure 4.1. (a) The boxfish carapace, the red zoomed box presents the hexagonal scutes, (b) schematic of shear tests between two boxfish scutes, (c) cracks propagating around sutures area in mineralized plate after the shear test.

4.1.2 Coating technique used in material science

Coating hard thin ceramics on the soft substrate is an engineering technique to increase the performance and mechanical properties of the brittle materials. This technique can be found in a

variety of applications from wear, corrosion, thermal, and electrical resistance applications to ceramic armor, laminated windows, eyeglasses, and biomedical applications such as dental crown and hip prostheses (Deng et al., 2002). Since these coatings are mainly brittle, the life of the components is limited by the failure of these brittle coatings or plates. The damage is mainly caused due to the stress concentration arising from contact loading. Therefore, many studies have been done to gain an understanding of the damage mechanisms of brittle, thin plates on the soft substrate (Lawn et al, 2004; Kim et al., 2003). The observations by Lawn et al. in 2004 revealed a competing mechanism between damage modes in the bi-layers material. These competing mechanisms can be described as i) cone cracks or quasi-plasticity at the top (in the contact area), and ii) laterally extend cracks at the lower surfaces. The schematic of each damage mechanism for brittle plates is presented in Fig 4.2 (a). The relationship between cone crack (C) and quasi-plasticity (Y) with corresponding critical contact load have been investigated analytically and are presented in Equations 4.1 and 4.2 respectively (Lawn and Ceram, 1998, Guiberteau et al., 1994).

$$P_c = A\left(\frac{T^2}{E}\right)r \tag{4.1}$$

$$P_y = DH\left(\frac{H}{E}\right)^2 r^2 \tag{4.2}$$

Where E is the Young's Modulus, T accounts for toughness, "*H*" represents Hardness, and "*A*" and "*D*" are dimensionless coefficients. When $P>P_C$, cone cracks expand stably by Roesler's relation for penny-like cracks. The results from the bilayer material (brittle material on top of the soft substrate) present another damage mechanism. Under the same Hertzian contact condition, another stress state will show a mismatch between layer components. As a result, it can induce new stress states in the brittle plates such as ceramic due to the flexure on a soft base and finally generate subsurface radial cracks (R) (Lawn et al., 2002). This stress can become dominant as the thickness of the brittle plate becomes thinner (similar to the boxfish scute). The schematic of the bilayer sample under the Hertzian contact test is presented in Figure 4.2 (b).
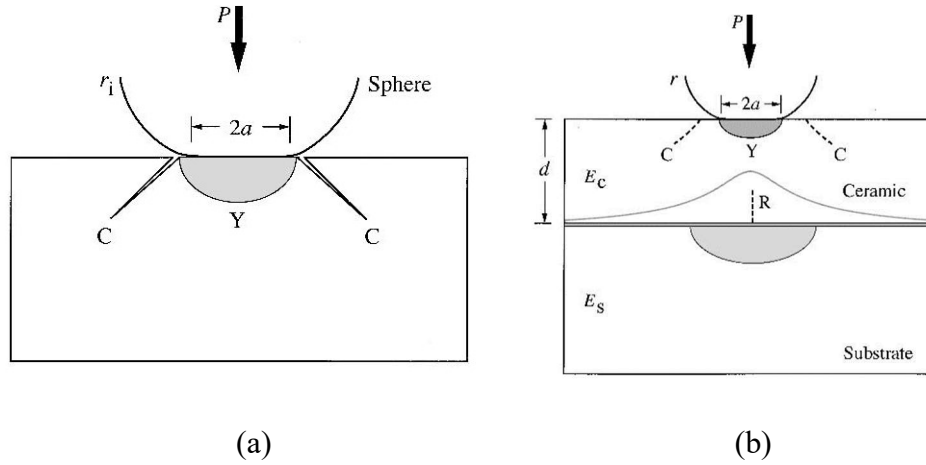
Figure 4.2. Schematic of Hertzian contact of the sphere of the radius of r_i under contact load of P and contact on top of (a) brittle plate, (b The bilayer sample(figure adopted from Lawn et al., 2002).

If the deformation of the substrate remains elastic (or the thickness of the brittle blade is larger than the subbase), then all the damage from external contact is carried out by brittle plate and Equations 4.1 and 4.2 can be used to calculate the critical applied load. For the thinner thickness of the brittle plate, flexural stresses become the primary reason for radial cracks initiation (Chai et al., 1999). The maximum tensile stress in the middle of the bi-layer sample (Figure 4.2(b)) can be determined by the plates theory on the elastic regime (Timoshenko and Woinowsky-Krieger, 1959). By substituting this stress to the flexural bulk strength, σ_C yields the critical load for radial cracking, as presented in Equation 4.3.

$$P_R = B\sigma_C d^2 / \log\left(C\, E_C / E_S\right) \tag{4.3}$$

Where B and C are dimensionless constant, and d is the flexing plate. σ_C is the strength and E_C/E_S is the modulus of ceramic to the soft substrate. In another study, the relationship between the various ratios of the brittle plate to the soft substrate is investigated by Chai et al. in 2004. Based on this study, ceramic layer thickness played an important role in damage mechanisms and caused four different categories of failure, as presented in Figure 4.3 (Chai et al., 2004).
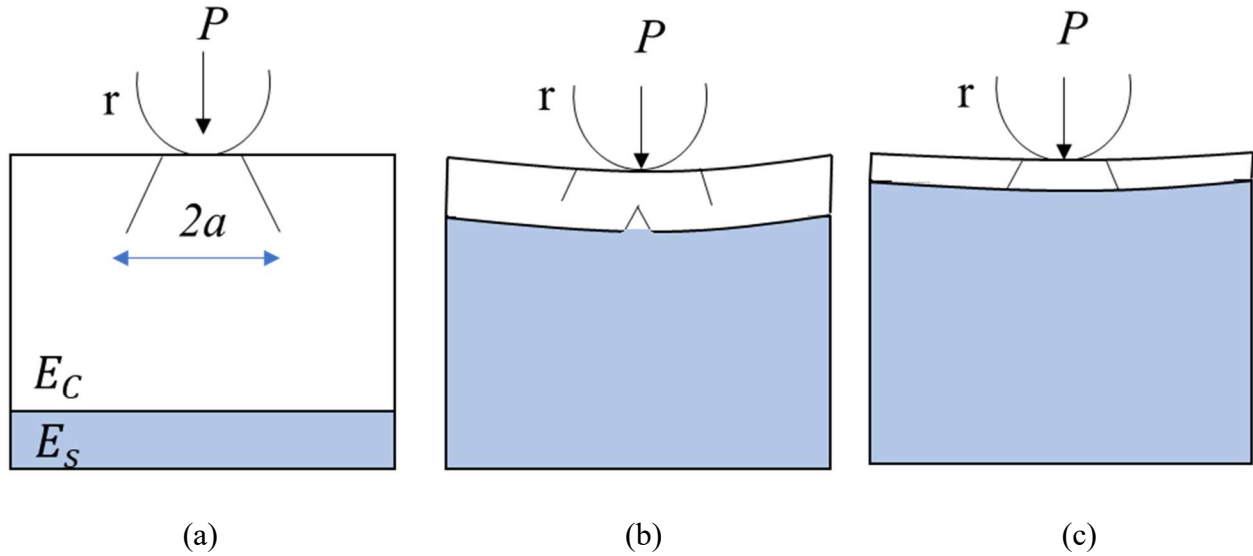
Figure 4.3. Schematic of bilayer architecture including brittle layer (thickness *d*) and young's modulus of *Ec* on a compliant base of modulus *Es* under sphere contact of radius *r* at load *P*. Competing fracture mechanism inside brittle plate:(a) cone crack at the top surface, (b) ring crack and radial crack at the top and bottom surface of brittle plate,respectively and (c) ring cracks through brittle plate (Figure reproduced from Chai et al., 2004).

The purpose of this study is to understand the mechanics of boxfish scute architecture (patterned geometry and material) in controlling the crack propagation direction under shear loading. Here, I try to explain how this architecture bio-inspired from boxfish scute can help in controlling the crack direction using analytical methods, numerical analysis, and experiments. To this aim, the biomimetic samples were created using gypsum (brittle phase, including sutures) and silicone (soft phase) for various cases. Similarly, the FE simulation of the biomimetic samples was created to get a better insight into the mechanics of this architecture. In the next, I will investigate the role of a kinked crack in bi-layered materials and the effect of material properties on the crack propagation angle.

4.2 Problem formulation

As discussed in the previous section, the boxfish scute architecture (both a combination of soft and brittle material and sutures existence) can help to control the crack propagation direction in the brittle plates. Brittle plates, including triangular sutures interfaces, were placed on top of soft material (Fig 4.4 (a)). In the brittle material consisting of sutures interface, under shear loading, it is hypothesized that at least one dominant crack propagates through the plates while adding soft material beneath can help to control the crack direction parallel to the loading as demonstrated in Fig 4.4 (b) and (c) respectively.

(a)   (b)   (c)
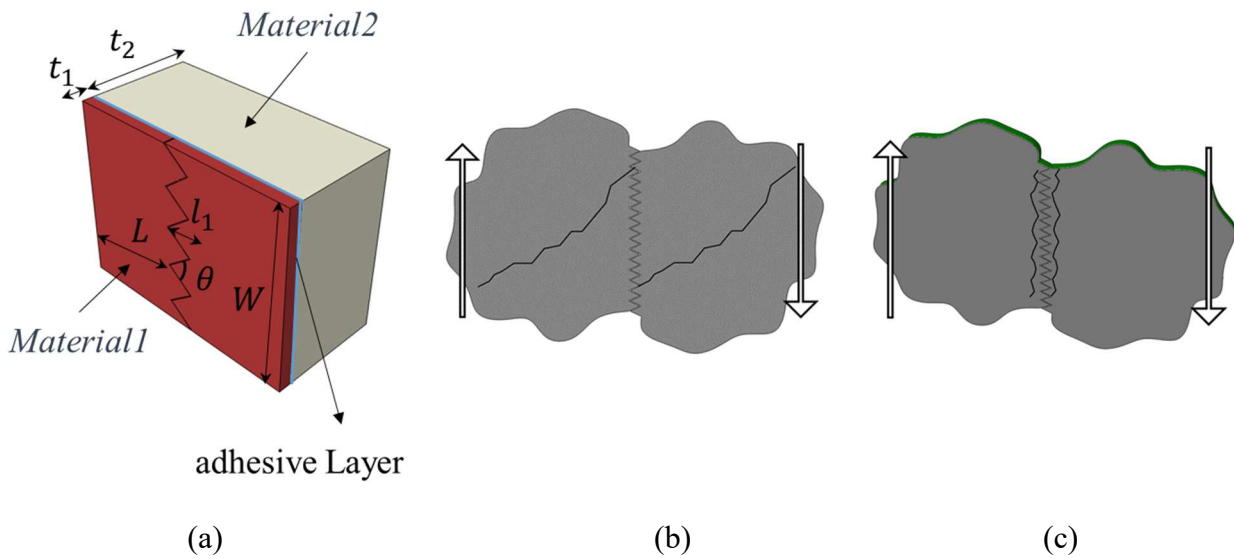
Figure 4.4. (a) Schematic of biomimetic sample bio-inspired by boxfish scute contains brittle material (Material 1), soft material (Material 2) , and an adhesive layer (highlighted in blue), (b) schematic of crack propagation including sutures for brittle plates under shear, (c) schematic of bi-layer material consisting sutures under shear loading and crack propagation.

4.3 Dimensionless analysis

In the bio-inspired sample, specific material properties for hard plates, soft sub-base, interface interlocking geometry, as well as the adhesive connection between hard and soft parts play an essential role in crack propagation, delaying the crack, and overall performance of the bi-layered materials. Therefore, we require a dimensionless analysis to obtain model parameters that have the most effect on the behavior of the system, such as toughness, energy dissipation, and angle of crack propagation. Based on the test geometry and material properties, the following dimensionless groups are needed to be investigated for the geometrical parameters $(\theta, l_1, L, W, t_1, t_2)$, material properties $(E_1, \nu_1, \sigma_{fb}, K_{Ic}, K_{IIc}, E_2, \nu_2, \sigma_{fs})$, and the cohesive law parameters $\sigma_{max}, \Lambda_1, \Lambda_2, \delta_n, \delta_t$. The schematic of the sample with the variables is presented in Fig 4.4 (a). In order to prevent delamination between a brittle plate and soft substrate, we assume perfect bonding between the brittle plate and soft substrate, and therefore, the parameters regarding the adhesives can be removed from the analysis. The parameters considered in this study are presented in Eqn.4.4.

$$P_{max}, \alpha, K, E = f(\theta, l_1, L, W, t_1, t_2, E_1, \nu_1, \sigma_{fb}, K_{Ic}, K_{IIc}, E_2, \nu_2, \sigma_{fs}) \tag{4.4}$$

Where P_{max} is the maximum load that can be achieved during the shear test, α is the crack propagation angle with respect to the original crack, and G and E are the energy absorption and initial stiffness respectively. Following Buckingham's 'Π-theorem' (Buckingham, 1914), the total number of variables is equal to thirteen. Based on Buckingham's Π theorem, one can also express them in terms of π_i where $F(\pi_1, \pi_2, ..., \pi_p) = 0$. Considering this, we will end up with ($p = n - k = 15 - 2 = 13$) twelve dimensionless groups. Finally, the following dimensionless group is utilized in Equation 4.5;

$$\frac{P_{max}}{E_1 WL}, \alpha \frac{G}{K_{IC}}, \frac{E}{E_1} = \Psi\left(\theta, \frac{l_1}{L}, \frac{L}{W}, \frac{t_1}{t_2}, \frac{t_1}{L}, \frac{E_1}{E_2}, \nu_1, \frac{\nu_1}{\nu_2}, \frac{\sigma_f}{E_1}, \frac{\sigma_{fb}}{\sigma_{fs}}, \frac{(K_{Ic}/\sigma_{fs})^2}{L}, \frac{(K_{IIc}/\sigma_{fs})^2}{L}\right) \tag{4.5}$$

In the above Equation, the geometrical values such as L, W, and thicknesses can assume to be constant. I also assumed that the Poisson's ratio does not affect the results, the following dimensionless group were selected for this study

$$\frac{P_{max}}{E_1 WL}, \alpha \frac{G}{K_{IC}}, \frac{E}{E_1} = \Psi\left(\theta, \frac{E_1}{E_2}, \frac{\sigma_{fb}}{\sigma_{fs}}\right) \tag{4.6}$$

4.4 Biomimetic samples bio-inspired from boxfish scute under shear loading

To get a better insight into the role of architecture, the following experiment is designed using gypsum and silicone as hard and compliant parts, respectively. Gypsum is selected because of its hard and brittle nature. It can also replicate similar behavior as organic ceramics such as hydroxyapatite that can be found in boxfish carapace. Similarly, silicone demonstrates hyperelastic behavior similar to the type-I collagen in boxfish scute. Also, the aspect ratio of brittle to soft material in both boxfish and biomimetic samples are very close to each other (see Table 4.1). Due to the brittle nature of the gypsum, creating patterned interfaces are very hard. Therefore, the molding technique (using silicone and 3D printing parts) The connection between silicone and gypsum is made through Loctite adhesive. Loctite adhesives are known for their intense nature of the connection, and it can create perfect bonding between gypsum and the silicone.

Table 4.1. Comparison between material properties in Boxfish scute and biomimetic samples

Material	E (MPa)	ν
Hydroxyapatite (Boxfish scute)	1000-2000	0.3
Collagen Type I (Boxfish scute)	40-50	0.22
Gypsum	50-55	0.3
Silicone	0.5-1	0.2

4.4.1 Methodology for creating molds and performing shear tests

In order to create samples using brittle material such as gypsum with interdigitated (zig-zag shape) sutures, I used the silicone molding technique. The 3D printed samples with triangular sutures are used as a negative part, and silicone is used to create a mold. In this study, the master part is created using 3D printing machine (Connex 350) as shown in Figure 4.5 (a). In order to set the master part in position, a plexiglass plate is required, and the master part needed to be attached to this plate (the hot glue was used to connect the master part to the plexiglass plate). Then, the wall created around the master part using cardboard plates. The silicone AM128 is used as a mold and pour on top of the master part. After 24 hours, the walls and plexiglasses are removed, and the negative part was ready to use. In order to create the gypsum samples, the gypsum powder is combined with water using the aspect ratio of 2:1. After the gypsum samples dried, the sample removed from the mold and preserve 72 hours in the oven with 40°F to achieve stable material properties. The 3D printing sample, silicone mold, and gypsum samples preparation are shown in Figure 4.5(a-d), respectively.
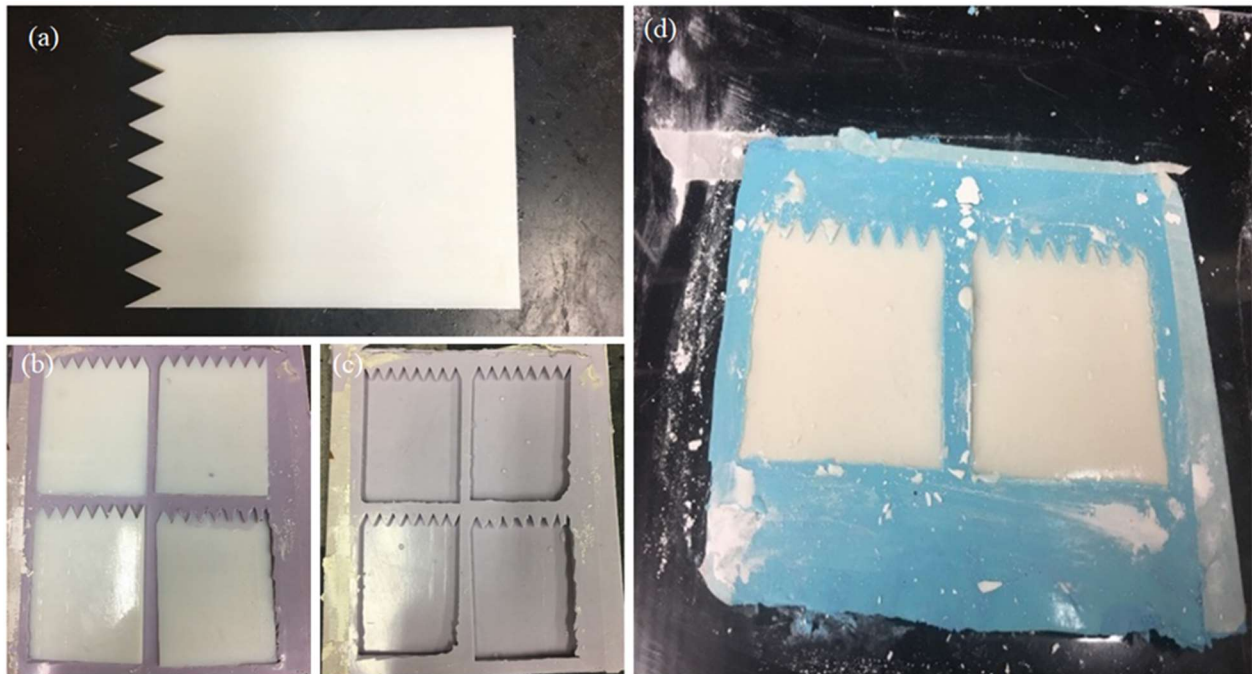
Figure 4.5. (a) 3D-printed master part, (b) mold created from 3D printed parts, (c) negative mold can be used to create gypsum sample, (d) creating gypsum samples from the negative mold.

To perform the shear test on the samples, the frame is designed using 2080 aluminum extrusions in order to be used in conjunction with the universal tensile testing machine (MTS). As shown in Fig 4.6 (c), the left side of the girder can move in tension while the other side constrained against the movement.

4.5 Biomimetic shear tests

As explained in the previous section, two types of biomimetic samples with various suture angles developed from the gypsum (Fig 4.6 (a)) and gypsum with silicone (Fig 4.6 (b)). All the samples tested under shear. The shear testing apparatus is shown in Fig 4.6 (c). The purpose of this section is to understand the role of sutures angle in enhancing the mechanical properties of a brittle material such as gypsum (see section 4.5.1). This section follows by series of tests when silicon subbase added to the system in order to understand the role of soft subbase in this architecture (section 4.5.2). Both simulations and experiments used alongside each other to get a better insight into the mechanics of this architecture in controlling the crack direction.

(a)   (b)   (c)
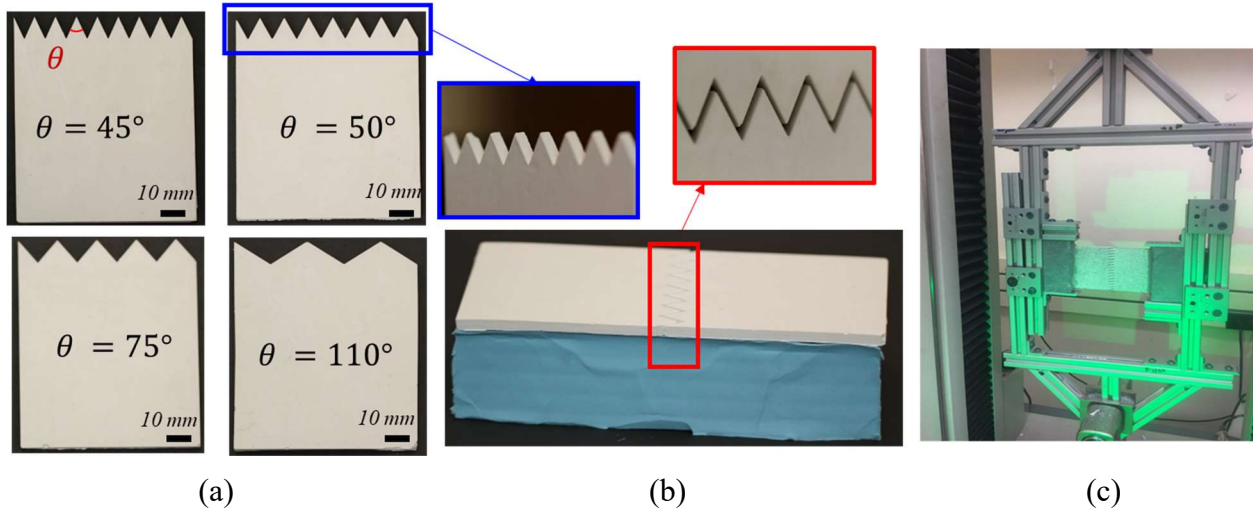
Figure 4.6. (a) biomimetic samples developed from Gypsum with θ=25°,45°,50°,75°, 110°, (b) biomimetic sample include gypsum (brittle) and Silicone (soft substrate), (c) Apparatus for performing shear test developed from 8020 extrusions.

4.5.1 Crack modeling using Extended Finite Element Method (XFEM)

In ABAQUS, modeling discontinuities such as cracks can be utilized using XFEM method. The XFEM concept is developed from the theory of partition unity. This method provides discontinuities in an element by enriching degrees of freedom using displacement functions to model discontinuities (i.e., cracks) as an enriched feature. This method avoids the limitation of remeshing technique and improves the limitations related to meshing crack surfaces (Belytschko and Black (1999)). The special enriched functions ensure the presence of discontinuities in combination with additional degrees of freedom. The nodal enrichment functions are presented in Eqn 4.7

$$u = \sum_{I=1}^{N} N_I(x)[u_I + H(x)a_I + \sum_{\alpha=1}^{4} F_\alpha(x)b_I^\alpha] \tag{4.7}$$

Where $N_I(x)$ is the nodal shape function, u_I is nodal displacement vector in the continuous part, a_I represents the nodal enriched degree of freedom, and $H(x)$ accounts for the discontinuous jump function around the crack surfaces. The last term consists of the nodal enriched degree of freedom vector, b_I^α, and the elastic asymptotic crack-tip functions, $F_\alpha(x)$. The first term on the Eqn4.7 defines the nodal displacement for all the nodes in the model; the second term applies to the nodes that are cut by the crack, and finally, the third term defines for nodes that are cut by the crack tip. The demonstration of a coordinate system in XFEM model is presented in Figure 4.7.
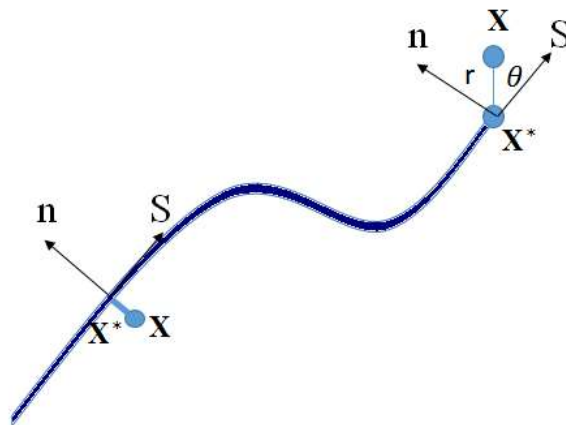
Figure 4.7. Local coordinates for a smooth crack

In Figure 4.7, X presents Guass point while as discussed in the previous paragraph, the discontinuous jump function for the crack surface is presented by $H(x)$. The value of $H(x)$ is equal to (1), if $(x - x^*).n \geq 0$, otherwise, it has the value of (-1). Finally, the equation of the asymptotic crack tip functions in isotropic elastic material, $F_\alpha(x)$ are given by Eqn 4.8.

$$F_\alpha(x) = \left[\sqrt{r}sin\frac{\theta}{2}, \sqrt{r}cos\frac{\theta}{2}, \sqrt{r}sin\frac{\theta}{2}cos\frac{\theta}{2}, \sqrt{r}sin\theta cos\frac{\theta}{2}\right] \tag{4.8}$$

Where a polar coordinate system placed at the crack tip and represents by (r, θ). Besides, modeling the crack-tip singularity requires continuously updates as the crack propagates and it depends on the location of the crack in the material. Abaqus only consider asymptotic singularity functions for modeling stationary crack approach. For the moving crack, the procedure to simulating crack initiation and propagation is based on traction-separation cohesive behavior within the XFEM framework which is called *XFEM-based cohesive segmented* method. In the cohesive method, the cohesive surfaces are associated with the element boundaries and result in crack initiation and propagation in an arbitrary path. Therefore, the *XFEM-based cohesive* does not account for the stress singularity and only consider displacement jump across a crack element. Another method is XFEM based on the LEFM concept by using the Virtual Crack Closer Technique (VCCT) which also accounts for the stress singularity. However, in this method, the crack should exist inside the model and it can not predict the crack initiation. In this analysis, first the XFEM *XFEM-based cohesive segmented* method is used to predict the crack initiation and then the XFEM based on LEFM approach was used for the crack propagation.

4.5.2 Shear tests on Gypsum samples without silicone sub base

The strain distribution form both FE simulations and experiments for gypsum samples for different values of $\theta = 25°, 45°, 50°, 75°, 110°$ are presented in Fig 4.8 (a) side by side. The Digital Image Correlation technique was utilized along with the experimental shear test to capture the strain distribution during the tests. For all the cases, the values of thickness, width, and length of the samples kept constant and equal to 5mm, 70.5 ± 0.5 mm, and 60 mm respectively. Thus, as the angle θ increases, the number of sutures inside the width decreases. It is also notable that by decreasing the angle size, the contact area increases and thereby, one expected to see the higher mechanical properties, however, in brittle material another competing mechanism plays a role which is the crack angle and fracture. The results from both FE simulations and experiments confirm the presence of at least one main crack in all the cases, except for the case with $\theta = 25°$. This could be explained by the fact that under the same loading condition, based on the sutures angle, the crack starts to propagate from various angles. Also, the comparison between normalized peak load, normalized toughness, and stiffness reveals that the maximum values occur at $\theta = 45°$ (see Fig 4.8(b)). In Fig 48(b) All the values normalized with respect to the $\theta = 45°$. In the previous study by Yang et al., 2015 stated that the boxfish sutures angle ranging between $\theta = 45°\sim50°$ and for all the samples $l_1/L = 0.2$. The green column in Fig 4.7(b) presents the sutures range in boxfish scute.
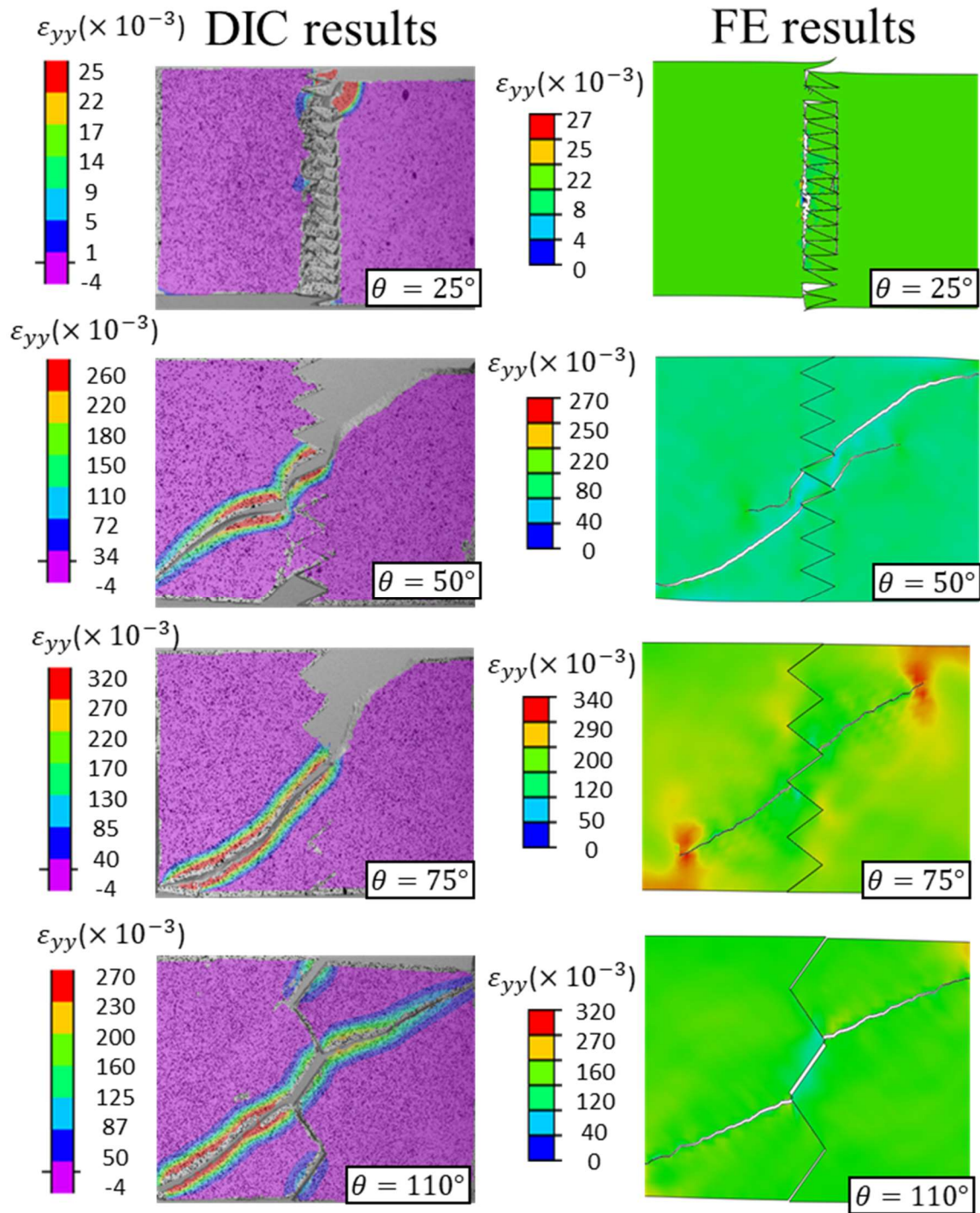
(a)

Figure 4.8. (a) Comparison between FE simulations and Experiments using gypsum samples, (b) Comparison between normalized peak load, stiffness, and toughness of experiments and simulations (results are normalized with respect to angle 45 (θ=45°).

Figure 4.8 continued

(b)
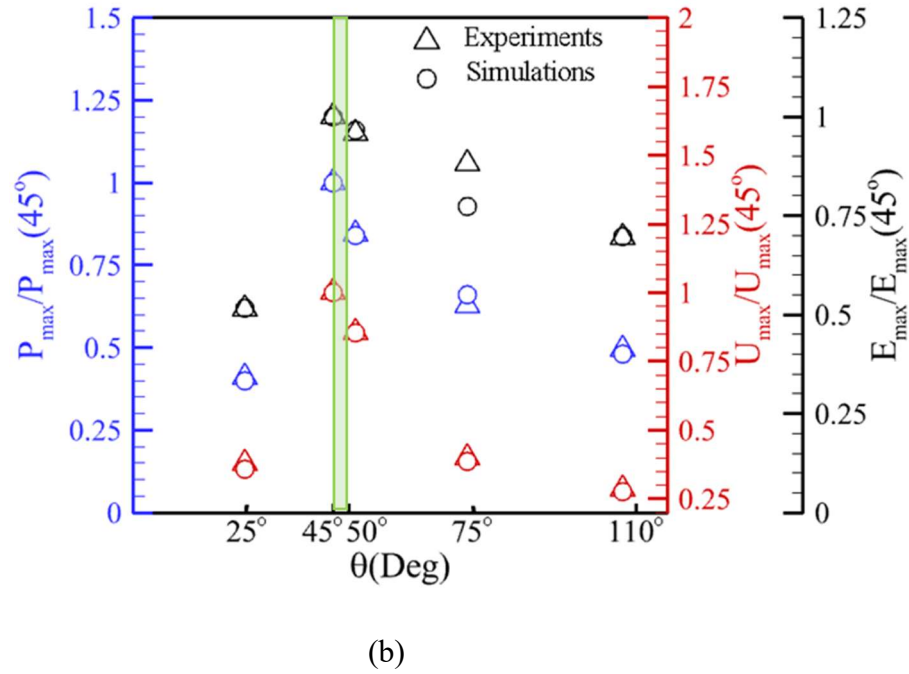
4.5.3 Shear tests on gypsum samples with silicone subbase

In section 4.5.1 role of suture interfaces of various angles was studied for gypsum samples. In this section, the silicon was bonded to the gypsum samples using the Loctite adhesive (Fig. 4.6(b)). Boundary conditions and loading are similar to the previous section. Both experimental and FE simulation results confirm that the crack angle direction is controlled by adding silicone subbase. Also, adding soft subbase helps to develop multiple cracks around the sutures in comparison to the gypsum samples, where one main crack develops and propagates through the entire plate (Fig 4.9(a)). A comparison of the mechanical properties of normalized peak load, normalized stiffness, and normalized toughness, reveals that the sutures with angle $\theta=45°$ show higher values in comparison to the other sutures angle (Fig 4.9(b))

(a)
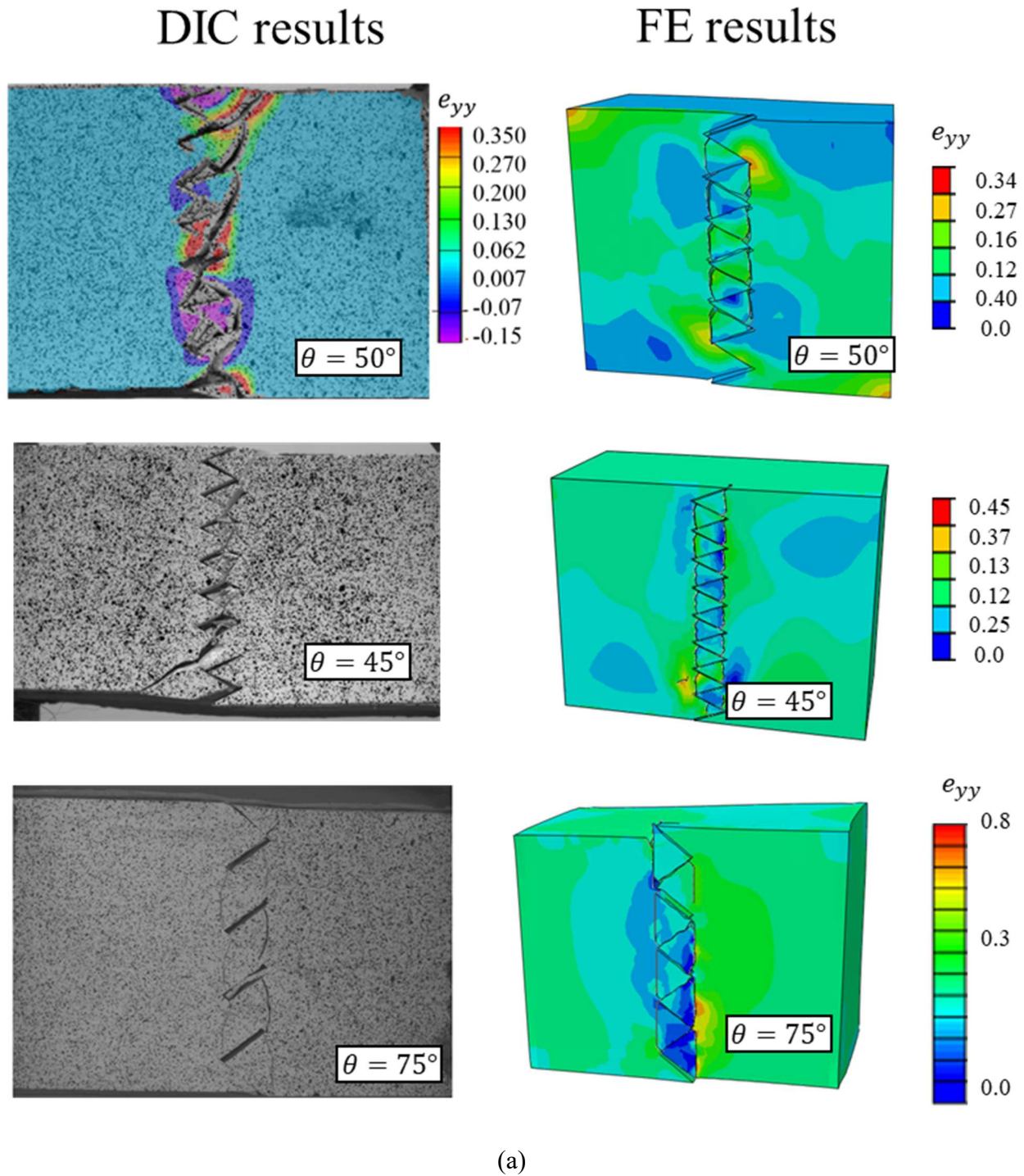
Figure 4.9. (a) Comparison between FE simulations and Experiments using gypsum and silicone samples, (b) Comparison between normalized peak load, stiffness, and toughness of experiments and simulations (results are normalized with respect to angle 45 (θ =45°).

Figure 4.9 continued
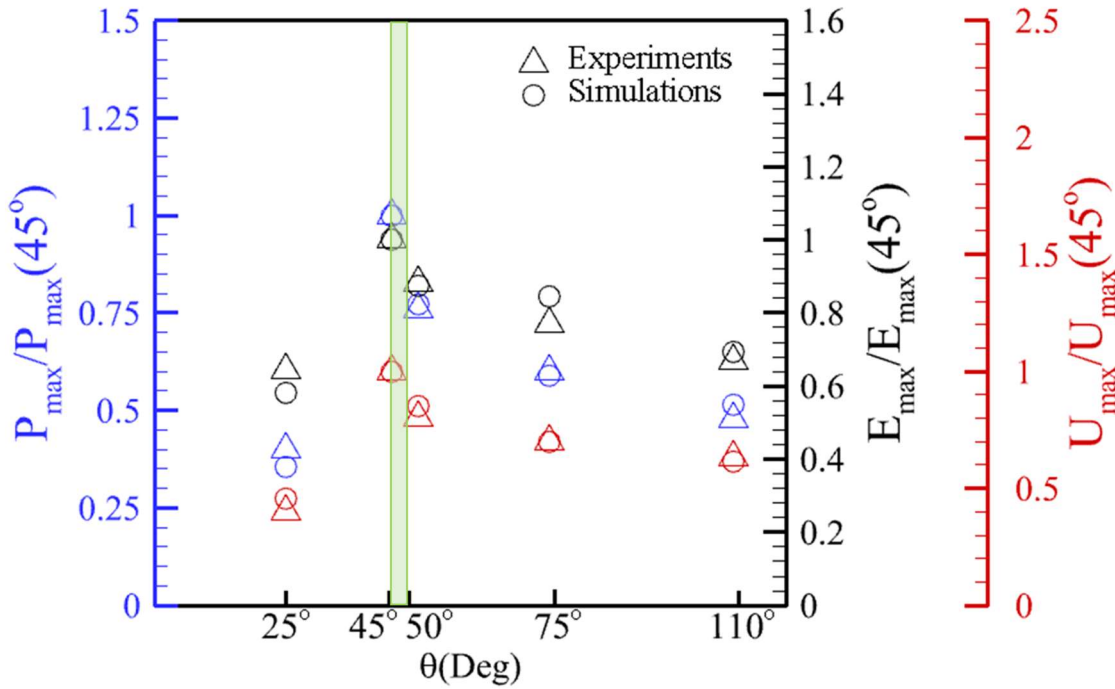
(b)

4.6 The analytical method to predict crack angle propagation in brittle materials

As discussed in section 4.5.1, when two brittle plates containing sutures come in contact and loaded under shear, the crack starts to propagate at an angle with respect to the sutures angle and far from the sutures the angle becomes equal to 45° (Hedayat., 2013). In this section, I am planning to use some simplification in order to use LEFM concepts in the prediction of crack angle propagation. The schematic of two brittle plates contains suture under shear loading condition is presented in Fig 4.10 (a). It is assumed that the shear loading is applied far away from the sutures. As shown in the red zoomed box, in a single suture under shear, the top kinked is under compression while the bottom kinked is under tension. The kinked under tension is responsible for crack propagation. Therefore, a single suture can be estimated by a kinked crack under pure shear. Based on the Mohr's circle, the stress state on pure shear can be transformed to biaxial loading using 45° rotation as presented in Fig 4.10 (a). For all the cases in this study, θ represents the sutures angle and $\theta/2$

represents the angle between the suture kinked and horizontal line. The angle β is defined as an angle between a vertical line and kinked crack in a new coordinate system (after 45° rotation) and can be calculated as $\beta = 45 - \theta/2$. The construction of a single kinked crack model under biaxial loading for different angle $\theta = 25°, 45°, 50°$ are presented in Fig 4.10(b). The FE result from the kinked crack with $\beta = 22.5°$ is presented in figure 4.10 (c). As shown in Fig 4.10 (c), the crack starts to propagate in angle, α_{bi} (the initial crack angle propagation) followed by secondary crack angle propagation α_{bf}.

(a)

(b)
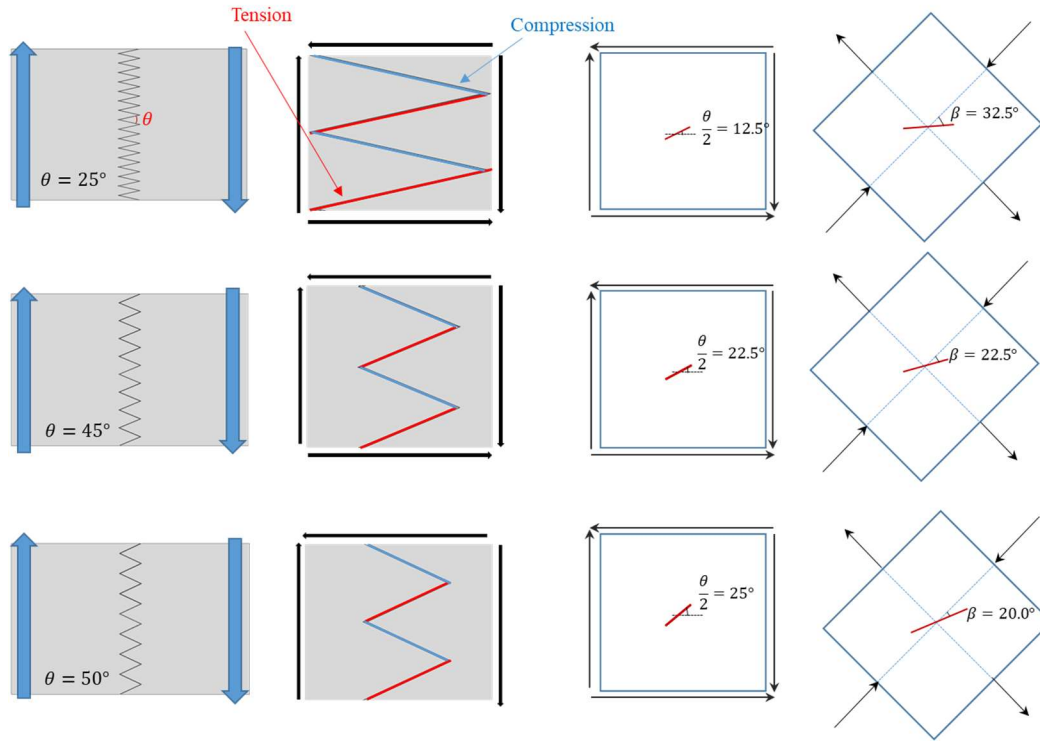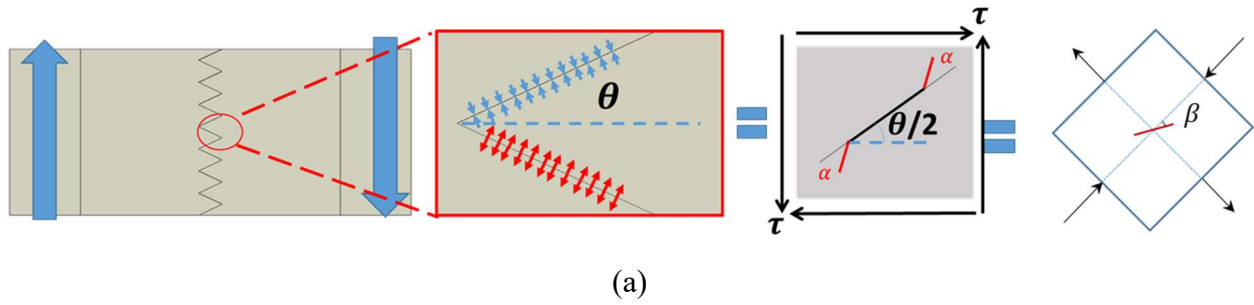
Figure 4.10. (a) Estimating the crack angle propagation in brittle sutures using kinked crack approximation (b) schematic of converting sutures θ =25, 45, 50 to the equivalent kinked crack under bi-axial loading, (c) schematic of crack propagation forθ=25, α_{bi} presents the initial crack angle propagation, α_{bf} presents final crack angle propagation.

Figure 4.10 continued

(c)
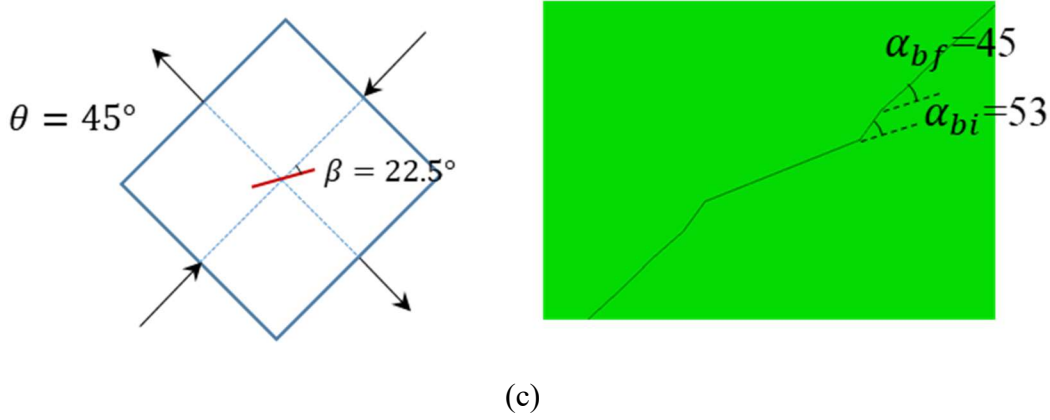
The analytical solution for the kinked crack under pure shear for brittle materials developed based on the maximum principal stress method (MTS) (Godoutos et al.,2013). Based on Linear Elastic Fracture Mechanics (LEFM) concept the cylindrical stress state at the crack tip can be presented as follow (Fig 4.10(a));

$$\sigma_\theta = \frac{1}{\sqrt{2\pi r}}\left[\left\{\frac{K_I}{2}cos\frac{\theta}{2}(1+cos\theta)\right\} - \left\{\frac{3K_{II}}{2}sin\frac{\theta}{2}(1+cos\theta)\right\}\right] \tag{4.9}$$

$$\sigma_r = \frac{1}{\sqrt{2\pi r}}\left[\left\{\frac{K_I}{2}cos\frac{\theta}{2}(3-cos\theta)\right\} - \left\{\frac{3K_{II}}{2}sin\frac{\theta}{2}(1-3cos\theta)\right\}\right]$$

$$\tau_{r\theta} = \frac{1}{\sqrt{2\pi r}}\left[\left\{\frac{K_I}{2}sin\frac{\theta}{2}(1+cos\theta)\right\} - \left\{\frac{K_{II}}{2}cos\frac{\theta}{2}(1-3cos\theta)\right\}\right]$$

Based on MTS criteria, the following equations are needed to be satisfied in order for the crack to propagates;

$$\frac{\partial \sigma_\theta}{\partial \theta} = 0 \tag{4.10}$$

$$\frac{\partial^2 \sigma_\theta}{\partial \theta^2} < 0 \tag{4.11}$$

By substituting Eqn 4.9 into Eqn. 4.10 and 4.11, we will have

$$tan^2\frac{\theta}{2} - \frac{K_I}{2K_{II}}\,tan\frac{\theta}{2} - \frac{1}{2} = 0 \tag{4.12}$$

$$\frac{3}{2}\left[\left(\frac{1}{2}\,cos^3\,\frac{\theta}{2} - cos\frac{\theta}{2}sin^2\,\frac{\theta}{2}\right) + \frac{K_{II}}{K_I}\left(sin^3\,\frac{\theta}{2} - \frac{7}{2}sin\frac{\theta}{2}cos^3\,\frac{\theta}{2}\right)\right] < 0 \tag{4.13}$$

Also, in a biaxial loading (see Fig 4.11(b)), we will have:

$$K_I = \sigma(sin^2\beta - cos^2\beta\sqrt{\pi a}) \tag{4.14}$$

$$K_{II} = -2\sigma\,sin\beta\,cos\beta\sqrt{\pi a}$$

Finally, the analytical solution can be obtained by inserting Eqn 4.14 into Eqns 4.12 and 4.13 and satisfying the condition for these equations. The analytical solution for kinked crack based on angle β is presented in Fig 4.12.
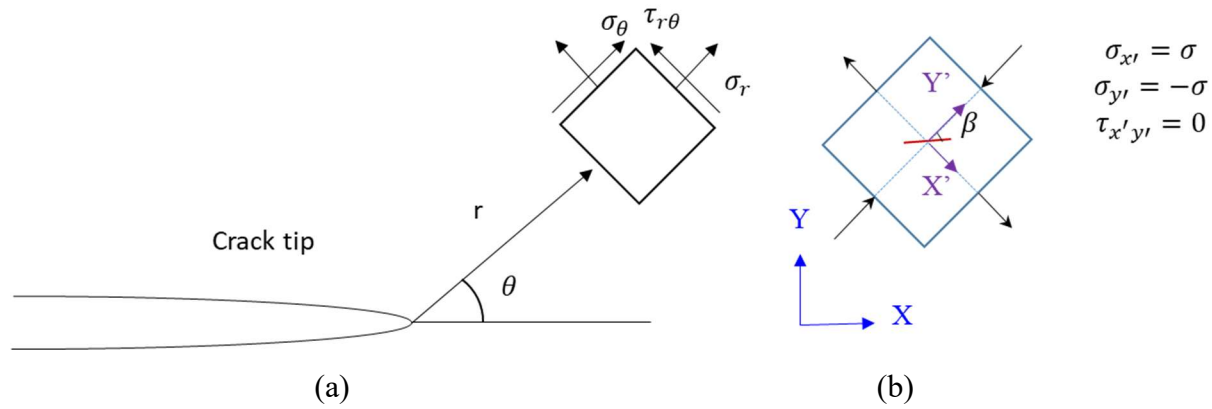
Figure 4.11. (a) spherical coordinate around the crack tip, (b) stress state for the biaxial load

Finally, the comparison between analytical solution for the kinked crack under pure shear, and the crack angle prediction from both experiments, and FE simulation of interdigitated sutures under simple shear indicates a good match between analytical prediction, FE simulation, and experiments (see Fig 4.12).
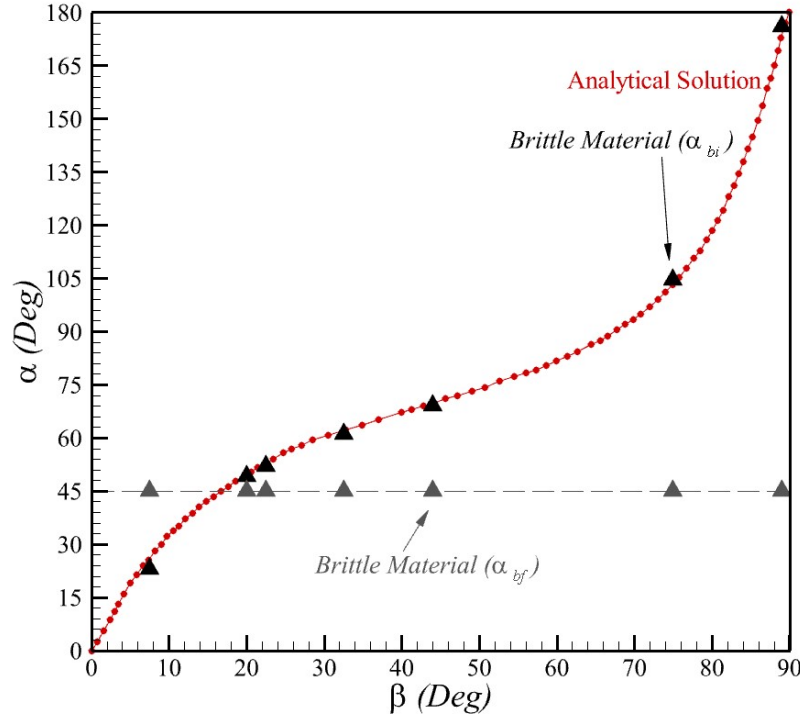
Figure 4.12. Analytical solution for the kinked crack under biaxial load as shown in red, the FE results for initial crack angle propagation (α_{bi}) of different values of β is shown in black, while the results from final crack angle propagation are shown in grey

4.7 Role of soft material in controlling

4.7.1 Effect of soft material elastic modulus with respect to the brittle plate modulus

In this section, the role of soft material beneath the brittle material in controlling the crack direction is investigated for the kinked crack under pure shear loading (rotated biaxial loading). This section aims to study the effect of elastic modulus of the soft substrate with respect to the brittle plate in controlling the crack angle propagation. Therefore, a set of parametric analyses was developed in such a way that the elastic modulus of soft material is changing while the other parameters in the model are kept constant. As a result, for each value of kinked crack angle β, different values of the modulus aspect ratio exist. The modulus aspect ratio of soft to brittle modulus are ranging between $E_1/E_2 = 0.001 - 1$. Where, E_1 and E_2 represent the modulus of soft material and brittle material, respectively. Figure 4.13 (a) presents the XFEM results from the plate with a soft substrate beneath the brittle plate for different values of E_1/E_2 and three selected kinked angle ($\beta = 20°, 22.5°, 32.5°$). The results for three selected angles (β=20°, 22.5°, and 32.5°) for various

values of E_1/E_2 are presented in Fig 4.13(a). As shown in Figure 4.13 (a)and(b), when the value of E_1/E_2 is small ($E_1/E_2 = 0.001$), it does not help in controlling the crack direction, as the value of modulus aspect ratio increases, the crack starts to deviate and propagate in a larger angle with respect to the kinked crack. The maximum change in the crack angle propagation can be observed when $E_1/E_2 = 0.1$ and then decreases as the aspect ratio increases. As a result, one could see that the optimized value of the aspect ratio is equal to 0.1. Also, the shear strain contour for three selected aspect ratio is presented in Fig 4.13 (b),(c), (d). The results state that for the soft base with lower values of stiffness, more damage can be observed in soft material, and in the onset of crack propagation, the crack propagates unstably. As we increase the E_1/E_2 to 0.1 it adds more shear to the system in comparison with $E_1/E_2 = 0.01$, and it helps to change the crack propagation direction by developing stable crack propagation (see Figure 14(c)). Finally, for the case with high elastic modulus aspect ratio($E_1/E_2 = 1$), a little damage can be observed in the silicone. After crack initiation, the crack propagates unstably and soft material does not play a role in controlling the crack direction.

(a)
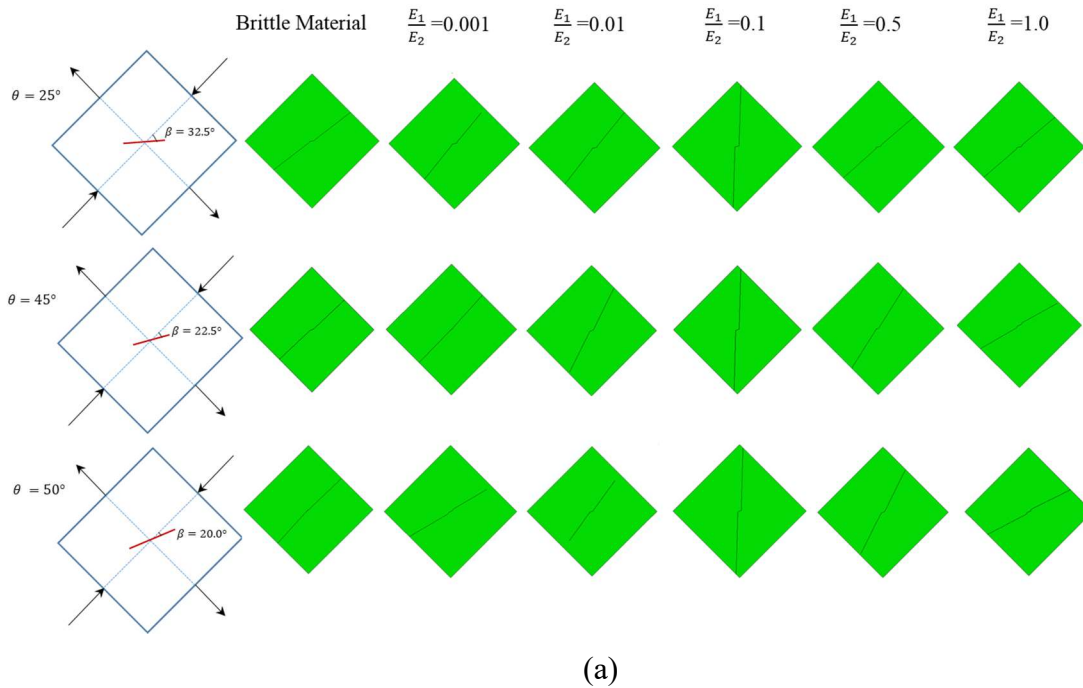
Figure 4.13. Effect of the modulus aspect ratio of brittle to soft material presented for $\theta = 25°$, 45°, 50° and $E_1/E_2 = 0.001 - 1.0$. (b) $E_1/E_2 = 0.01$, (c) $E_1/E_2 = 0.1$, (d) $E_1/E_2 = 1$ for $\theta = 45°$.

Figure 4.13 continued

Before crack initiation At crack initiation In the middle of propagation

$E_1/E_2 = 0.01$

Brittle plate on top
of soft substrate

Soft substrate

-0.02   0.02
ε_{12}

(b)

Before crack initiation At crack initiation In the middle of propagation

$E_1/E_2 = 0.1$

Brittle plate on top
of soft substrate

Soft substrate

-0.02   0.02
ε_{12}

(c)

Figure 4.13 continued

Before crack initiation   At crack initiation   In the middle of propagation

$E_1/E_2=1$

Brittle plate on top
of soft substrate

Soft substrate

-0.02   0.02

ε_{12}

(d)

4.7.2 Effect of soft material strength with respect to the brittle plate strength

In this part, I investigated the effect of soft material strength with respect to the brittle plate strength by considering three values of $\sigma_{fs}/\sigma_{fb} = 0.0075, 0.075, 0.75$ when $E_1/E_2 = 0.1$ Where, σ_{fs} and σ_{fb} accounts for material strength of the soft substrate and brittle plate, respectively. The results for three values strength ratios are presented in Figure 4.14. As expected, when the strength of soft material with respect to the hard plates is low or very high, it is not beneficial in controlling the crack direction. While with the correct strength ratio, we are able to control the crack direction.
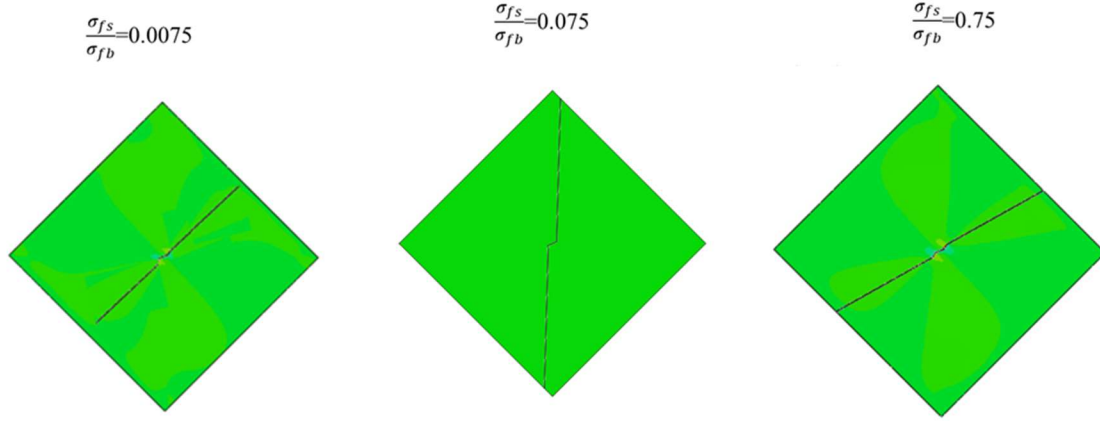
Figure 4.14. Effect of the soft material to brittle material strength ratios for $\sigma_{fs}/\sigma_{fb} = 0.0075, 0.075, 0.75$

The schematic of the kinked crack angle under biaxial loading is presented in Fig. 4.15 (a). The coordinate system (shown in black) is defined in the center of the square and is parallel to sides of the square. Angle β is defined as an angle between the vertical line in a coordinate system and a kinked crack. The local coordinate system is defined at the tip of a kinked crack (shown in purple). Under biaxial loading, the crack starts to propagate in an angle with respect to the kinked crack. For the brittle material, the initial crack angle propagation (α_{bi}) is defined as an angle between the crack and horizontal line in the local coordinate system, as presented in Fig 4.14(a). Since the kinked crack is much smaller in comparison to the size of the sample (the LEFM approach can be used along with XFEM method), in the brittle material and far away from the crack tip, the crack starts to change the direction due to the loads and boundary conditions. Therefore, a secondary crack angle propagation is defined with respect to the local coordinate system (α_{bf}). Both α_{bi} and α_{bf} are defined for the case with the brittle plate (no soft material exists). When soft material exists beneath the brittle plates, the angle of crack propagation with respect to the local coordinate system is defined by α'.

A comparison between the crack angle propagation (α) vs. different values of β is presented in Fig 4.15(b). As shown in Fig 4.15 (b), the higher value of crack angle propagation occurs when $E_1/E_2 = 0.1$. Although the aspect ratio of the soft to brittle material plays an important role in control the crack, based on Buckingham's theorem that discussed in section 4.3, the role of soft material strength also needed to be considered.

As previously discussed, the sutures angle θ under simple shear can be estimated by a kinked crack of angle β. The results from normalized peak load, normalized stiffness, and toughness reveal that the maximum performance occurs when the sutures angle θ is equal to 45°.
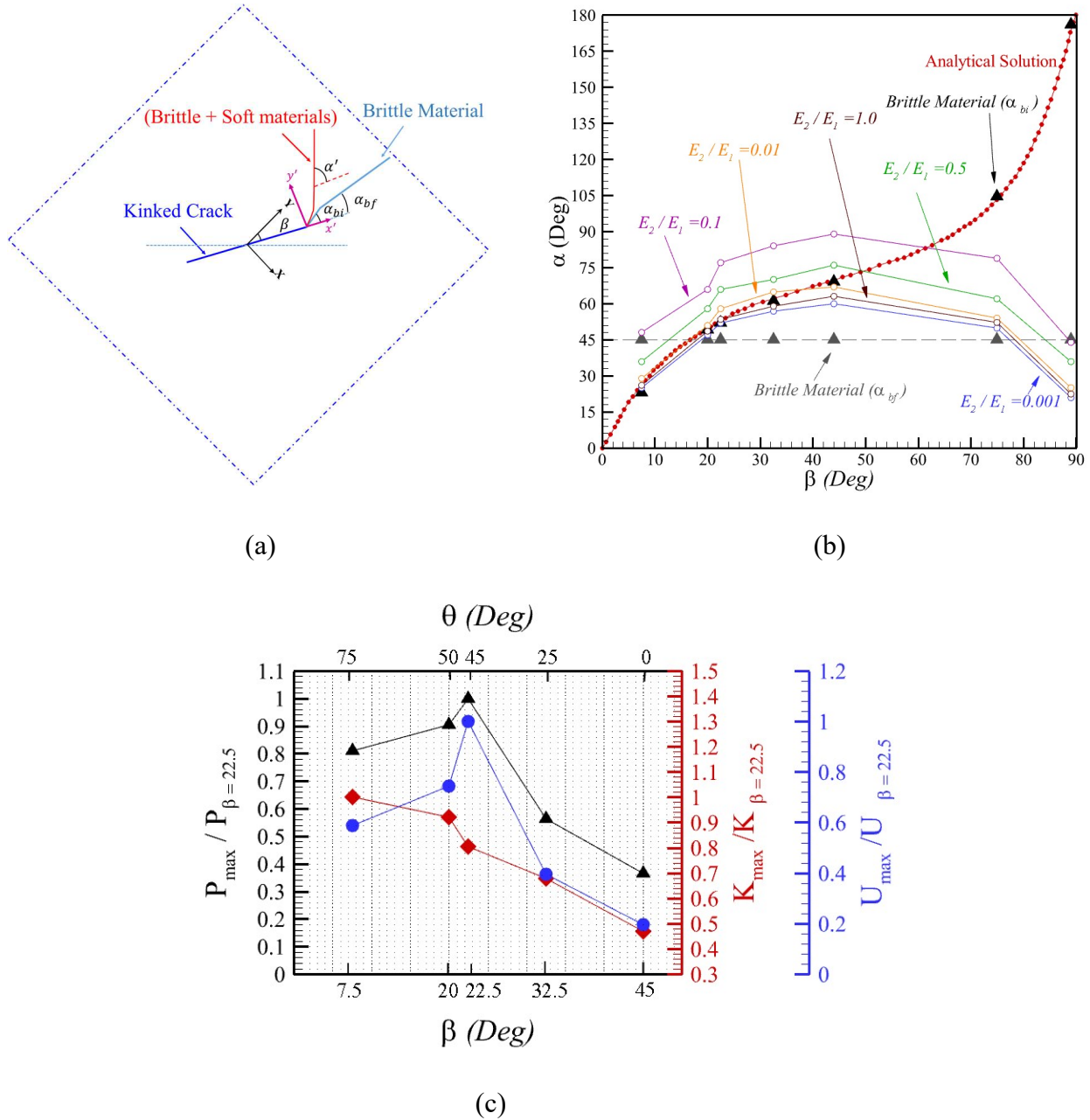
Figure 4. 15. (a) schematic of RVE under biaxial load, β (angle between kinked crack after 45° rotation and horizontal line in the local coordinate system; α_{bi} and α_{bf} are initial crack angle and secondary crack angle propagation in brittle material with respect to the kinked angle, α' is the crack angle propagation for composite models (include brittle and soft substrate), (b) Kinked crack angle (θ) vs. crack angle propagation (α); (c) Comparison between normalized peak load, stiffness, and toughness of different kinked angle for $\frac{E_1}{E_2} = =0.1$.

4.8 Summary and Conclusions

In this chapter, the role of architecture bio-inspired from boxfish scute carapace was investigated in controlling the crack direction. The boxfish carapace contains hexagonal dermal scutes, a combination of the brittle hexagonal plate (hydroxyapatite) on top of a very compliant (collagen) material. While the mineral plates are separated by patterned sutures (triangular interlocking patterns), there is no interphase material connecting them. Instead, the connection between mineralized plates is done through the collagen base. The *in-situ* experiments between two boxfish scute under shear loading condition reveal that the fracture occurs around the suture areas and cracks did not propagate through the mineralized. Therefore, a set of parametric studies using gypsum (brittle material) and silicone (soft material), including different sutures angle were developed along with FE simulation to understand the role of this architecture. Also, the role of soft material (i.e., the role of soft material elastic modulus to brittle material modulus) was investigated using FE simulations. The following results were obtained from this study,

1) a parametric study for different values of sutures angle on top of soft material confirmed that the maximum value for peak load, stiffness, and toughness could be obtained when sutures angle is equal to 45°. Also, the existence of soft material beneath of brittle material can control the crack direction.

2) In brittle material containing sutures under shear loading, the crack starts to propagate with an initial angle. This angle can be estimated using a simplified LEFM model with kinked crack.

3) The FE simulation from a bi-layered material (consisting kinked crack in brittle material) under pure shear confirmed that the best performance in controlling the crack propagation angle direction could be obtained when $E_1/E_2 = 0.1$, $\sigma_{fs}/\sigma_{fb} = 0.075$. Therefore, one can optimize this architecture for shear loading by selecting the sutures angle equal to 45°.

CHAPTER 5. INVESTIGATING THE ROLE OF IRONCLAD BEETLE CUTICLE IN ENHANCING THE MECHANICAL PROPERTIES

5.1 Introduction

Beetles are the subclass of arthropods and have lived on earth for over 300 million years. Their resistance against the attack of various predators and their structural and mechanical performance across flying terrestrial make them an attractive option for research. One of the terrestrial beetles is the Zopherinae, ironclad beetles. The Ironclad beetle's exoskeleton is known to bend entomologist's steel pins and withstand high compressive loads, including the occasional automobile that would prove fatal to most insects. This study focuses on the abdominal portion of the exoskeleton, consisting of the elytra and ventral cuticle. The ordered arrangement and complex architectures found within the exoskeleton (elytra) of this specially adapted insect result in extremely high compressive resistance, far beyond any other beetle identified to date. More specifically, to understand the role of sutures connecting elytra parts in the Ironclad beetle. To date, structure-mechanical property relationships of blades have not yet been fully realized for the ironclad beetle's exoskeleton. Here, using a combination of optical and electron microscopy, computed tomography and mechanical testing, 3D printing prototype, and finite element analysis, the unique adaptations, novel architectural design features and interfacial structures have been revealed within the exoskeleton of *P. diabolicus* and their divergence from terrestrial Coleoptera. The architecture of the suture region of the elytra, modified for terrestrial living, has a unique architecture consisting of specially modified interlocking blades, whose elliptical geometry, laminated microstructure and frictional interfacial features, enhances coupling strength, provides a uniform stress distribution and increases toughness significantly more than other terrestrial beetles. This model system represents a tough, damage tolerant biological material that exemplifies a departure from other types of beetles. In this chapter, I will investigate the role of Ironclad beetle cuticle under compression. Also, the role of blades in elytra will be investigated using both FE simulations and 3D printing mechanical testing.

5.2 Compression resistance nature of Ironclad beetle (P. diabolicus)

The exoskeleton's resistance to an external load in Ironclad beetle is investigated by comparing the maximum compressive force of other beetles native to the southern California region (see Figure 5.1). To this aim, Asbolus verrucosus, Eleodes grandicollis, and Cryptoglossa muricata were chosen for comparison due to their defense mechanisms (thanatosis), areas of prevalence and terrestrial nature (Rivera et al., 2019). Representing the bulk of the exoskeleton, the abdomen of the beetles consists of the elytra, sclerotized forewings that cover membranous hindwings, and ventral cuticle (Figure 5.2 (a)-(b)). For the insects tested, their elytra consist of two interdigitated, highly sclerotized elytron that does not separate (Figure 5.1 (d) and Figure 5.2 (b)). To date, structure-mechanical property relationships have not been fully realized for the ironclad beetle's exoskeleton, but recent publications have examined other insect cuticles. Peak compression forces showed P. diabolicus fractured at 150 N with an average of 133 ± 17.0 N ($\sim$39,000 times its body weight) and exhibited a stiffening nature as it was compressed, indicating a complexity in the material properties of its exoskeleton or the arrangement of its constituents (Figure 5.1(b)). In contrast, the other beetles reached a peak load of 53N and exhibited a relatively diminished strength to weight ratio (inset Figure 5.1(c)). With beetle exoskeletons composed of non-mineralized alpha chitin fibers embedded in a proteinaceous matrix, it is hypothesized that the principal factors in compression resistance of P. diabolicus remain the bulk geometry and arrangement of the ultra and microstructure. In all specimens, fracture of the elytra along the medial suture marked the prime mode of failure, as stress typically concentrates between interlocking segments of insect exoskeletons. I further analyzed transverse cross-sections of the abdomen and identified the interfacial regions of interest denoted by the medial suture and lateral supports. Optical microscopy of polished cross-sections highlights varying thickness and degree of interdigitation between the sutures of the distinct species with the greatest geometric complexity joining the elytra of the ironclad.
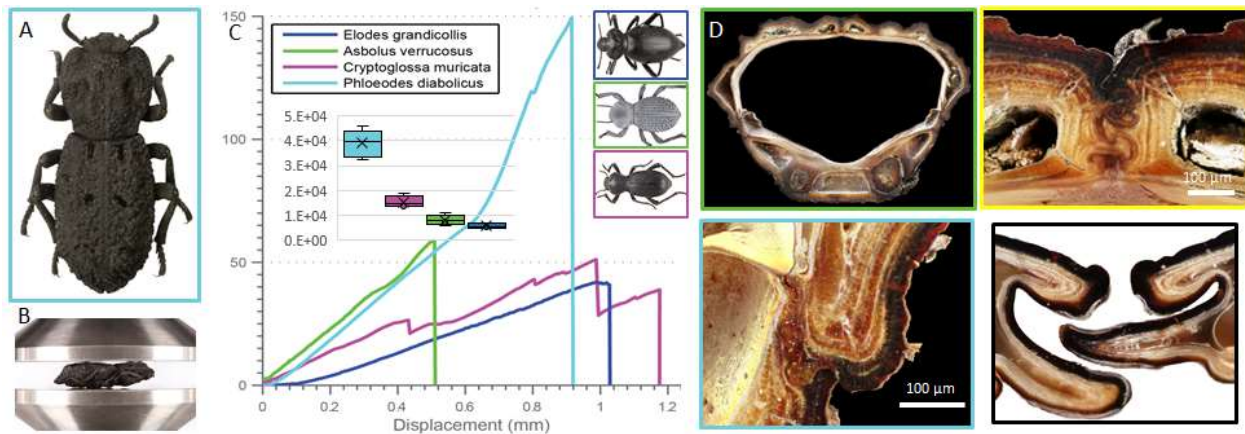
Figure 5.1. Mechanical properties of beetles during compression and unique architectures. a) Diabolical Ironclad beetle (P. diabolicus), Scalebar 5 mm; b) Ironclad beetle under compression, c) Force vs. displacement curves for various beetles tested d) Optical micrographs of a transverse cross-section (green box), lateral supports (blue box) and medial sutures (yellow box). Bottom left: suture in Japanese flying beetle(Figure adapted from Rivera et al., 2019).

5.3 Ironclad beetle microstructure

The unique architecture within the exoskeleton of P. diabolicus that varies from the conventional terrestrial beetles and contributes to enhanced mechanical performance is presented in Figure 5.2. The exoskeleton primarily comprises of alpha chitin fibers in layers of assembled bundles (Balken) that are joined together by a proteinaceous matrix (Rivera et al.,2019). I further reveal toughening mechanisms resulting from the macro-structural architecture along with mechanical interfacial features (role of blades existence in elytra) that could provide insight into the fabrication of tough, impact-resistant composite materials.

<div align="center">(a)   (b)</div>
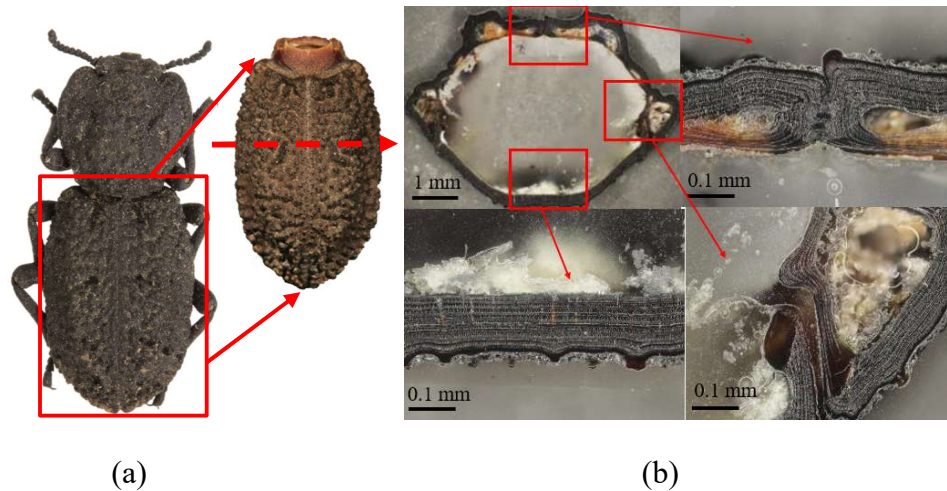
Figure 5.2. (a) The diabolical ironclad beetle along with an isolated section of the abdomen section of the insect. b) a cross-section highlighting: the medial suture in the elytra, lateral support, and ventral cuticle (Figure Courtesy to Jesus Rivera UC Riverside).

5.4 Finite element modeling of entire cuticle under compression

To identify the origins of compression resistance, I develop a 3D finite element model of the full abdominal area of Ironclad beetle using the CT scan of the real Ironclad. FE simulation on the entire abdomen is very similar to the real tests on Ironclad beetle. Both mesh and CT scans are provided by Amira software, then the mesh transferred into ABAQUS software for further analysis. The mesh from the elytra and ventral part of the abdomen are presented in Figure 5.3.
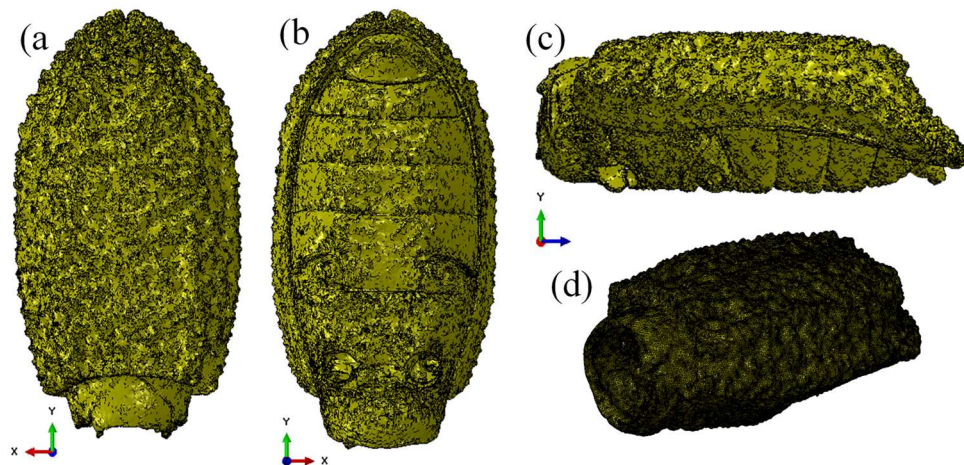
Figure 5.3. The CT scan from the abdomen of Ironclad beetle (a) elytra view (top view), (b) ventral view (bottom view), (c) side view, (d) meshed view of the entire abdomen used in ABAQUS software

Analyzing a transverse cross-section of the abdomen, the exoskeleton can be divided into three distinct regions, the elytra (comprised of two sclerotized-hardened forewings), the lateral supports and the ventral cuticle. With stress typically concentrating between interlocking segments. The Ironclad beetle had been developed variation in lateral supports promotes the region with specific stiffness to protect vital regions. Micro-computed tomography of the ironclad's exoskeleton uncovers three region-specific interfaces between the elytra and ventral cuticle, providing lateral support. Polished transverse cross-sections of these regions reveal interdigitated, interlocking, and free-standing support variants (Figure 5.4). Besides, the top part of the elytra also connected by interdigitated blades (Figure 5.2 (b)).

(a)   (b)

(c)   (d)
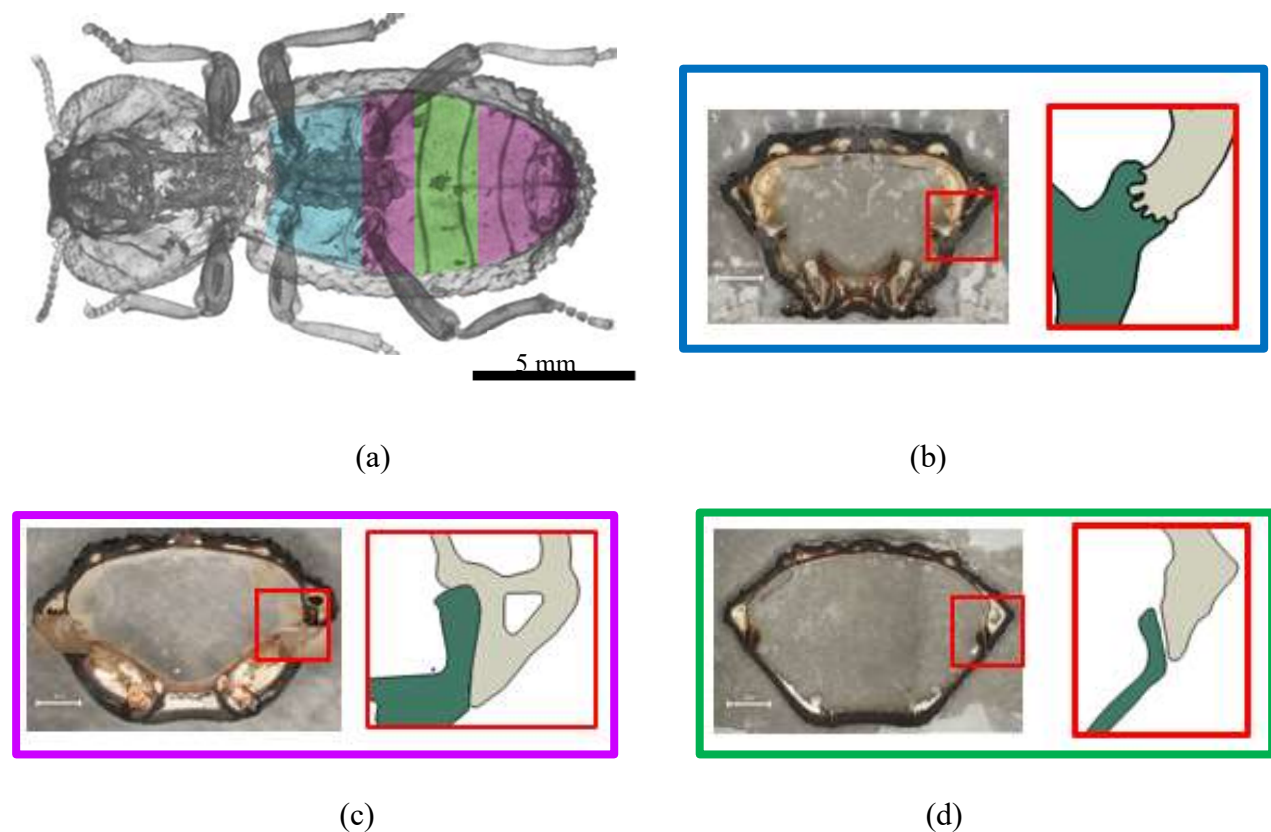
Figure 5.4. (a) CT scan from Ironclad beetle cuticle (photo courtesy to Jesus Rivera), location, and shapes of lateral supports (figure adapted from Rivera et al., 2019), (b) interdigitated support, (c) latching support, (d) free-standing support.

In FE simulations, the entire abdomen of the beetle is located between two rigid plates and the compression load is applied quasi-statically on top of the elytra (Figure 5.5). The maximum principal stress distribution of the entire abdomen under compression along the length of the beetle is presented in Figure 5.6.

(a)   (b)
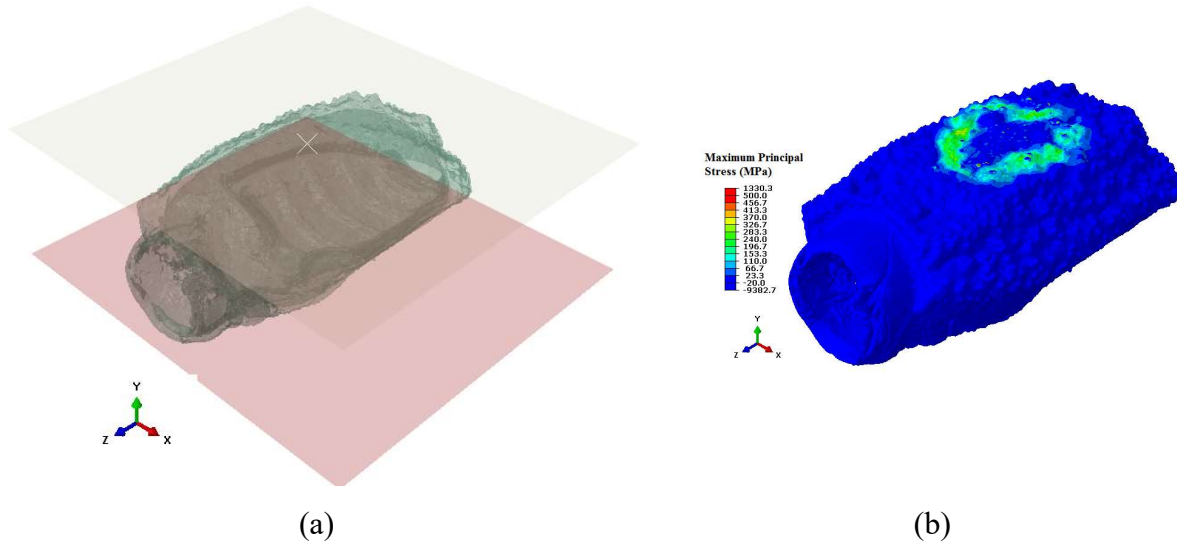
Figure 5.5. (a) The geometry of Ironclad beetle under compression, (b) the maximum principal stress distribution along the beetle cuticle.

The results from the maximum principal stress contour along different cross-sections confirm that the maximum stress concentration occurs around the places were sutures exist while lower stress concentration can be observed in places without sutures (e.g., latching or free-standing supports). This analysis gives us an insight into the performance of Ironclad beetle. Therefore, Investigating the effect of interlocking blades is a great interest in this research. It is essential to understand the role of the blade and its mechanism in protecting beetle carapace. Both experimental and numerical results confirmed higher stress concentration around interdigitating supports in comparison to latching/free-standing supports. The results also present higher stress concentration in elytra, where interdigitated sutures (blades) exist. The 3D model from the entire abdomen does not include any blades geometry, and thus, in the next section, a 2D models are developed in order to capture the role of blades geometry in Ironclad beetle.
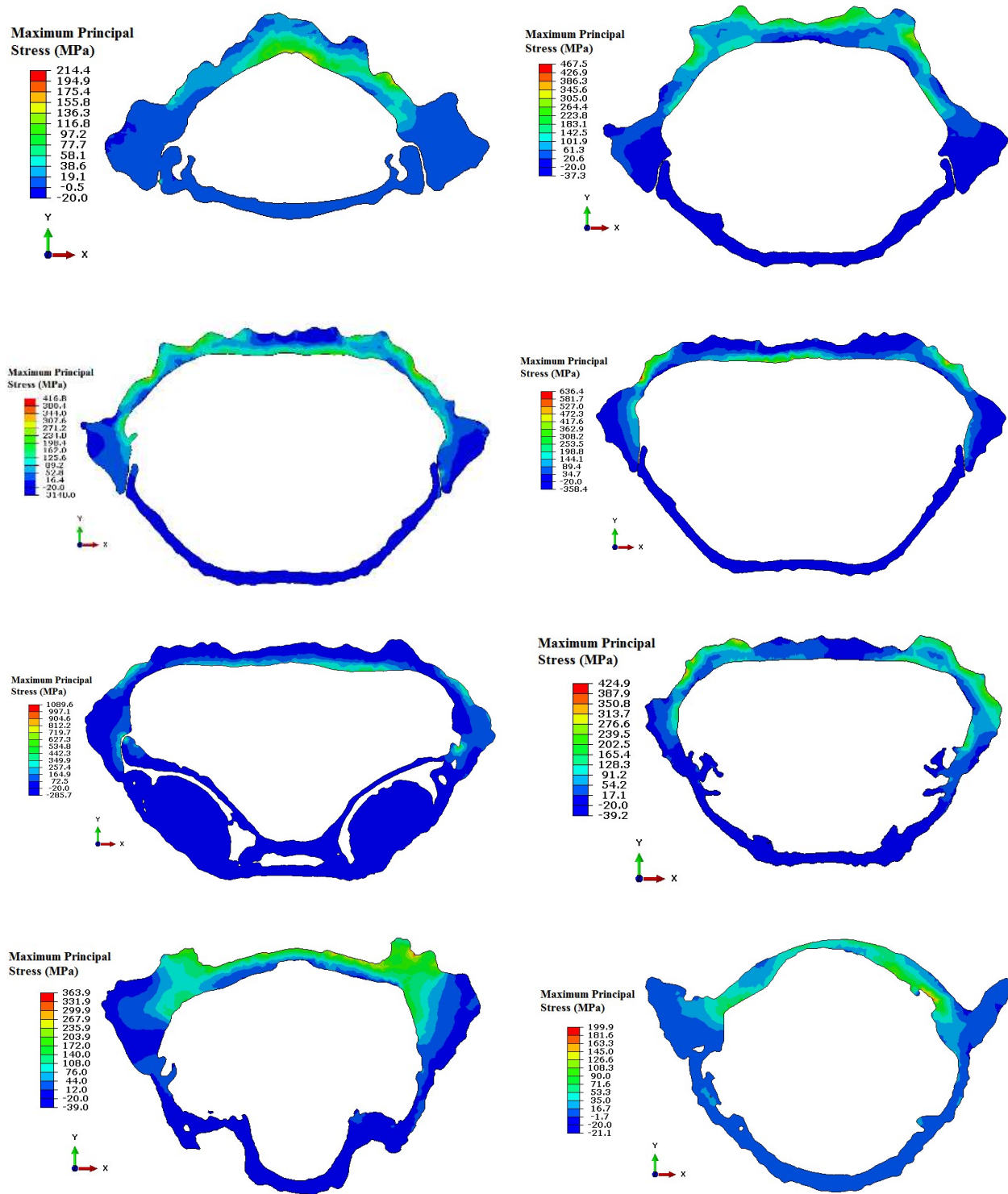
Figure 5.6. The maximum principal stress for different cross-sections along the length of the beetle cuticle (3D FE model of abdomen).

5.5 2D Finite element models of Ironclad beetle cross-section.

Higher stress concentration was observed in the areas where interface connections (blades) exist; however, the 3D model does not include blades geometry either in elytra or in the ventral part (lateral supports) due to the limitation with Amira software. Therefore, 2D models of various cross-sections (i.e., interdigitated, interlocking, and free-standing) of the Ironclad beetle were developed using CT scans and ABAQUS to understand the role of blades and interlocking mechanisms. The maximum principal stress distribution for all three types of lateral supports under compression loads are presented in Figure 5.7 (a)-(c). A comparison between load-displacement for all three types of lateral supports reveals that the cross-section with interdigitating supports presents higher values for load-displacement curves in comparison to two other cases. Besides, the load-displacement curves in Figure 5.7(d) presents two different slopes before failure, based on FE simulation and experimental observations, the first slope is due to engaging of the lateral supports while the second slop is related to the sutures engagement in elytra up to the failure point.
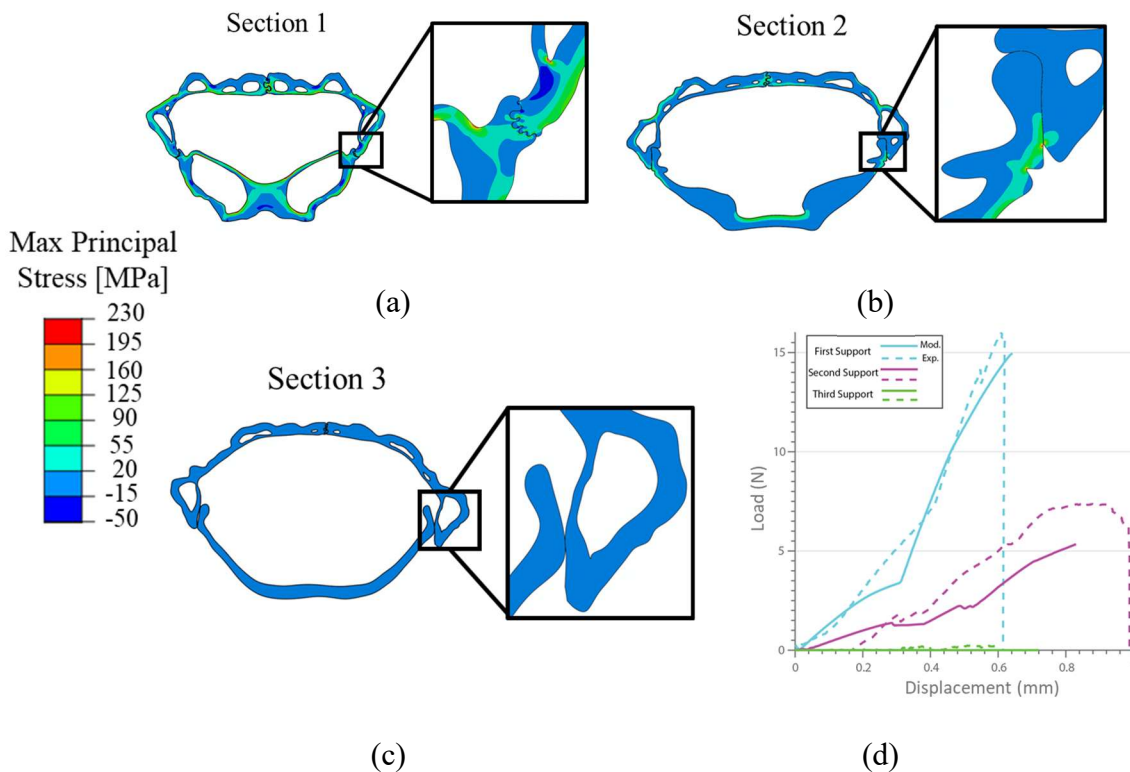
Figure 5.7. 2D simulations of various cross-sections include lateral support. (a) section1, interdigitating lateral support, (b) interlocking lateral support, (c) free-standing lateral support, and (d) comparison between the load-displacement curve of FE simulations and Experiments.

As presented in Fig 5.7, blades in interface areas play an essential role in increasing the deformation, and subsequently compression resistance nature of the cuticle, however, many unknowns needed to be investigated, For example, the role of size, shape, and number of the blades are still unknown. Besides, the maximum principal stresses from FE simulations confirm that blades in elytra regions are mostly in tension (see Fig 5.8). For the rest of this study, all the simulations and experiments were performed under tensile loading condition.
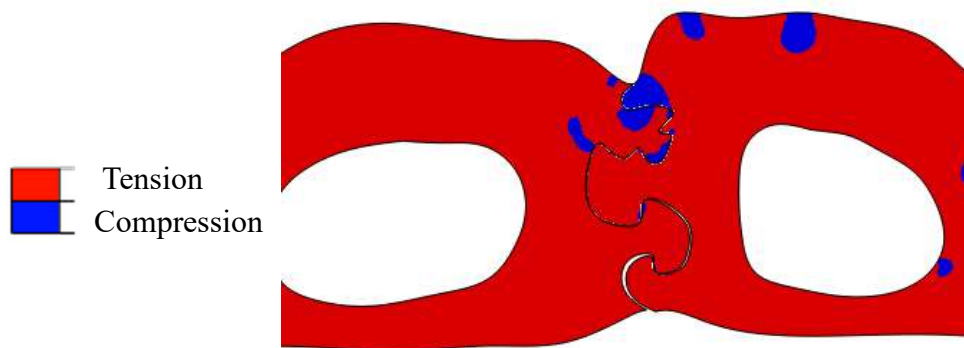
Figure 5.8. Local tensile and compressive stress on the suture while the section is subject to a compressive load.

5.6 Investigating the role of the blades bio-inspired from Ironclad beetle elytra

As discussed in previous sections, compared to flying beetles, the evolution of terrestrial variants has dictated the incorporation of additional interlocking features in the elytra, increasing the coupling strength of the suture. Hence, I attempt to quantify the variance between blade number and geometry using Finite element analysis (FEA) modeling of the biological structures and mechanical testing of additive manufactured mimics in tension (the credit of experimental work goes to Jesus Rivera from UC San Diego). FEA models of the bulk highlight stress concentration in sutures, with tension being the primary mode of loading, but one can also see localized regions of compression in the top regions of the blades (Figure 5.8). Further analysis of the sutures reveals the largest principal stresses in the necks and contact regions of the blades. During loading, the addition of blade segments results in relatively uniform stress distribution, while the geometry of the blade controls the localized stresses. In order to understand the role of blades size and geometry, 3D printed samples were tested in tension to determine the failure mode. For this purpose, two sets of the parametric study were done to understand the role of size and number of

the blades. Finite element models were adopted along with 3D printed prototypes technique to evaluate variations in stiffness, toughness, and peak tensile load based on the number and geometry of the sutural blades under tensile load. To this end, two sets of parametric tests were designed. For the first set of tensile tests, case 1 (quantity variation), the number of the blades (with the naturally observed geometry) was varied up to five blades (See Figure.5.10 (b)). For case 2 (capacity variation), the number of blades was increased while keeping the area constant, resulting in a decrease of feature size (Figure. 5.15). The geometry of each blade developed from three ellipses, as presented in Figure 5.9 (b). Geometric analysis of P. diabolicus' blades (Fig. 5.9(a)) reveals a 1.8:1 ratio between the semi-major axis, with the primary geometry of each blade parametrically represented as three identical ellipses connected with a specific angle, θ (Fig. 5.9(b)). Here, θ is defined as the angle between the centers of two adjacent ellipses and a horizontal line. In Ironclad beetle, the contact angle is 25° between ellipses. These elliptical elements appear to be optimized to distribute load uniformly while preventing slip under tension (as is seen in circular elements).

(a)   (b)
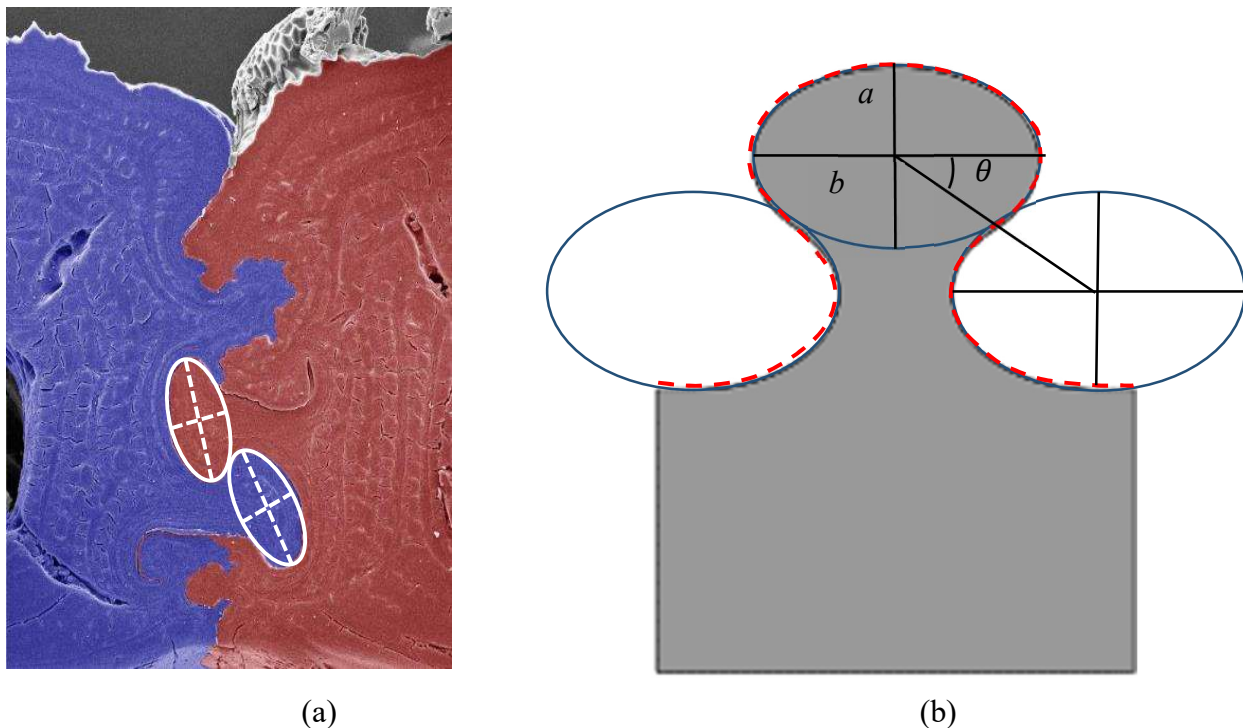
Figure 5.9. (a) Blades geometry bio-inspired from Ironclad beetle elytra, (b) representative blade geometry used for both FE simulation and 3D printed samples.

5.6.1 Identifying role of blades number (Case1-parametric study)

The dimensions and geometry of blades for Case 1 are presented in Figure 5.10 (a) and (b), respectively.
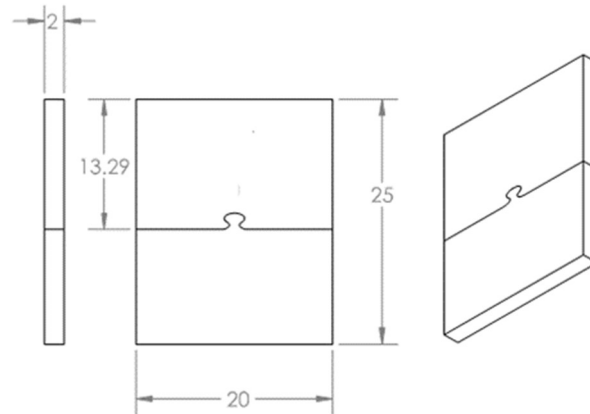
(a)

(b)

Figure 5.10. (a) geometry and the dimension of the sample used for the 3D printing and FE models, (b) the CAD geometry for the various number of blades under tensile loading condition.

The tough resin is used to print the samples using forms lab 3D printer. The dogbane samples from tough resin were 3D printed and tested to get a material characterization of the tough resin using the ASTM D638 method. This material is used later in the analysis (Figure 5.11). The maximum principal stress distribution for one to four blades is presented in Figure 5.12 (a)-(d), respectively. The load-displacement curves from both experiments and finite element results for different blades number for case 1 are presented in Figure 5.13(a)-(d).

(a)   (b)
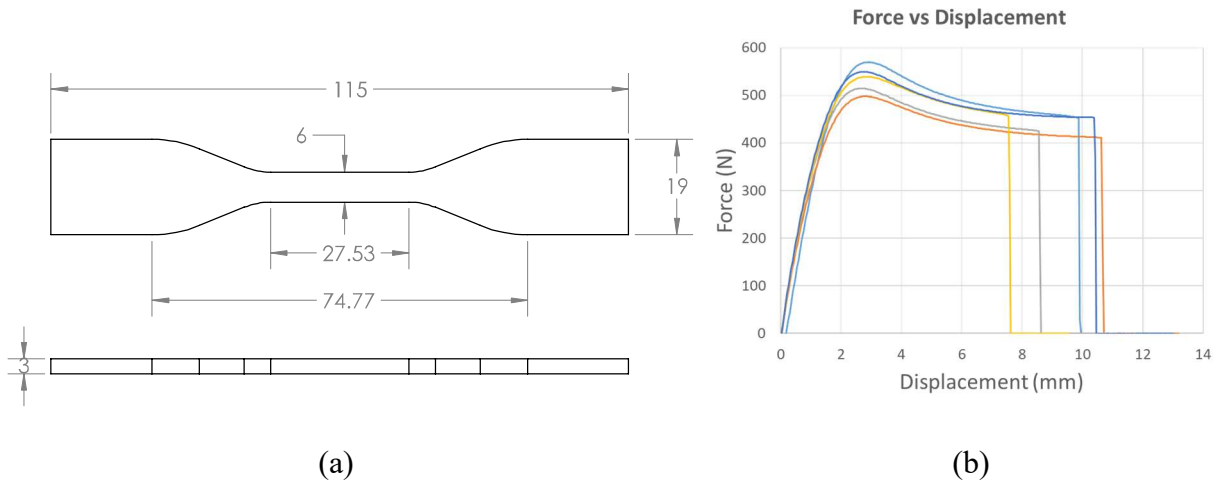
Figure 5.11. Material characterization for tough resin using tensile dogbone, (a) The dogbone geometry (based on ASTM D638), (b) Force vs. Displacement results of 3D printed dogbone samples under tensile loading (results courtesy to Jesus Rivera).
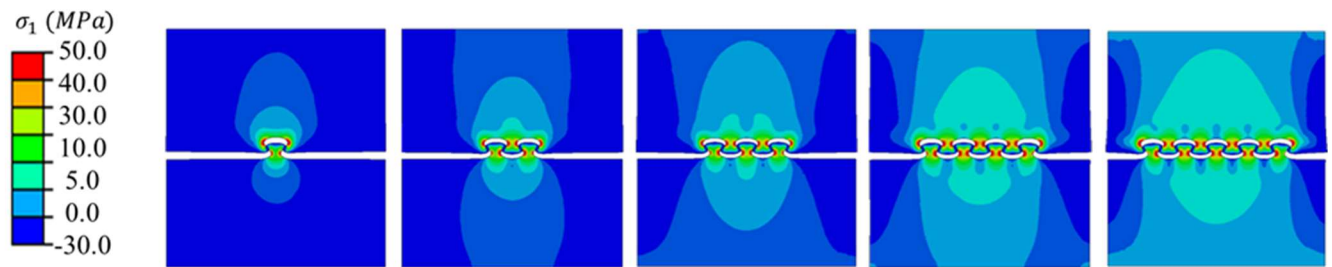
Figure 5.12. Maximum principal stress distribution contour for case 1 with (a)one blade, (b) two blades, (c) three blades, (d) four blades, (e) five blades.

(a)   (b)

(c)   (d)
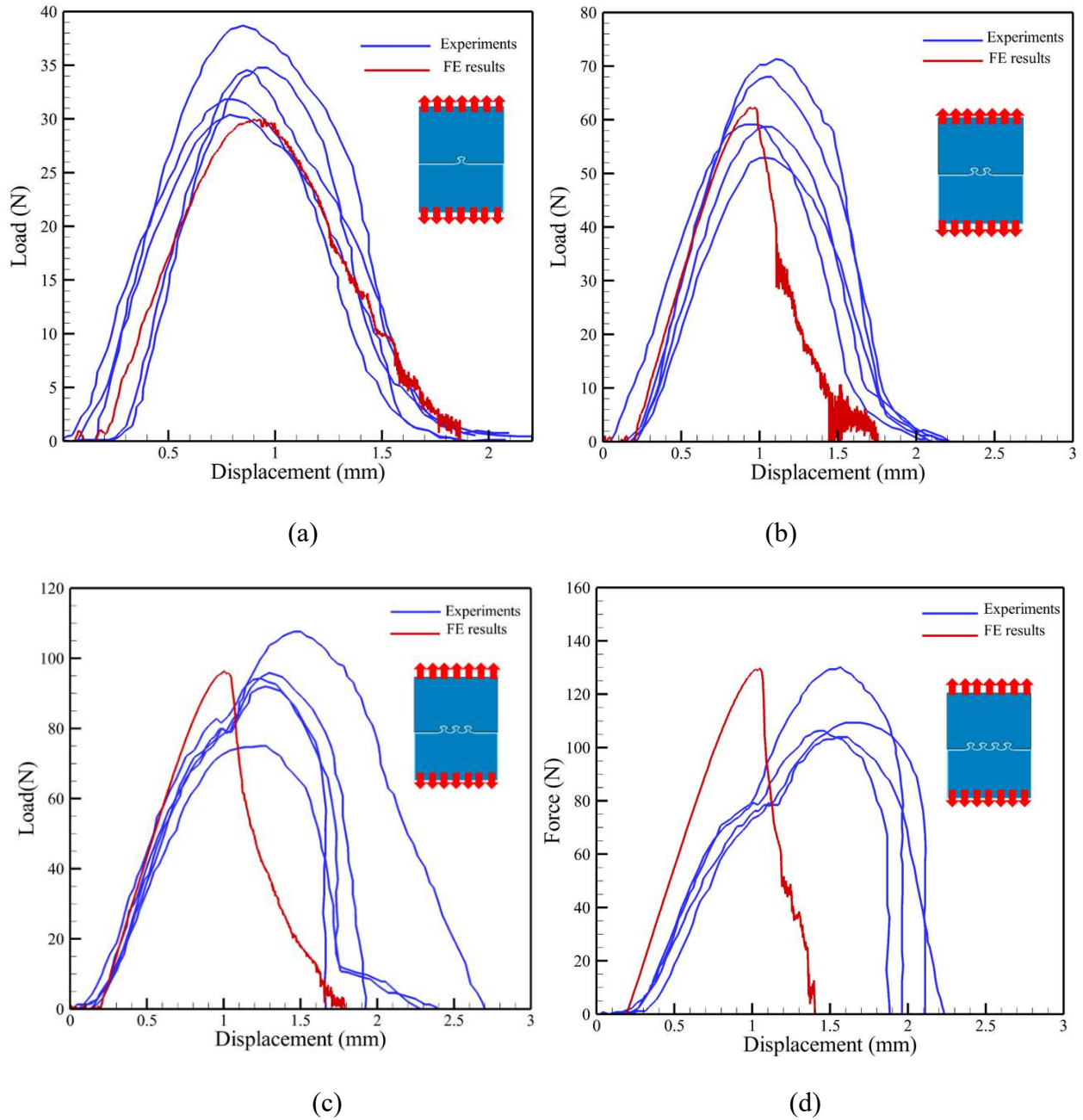
Figure 5.13. load-displacement curves from both experimental and FE results under tensile loading, (a) one blade, (b) two blades, (c) three blades, and (d) four blades.

Tensile tests of 3D printed specimens and FE models of Case 1 highlight a linear trend between the number of blades and the mechanical properties (i.e., increased stiffness, toughness, and normalized peak load) of the sutures (Figure 5.14). Moreover, the FE models suggest that the initial stiffness increases with the number of blades, yet the 3D printed tests show the result in a stiffness plateau increases upon reaching three blades. This could result from the material limitations and air bubbles or uncured resin in the 3D printed polymer weakening the relatively small blades (Dizon et al., 2018). Furthermore, the increasing number of blade elements may raise the lateral bending and transverse strains during pullout, causing a plateau in the rate of deformation of the sample due to the lack of support material at their extremities. Therefore, we do not see an increase in stiffness beyond three blades, but we see an increase in maximum load and toughness. With broader samples at a greater scale, we expect a linear trend in stiffness, toughness, and normalized peak load with an increased number of blades mirroring the FE models.
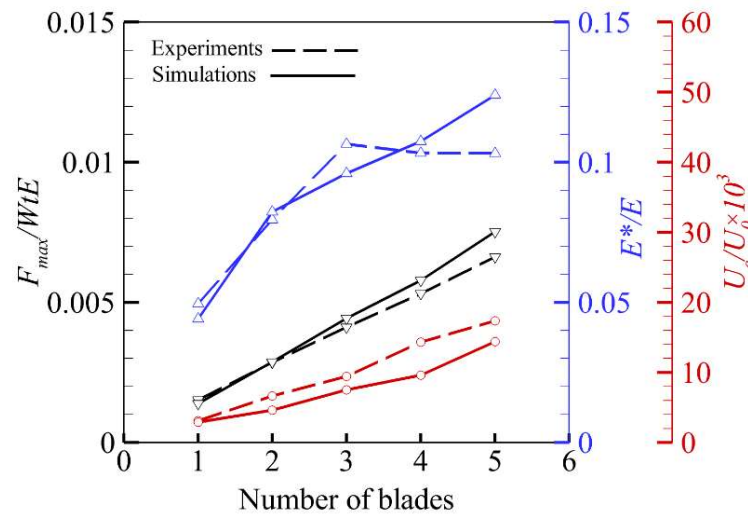
Figure 5.14. Parametric study samples (Effect of blades number). Comparison between Normalized Peak load, Stiffness, and Toughness of Experiments and Simulations

5.6.2 Identifying the role of blades number and size (Case2- parametric study)

In the next parametric study, for the constant values of dimensions (width, length, and thickness), the blades are designed in such a way that they cover the entire width of the connection. The purpose of this section is to understand the role of the number and size of blades. The purpose of this section is to respond to the following question.

Why the Ironclad beetles have been developed two blades instead of having multiple smaller blades or one extremely large blade (the blade that covers the entire width of the beetle)?

To answer the above question, five different blades geometry (see Figure 5.15 (a)-(e)), Case 2, was developed. All dimensions kept constant except the geometry of the blades (needs to cover the entire area). The maximum principal stress contour distribution under tensile test at peak load for all different blades geometries are presented in Figure 5.16(a)-(e). The material property of all the models assumed to be tough resin similar to case 1.

(a)   (b)   (c)   (d)   (e)
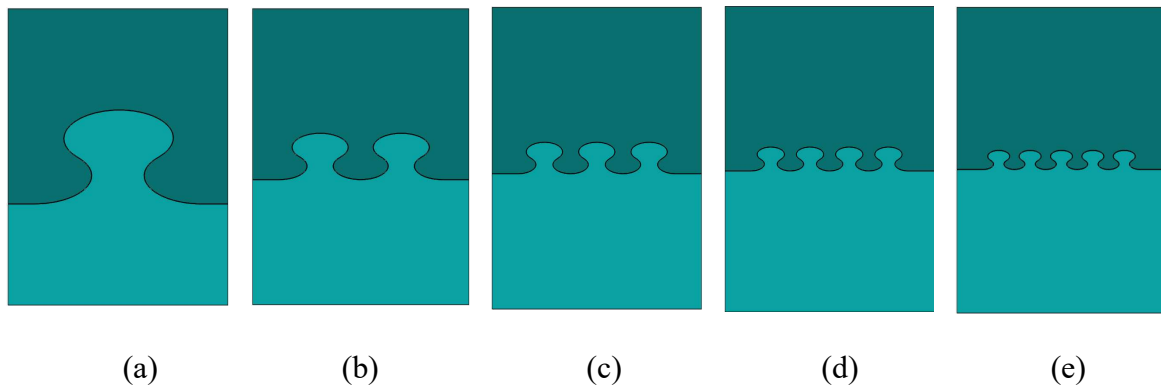
Figure 5. 15. The model geometries for Case2-parametric study

The load-displacement curves with different numbers and sizes of blades are presented in Figure 5.17. The results from Case 2, with one large blade, shows a smaller peak load in comparison to the other geometries. However, it exhibits more ductility, or in other words, it has the most significant failure strain in comparison with the other four models. As the number of blades increases, the maximum required force increases (up to four blades), and fracture strain decreases. As a result, for the constant value of the width, by increasing the number of the blades, the peak load increases due to the interlocking of the blades, and fracture strain decreases (less ductility) due to the damage in the blades. It is also notable that peak load increases by increasing the number of blades up to four blades and then decreases for the case with five blades. This could be explained

due to the fracture of blades; however; it might be happening due to the nature of the resin. Finally, the results from these tests can respond to the question at the beginning of the section.

(a) (b) (c) (d) (e)
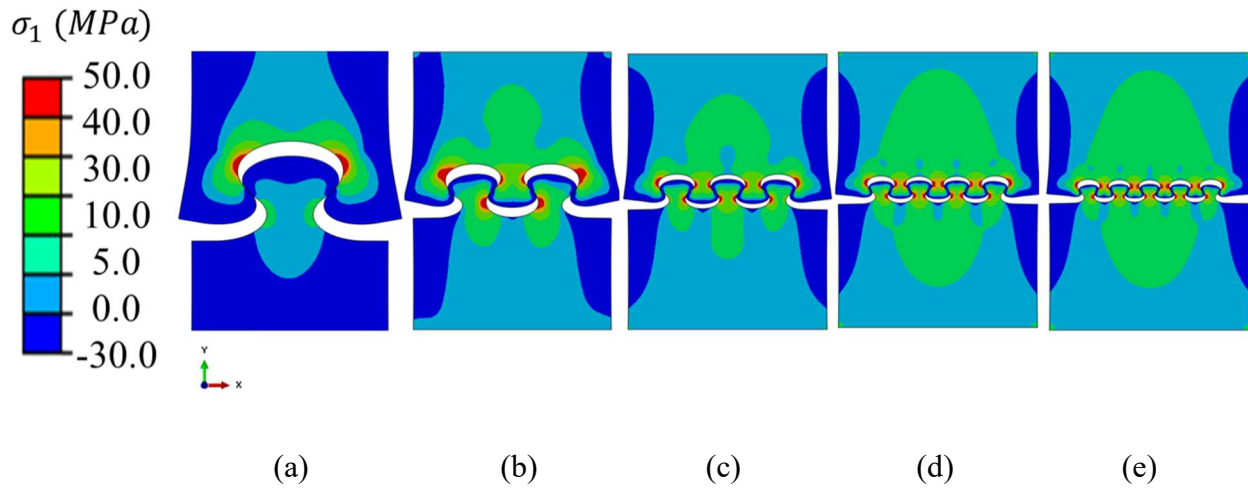
Figure 5.16. Maximum principal stress distribution for Case 2, (a) one blade, (b) two blades, (c) three blades, (d) four blades, and (e) five blades.
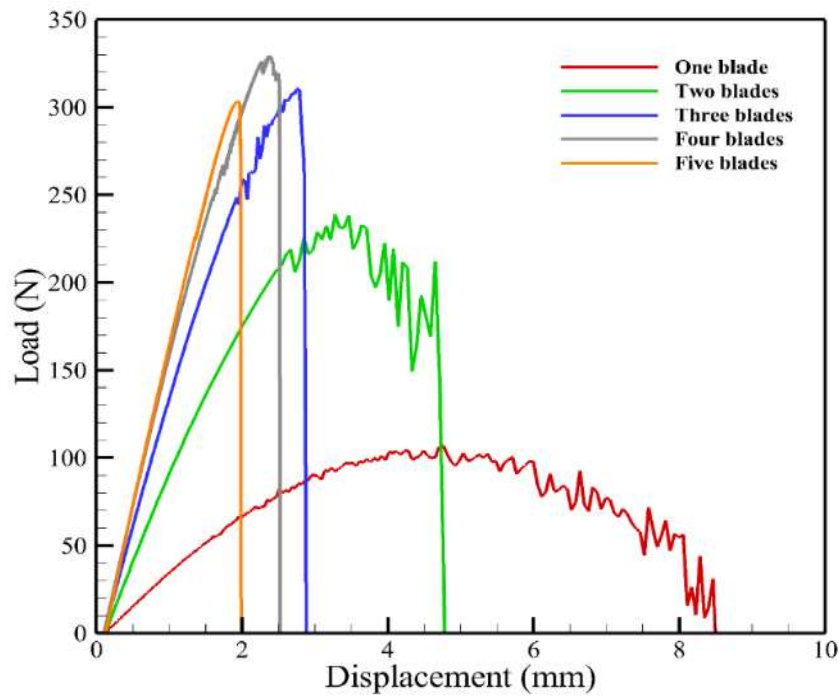
Figure 5.17. Load-displacement curves of case 2 for one-five blades from FE simulation

Case 2 parametric study also provides insight into the competing mechanisms that exist between the scale and number of blades. As the quantity of features (i.e., blades) increases, we see a more uniform inelastic strain distribution leading to properties reminiscent of a homogenous material, higher stiffness, at the cost of decreased extensibility (Figure 5.17 and 5.18). FE models and

tensile experiments indicate that the maximum toughness, occurs for sutures with two blades, while the maximum stiffness and peak load occur in the sample with four blades (Figure 5.18). As fewer blade elements are utilized, there is a reduction in the inelastic strain concentration within the neck areas of the blades. This inelastic strain distribution can explain the transition from ductile-like failure (pull out with damage around the blades) to brittle-like failure (failure around the neck area) by increasing the number of the blades (or reducing the size of the blades) as presented in Figure 5.17.
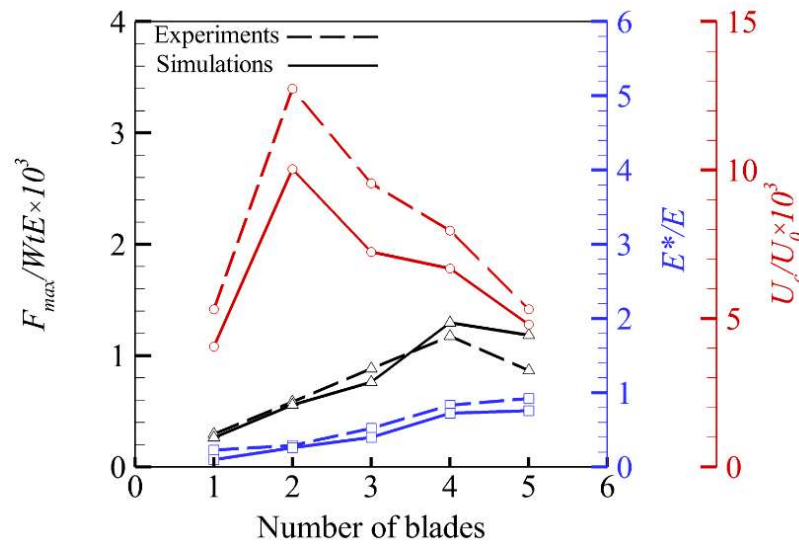
Figure 5.18. Parametric study samples (Effect of blades number and size). Comparison between Normalized Peak load, Stiffness, and Toughness of Experiments and Simulations

Additionally, a plot of maximum and minimum principal stress vectors (see Fig 5.19 and Fig 5.20) indicates that as the number of the blades increases, a higher compression load is observed across the width of the center part of the blades as well as higher vertical tensile stress inside the neck area. The compressive stress provides confinement as the number of the blades increases and, therefore, higher values of stiffness can be expected for the sample with five blades. As the confinement increases, the tensile stress in the neck region increases. This leads to energy dissipation due to inelastic deformation to a point where brittle fracture at the neck becomes a competing mechanism. As such, the sample with two blades exhibits the highest toughness.

Minimum Principal Stress
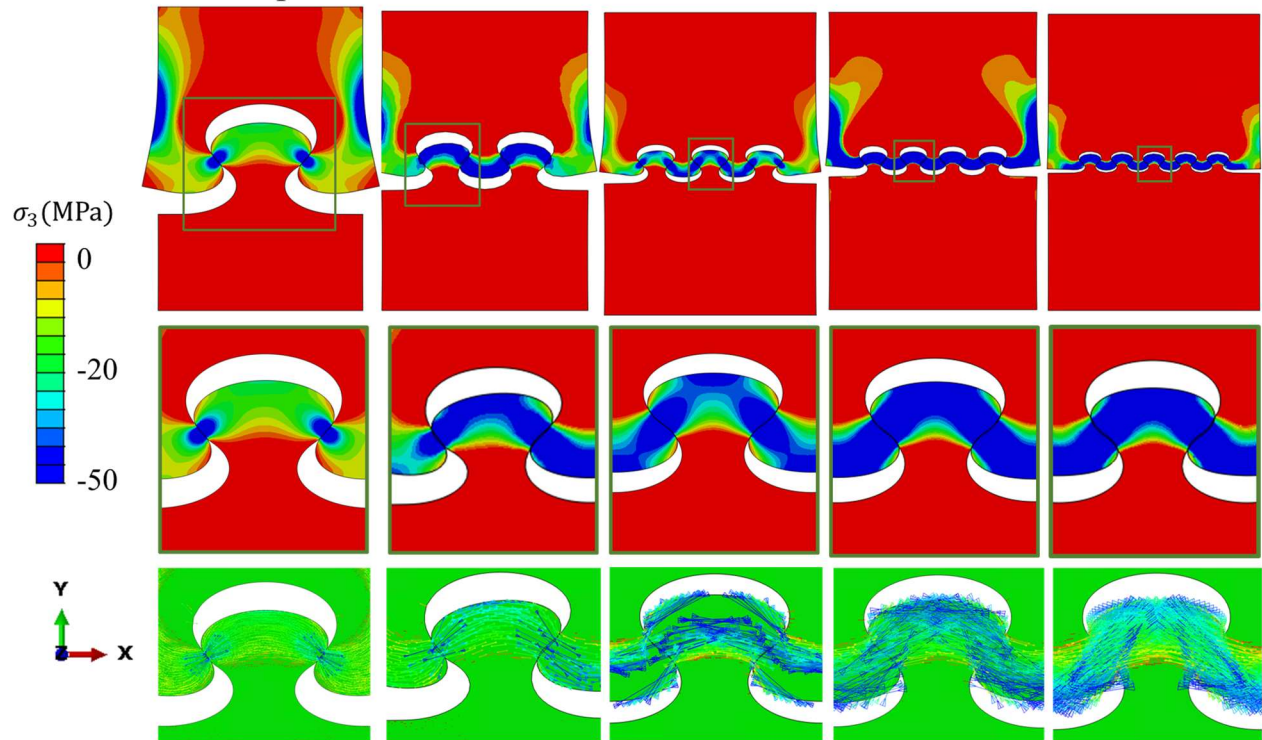
Figure 5.19. Compressive stress and confinement as a function of blades. First row: Minimum Principal stress contours for one blade (a), two (b), three (c), four (d), and five (e) blades; at the point of maximum load. Second row: Details of a central blade. Third row: distribution of the principal directions associated with the minimum principal stress.

Maximum principal stress
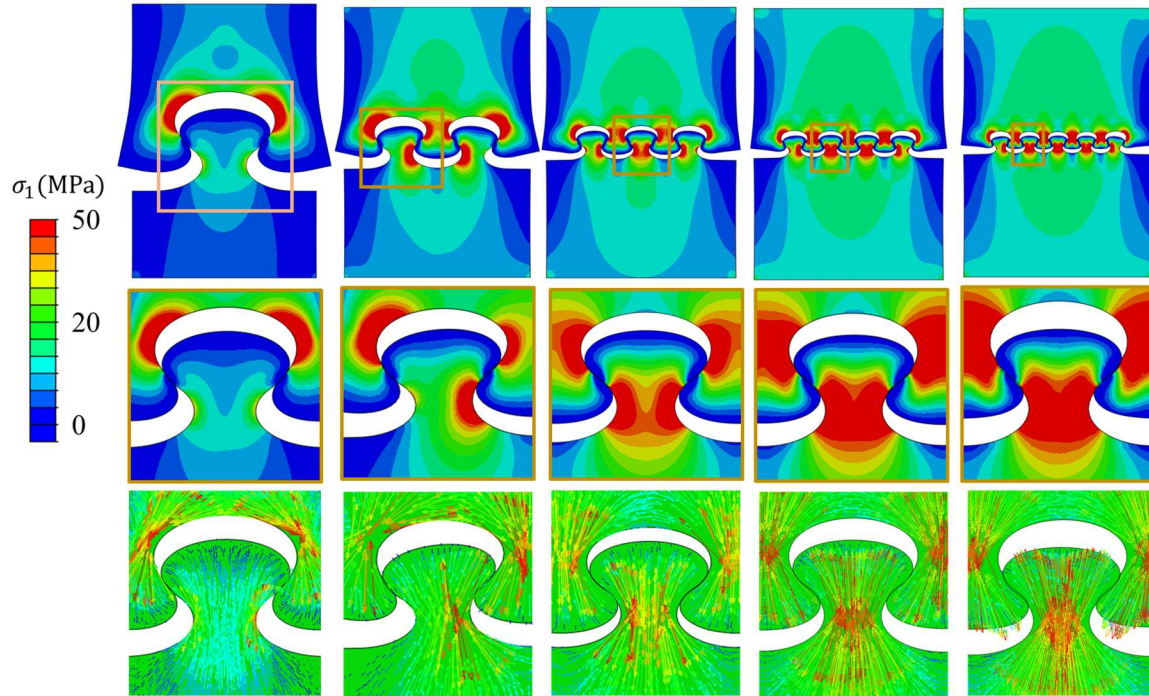
Figure 5.20. Tensile stress as a function of blades. First row: Maximum Principal stress contours for one blade (a), two (b), three (c), four (d) and five (e) blades; at the point of maximum load. Second row: Details of a central blade. Third row: distribution of the principal directions associated with the maximum principal stress.

By comparing the results, one can conclude that two and three blades could be a proper choice for the number of blades. However, there is a tradeoff between failure strain, peak load, stiffness, and toughness, which might be affected by the material properties. In situations where higher toughness is required, two blades could be the right choice while, for the cases where less toughness is required, and instead more stiffness is desired, three blades could be a good option and this could also explain why Ironclad beetle selected two blades to connect elytra part.

5.7 Summary and conclusions

In this chapter, the role of interfacial features (blades) in the elytra of the diabolical ironclad beetle, *Phloeodes diabolicus*, that assist the organism in withstanding predation and other external loads. At the macro scale, the exoskeleton incorporates varying lateral supports with stiffness gradients to protect vital organs and distribute the load throughout the elytra. Further analysis and mechanical characterization using finite element simulations and experiments of the elytra show the advantageous mechanical response of the interdigitated suture in *P. diabolicus* associated with the geometry and number of elements. Specifically, the shape of the ellipsoidal blade provides mechanical interlocking as well as stress distribution. The parametric study on the blades revealed that by varying number of blades during a tensile test, two blades have the greatest toughness while stress distribution, stiffness, and peak load seem to plateau after four blades. Yet, more work needs to be conducted on the role of architecture inside the interlocking blades.

CHAPTER 6. ROLE OF INTERLOCKING LAMINATED BLADES BIO-INSPIRED BY IRONCLAD BEETLE BLADES

6.1 Introduction

Biological systems are distinct for the extraordinary nature of their structures and due to their optimal design and improvement of mechanical properties (i.e., ability to demonstrate high stiffness and toughness). These microstructures are of interest to many bio-inspired studies (Fratzl et al., 2004; Espinosa et al., 2011). Nature utilized various techniques to protect different species against attack or penetration, for instance, the bouligand fiber orientation is an example of architecture that can be found in many biological systems such as dactyl club of Mantis shrimp (Weaver et al.,2012), collagen base in boxfish (Besseau and Bouligand 1998, and Garner et al., 2019), exoskeleton of arthropods such as beetles (Cheng et al., 2019; Libby et al., 2014; Jewell et al.,2007; Yang et al., 2017). Bouligand architecture in Nature is a hierarchical structure that features uniaxial fiber layers assembled periodically into a helicoidal pattern. A recent study by Suksangpany et al. in 2017 reveals the role of bouligand architecture in developing multiple twisting microcracks as a source of energy dissipation and stress relaxation to prevent catastrophic failure (Suksangpanya et al., 2017).

Patterned interfaces (including both interlocking and non-interlocking) are another technique utilized by Nature to enhance the mechanical properties of organic materials. The bony plates in leatherback sea turtle osteoderm connected using 3D triangular pattern (sutures) interfaces, this technique not only create a smooth surface in the osteoderm but also helps to spirit damage in the sutures areas, and thereby, enhancing energy absorption of the system (Chen et al., 2015). Similarly, interlocking sutures in the carapace of red-eared slider turtles connect the rigid ribs and increase the fatigue resistance of the entire osteoderm (Archai and Daniel Wagner, 2015). The bony plates in the alligators osteoderms are also connected by using both sutures and collagen sharpey's, which offer both flexibility and protection (Sun et al., 2013). Fish families such as arapaima, teleost, and boxfish also contain bony rigid elements, embedded in a compliant skin and help to protect them against attacks of predators (Vereney and Barthelat, 2014; Brute et al., 2008; Meyers et al., 2012; Lin et al., 2011). The carapace of the boxfish contains scutes, and each scute includes highly mineralized plate and a compliant collagen base. The mineralized plates connected

using triangular sutures shape, and unlike most other species in Nature, the collagen sharpy's does not exist between the teeth. The study by Hosseini et al., 2020 suggested that these architecture helps to control the direction of the cracks and also arrest the crack in the sutures areas (Yang et al., 2015; Hosseini et al., 2020). Woodpeckers are another remarkable example in Nature with capability of repeated pecking on a tree at remarkably high deceleration (10000 ms $^{-2}$) without any brain injury (Gibson, 2006). The study on the red-bellied woodpecker beak revealed that the beak develops suture lines which are responsible for increasing the ability to bear the compressive loads (Lee et al., 2014). Therefore, patterned interfaces are a solution from Nature to connect various parts in the exoskeleton/carapace and at the same time enhancing the mechanical properties. Both interlocking and non-interlocking patterned interfaces have been bio-inspired through many studies. For example, in a study by Ortiz group, the role of patterned interfaces for four categories of sutures geometry (i.e., triangular, rectangular, trapezoidal, and anti-trapezoidal) was investigated through an analytical framework (using the principle of virtual work). The results stated that the triangular pattern shows higher values for stiffness, strength, and toughness while the anti-trapezoidal pattern performs better in terms of damage tolerance (Lin et al., 2014).

Zavattieri and co-workers investigated the role of the geometry of non-interlocking patterned interfaces in increasing toughness under remote mode-I loading conditions following a Linear Elastic Fracture Mechanics (LEFM) concept. The results stated that the shape behind the crack tip affects the small period of stable crack propagation before the unstable failure, while, the crack tip position and shape of the initial open crack does not affect the final value of the effective toughness as long as the crack tip follows the patterned interface. Besides, the effective toughness can be improved by increasing the amplitude to wavelength aspect ratio (A/λ). Their results also provide a new guideline for designing patterned interfaces in such a way that the higher values of effective toughness can be obtained by selecting the $l_{cz}/\lambda < 1$ and the largest possible values of A/λ (Zavattieri et al., 2007 and 2008; Hosseini et al., 2019).

Previously, the role of jigsaw-like interlocking blades (specific case for figure 6.1 (d), when a/b = 1.0) was studied using the 3D printed jigsaw blades under tensile loading condition. Based on this study, two types of competing mechanisms can be expected due to material properties and blade geometries; i) pull out, and ii) fracture in the blades. Although the authors demonstrated that by using multi-stable and bi-stable blades, one could increase energy absorption, the study is limited

only to the geometries with pullout conditions and avoided discussion regarding the damage in the blades (Malik and Barthelat in 2016; Mirkhalaf and Barthelat, 2017).

6.2 Ironclad beetle

In recent years, the exoskeleton of arthropods such as beetles gets more attention due to specific microstructure, which enables these species not only to resist penetration or attack and but also to develop a lightweight cuticle (Rivera et al., 2019). Their resistance against the attack of various predators and their structural and mechanical performance across flying terrestrial make them an attractive option for research. One of the terrestrial beetles is the Zopherinae, ironclad beetles. The Ironclad beetle's exoskeleton is known to bend entomologist's steel pins and withstand high compressive loads, including the occasional automobile that would prove fatal to most insects. The geometric features and morphologies of beetle elytra have been bio-inspired through many aviation applications for designing lightweight structures (Dai and Zhixiang, 2010). The Ironclad beetle exoskeleton contains chitin-fiber composite stack in a helicoidal pattern (bouligand orientation) consisting of three distinct regions named as epicuticle, exocuticle, and endocuticle, where the epicuticle is the outermost layer while the endocuticle is the last interior layer. The SEM images and Nano-indentation confirm that the epicuticle consists of three layers: cuticulin, protein, and waxy layer (Le Nguyen, 2017). The cuticulin thickness is approximately ranging between 12-13 nm (depending on the species) and is the outer layer. The protein is the middle layer, while the wax is the last layer in the epicuticle region. The wax layer acts as a coating layer and prevents water penetration to the beneath layers (Wigglesworth 1972). Since epicuticle is a thin region, it is believed that the other two areas (the exocuticle and endocuticle, also known as procuticle) are responsible for enhancing the mechanical properties related to the beetle performance because the chitin-protein matrices that found in procuticle regions develop bouligand microstructure.

In addition to the microstructure inside the beetle cuticle, further investigation by Rivera et al., 2019 reveals another important geometric feature that exists inside the elytra. As presented in Figure 6.1 (a); the beetle elytra contain parts connected using interlocking dovetail joints blades, and each blade contains microstructure (layers of alpha-chitin fibers) that cause delamination under compression and tensile loadings (Rivera et al., 2019). Therefore, delamination can be observed as another competing mechanism along with pull out and failure. The image of the

Ironclad beetle cuticle is presented in Fig 6.1(a). The blue zoomed box presented the cross-section of the Ironclad beetle elytra, and the zoomed red box shows the blades were connecting the two separate parts in elytra (see Fig6.2 (b)). The geometry of the blades can be estimated by three adjacent ellipses, as presented in SEM Image and schematics in Fig 6.1 (c) and (d), respectively.

In objectives for this study can be presented as follows;

Objective1:

Understanding the effect of blade geometry in enhancing the mechanical properties in homogenous materials.

- To date, there is no study to reveal and understand this role of blade geometry. To this aim, three different materials (such as VeroWhite, Steel, and Ceramic) were studied for various values of aspect ratios and angle θ (the angle between the horizontal line and center of two adjacent ellipses).

Objective 2:

Role of architecture and delamination in enhancing the mechanical properties (i.e., toughness and energy dissipation) of the interlocking blades with limited ductility.

- I developed the parametric and systemic finite element models to understand the competing mechanism between delamination, pull-out and fracture. The main goal of this study is to understand the trade-off between energy dissipation due to delamination and plastic deformation. I mainly wanted to address the following question,
  "What are the benefits of having delamination and when delamination has priority over plastic deformation and fracture."
- Understand the role of other parameters such as interfacial friction, material strength, fracture toughness, and fracture strain.

Objective 3:

Derive systematic design solution for the puzzle-like architecture materials using the information of a single interlocking multi-layered blade to avoid damage localization and increase energy dissipation

- This work is one of the outcomes of the parametric study of the single blade. I mainly wanted to address the following question,

  "*can we predict the behavior of puzzle-like multilayer architecture composite by studying only a single interlocking blade or unit cell*?*"*

Figure 6.1 (a) presents the abdominal view of the Ironclad beetle. The cross-section view of the abdomen is presented in Figure 6.1 (b), and interlocking sutures on the top part of elytra are presented in Figure 6.1(b). Figure 6.1(c) shows the SEM image from the interlocking blades in elytra

(a) (b)

(c) (d)
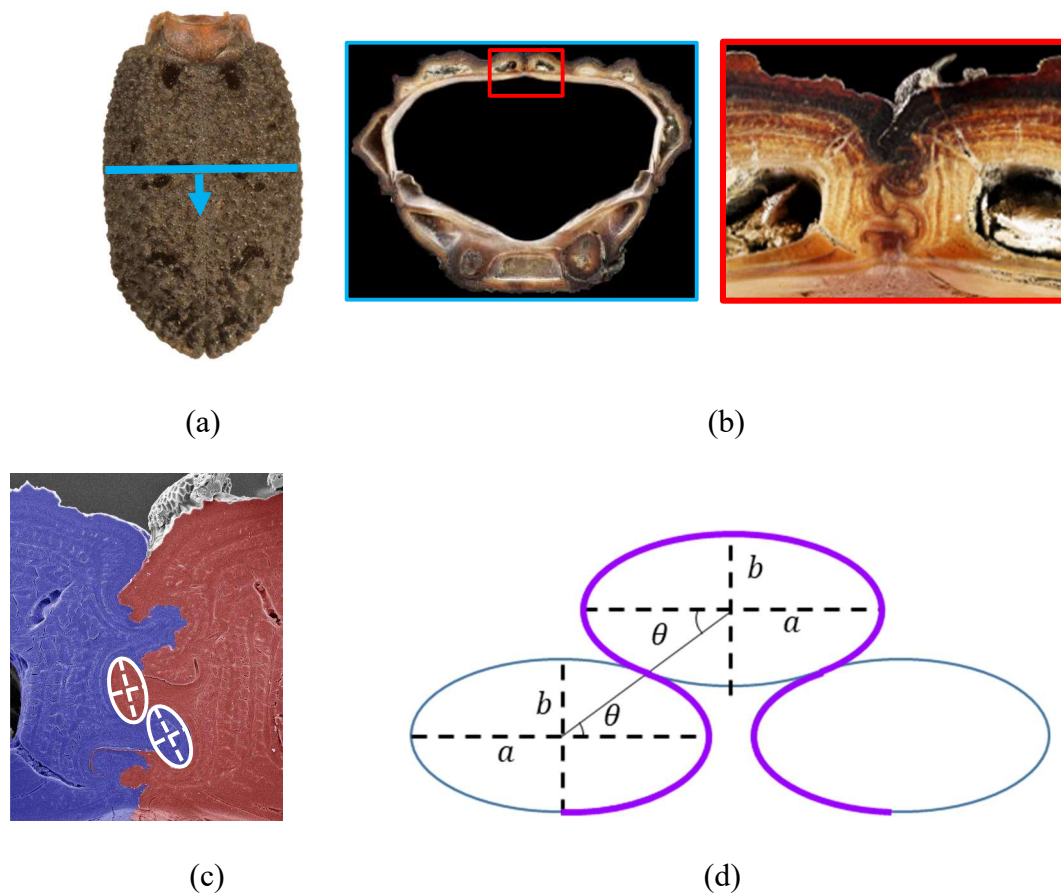
Figure 6.1. (a) Image of Ironclad beetle cuticle, (b) cross-section view of Ironclad beetle elytra (blue zoomed box), and dovetail joints blades which connected the two separate parts from elytra, (c) SEM Image from dovetail joints blades connect the elytra, (The courtesy of Figure 6.1 (a), (b), and (c) goes to Jesus Rivera, University of California Riverside) (d) dovetail joint blades developed from three adjacent ellipses with major axis of a and b. The angle θ is an angle between the horizontal line and center of the adjacent two ellipses.

Based on Fig6.1 (d), the geometry of the blades can be approximated by three adjacent ellipses, however, the role of both geometric parameters such as aspect ratio ($\frac{a}{b}$) and angle θ needs to be investigated and considered for further analysis. In Ironclad beetle cuticle the ($\frac{a}{b}$ = 1.8-2.0) and value of $\theta = 25°$. Here I want to understand why Ironclad beetle has been selected this aspect ratio range and value of θ.

6.3 Design of dovetail joints blades geometry

The design of the blades is based on dovetail joint contour built from a series of three adjacent ellipses that are connected (center to center) by angle θ. In this study, I did not consider any adhesive at the blades interface, so the mechanical interlocking, friction, and contact mechanics control the interaction between blades. Due to the definition of this type of dovetail joints geometry, for each aspect ratio ($\frac{a}{b}$), there exists a critical value θ, that blades geometry become physically inadmissible if the values of θ become larger than $\theta_{Critical}$. Figure 6.2 (a) presents the dovetail joints blades geometry developed from three blades with all the required variables.

The ellipse equation and the aspect ratio of an ellipse major axis are defined by Eqn 6.1 and 6.2, respectively. As presented in Fig 6.2(a), the intersection between the tangent of two adjacent ellipses and the centerline is presented by point m(x,y). Therefore, the angle θ can be defined by Eqn 6.3.

$$\frac{x^2}{a^2} + \frac{y^2}{b^2} = 1.0 \tag{6.1}$$

$$\frac{a}{b} = k \tag{6.2}$$

$$tan\theta = \frac{y}{x} \tag{6.3}$$

By inserting Eqns. 6.2 and 6.3 into Eqn. 6.1, the Eqn. 6.1 can be redefined as a function of angle θ, and aspect ratio k and therefore, the intersection point (m(x,y)) can be determined as presented in Eqn. 6.4.

$$\frac{x^2}{(bk)^2} + \frac{(xtan\theta)^2 k^2}{(bk)^2} = 1.0 \tag{6.4}$$

$$x = \frac{bk}{\sqrt{1 + k^2 tan\theta^2}}$$

$$y = \frac{bktan\theta}{\sqrt{1 + k^2 tan\theta^2}}$$

Based on similar triangle rules, the values of x_1 and y_1 can be determined as follows:

$$\frac{x_1}{y_1} = \frac{x}{y} = \frac{l}{2l} = \frac{1}{2} \tag{6.5}$$

In order to find the $\theta_{Critical}$, the Eqn 6.6 should be satisfied (see Fig 6.2(a)). Where, w_N represents the width of the neck in dovetail joint geometry.

$$\frac{w_n}{2} = x_1 - a = 2x - a \geq o \tag{6.6}$$

The critical value for θ can be obtained when Eqn 6.6 is equal to zero. By substituting a value for x from Eqn 6.4 to Eqn 6.6, I will have;

$$\frac{4bk}{\sqrt{1 + k^2 tan\theta^2}} - 2a = 0 \tag{6.7}$$

Solving the Eqn 6.7, the value of $\theta_{Critical}$ can be calculated as presented in Eqn 6.8.

$$\theta_{Critical} = arctan\left(\frac{\sqrt{3}}{k}\right) = arctan\left(\frac{\sqrt{3}}{\left(\frac{a}{b}\right)}\right) \tag{6.8}$$

Since the values of aspect ratios are known, the values of $\theta_{Critical}$ can be calculated using Eqn 6.8. Figure 6.2(b) presents the value of $\theta_{Critical}$ vs. a/b; the zoomed box shows the same graph up to $a/b = 10.0$. Similarly, using the same strategy, various blades geometries for different value of a/b and θ is presented in Fig.6.3. For all the cases, the total, width, length, and thickness of the samples are kept constant.

(a)   (b)
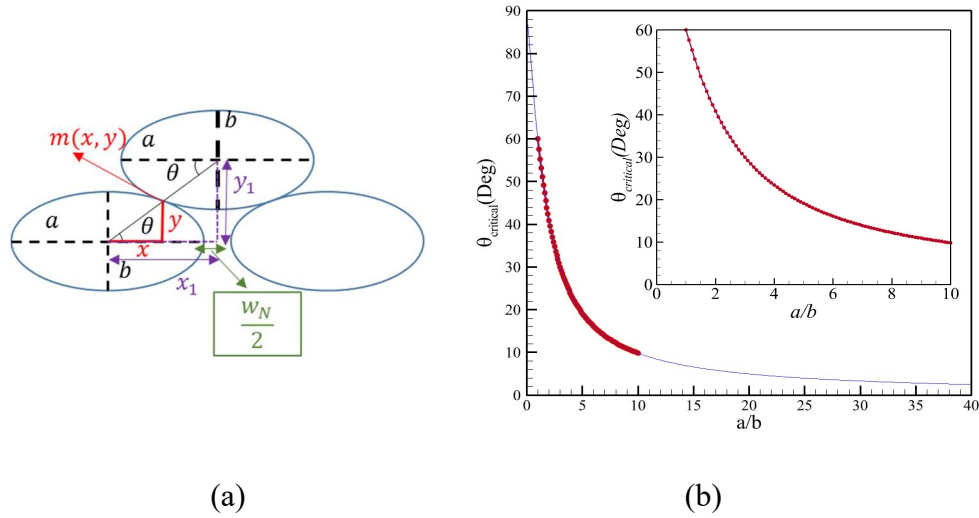
Figure 6.2. (a) Schematic of the geometry of the blade developed from three adjacent ellipses with all the required dimensions, (b) $\theta_{Critical}$ vs. a/b; the zoomed box shows the same curve up to $\frac{a}{b} = 10$

Based on Figure 6.2(a), Eqn 6.8, the $\theta_{critical}$ for each value of a/b can be determined. The schematic of a single homogenous blade for various aspect ratios ($0.8 \leq a/b \leq 10$) and values of θ are demonstrated in Figure 6.3.
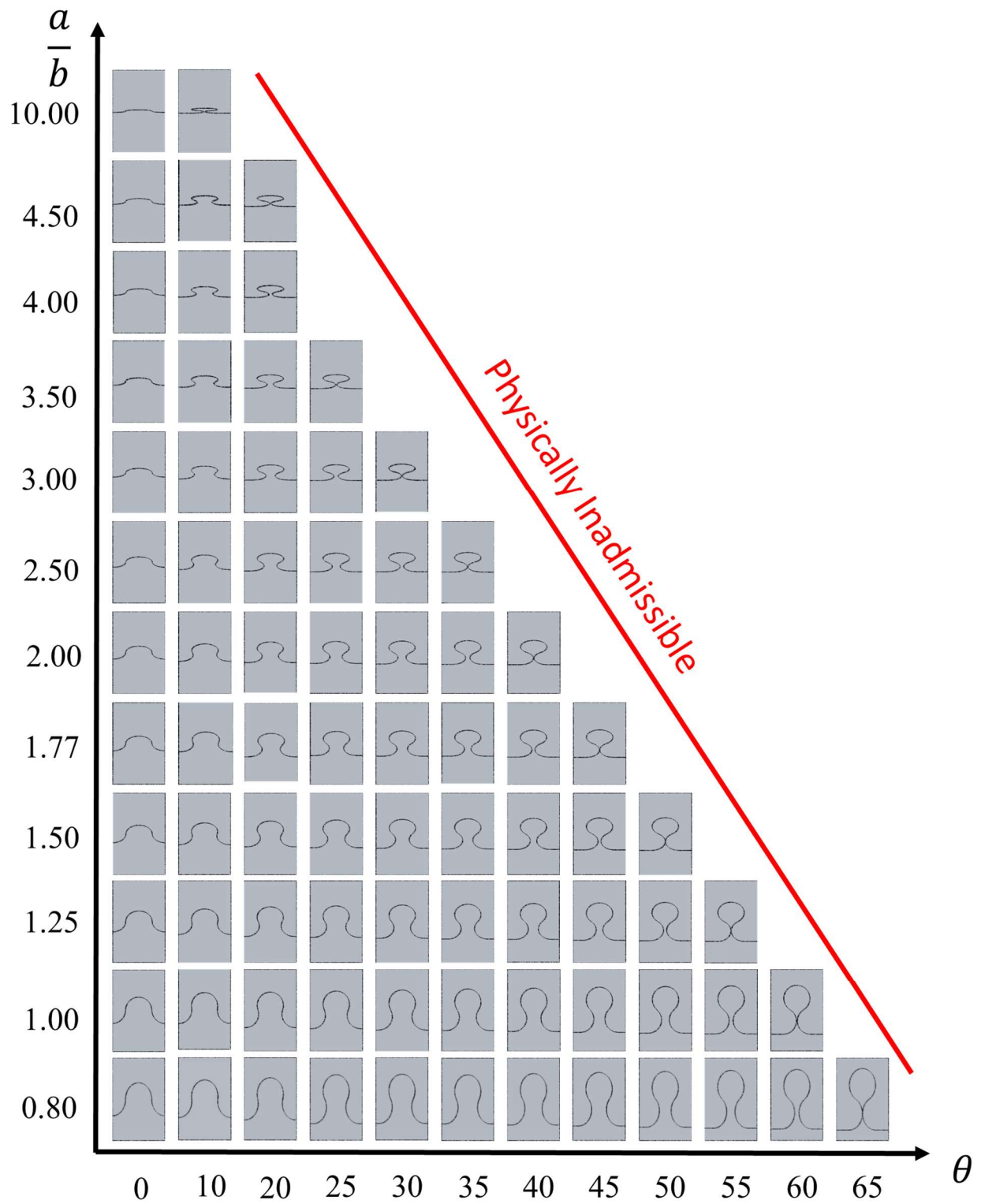
Figure 6.3. Various blades geometries developed from three adjacent ellipses for different values of a/b and admissible θ

6.4 Parametric analysis of homogeneous blades

6.4.1 Boundary condition

For all the cases, the displacement control load is applied on the top nodes of the sample. The bottom nodes of the sample are fixed against translational directions. The roller applied on the right side of the sample. Finally, the Homogenous Boundary Condition (HBC) is applied to the nodes on the left side of the sample. Using the theory developed by Aboudi in 1991 (Aboudi 1991), the homogenous boundary condition can be defined by satisfying the following conditions;

   i.   Kinematic uniform boundary condition:

$$u_i(\Gamma) = \varepsilon_{ij}^0 x_j \qquad \forall x_j \in \Gamma$$

Where ε_{ij}^0 is a constant tensor representing the global strain and independent of x_j and u_i is the displacement at point x_i

   ii.   Static Uniform Boundary condition:

$$t_i(\Gamma) = \sigma_{ij}^0 n_j \qquad \forall x_j \in \Gamma$$

Where t_i is the traction vector at the boundary Γ and σ_{ij}^0 is represented the global stresses, and finally, n_j is the vector normal to the Γ at the selected x_j.

For all the cases in this study the HBC boundary conditions are applied. The HBC under tensile uniaxial loading is presented in Figure 6.4. By fixing the normal directions of side faces in the blade and applying the Equation constraint, we will have the following constraint;

General condition:

$$u_1^{left} = 0 \qquad , \quad u_1^{right} - u_1^{Ref} = 0 \qquad \text{(X-direction)}$$

$$u_2^{bottom} = 0 \qquad , \quad u_2^{top} - u_2^{Ref} = 0 \qquad \text{(Y-direction)}$$

$$u_3^{rear} = 0 \qquad , \quad u_3^{front} - u_3^{Ref} = 0 \qquad \text{(Z-direction)}$$

In the above equation, u_j^i is represents the displacement and "i" is account for the nodes set, while "j" represents the degree of freedom. Since our model is homogenous in the X direction, only the first equation is used for all the models.
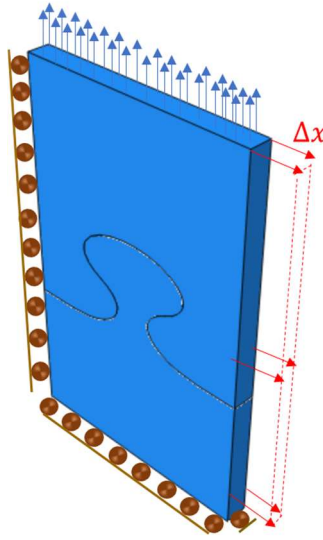
Figure 6.4. Homogeneous Boundary Condition (HBC) applied on a representative model
$(a/b = 2, \ \theta = 25°)$

6.4.2 Understanding the effect of blades geometry

Previously, the role of circular blades geometry for a single and multi-stable circular blade was investigated by Barthelat and his co-workers (Malik and barthelat, 2016; Mirkhalaf and Barthelat, 2017). In that study, the geometry of the circular blade was selected due to symmetry and uniform stress distribution. However, the dovetail joints blades are commonly used in many engineering applications, such as joints connecting blades to the disc in gas turbines (Ruiz et al., 1984; Witek et al.,2006). These types of blades are usually more ellipse like than circular shape. To this date, there is no study to understand the role of dovetail joints geometry on the mechanical properties and performance of the blades. Therefore, this section aims to understand the role of blade geometries (both a/b and θ) and its effect on mechanical properties such as peak load, stiffness, and energy absorption.

For this purpose, several FE models were developed for various aspect ratios and values of θ (see Figure 6.3). The material properties ranging from VeroWhite (polymer used for 3D printing), steel, and ceramic are assigned to the models and tensile loading is applied to the top surface of the blades. The HBC boundary condition was applied to all the models (see Figure 6.4). The width, length, and thickness of the entire models are constant and equal to 130 mm, 200 mm, and 12 mm respectively. The material for polymer (Vero white) is characterized by myself and modeled as an

elastic-plastic with the assumption of failure strain using ductile damage model in Abaqus and the material properties of steel and ceramic (Silicon carbide) are adopted from (Kopp and Dohmen,1990) and (Holmquist and Johnson, 2005), respectively. The normalized results of the peak load (results are normalized with respect to $a/b = 1$) vs. a/b and θ are presented in Figure 6.5 (a) and (b), respectively. The results showed that the higher values of normalized peak load for the brittle material such as silicon carbide occurs at the lowest aspect ratio and minimum allowable θ. The results also state that by increasing the values of θ and a/b, the normalized peak load decreases (Figure 6.5 (a), (b)). Similarly, the normalized values of energy dissipation for different values of aspect ratios reveal that by increasing θ and a/b, the amount of energy dissipation decreases (Figure 6.5(c), (d)). Finally, the comparison between various aspect ratio confirmed that the blades with $a/b < 1$ shows better performance with respect to circular blade in terms of both peak load and energy dissipation.

The second material used for this study is VeroWhite, which is the family of a tough polymer used as 3D print materials in poly jet 3D printers (i.e., Connex350), and it behaves in an elastic-plastic with fracture strain of 0.2. The comparison between normalized peak load vs. a/b and θ are presented in Figure 6.6 (a) and (b), respectively. Taking a closer look at the results confirm that the higher values of normalized peak load for various θ can be achieved when a/b ranging between 1.5-2.5. In addition, the comparison between normalized energy dissipation with respect to the a/b and θ reveals that for high aspect ratios ($a/b > 2.5$), Lower values of θ dissipate more energy. However, for $a/b > 2.5$, the highest values of energy dissipation can be obtained when $20 \leq \theta \leq 30$. Moreover, for the very low aspect ratio ($a/b = 0.8$), the highest value of energy dissipation occurs at $\theta = 40°$.

The last material used for this parametric study is steel. The comparison between normalized peak load and energy dissipation with respect to a/b and θ are presented in Figure 6.7(a)-(d), respectively. Although steel shows higher values of peak load and energy dissipation in comparison to the polymer, the trends of the results for both peak load and energy dissipation are similar.
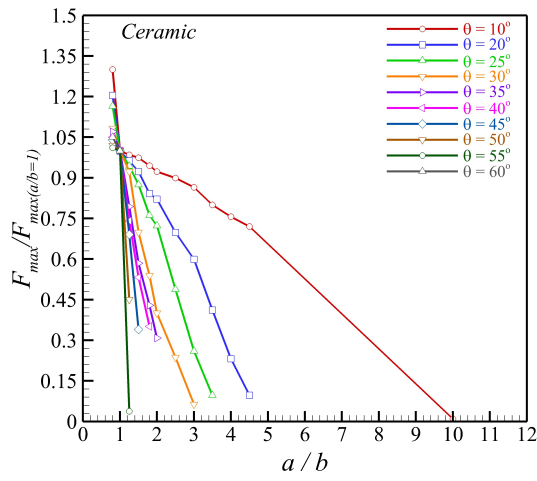
(a)
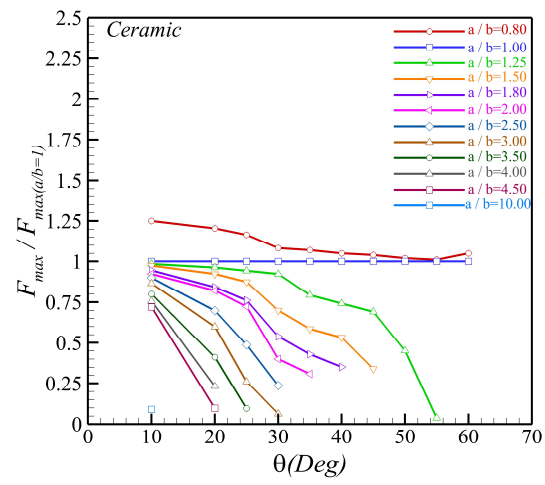
(b)
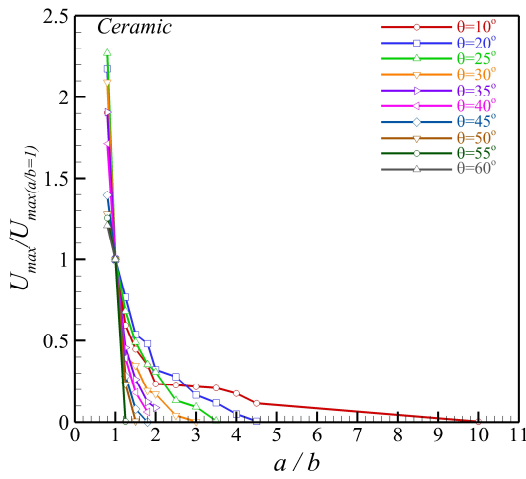
(c)
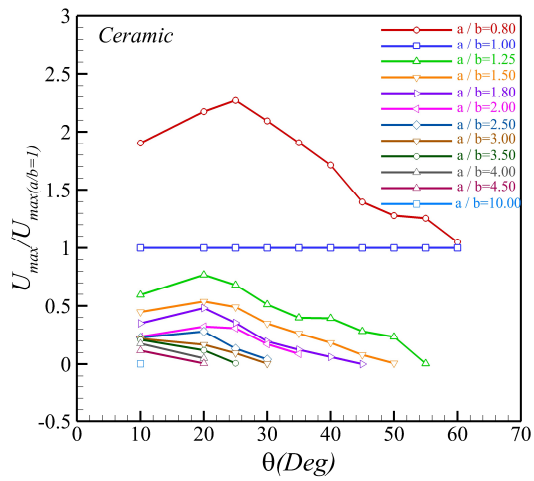
(d)

Figure 6.5. The FE results of the blade including various a/b and θ for ceramic (Silicon carbide), all the results normalized with respect to a/b=1, (a) normalized peak load vs. a/b, (b) normalized peak load vs. θ, (c) normalized energy vs. a/b, (d) normalized energy vs. θ
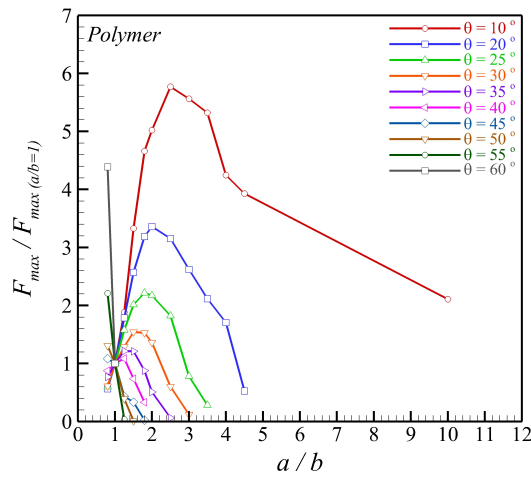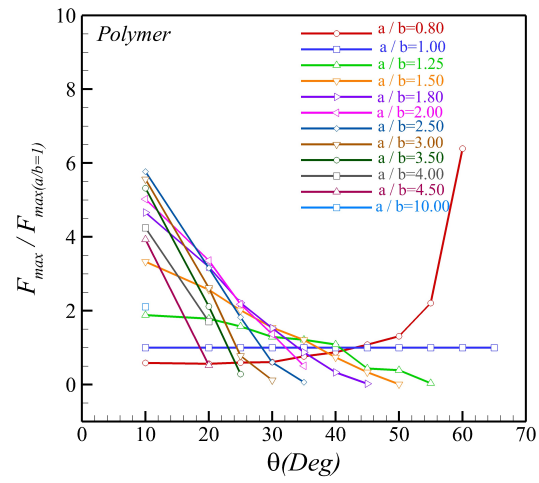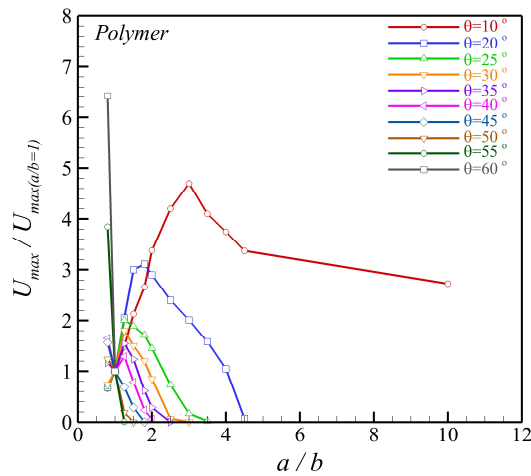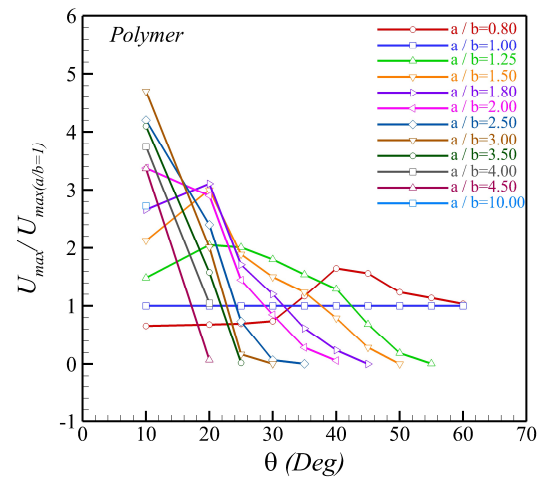
Figure 6.6. The FE results of the blade including various a/b and θ for polymer (VeroWhite), all the results normalized with respect to a/b=1, (a) normalized peak load vs. a/b, (b)normalized peak load vs. θ, (c) normalized energy vs. a/b, (d) normalized energy vs. θ
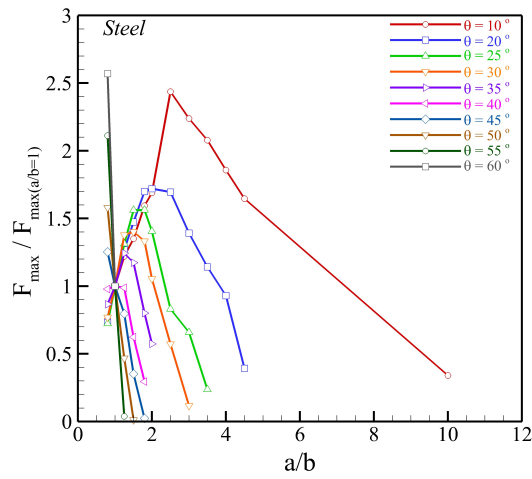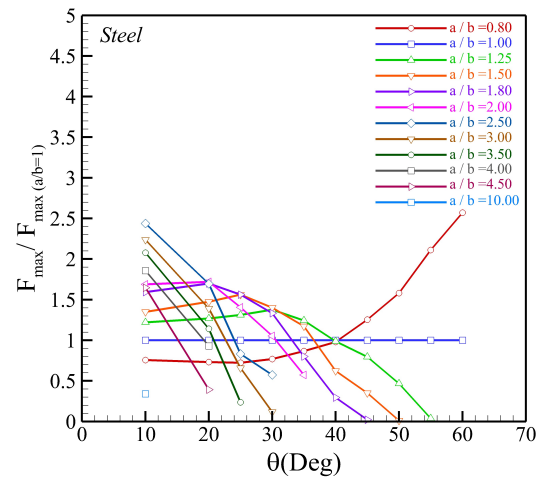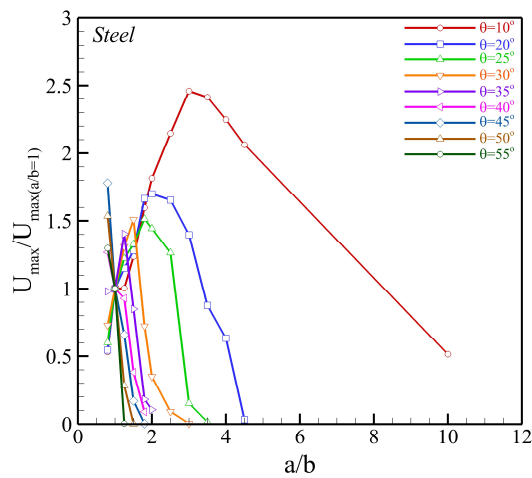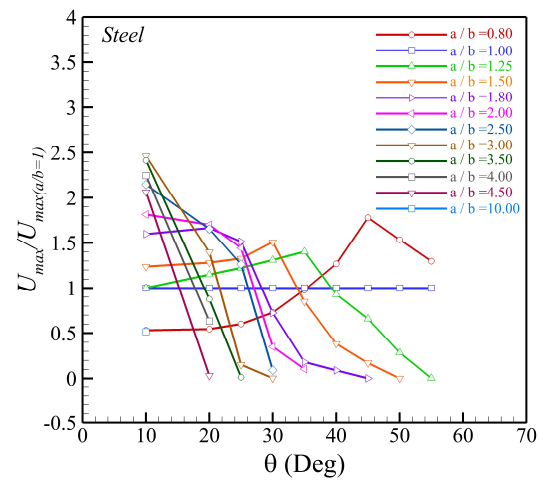
Figure 6.7. The FE results of the blade including various a/b and θ for Steel, all the results normalized with respect to a/b=1, (a) normalized peak load vs. a/b, (b) normalized peak load vs. θ, (c) normalized energy vs. a/b, (d) normalized energy vs. θ

The Ashby plot of peak load and Energy (the area under stress-strain curves) of the three selected materials in this study with different values of aspect ratio and θ is presented in Figure 6.5(a), and (b) respectively. The results stated that the higher values of peak load could be obtained for the ceramic in comparison to the other two materials. Ceramics are very brittle, and therefore for all the cases, failure occurs inside the neck. Although higher values of peak load can be obtained with ceramics, the values of toughness are the lowest in comparison to the steel and polymer. In contrast, the blades containing steel have higher energy absorption due to the ductility and nature of the material. Finally, the comparison between peak load vs. energy of all three cases for all the possible values of θ is presented in Figure 6.8(c).

This parametric study enables us to understand the role of blade geometry in homogenous material using three different material properties (ceramic (brittle), polymer, steel (ductile)). From all these studies, one can conclude that the ellipse shape for the blades performs better in terms of peak load and energy dissipation in comparison to the circular blade. For the brittle material, the higher values of peak load and toughness can be achieved by selecting the lower possible values of a/b , θ. While for the polymer (low ductility) and steel (high ductility), the best performance can be obtained by choosing $1.5 \leq a/b \leq 2.5$, and $20 \leq \theta \leq 30$. Although, we could find the possible range for the aspect ratio and values of θ, separate simulations needed to be done to find the optimized aspect ratio and θ.

(a)

(b)

(c)
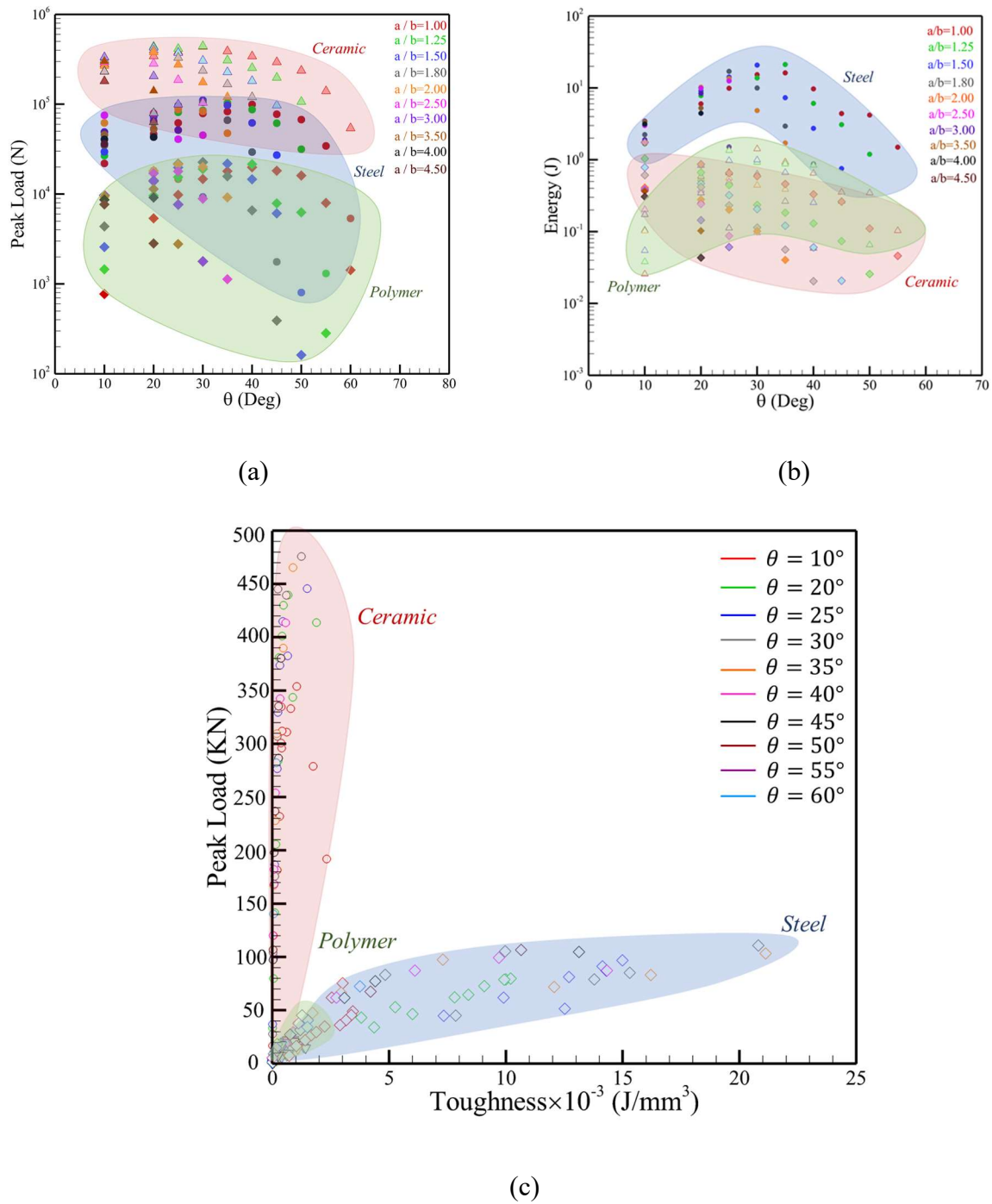
Figure 6.8. Ashby plot of a single blade of different a/b and θ, and three distinct based material (steel, ceramic, polymer), (a) peak load vs. θ, (b) energy absorption vs. θ, (c) peak load vs. Toughness for various values of θ.

6.5 Observation from Ironclad beetle (learning from Nature)

The compression test of the Ironclad beetle cuticle and SEM images confirm the presence of laminated structure inside the interlocking joints (Figure 6.9 (a), (b)) in the elytra. Delamination is a key factor in this study since it brings another competing mechanism along with pull-out and fracture. Figure 6.9 (c), (d) presents the beginning of the delamination and failure of the cross-sections of medial suture inside the elytra, respectively.

| (a) | (b) | (c) | (d) |
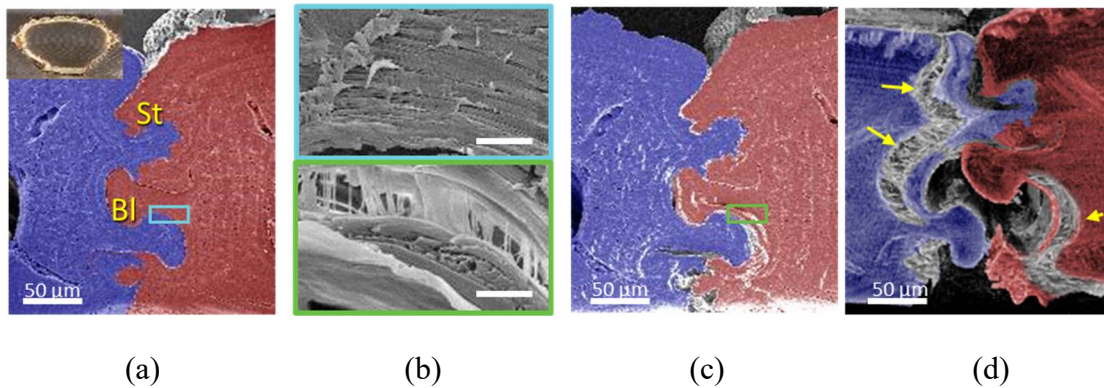
Figure 6.9. SEM image from dovetail joint blades inside the elytra, (a) uncompressed cross-sectional view, (b) highlighted crack initiation around the blade region, (c) fiber bridging and deamination inside the blade, (d) fracture blades with delaminated fiber inside the blades (photo courtesy to Jesus Rivera UC Riverside).

To understand the role of architecture and geometry of the blades, three different "jigsaw" blades (see Figure 6.10 (a)) were developed using 3D printing prototype technique and FE simulations by varying the angle, θ, to 15°, 25°, and 50°. In all three cases, the primary aspect ratio of the ellipses is constant and set equal to 1.8:1 and the 3D printed jigsaw-shaped blades incorporate the layered architecture that mimics the ironclad beetle laminated microstructure. The Lagrangian strains during the tensile loading are presented for all geometries. The blade representing the Ironclad beetle (i.e., 25°) demonstrated relatively higher normalized values of peak load and toughness (Fig. 6.10(b)). Digital Image Correlation (DIC) results confirm pull out of the low angle (i.e., 15°) and nearly circular blade, with no strain or delamination occurring. However, when θ is increased to 25° (i.e., that which is found in the diabolical ironclad beetle), significant strain develops within the blade with subsequent delamination, followed by pullout. Finally, in the highly curved blade (θ =50°) significant strain is observed at the neck, followed by fracture (with no apparent delamination). A comparison between peak load and energy release rate of these three

cases are shown in Figure 6.10(c). The results for the case with θ=25° show higher values in comparison to the other two angles. Thus, these three different prototypes can confirm the presence of competing mechanisms based on blade geometry to provide maximum interlocking, while preventing localized stresses that would cause failure at the neck. This parametric study highlights the role of delamination to relieve strain, while maximizing the interfacial strength at the suture, revealing a new competing mechanism along with pullout and failure in these jigsaw puzzle-like architectures. Finally, a comparison between FE simulation and experiment between the $\theta = 25°$ is presented in Figure 6.7(d). The strain distribution presence a good agreement between FE model and the experiment. More discussion regarding FE simulations will be presented in the following sections.
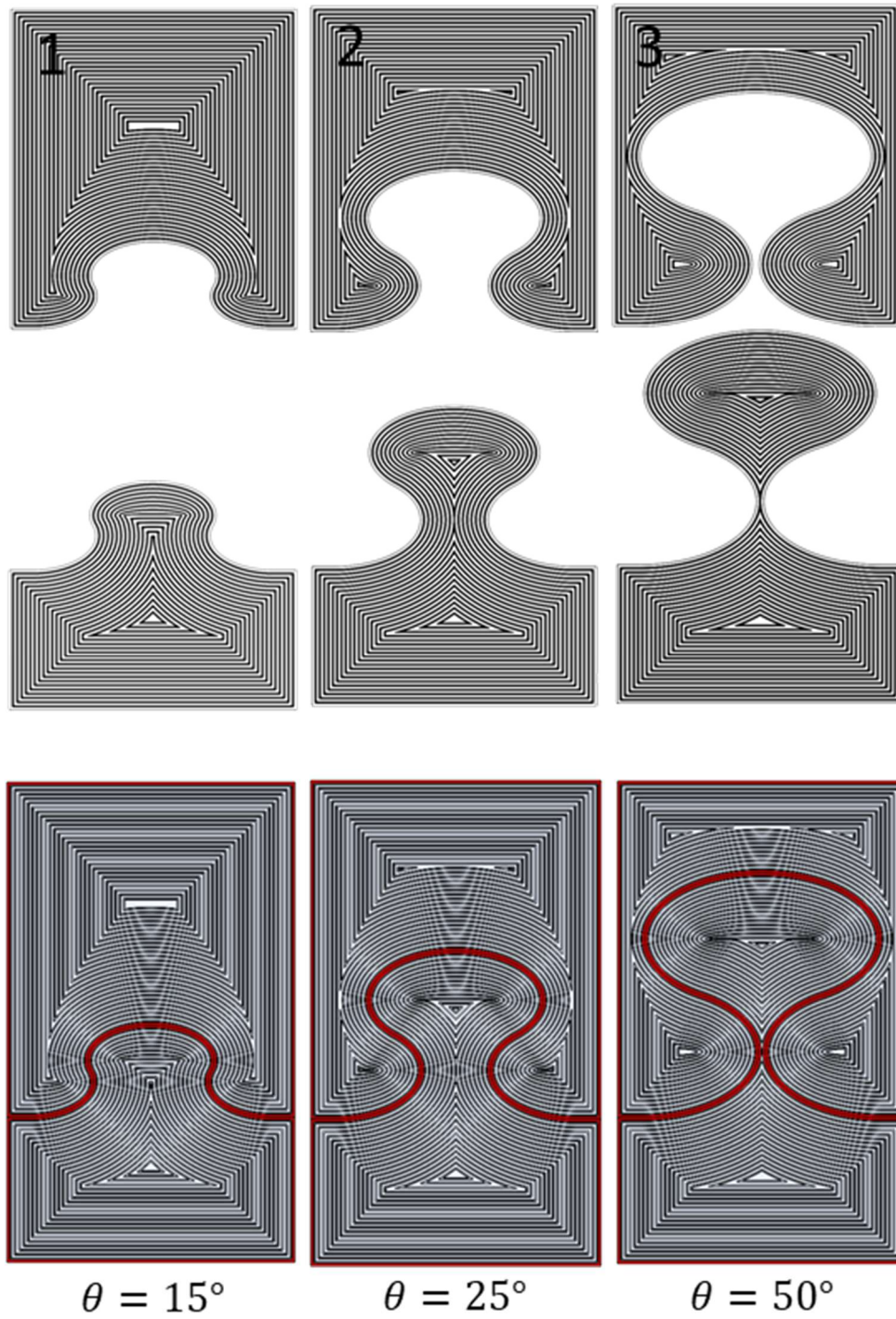
$$\theta = 15° \qquad \theta = 25° \qquad \theta = 50°$$

(a)

Figure 6.10. (a) CAD model for the 3D printed geometries including $\theta = 15°, 25°, 50°$, (b) A lagrangian strain distribution of the blades using DIC technique, (c) A comparison between normalized peak load and energy dissipation in three cases with different values of θ, (d) A side by side comparison between FE simulation and experiment for the case with $\theta = 25°$.

Figure 6.10 continued
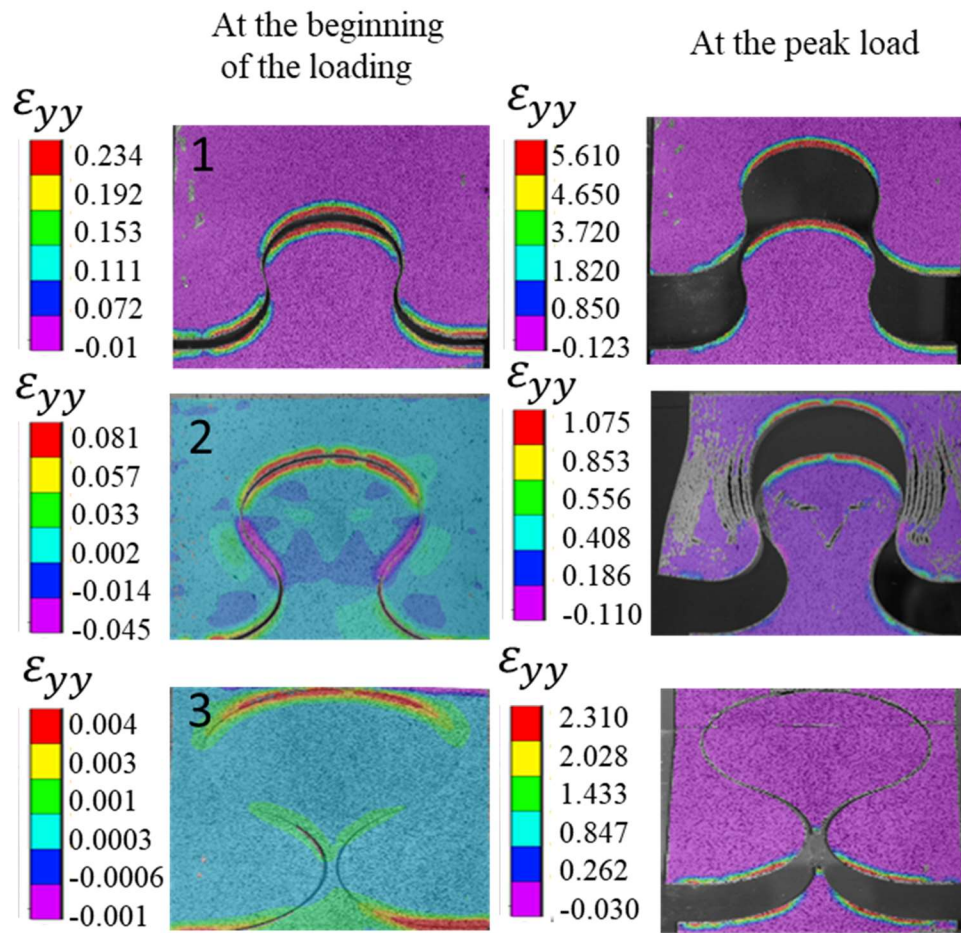
(b)
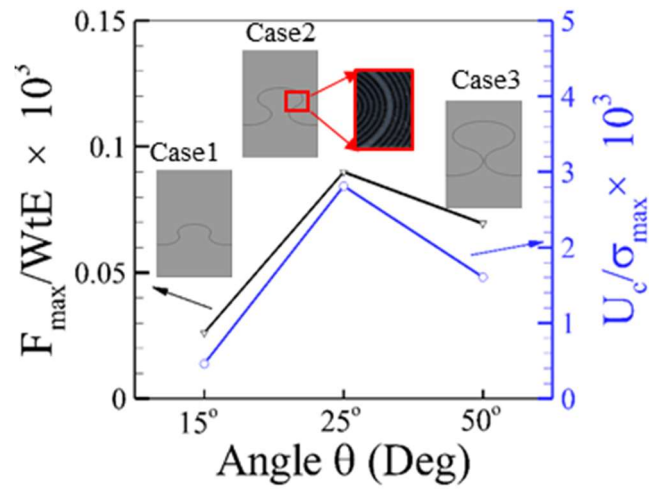
(c)

Figure 6.10 continued

(d)
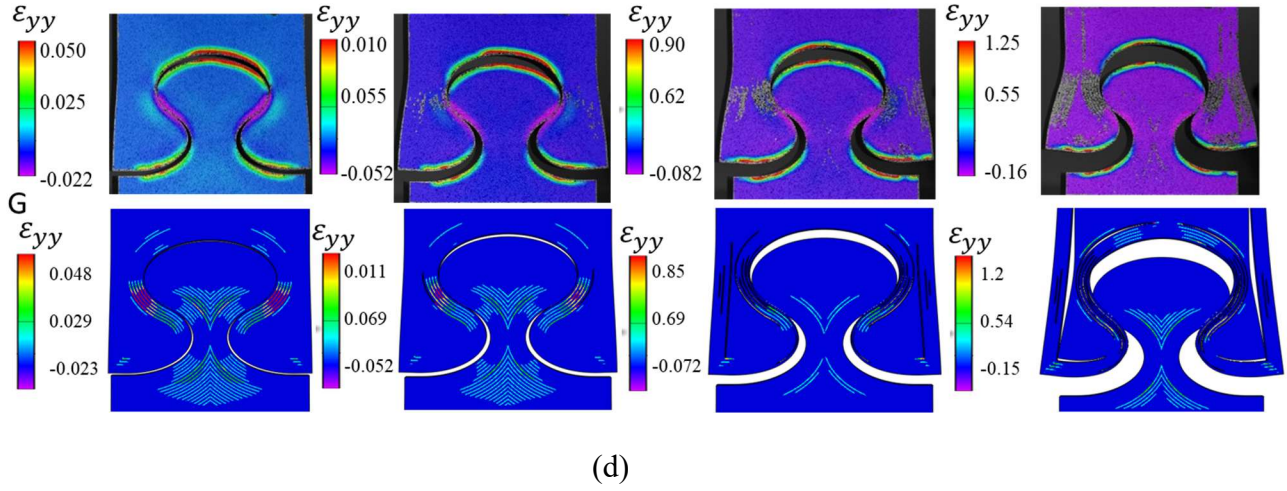
6.6 Homogeneous polymer blade (side-free boundary condition)

In section 6.4, the role of material properties, a/b, and θ were investigated for a single blade by employing the HBC boundary condition. Based on the observation from the real cuticle of the Ironclad Beetle, the dovetail joints connecting the elytra part are free to move due to the space inside the abdomen, therefore, for the rest of this study, the HBC boundary condition is removed from all the models.

The load-displacement curves for different values of a/b and θ of single blade containing VeroWhite polymer are presented in Fig 6.11(a). In these sets of tests, the HBC condition is removed from the model, and tensile loading is applied on the top while the bottom surface fixed against translational directions. Theoretically, as the value of aspect ratios or θ increases, it is expected to have a higher peak load due to the increase in the contact area. For this particular material, the peak load increases by increasing the aspect ratio and θ up to $a/b = 2.5$ and then decreases for higher aspect ratios due to the fracture inside the neck. Besides, the peak load also increases by increasing the angle θ. Depending on material properties (i.e., ductile, brittle, etc.) and damage mechanisms, different optimized aspect ratio and θ could be expected (see section 6.3). Although optimization is not the aim of this section, one could see that ellipse geometry perform better in comparison to circular blades. Also, this section helps me to select the proper aspect ratios for the ellipse for the rest of this study and parametric analysis (i.e., including multi-layered puzzle-like structure)

The normalized value of peak load, stiffness, and toughness (energy absorption) for all the cases with different values of aspect ratio is shown in Fig 6.11 (b), (c), and (d), respectively. The results show that the normalized peak load increases by increasing θ up to a/b =1.5 since no fracture or failure observed inside the blades. For a/b =1.8, 2.0, the maximum peak load occurs at $\theta = 30°$ and then decreases (this happens because of damage occurs in the blades for the values of θ higher than $\theta = 30°$). Finally, for the large aspect ratio (a/b =4.5), the peak occurs at $\theta = 10°$ and the value is much lower than the peak for a/b =2.5 as can be seen in Fig 6.4(b). Similarly, the normalized value of stiffness increases by increasing the aspect ratio (the highest values can be observed for a/b=3.5). In addition, the values of stiffness increase by increasing θ and then decreases after damage occurs in the neck. For example, for the a/b = 1.5, the stiffness values increase up to angle $\theta = 35°$ and then decreases for larger values of θ due to the damage occurrence. The comparison between energy absorption (toughness) for different values of a/b and θ is presented in Fig 6.11 (d). The results state that the larger values of energy absorption belong to the a/b = 1.8 when $\theta = 30°$ (for this specific material). Finally, by comparing results from Fig 6.11, (b)-(d) one could see that there is a tradeoff between stiffness, toughness, and peak load. Therefore, for the rest of this study (understand the effect of puzzle-like architecture), the following three aspect ratios (a / b= 1.8, 2.0, 2.5) were selected based on their performance with respect to the other aspect ratios in enhancing the mechanical properties.
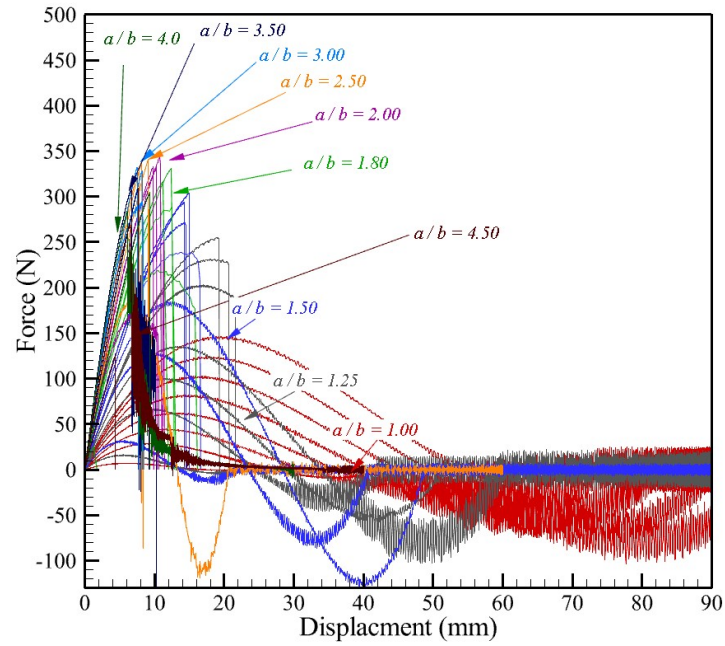
(a)
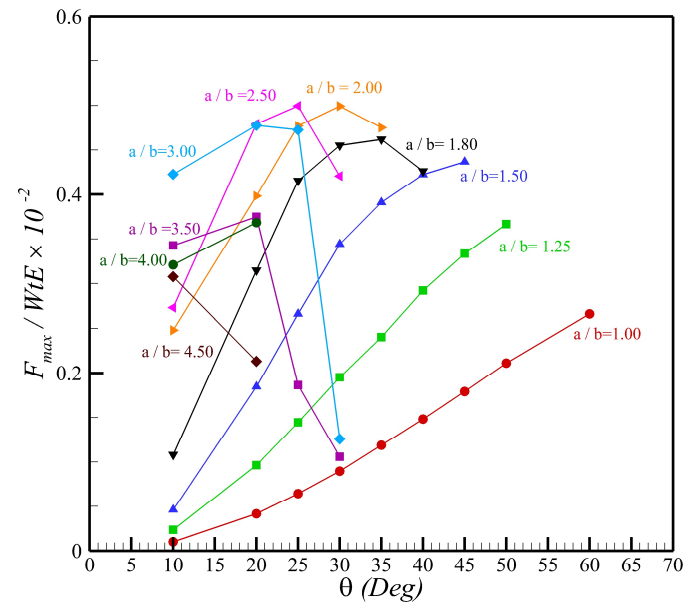
(b)

Figure 6.11. Role of blades shape for various a/b and θ, (a) Load vs. Displacement curves, (b) normalized peak load, (c) normalized stiffness, (d) normalized toughness

Figure 6.11 continued
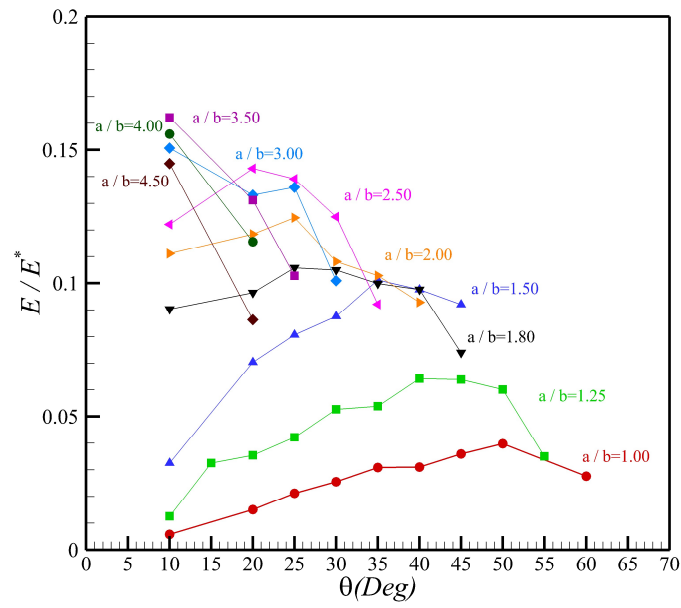
(c)
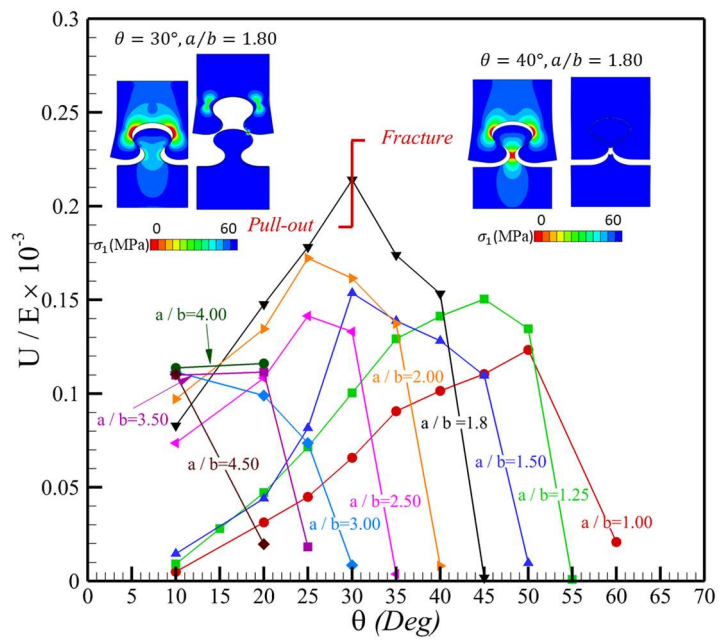
(d)

6.7 Role of blades microstructure

As previously discussed in section 6.5; Ironclad beetle developed microstructure (layers) from alpha-chitin fibers inside its cuticle. The interlocking blades are responsible for connecting separate parts inside elytra. These alpha-chitin layers of fibers also exist inside the interlocking joints and as discussed in section 6.5, under loading conditions (compressive or tensile) cause delamination inside the joints as failure mechanisms. Based on a study by Malik and barthelat 2016, two types of competing mechanisms can be expected in the interlocking joints containing homogenous materials; i) pullout and ii) fracture. During loading, unlike homogenous blades, blades inside beetle elytra developed delamination as another competing mechanism. Therefore, the primary purpose of this study is to understand the role of multi-layered structure inside blades bio-inspired by Ironclad beetle, and if this technique could help to enhance the mechanical performance of the structure. To this aim, a set of systematic and parametric study is required to understand the role of the multilayered structure. Figure 6.12(a) presents a single blade (develop from three adjacent ellipses) contains multilayered. The required parameters for this study are discussed in the following sections.

6.7.1 Dimensionless Analysis

Based on the presented geometry and material properties for a blade (Figure 6.12(a)), the following dimensionless groups are needed to be investigated for the geometrical parameters $(a,\ b,\ \theta, n,\ L,\ W,\ t,\ t_1)$, material properties $(E_1, \nu_1, \sigma_f, \varepsilon_f)$, and the cohesive law parameters $(\sigma_{max}, \tau_{max},\ G_{Ic}, G_{IIc})$. The schematic of the sample with the variables is presented in Fig 6.12 (a).

$$P_{max},\ G_c = f(a,\ b,\ \theta, n,\ L,\ W,\ t,\ t_1, E_1,\ \nu_1,\ \sigma_f, \varepsilon_f, \sigma_{max}, \tau_{max}, G_{Ic}, G_{IIc}\ , f_{friction}) \quad (6.9)$$

Where P_{max} is the maximum load that can be achieved during the tensile test, G is the energy absorption. Since adhesives between laminated layers are modeled with zero thickness cohesive elements, no change is expected to occur in the initial stiffness of all the samples in comparison to the homogenous case. Following Buckingham's 'Π-theorem' (Buckingham, 1914), the physical variable in Equation 6.9 can be combined in different dimensionless groups. The total number of variables is equal to eightteen. Based on Buckingham's Π theorem, one can also express them in terms of π_i where $F(\pi_1, \pi_2, ..., \pi_p) = 0$. Considering this, we will end up with ($p = n - k =$

$18 - 2 = 16$) sixteen dimensionless groups. Finally, the following dimensionless group is utilized in Equation 4.5;

$$\frac{P_{max}}{E_1 wt}, \frac{G_c}{G_{Ic}}$$

$$= \Psi\left(\theta, n, \frac{a}{b}, \frac{t_1}{a}, \frac{\sigma_{max}}{E_1}, \frac{\sigma_{max}}{\tau_{max}}, \nu_1, \frac{\sigma_f}{E_1}, \varepsilon_f, \frac{(G_{Ic}/\sigma_f)^2}{w_n}, \frac{(G_{IIc}/\sigma_f)^2}{w_n}, \frac{G_{Ic}}{G_{IIc}}, \frac{W}{w_n}, \frac{L}{W}, f_{friction}\right) \quad (6.10)$$

In the above Equation, the geometrical values such as L, W, and blade thickness are assumed to be constant and as a result, they are removed from the calculations. In this study, firstly, the effect of geometrical parameters will be investigated for various aspect ratios ($a/b = 1.8, 2.0, 2.5$). These aspect ratios are selected due to the results that I obtained in section 6.6 for the blades with homogenous material. Vero White is selected for the layers and tango black plus is selected as an adhesive. Also, the effect of θ, for each aspect ratio is considered separately. Finally, four different values for $t_1/a = 0.05, 0.1, 0.25, 0.45$ is considered in order to understand the role of the number of layers in the mechanical properties of the blades (Figure 6.12 (b), (c)).

(a)

(b)
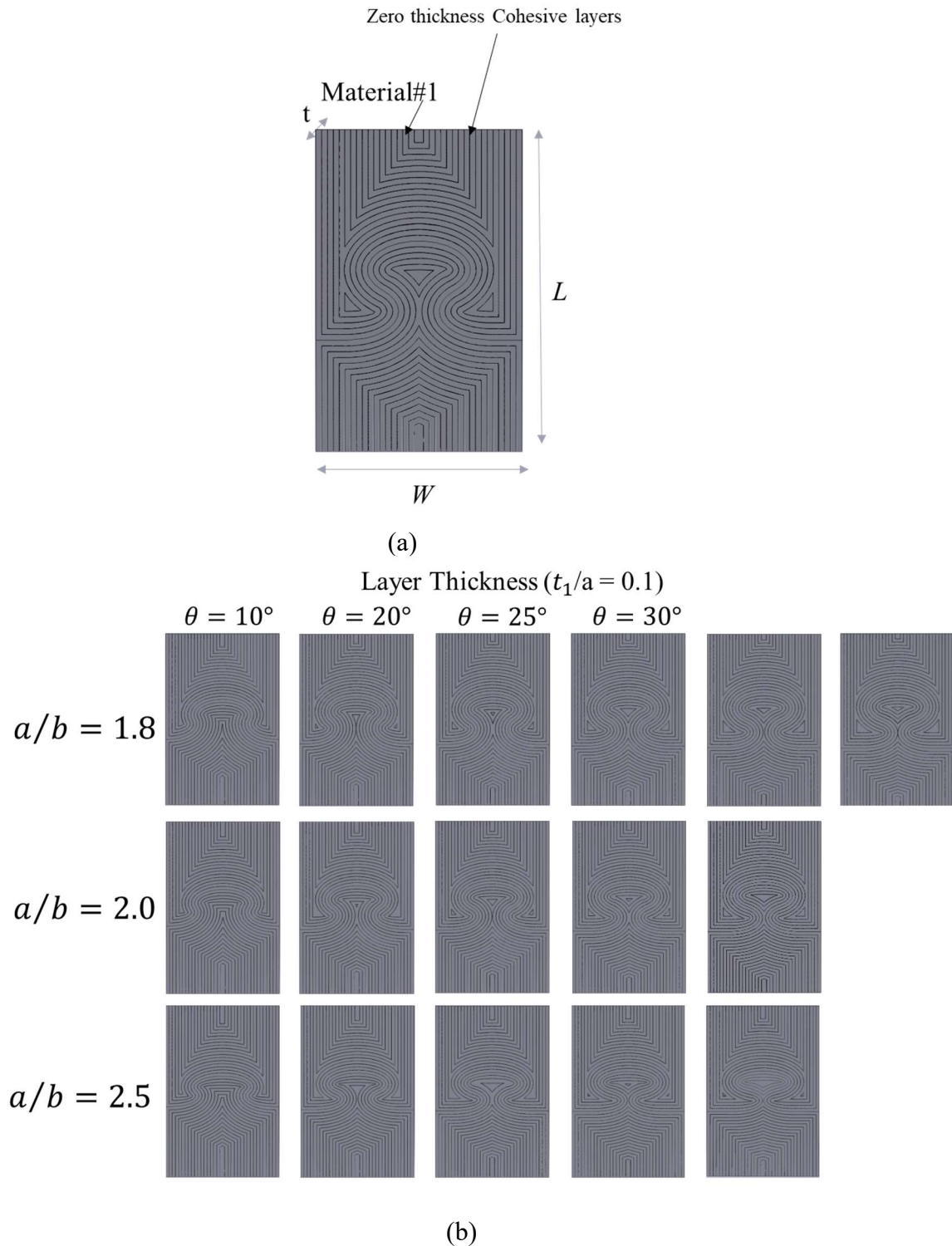
Figure 6.12. (a) Schematic of FE simulation for different values of aspect ratio and angle θ for $t_1/a = 0.1$. (b) Multi-layered puzzle-like architecture geometries for a/b =1.8, 2.0,2.5, and all the admissible values of θ when $t_1/a = 0.1$, (c) four values of $t_1/a = 0.05, 0.1, 0.25, 0.5$ for a representative model with a/b = 2.0, $\theta = 25°$

Figure 6.12 continued

$$\frac{a}{b} = 2.0, \theta = 25°$$

$\frac{t_1}{a} = 0.05$ $\frac{t_1}{a} = 0.1$ $\frac{t_1}{a} = 0.25$ $\frac{t_1}{a} = 0.45$

(c)
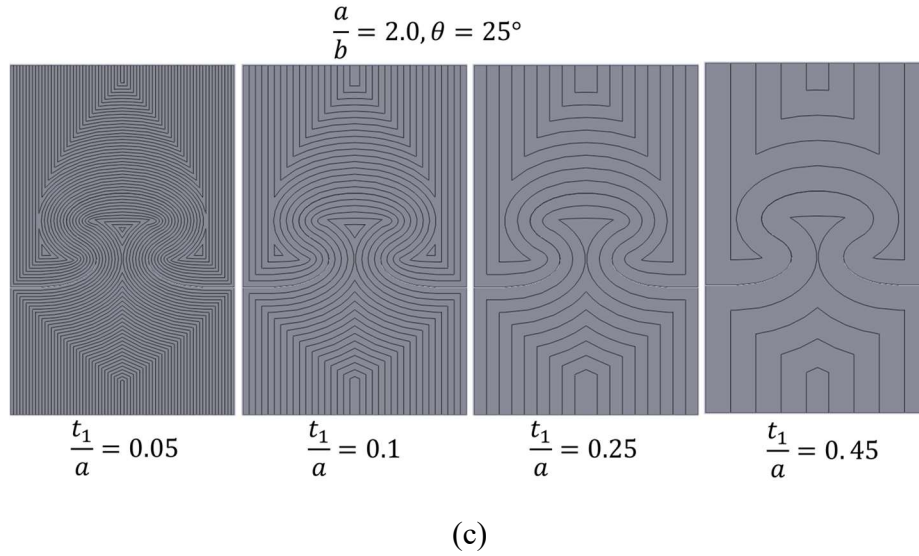
6.8 Parametric study of architecture inside the interlocking joint (role of $\frac{t_1}{a}$)

In this section, the role of energy dissipation for various aspect ratios, angleθ, and t_1/a (layers thickness normalized with respect to the major axes of the blade) will be investigated for a single multi-layered puzzle-like blade. A comparison between energy dissipation due to the plastic deformation and delamination will be studied for different values of θ, t_1/a, and, a/b in order to understand the role of both geometry and architecture (puzzle-like multilayered structure). To this aim, Figures 6.13-6.16, present the comparison between the energy dissipation due to delamination and plastic deformation for three values of aspect ratios and admissible blade geometries when t_1/a=0.05, 0.1,0.25,0.45.

6.8.1 Case study 1 ($\frac{t_1}{a} = 0.05$)

The comparison between the energy release rate when t_1/a=0.05 for different values of aspect ratios and θ is presented in this section. This set of parametric study contains the maximum number of layers in comparison to other t_1/a ratios. For all the cases, no fracture or damage observed in layers and delamination was responsible for total energy dissipation. The comparison between energy dissipation due to delamination and plastic deformation for different values of θ and a/b=1.8, 2.0,2.5 are presented in Figure 6.13 (a)-(c), respectively. The results stated that by

increasing both $\frac{a}{b}$ and θ, the energy dissipation due to delamination increases. Also, Due to the high number of layers, most of the energy dissipation occurs through delamination even for the high aspect ratio of a/b = 2.5.

The results also revealed that, for the lower angles or aspect ratios the energy mostly dissipated through delamination, while for the model with high aspect ratios and angle (i.e., $\theta = 35°, \frac{a}{b} = 2.5$), the energy not only dissipated through delamination but also through plastic deformation. Although the value of energy dissipation due to plastic deformation is much lower in comparison to the delamination. Finally, by comparing Figure 6.13 (a)-(c) one can observe that by increasing the aspect ratio, the rate of energy dissipation increases for each value of θ.
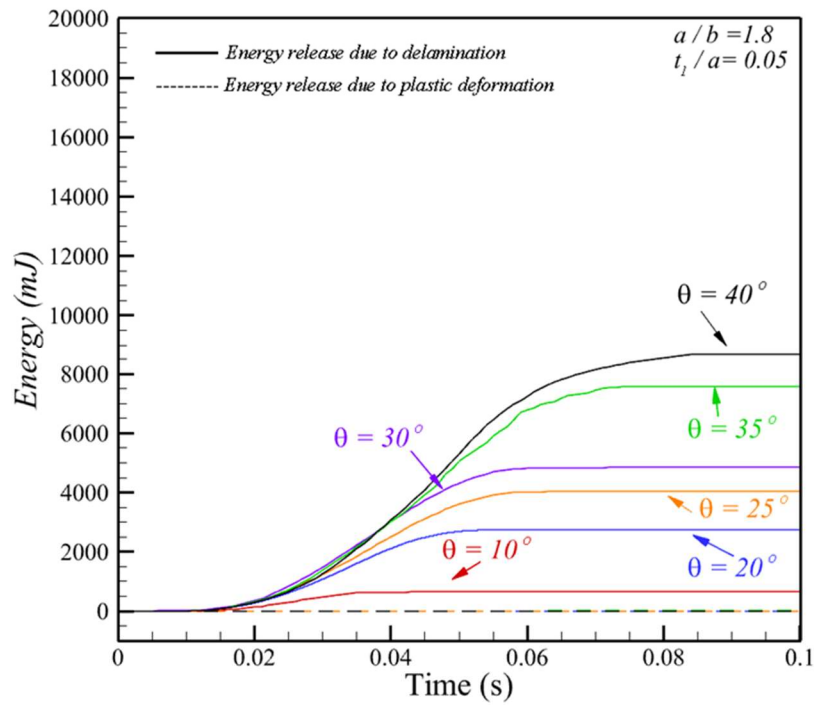
(a)

Figure 6.13. Comparison of energy release rate for different values of aspect ratio and θ for $t_1/a = 0.05$, (a) a/b=2.5, (b) a/b=2.0, and (c) a/b=1.8.

Figure 6.13 continued
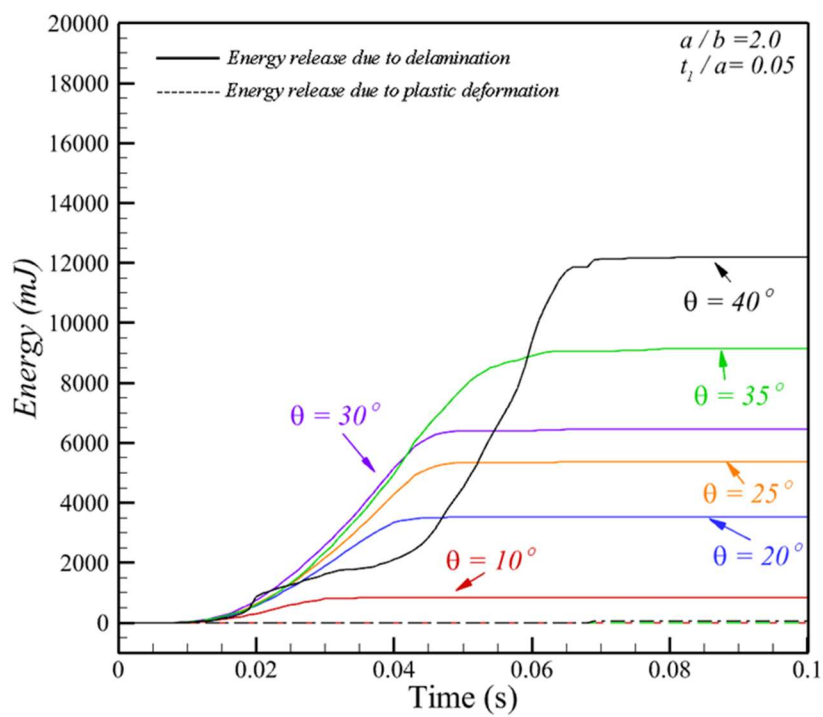
(b)
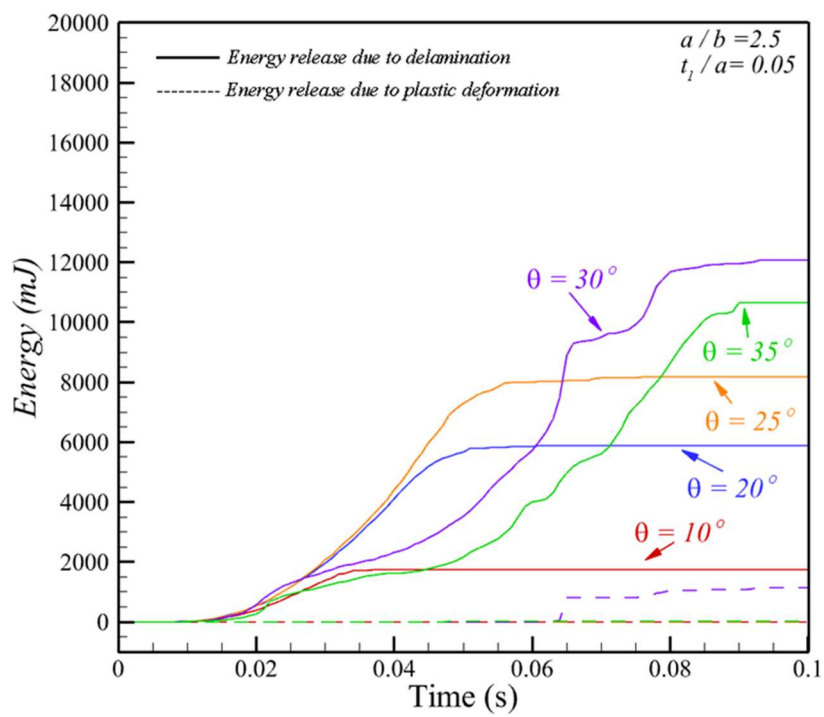
(c)

6.8.2 Case study 2 ($\frac{t_1}{a} = 0.1$)

In this section, the energy dissipation is investigated when $t_1/a = 0.1$. The energy dissipation due to plastic deformation and delamination for three values of aspect ratios are shown in Figure 6.14(a)-(c). For t_1/a =0.1, the energy mostly dissipated through delamination, however, the small portion of energy dissipated through plastic deformation for all the aspect ratios. For instance, for the model with a/b=2.5, a slight increase in the energy dissipation caused by plastic deformation can be observed for $\theta = 30°, and\ 35°$. Also in all the cases the rate of energy dissipation increases in comparison to the models with $t_1/a = 0.05$.
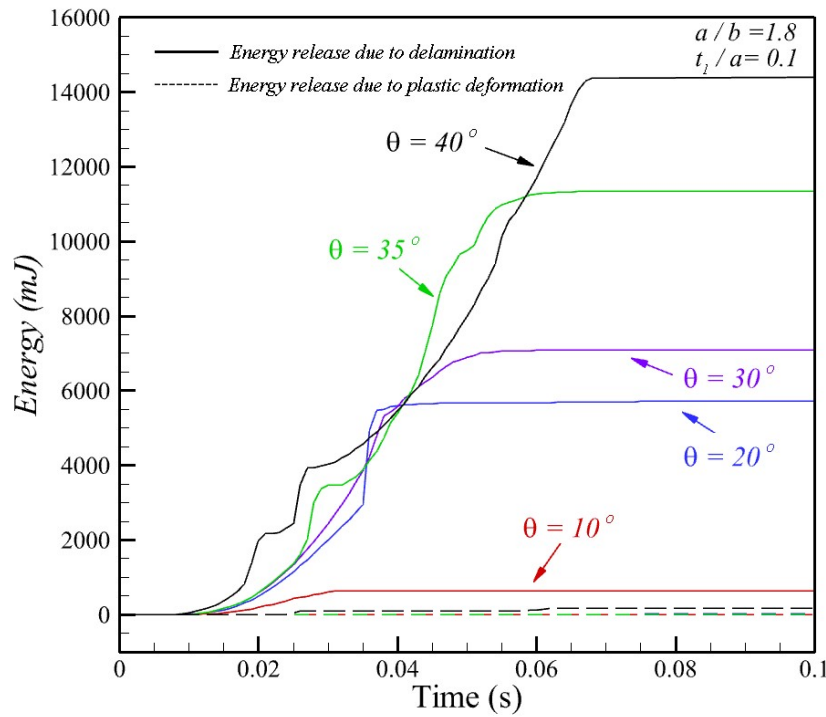
(a)

Figure 6.14. Comparison of energy release rate for different values of aspect ratio and θ for $t_1/a = 0.1$, (a) a/b=1.8, (b) a/b=2.0, and (c) a/b=2.5.

Figure 6.14 continued
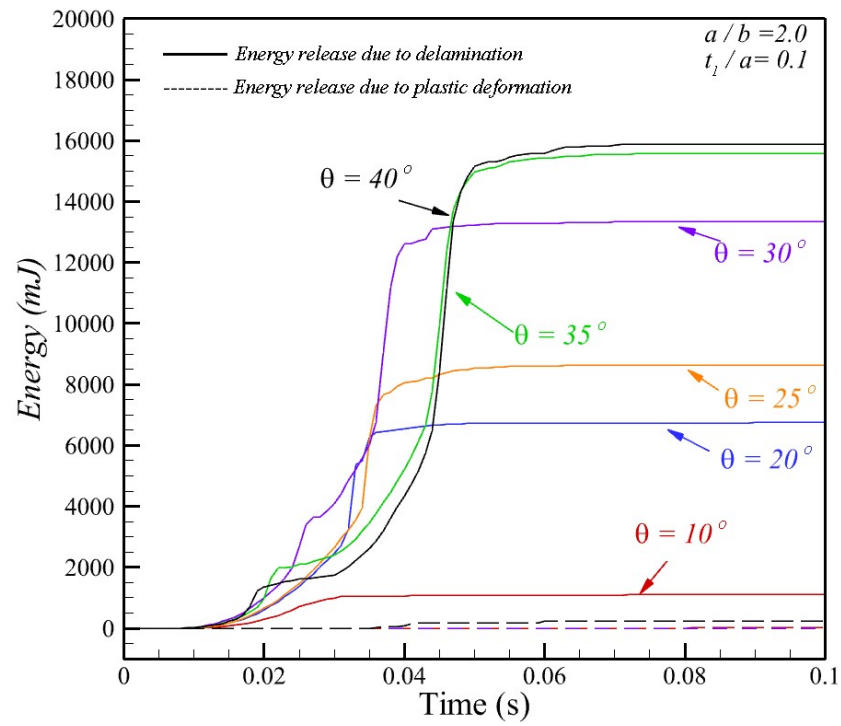
(b)
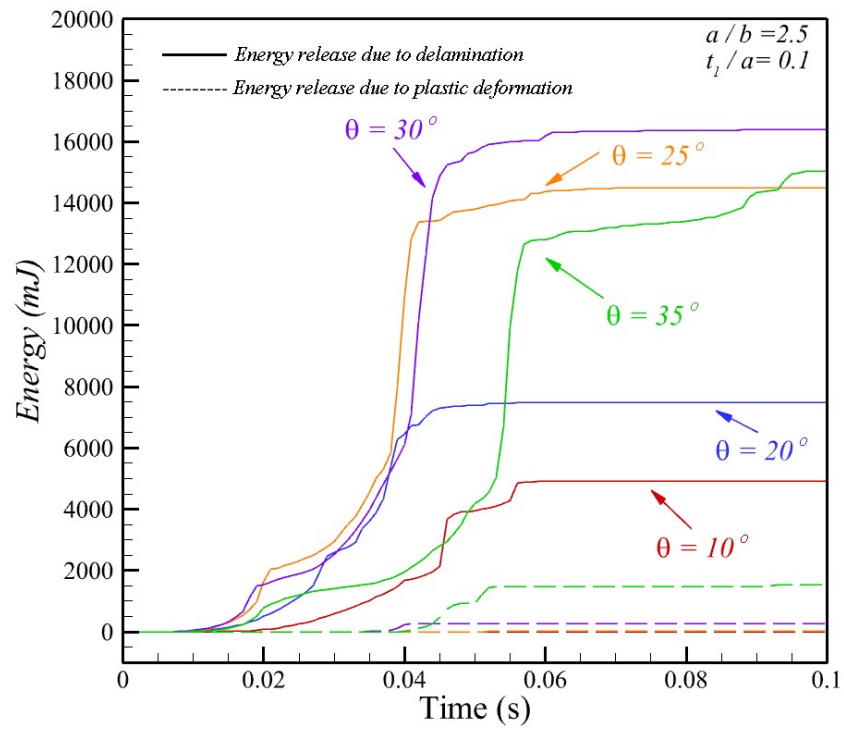
(c)

6.8.3 Case study 3 ($\frac{t_1}{a} = 0.25$)

By increasing the value of t_1/a to 0.25 (using a smaller number of layers inside a single blade), one can observe that the value of energy dissipation due to delamination for different aspect ratios and values of θ is very close to the case where $t_1/a = 0.1$. However, for the a/b =2.5, the results show higher energy dissipation due to plastic deformation, and as a result, the total energy dissipation is higher for $t_1/a = 0.25$ in comparison to the $t_1/a = 0.1$ (see Fig 6.12(c)).
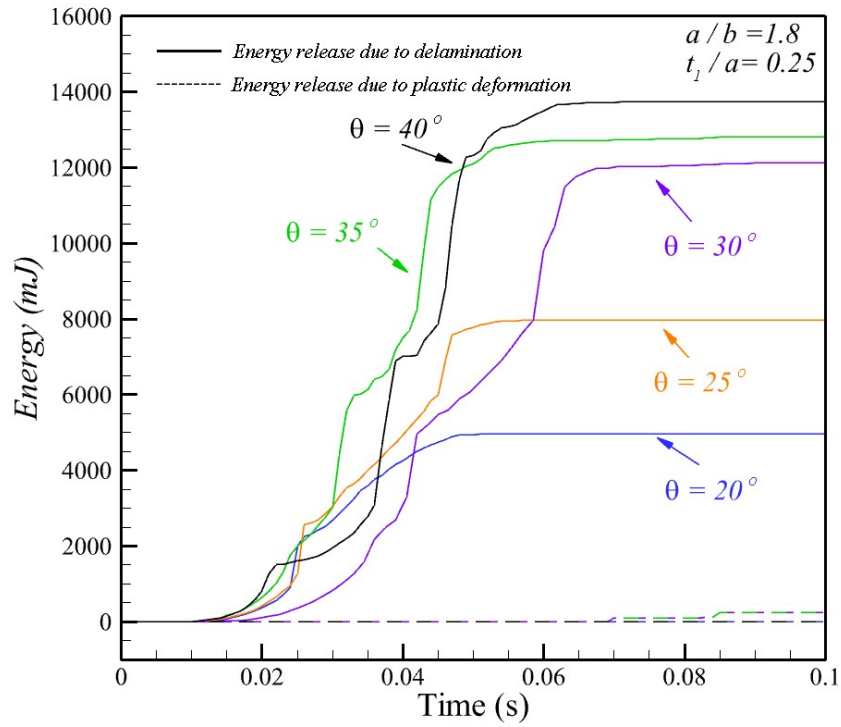
(a)

Figure 6.15. Comparison of energy release rate for different values of aspect ratio and θ for $t_1/a = 0.25$, (a) a/b=1.80, (b) a/b=2.0, and (c) a/b=2.50.

Figure 6.15 continued
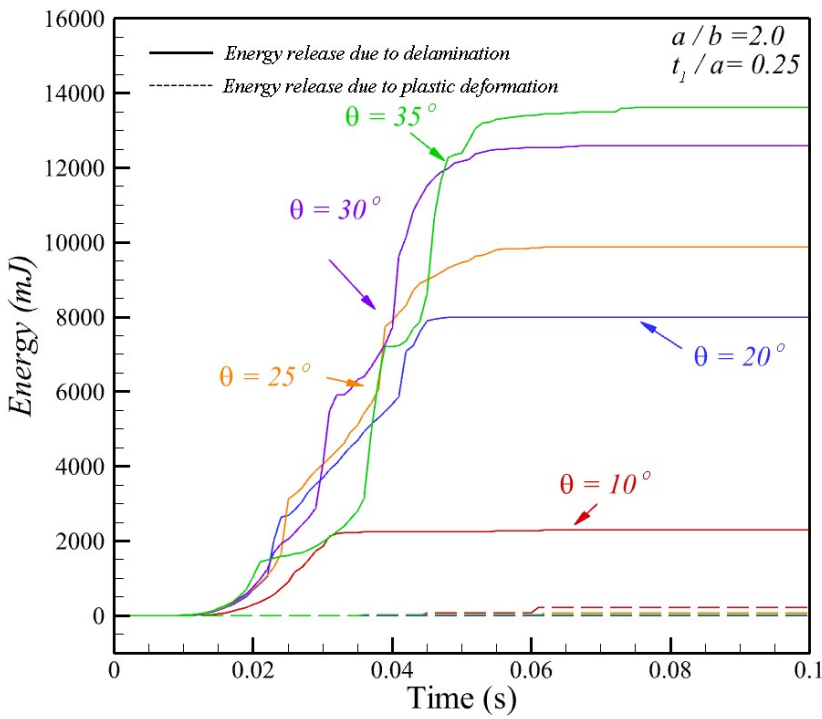
(b)
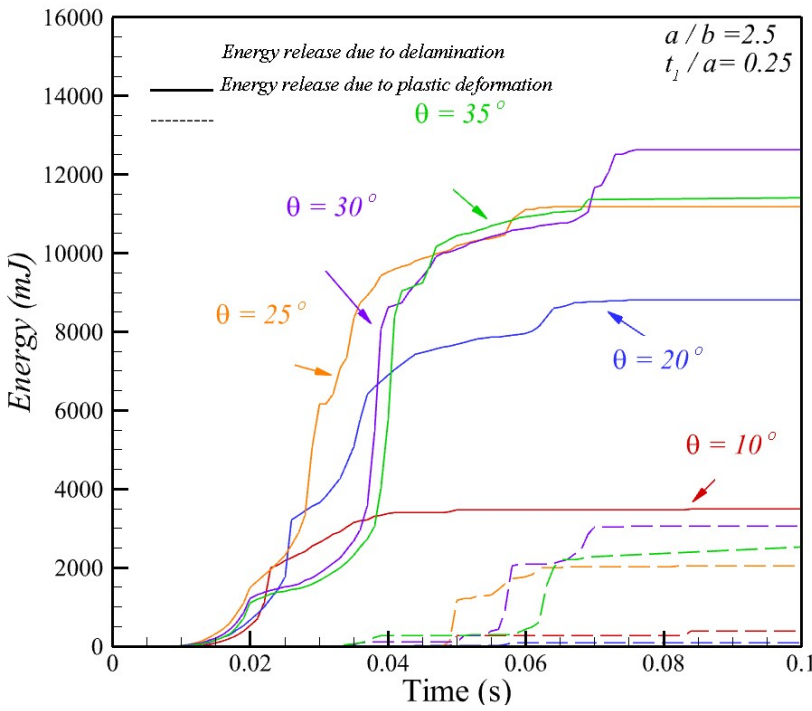
(c)

6.8.4 Case study 4 ($\frac{t_1}{a} = 0.45$)

Finally, the comparison for the largest t_1/a ($t_1/a = 0.45$) in this parametric study is presented in Figure 6.16 (a)-(c). For this case, the results indicated the lower values of energy dissipation due to plastic deformation and delamination for all the aspect ratios and angle θ with respect to the three other values of t_1/a. This could be explained because of the smaller number of layers and excessive stress around the blade releases due to the delamination in fewer existing layers.
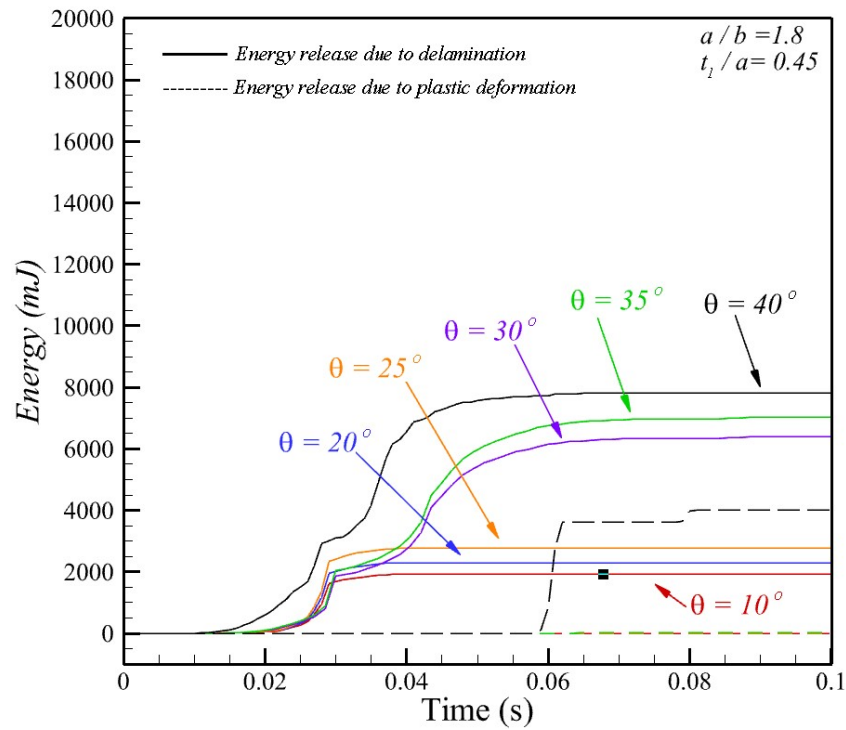
(a)

Figure 6.16. Comparison of energy release rate for different values of aspect ratio and θ for $t_1/a = 0.45$, (a) a/b=1.80, (b) a/b=2.00, and (c) a/b=2.50.

Figure 6.16 continued
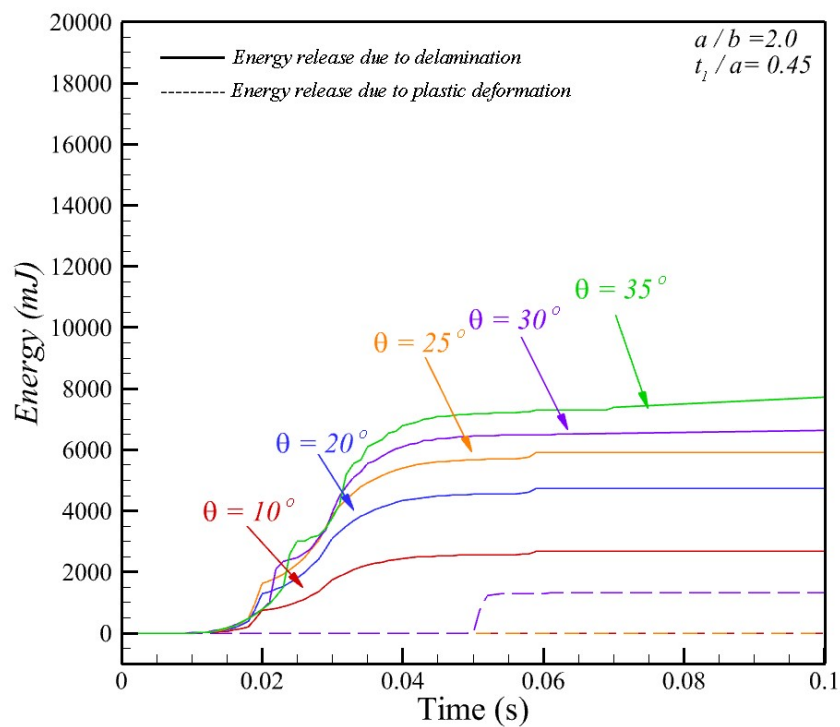
(**b**)
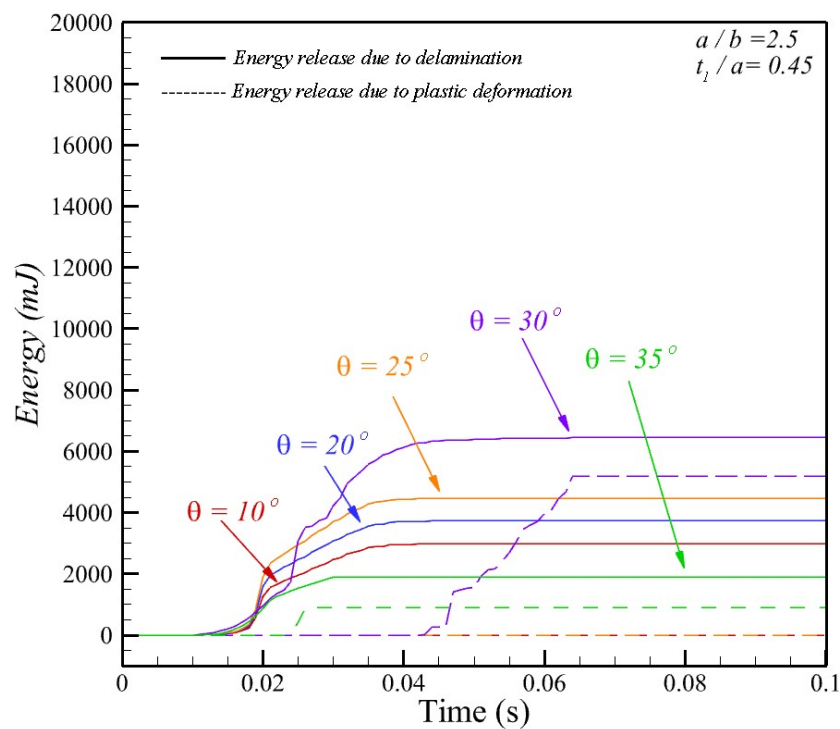
(c)

A side by side comparison between stress-strain curves and energy dissipation for a/b =2.0 and different values of t_1/a for two selected values of θ ($\theta = 20°$, and $35°$) are presented in Fig 6.17(a)-(d). As shown in Fig6.17(a), for the case of $\theta = 20°$, the values of stress increase up to a peak value and then decreases until the complete pullout occurs. Figure 6.17(b) shows that the energy dissipation for all the values of t_1/a occurs through delamination. Also, the highest energy dissipation was obtained for $t_1/a = 0.25$. A similar comparison is presented for a/b =2.0, and $\theta = 35°$ is shown in Fig 6.17(c) and (d). For the higher angle such as $\theta = 35°$, for all the models the stress increases up to the first peak (the first layer delaminated inside the male part). In the homogenous blade with a high angle ($\theta = 35°$), and under quasi-static tensile loading, there is drop-in stress after the first peak was reached. This happened due to the fracture in the neck area of the blade (for this specific material), while, for the model consisting multilayered, after the first peak, there is a drop-in stress-strain curve followed by an increase in stress values until the second peak achieved and finally pullout occurs in the system. The second peak for the cases with high angles confirms that by using multi-layers inside the blade, one can increase the toughness and energy dissipation of the system as shown in Fig 6.17(c) and (d). Also, a comparison between energy dissipation for different values of t_1/a reveals that the maximum energy dissipation occurs due to the delamination when $t_1/a = 0.1$. It is also notable that for both values of θ ($\theta = 20°$ and $35°$), a very large number of layers ($t_1/a = 0.05$) or a small number of layers ($t_1/a = 0.45$) demonstrate less energy dissipation in comparison to the two other t_1/a (0.1, 0.25). For the $t_1/a = 0.05$, the existence of a high number of layers causes lots of tiny delamination inside the blade and resulted in lower peak load and energy dissipation, however, by decreasing the number of layers or increasing the thickness of each layer, the energy dissipation occurs due to both plastic deformation and delamination inside the blades. Also, localization was observed inside the blades for the high value of t_1/a ($t_1/a = 0.45$).
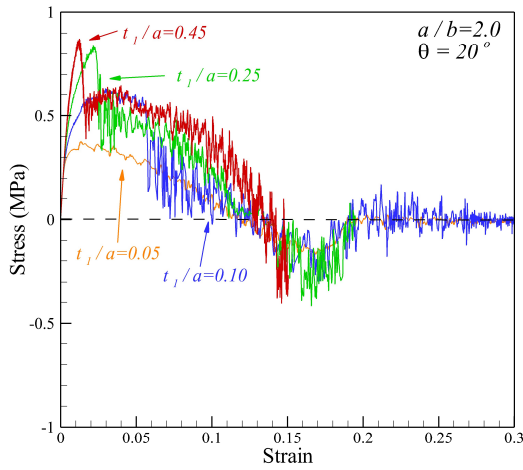
(a)
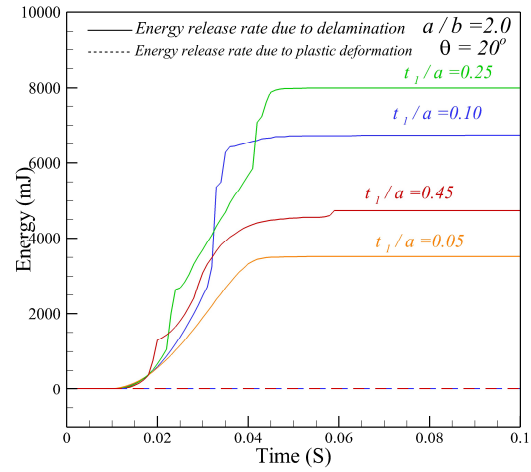
(b)
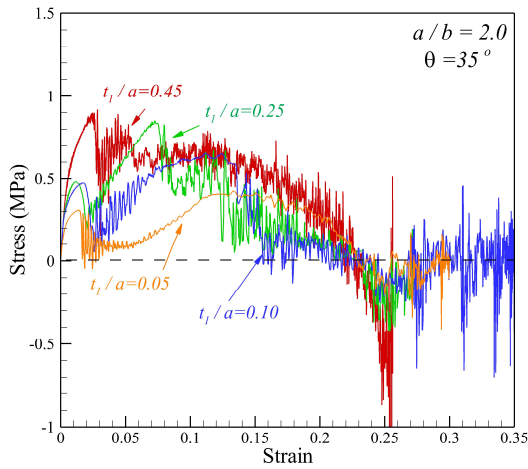
(c)
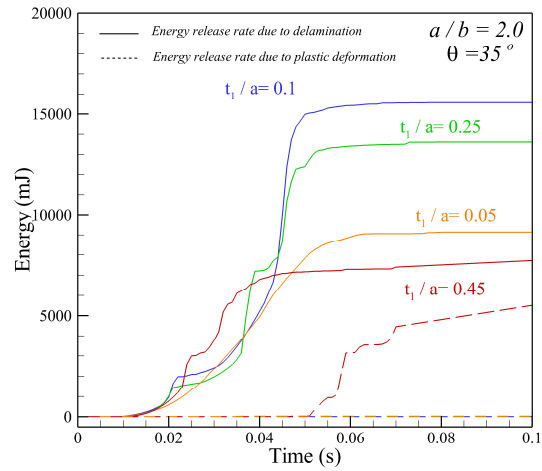
(d)

Figure 6.17. A comparison between stress-strain curves and energy release rate side by side for various values of $\frac{t_1}{a} = 0.05, 0.1, 0.25, 0.45$, (a) stress-strain curves for $a/b = 2$ and $\theta = 20°$, (b) Energy release rate due to delamination and plastic deformation for $a/b = 2$ and $\theta = 20°$, (c) stress-strain curves for $a/b = 2$ and $\theta = 35°$, (d) Energy release rate due to delamination and plastic deformation for $a/b = 2$ and $\theta = 35°$.

The normalized value for peak load and energy release rate vs. angle θ for various values of t_1/a is presented in Figure 6.18 (a) and (b), respectively. The results stated that when the values of t_1/a equal to 0.05, and 0.1; the value of peak load increases by increasing the angle θ. However, for larger values of t_1/a (i.e. $t_1/a = 0.25$), the value of normalized peak load increases and then decreases due to the fracture in the neck areas of the blades, because for the high angles and larger values of t_1/a, delamination layer does not exist inside the neck to dissipate strain concentration due to the interlocking. For example, when $a/b = 2.5$ and $t_1/a = 0.25$ the maximum peak load occurs in $\theta = 20°$, while for when $a/b = 1.8$ and $t_1/a = 0.05$, maximum peak load occurs at $\theta = 40°$. This can be explained because there are competing mechanisms between the peak load and a number of the layers. As the number of layers decreases, the peak load increases; however, it occurs at smaller angle θ, due to the fracture of the neck area for the higher angle. As the number of layers decreases, more localized damage can occur; also, the plastic deformation increases. Moreover, by increasing the angle θ, the contact area increases, therefore more toughness can be expected.

Finally, the maximum principal stress distribution at the peak load for $a/b = 1.8$, and different values of t_1/a for two selected θ ($\theta = 20°, 40°$) is presented in Figure 6.18(c). The results stated that when θ is small, delamination occurs in the female part follows by pull out even for the large values of t_1/a. However, for the large angle θ ($\theta = 40°$), the deamination starts in the male part except for the case with the largest number of layers ($t_1/a = 0.05$). It is also notable that for the homogenous blade material ($a/b = 1.8$) we observed plastic deformation followed by pull-out when $\theta = 20°$, and fracture inside the neck when $\theta = 40°$. Therefore, one could observe that adding delaminated layers inside the blade can help to relax the stress concentration via delamination specifically for samples with high angles (expected to see failure inside the neck). Thus, having multilayered puzzle-like architecture not only helps to relax the excessive strain and increases the toughness of the system but also helps to avoid failure in the neck and, therefore, resulted in large defamation followed pull-out.
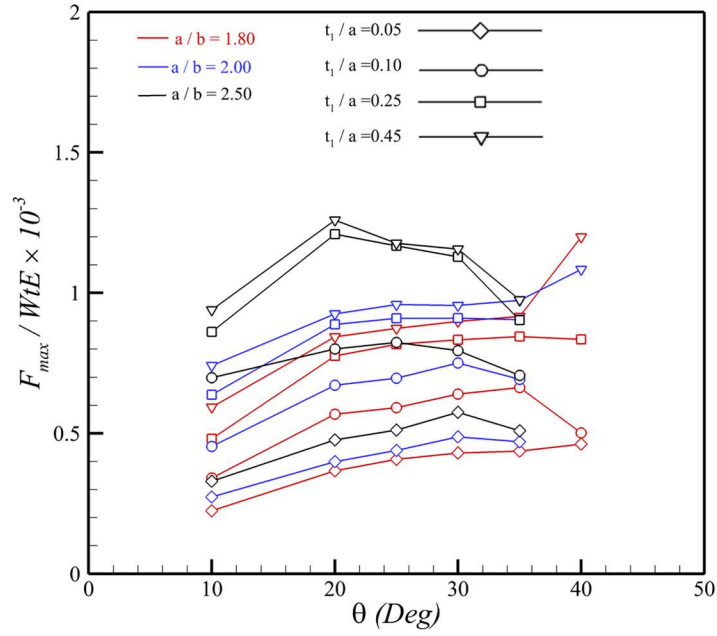
(a)
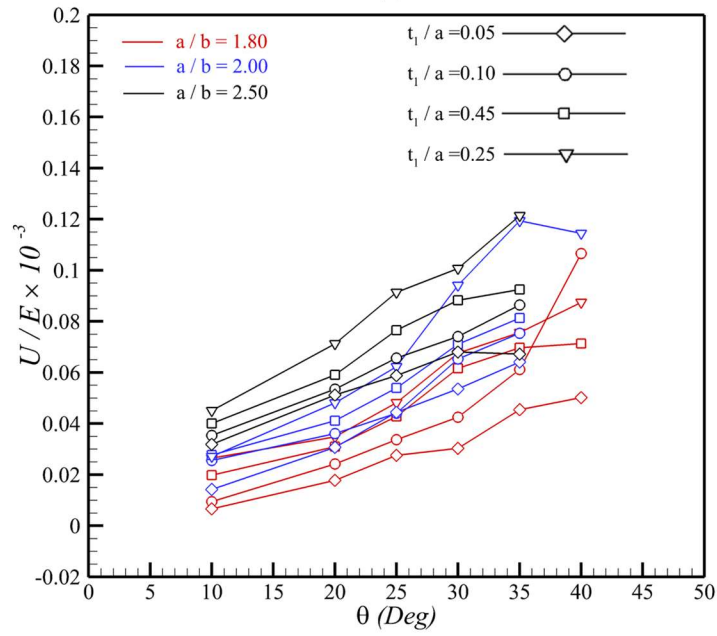
(b)

Figure 6.18. (a) Comparison for different values of aspect ratio with different number of layers (a) normalized peak load, (b) Normalized energy release rate, (c) maximum principal stress distribution for two selected θ and different values of $t_1/a = 0.05, 0.1, 0.25, and\ 0.45$ showing at the peak load for all the cases.

Figure 6.18 continued

$a/b = 1.8$

$t_1/a = 0.05$ $t_1/a = 0.1$ $t_1/a = 0.25$ $t_1/a = 0.45$

$\theta = 25°$

σ_1(MPa)   0   12   25

$\theta = 40°$

(c)
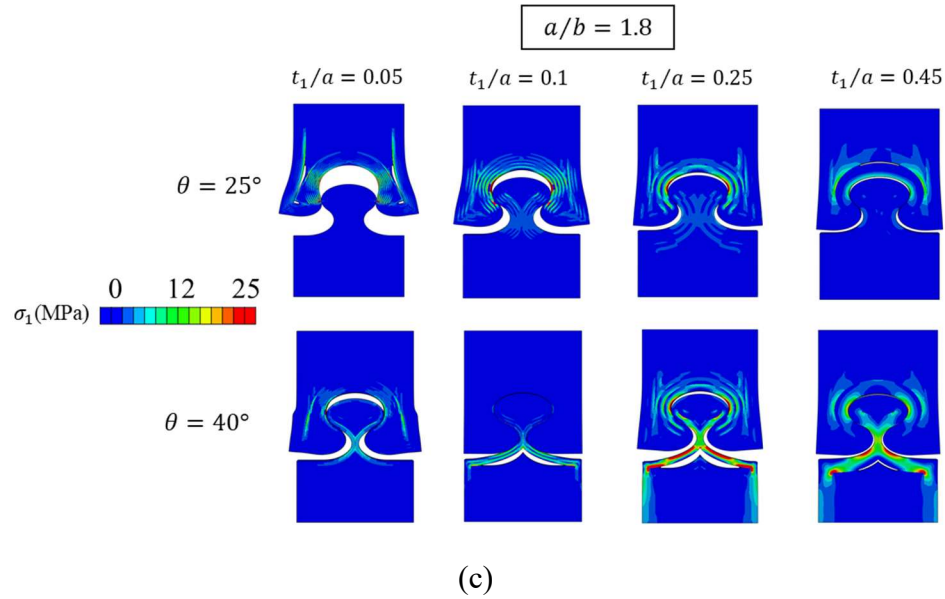
6.8.5 Comparison between Multi-layered model and homogenous blade

The comparison between the multilayered blade including Verowhite layers and Tangoblack adhesives with the homogenous blade of various angles is presented in Figure 6.19. The results indicate that adding delaminated layers can increase the toughness of the interlocking blades up to three times in comparison to the homogenous case by only sacrificing the peak load up to ten percent. The results from homogenous and multilayered blades are shown in green and purple colors, respectively.
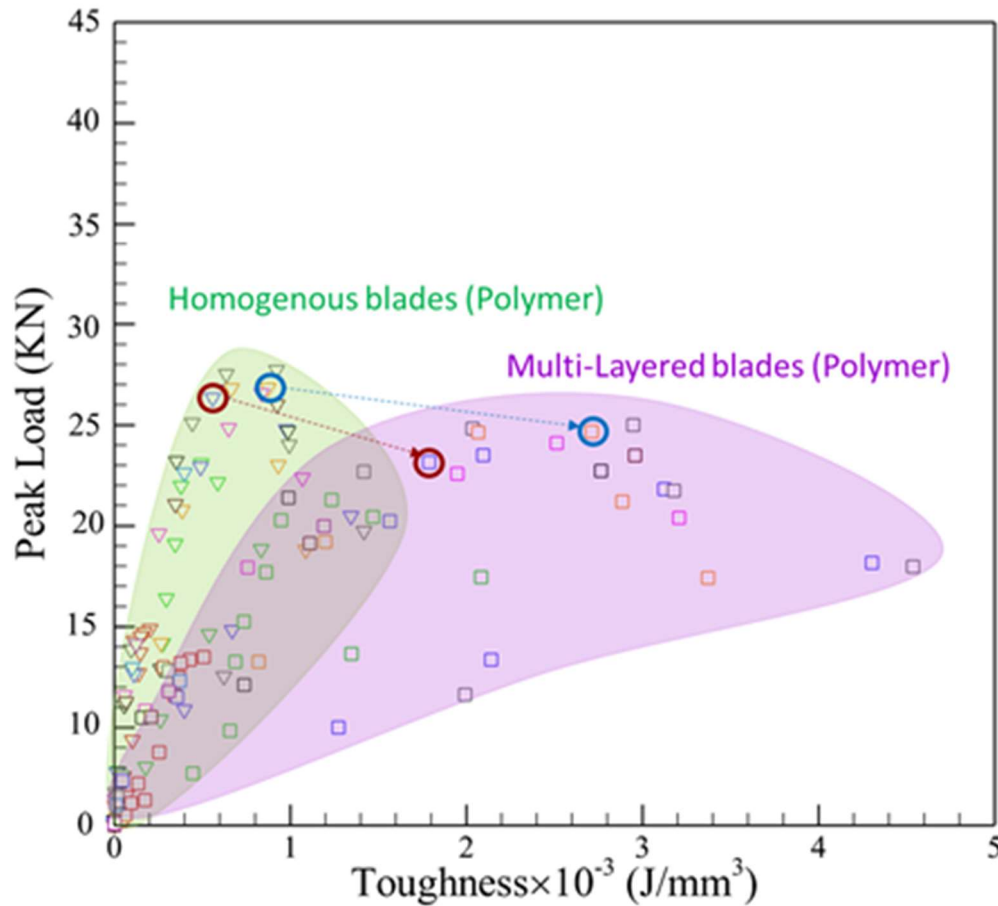
Figure 6.19, load vs. toughness, comparison between multilayered and homogenous blades

6.8.6 understanding the competing mechanism between energy release rates due to plastic deformation and delamination

The comparison between the normalized energy dissipation of the homogenous blade when a/b=1.00, and 2.50 with a multi-layered puzzle-like blade ($t_1/a = 0.1$) for different values of θ are presented in Figure 6.20 (a). This section aims to respond to the following question;

"When including multilayered architecture inside the interlocking joints (delamination) has priority over plastic deformation?"

As presented in Figure 6.20 (a), when a/b=1.00, the homogenous blades, including VeroWhite (polymer), show higher values of energy dissipation in comparison to a similar blade with multi-

layered puzzle-like architecture for all the values of θ. Similarly, for a/b=2.50, the values of energy dissipation in homogenous blade show higher values when $\theta < 25°$, however, the multi-layered architecture demonstrates higher values of energy dissipation in comparison to the homogenous case when $\theta > 25°$. This can be explained since, for a/b=1 and all the values of θ, a complete pull-out for the homogenous blade was observed and therefore, plastic deformation is responsible as the main source of energy dissipation. As a result, for all the values of θ and a/b=1, the plastic deformation is more beneficial than delamination. A similar explanation can be used for cases where $\theta < 25°$. However, presence of fracture inside the neck ($\theta > 25°$, and a/b=2) caused lower energy dissipation due to plastic deformation; therefore, for these cases delamination plays a key role and benefits the system. Therefore, one could observe that delamination is beneficial for the blades with limited ductility.
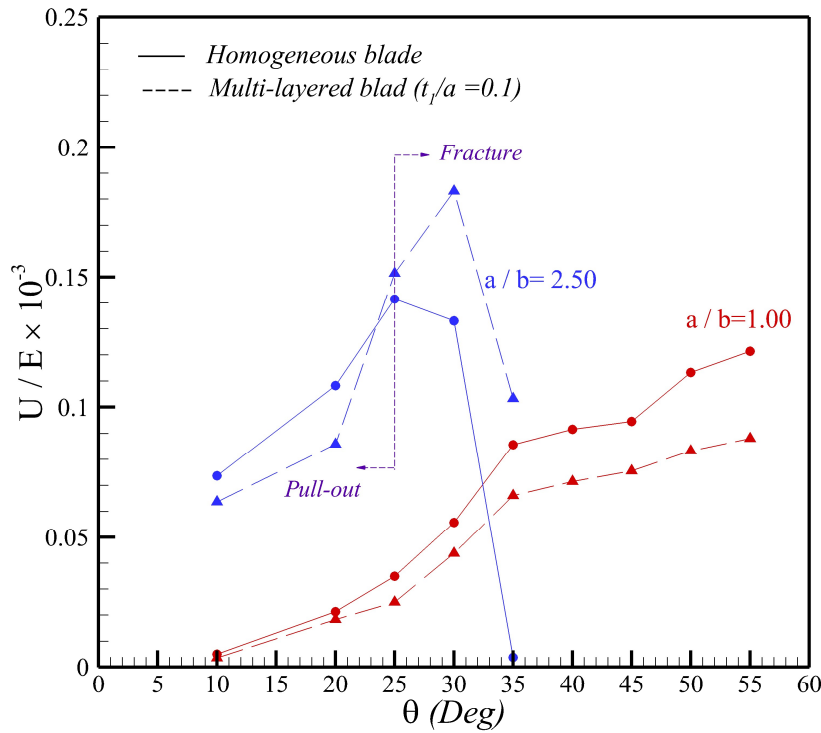
(a)

Figure 6.20. (a) A comparison between energy dissipation of homogenous blade and multi-layered puzzle-like blade for two aspect ratios $a/b = 1.00, 2.50$ for all the admissible values of θ, (b) A comparison between maximum principal stress distribution of homogenous blade and multilayered puzzle-like blade ($t_1/a = 0.1$) of $a/b = 2.50$ and all the admissible values of θ, (all the figures plotted at the peak load).

Figure 6.20 continued

(b)
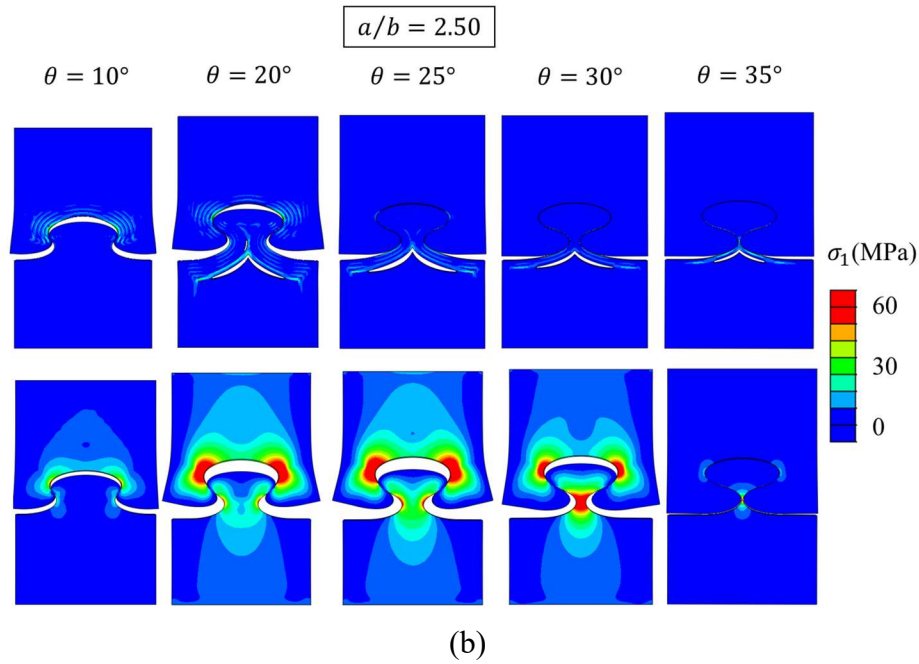
6.9 Role of Interface friction

In this section, the role of interface friction in multi-layered puzzle-like architecture is investigated. To this aim, the representative multi-layered model with a/b=2.5, $\theta = 30°$, and t_1/a=0.1 were is selected by employing two tangential friction coefficients (0.1, 0.5). The key is to understand if the interface friction between male and female parts can change the pull-out and load-displacement curve behavior. Figure 6.21 presents a comparison between the load-displacement curves of these two models. As presented in Figure 6.21(a), by adding friction into the system, a higher peak load can be achieved, as a result the toughness of the system will be increased (Figure 6.21(b)). Besides, adding friction can cause more delamination into the system (Figure 6.21(b)). Therefore, adding friction could be an effective way in increasing toughness of the system.

(a)

E_P : Energy dissipation due to plastic deformation
E_d : Energy dissipation due to delamination
COF=Coefficient of Friction
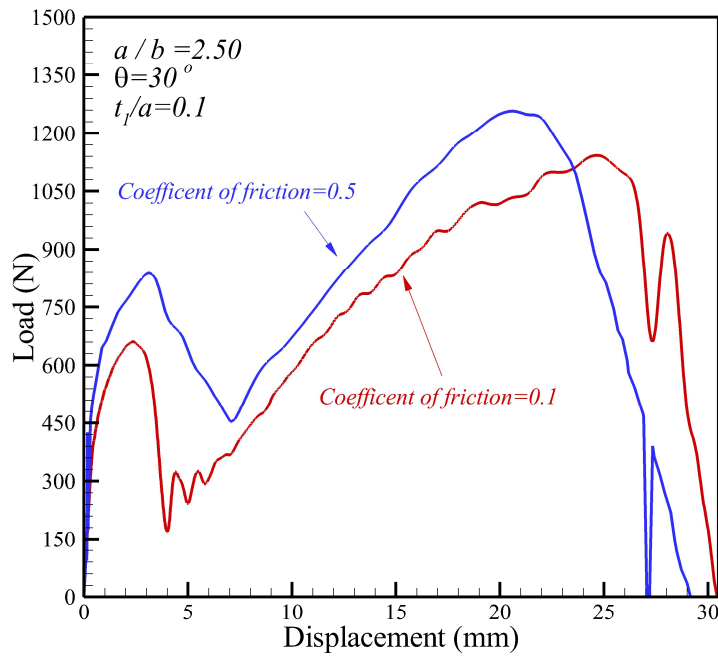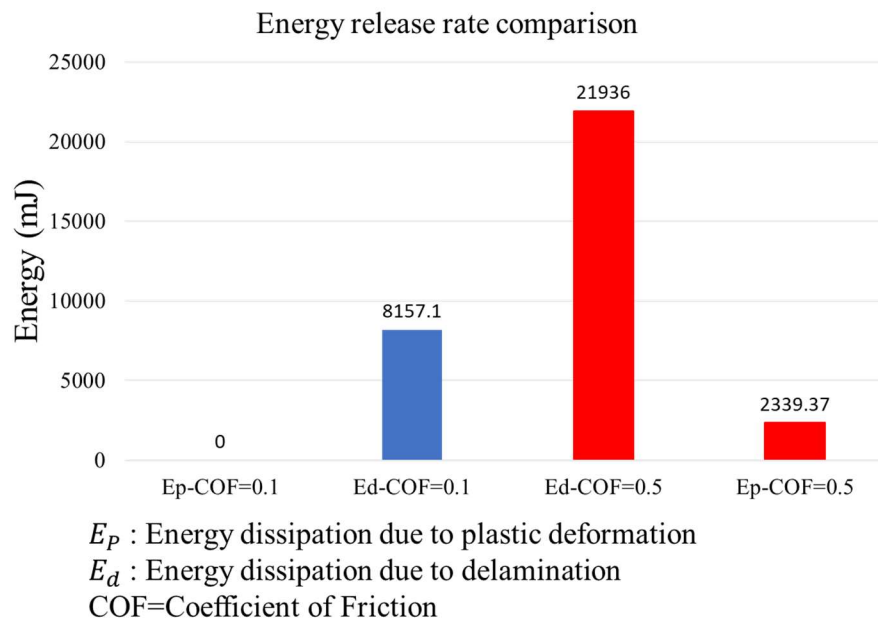
(b)

Figure 6.21. A comparison between the model with two coefficients of friction, (a) load vs. displacement, (b) comparison between energy release rate due to plastic deformation and delamination of two models with different coefficient of friction.

6.10 Role of number of blades with microstructure

In this section, the role of microstructure and blades number is investigated using both 3D printed prototype technique and FE simulation. The width, height, and thickness for all the samples are constant and equal to 128 mm, 200mm, and 12 mm, respectively. Also, geometrical features such as (a/b=1.8), θ=25° and ($t_1/a = 0.05$) is similar for all the samples. Figure 6.22(a) compare the FE simulation and experiments of the sample with different number of the blades at the peak load side by side. The comparison between normalized peak load, normalized stiffness, and toughness reveal that the maximum toughness occurs at two blades, while the maximum peak load and stiffness occur in the sample with four blades. Also, by increasing the number of blades, one can see that localization takes place in samples with three blades and higher. These results demonstrate why the sample with two blades contains higher toughness with respect to the other samples.
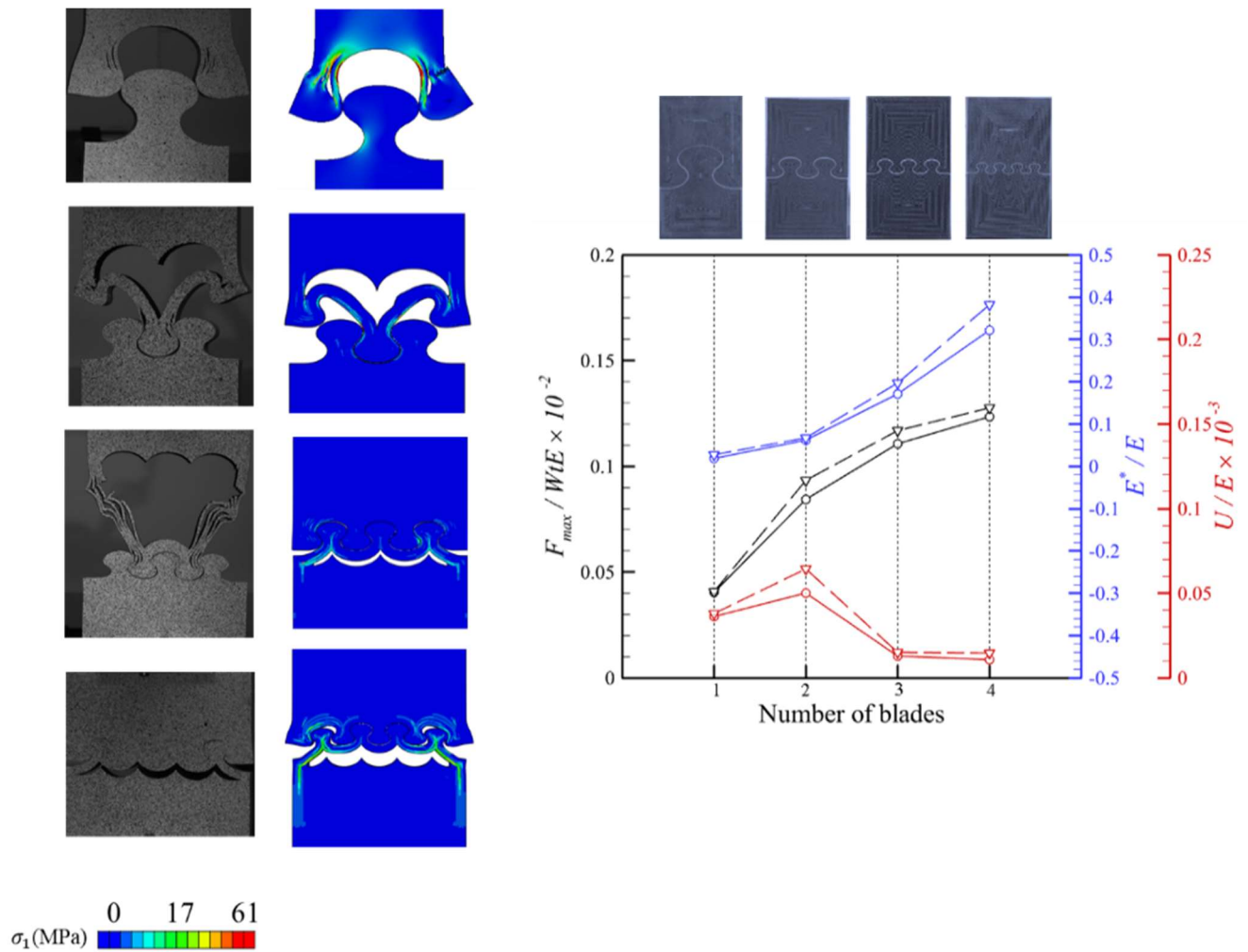
(a)   (b)

Figure 6.22. Role of blades number include microstructure (a) A comparison between FE simulations and Experiments, (b) A comparison between normalized, peak load, Normalized, stiffness, and normalized toughness (t_1/a=0.05) vs. blades number by keeping a/b =1.8 for all the cases

6.11 Understanding the stress-strain curve from a single blade

The stress-strain curve from single blades consisting of multilayers ($t_1/a = 0.25$) for two selected θ ($\theta = 10°$, $30°$) with $a/b = 2.5$ is presented in Figure 6.23(a). For $\theta = 10°$ (as shown in red), the stress-strain curve shows a peak load followed by the pullout (see the negative part in the stress-strain curve). However, for the value of $\theta = 30°$ (as shown in blue), the curve demonstrates a peak followed by negative stiffness and second peak. In homogenous material, for higher angles, we see fractures inside the neck. Delamination helps to dissipate more energy, add ductility to the system, and at the same time avoid failure inside the neck. The aim of this section is to understand a single blade in order to predict the behavior of a multi-layered composite. Figure 6.23(b) demonstrate the stress-strain curve for a multi-layered model of $a/b = 2.5$ and $\theta = 30°$. This stress-strain curve can be estimated using a single spring, and spring-mass connection where when the peak load reaches the final value (second peak (F_3)), the separation will occur. If we assume each blade as a unit cell (a combination of spring, and spring with mass), thus, a multilayered composite (see section 6.12) can be defined as a series of the unit cell and solution for this problem is already known. One of the main points in designing a multi-layered composite is to avoid the damage localization. Taking a look at the stress-strain curves and simplification model confirm that the value of F_3 should be higher than F_1 in order to avoid damage localization. Also the area under F-Δ curve (the solution to the simplified model of spring, mass, and spring) can represent the energy dissipation of the system. One way to increase the energy dissipation is to increase the area of the first peak as presented by area 1 in Figure 6.23(b). As discussed in section 6.9, adding friction is a way to increase the energy dissipation of the system in the area belongs to the first peak (Figure 6.21(a)).
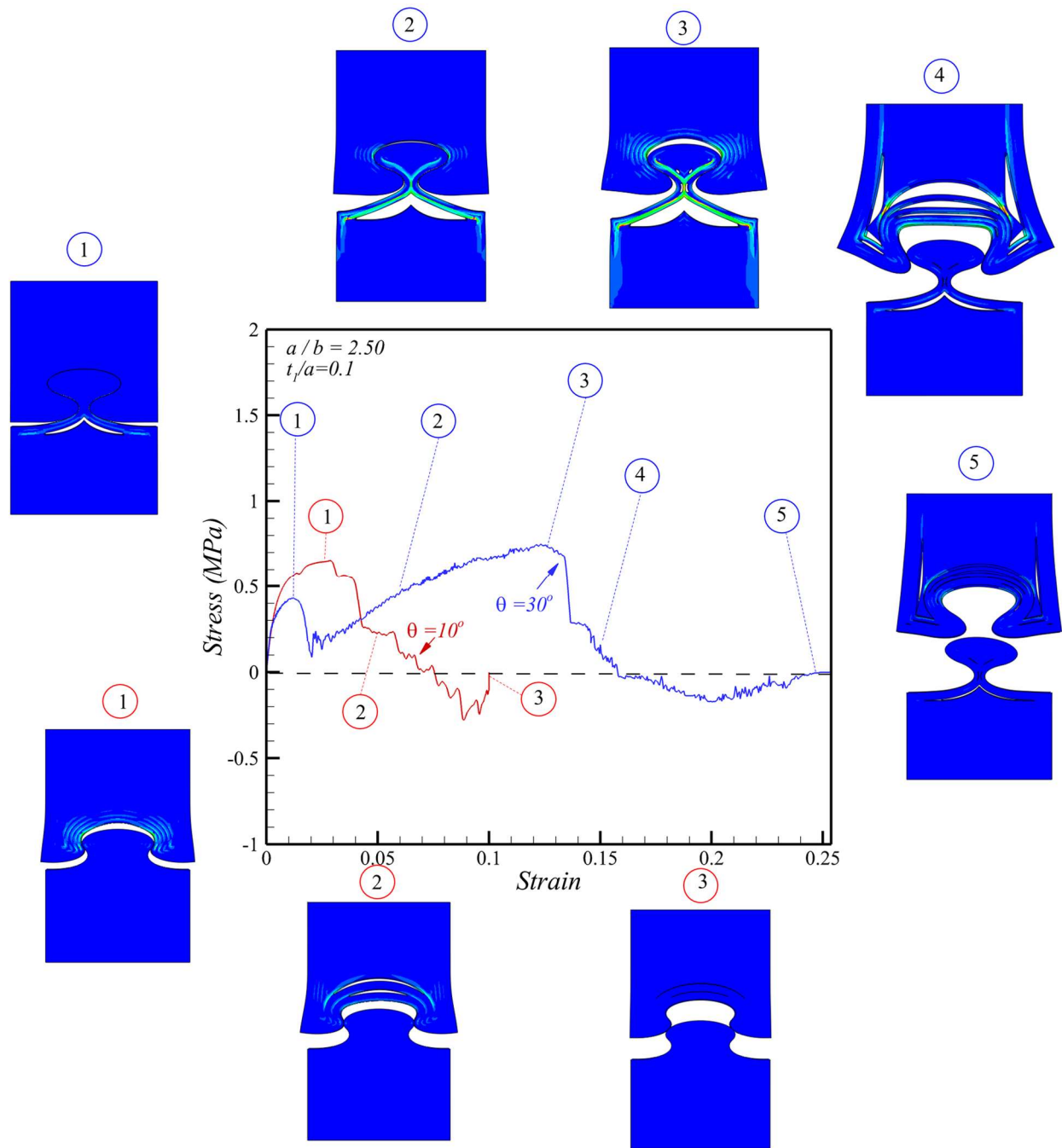
(a)

Figure 6.23. (a) Stress vs. Strain for one multilayer blade (a/b =2.5) with $t_1/a = 0.1$ for two selected θ (θ=10, and 30), (b) delamination process along the stress-strain curve (b) θ=30, (c) θ=10.

Figure 6.23 continued
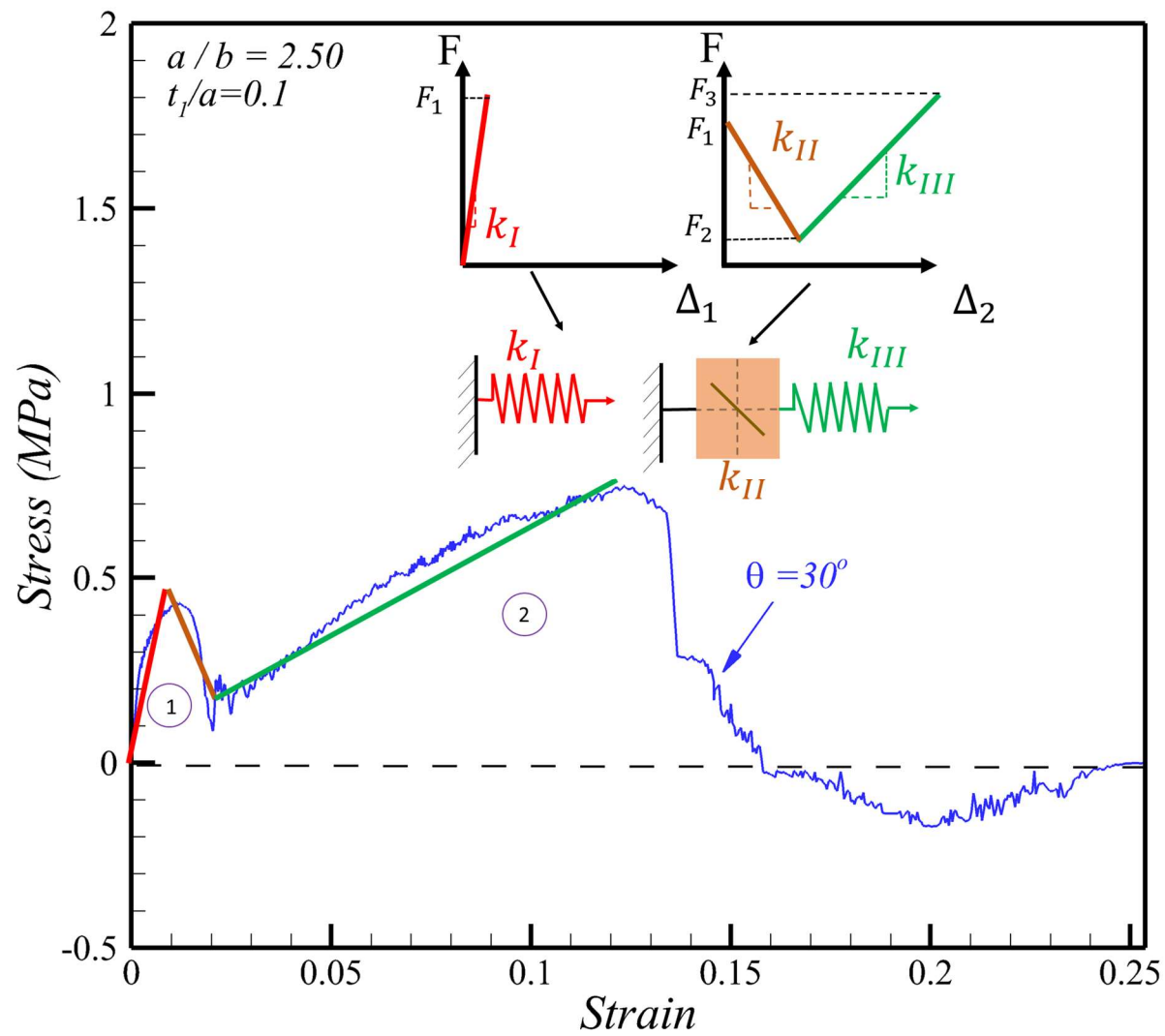
(b)

6.12 Composite bio-inspired from Ironclad beetle blades

In this section, the role of a puzzle-like composite inspired by a single multi-layered blade is investigated numerically. The primary purpose of this section is to provide a better understanding of the damage mechanism and energy dissipation of this architecture in composite materials. In order for this method to be successful, we should prevent damage localization. To this aim, I want to come up with the idea of how the parametric study of a single blade can help us to get a better insight into the damage mechanism of the puzzle-like microstructure and if this can let us improve the design and provide better insight for the architecture material. Therefore, two different models were developed, as presented in Fig 6.24 (a)-(b). The first model contains a single layer of a puzzle-like microstructure (see Figure 6.24(a)). The second model includes multilayers as shown in Fig 6.24(b). For all the models, the aspect ratio is equal to 2.0 and for the second model $t_1/a = 0.1$. This aspect ratio is selected to avoid damage localization. The width, height, and thickness of all samples are constant and is equal to 768mm, 192mm, and 15mm, respectively (Figure 6.25(a)-(b)). The quasi-static tensile load is applied on top of each sample, and the HBC boundary condition is applied to the side of the models. The final geometry and schematic of boundary conditions applied to the composite architecture are presented in Figure 6.25.

Puzzle Structure

(a)

Multi-Puzzle Structure

(b)
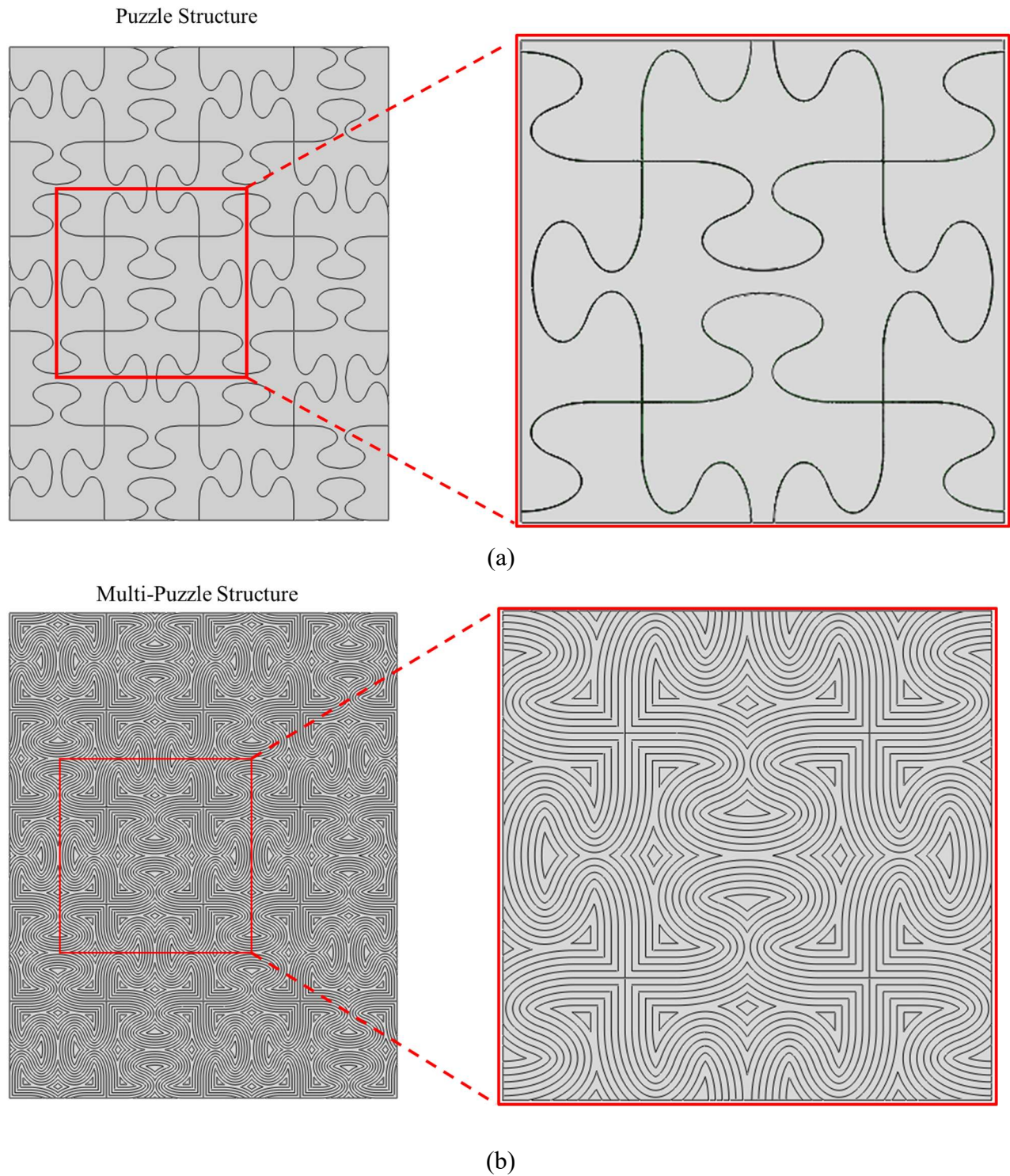
Figure 6.24. Developing multilayers composite bio-inspired from multilayered blades, (a) composite contains one layer of blades, (b) composite contain three layers of blades, (c) composite developed multilayers blades.

(a)

(b)
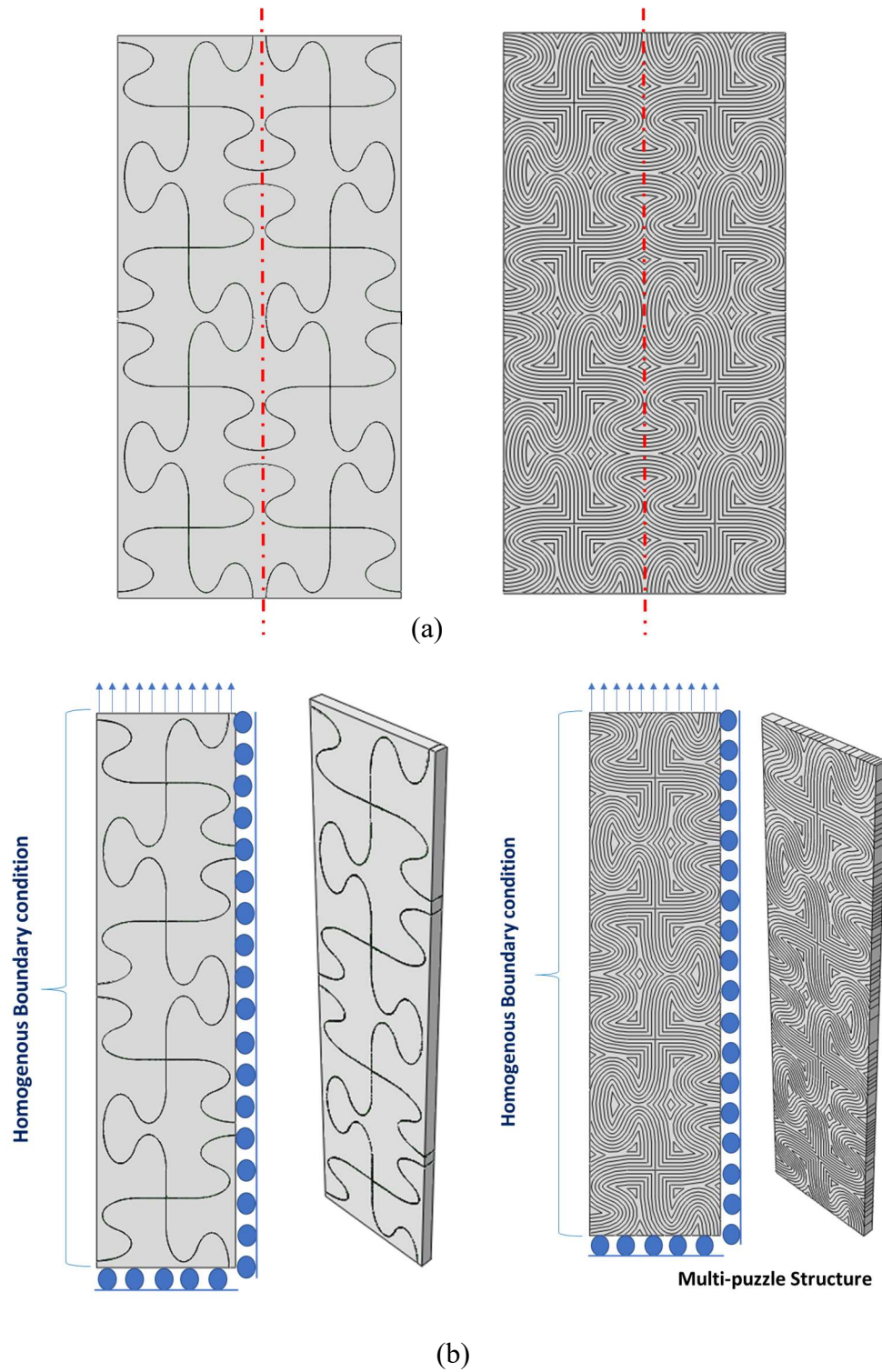
Figure 6.25. (a)The geometry of puzzle and multi-layered puzzle-like architecture composite, (b) Homogenous boundary condition applied on the side of the composites

The maximum principal stress distribution for all samples at the peak (when peak load occurs) and right before separation is presented in Figure 6.26(a)-(c). In puzzle-like architecture (Fig 6.26(a), delamination begins through puzzle-like paths followed by the fracture in the neck area of the blades. For the multi-layer composite model, several delaminations occur before fully separation occurred. The results indicate that the peak load in puzzle-like structure is higher in comparison to the multi-layered puzzle-like architecture. However, the sample with multi-layered architecture demonstrates higher toughness and energy dissipation in comparison with the puzzle-like architecture as shown in Fig 6.27. Also, the comparison between energy dissipation reveals that for the puzzle-like structure, energy dissipated through both plastic deformation and delamination shows lower values in comparison to multi-layered puzzle-like architecture. As the number of layers increases, the energy dissipation due to delamination increases. For example, in the case of the multi-layered puzzle, most of the energy dissipated through delamination, and this energy is five times of the energy dissipation (due to delamination) for a puzzle-like architecture (see Figure 6.27).

(a)

(b)
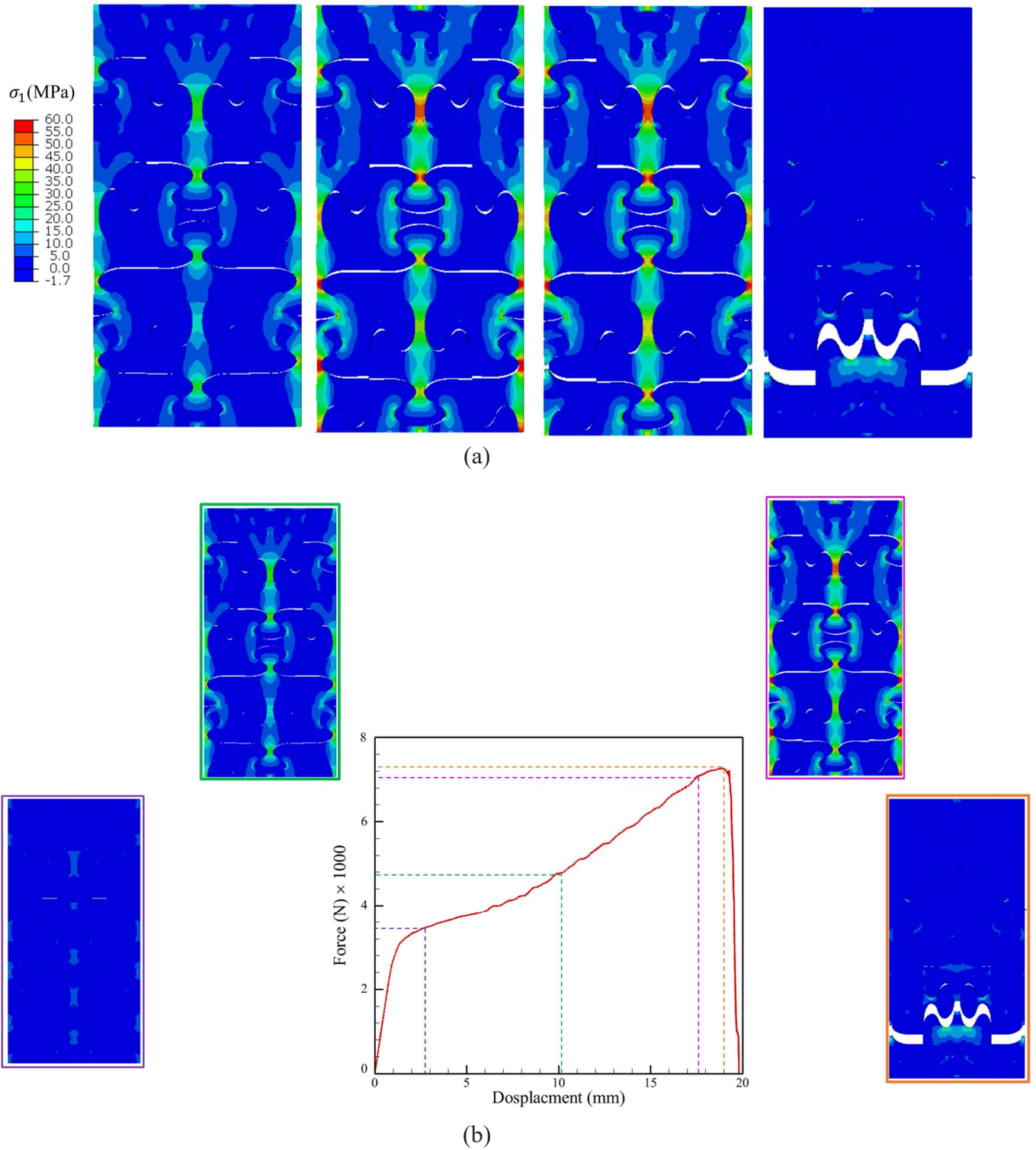
Figure 6.26. Maximum principal stress distribution for three cases studies, (a)puzzle-like microstructure, (b) three-layers puzzle-like structure, and (c) multilayered puzzle-like microstructure.

Figure 6.26 continued
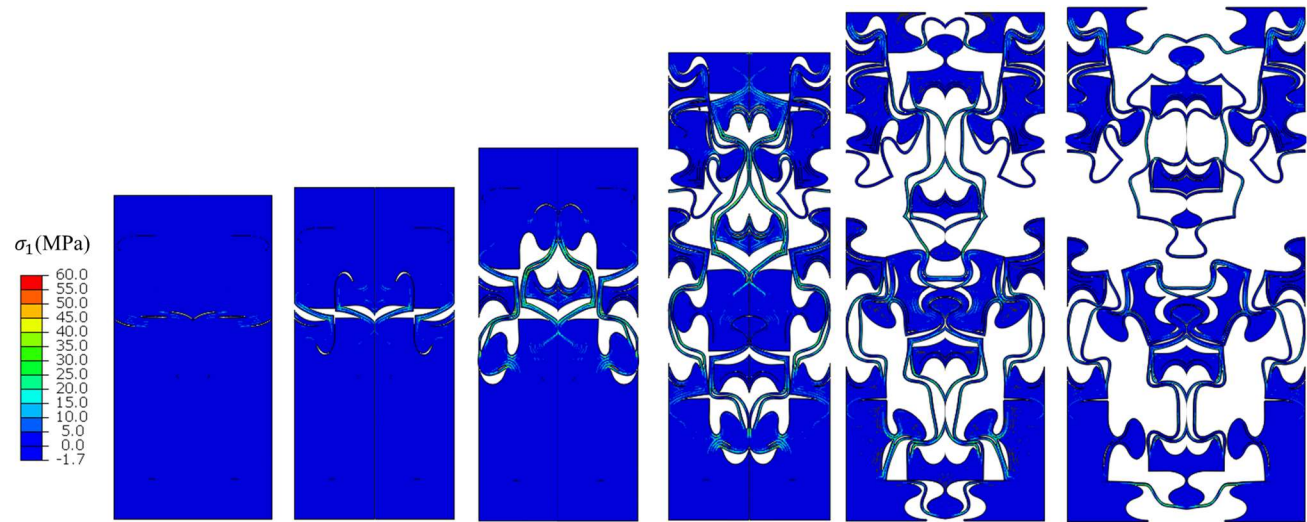
(c)
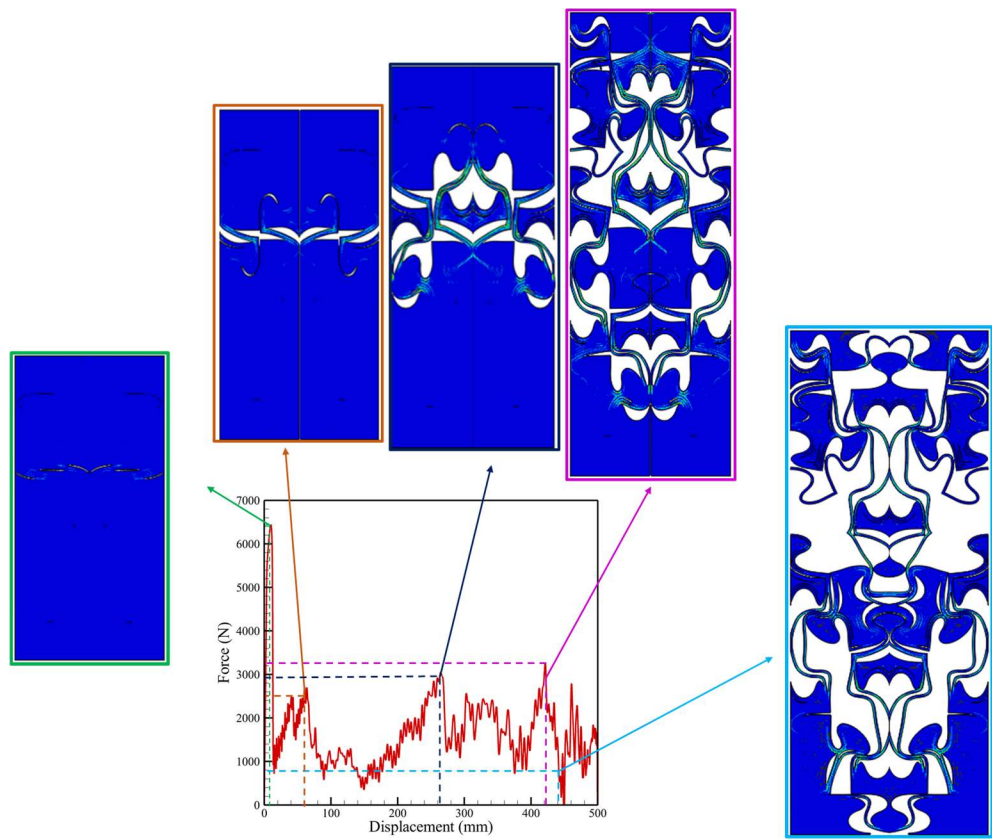
(d)
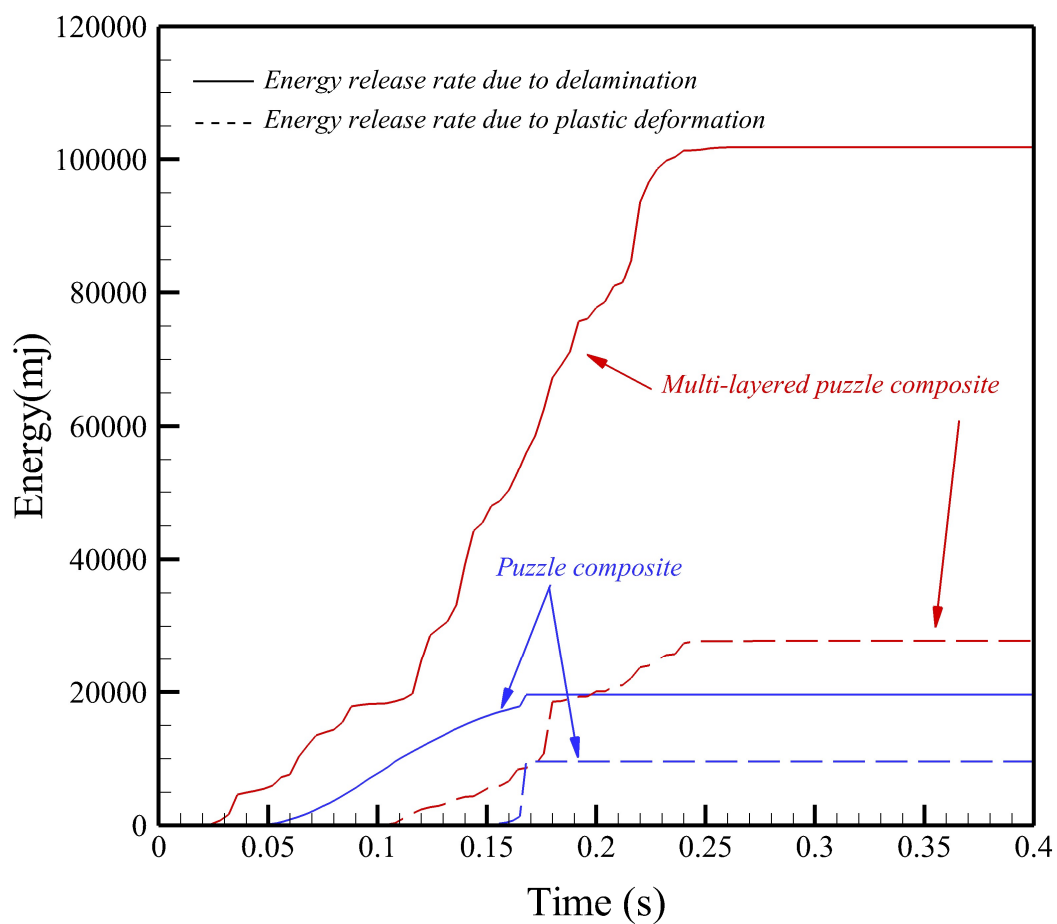
Figure 6.27. A comparison between energy dissipation due to plastic deformation and delamination for all three samples

6.13 Summary and conclusions

In this chapter, the role of microstructure bio-inspired by Ironclad beetle's blade was studied through FE simulations and 3D printing mechanical testing. The results indicated that by including microstructure inside the blade, one could increase energy dissipation due to delamination and avoid fracture or damage inside the blades. Adding layers into the blades microstructure can provide another competing mechanism to the system, which is different from two other expected mechanisms (i.e., pull out or fracture). Also, a comparison between blades with and without puzzle-like layers reveal that existing of architecture inside blade geometry can increase the energy dissipation up to four times with respect to the homogenous blades (depends on the puzzle-like layers number and angle θ). Finally, the study of a single blade consisting of a multilayered puzzle-like structure can be used as a guideline for designing the composite material in order to avoid localization. Based on the results of a single multi-layered puzzle-like blade, two types of stress-strain curves can be observed. The first type of stress-strain curve can be obtained for low angle θ (typically for $\theta < 30$), where the stress increases by increasing the stain up to the peak and then decreases until the pullout happened. While in the second type of stress-strain curves (for high angle θ (for $\theta > 30$), the first peak occurs at lower strain, follows by the second peak. Based on the comparison between these two cases, the multilayered blade with a high angle (is more desirable for the composite material since it avoids localization in the composites.

CHAPTER 7. SUMMARY AND CONCLUSIONS

The main objective of this study was to gain insight into the mechanics of patterned interfaces inspired by Nature (i.e., non-interlocking and interlocking patterned interfaces) and their role in enhancing the mechanical properties such as stiffness, toughness, and flexural strength. Firstly, the role of non-interlocking sinusoidal patterned interfaces of various aspect ratios investigated numerically, analytically, and experimentally under remote mode-I loading conditions. Specifically, the role of crack shape behind the crack tip was investigated on the effective toughness of the weak interfaces using sinusoidally patterned of various aspect ratios. As observed in most cases in Nature, cracks could be controlled by employing relatively weaker interfaces as a strategy to not only avoid catastrophic failure by arresting the cracks but also improving the mechanical performance of the system (Huang et al., 2019).

The models presented in Chapter2 assume that the interface is weak with respect to the bulk solid materials, and therefore the crack is constrained to follow the interface path direction without deflecting, penetrating or branching out into the solids. Therefore, it is important to keep in mind that there could be a critical value of A/λ that is sufficiently large at which the crack may choose to grow through the solid depending on the solid strength and toughness (He and Hutchinson, 1989).

For the sinusoidal patterned interfaces with values of $A/\lambda < 0.25$, the effective toughness of the interface could be estimated using a single kinked crack formula, and a single kinked crack model presents better performance in predicting the effective toughness in comparison to the double kinked crack approach. A double kinked crack model over the sinusoidal interface shows higher values of the effective toughness in comparison to the single kinked crack approach, notably, for the cases with higher values of aspect ratios. This confirms the importance of considering the shape of the crack behind the crack tip. However, the correct results still need to be calculated using numerical methods.

Moreover, the relationship between the interface geometric characteristic lengths (A, λ) and the interface material length scale (l_{cz}/λ) suggested that when l_{cz}/λ tends to zero, the shape of the crack behind the crack tip, and the crack kinking direction with respect to the remote loading conditions significantly contributes to the interface toughening mechanics. While in cases where $l_{cz}/\lambda \gg 1$, the contribution is mainly obtained by the increase in the crack propagation length or area and, thereby the l_{cz}/λ represents another key role for developing design guidelines, which can be used to improve the resistance to crack propagation at multiple material length scales in the sinusoidal pattern interfaces. Finally, higher values for K_{Ic}/K_0 can be obtained by selecting $l_{cz}/\lambda < 1.0$ and the largest possible value of the aspect ratio(A/λ). While applying a similar treatment to the other geometrical patterns is expected to yield similar results, this is a topic for future work.

Interlocking pattern interfaces can be seen through Nature. In this dissertation, the role of interlocking patterned interfaces was investigated for two representative species, boxfish, and Ironclad beetle. These two species were selected due to their extraordinary performance against attack or under compression loads. The boxfish carapace (Lactoria Cornuta) contains hexagonal dermal scutes, a combination of the brittle hexagonal plate (hydroxyapatite) on top of a very compliant (collagen) material. While the mineral plates are separated by patterned sutures (triangular interlocking patterns), there is no interphase material connecting them. Instead, the connection between mineralized plates is done through the collagen base. This is different from other naturally occurring sutures (e.g. sutures in turtle, alligator, armadillo). The in-situ shear test between two scutes in boxfish reveals that the damage only occurs around the suture areas, since the mineralized plates are brittle, and it is expected that at least one main crack propagates inside the entire plates, however, the cracks were arrested around the suture areas. Therefore, the soft collagen base plays an important role in controlling the crack direction. As a result, a systematic parametric study was developed using gypsum (brittle phase) and silicone (soft phase). The sutures angle θ varies between 25° and 110°. The results for the gypsum samples (without silicone on the bottom) including sutures under shear reveal the existence of at least one dominant main crack inside the brittle plates to propagates inside the plate. Also, a comparison between different values of sutures angle reveals that the maximum values of mechanical properties (i.e., peak load, stiffness, and toughness) can be obtained for angle $\theta = 45°$. Similar shear tests were performed with samples, including silicone as a sub-base material. The results state that adding silicone beneath the brittle plate can change the crack propagation angle direction and as a result, the cracks

arrested in the sutures areas. For the samples with gypsum plate and silicone base, the angle $\theta = 45°$ shows the higher value in terms of mechanical properties. Boxfish sutures angle also ranging between $45° - 50°$, this could explain that boxfish follows the optimized geometry. Finally, the role of soft material modulus and strength with respect to the brittle material modules was investigated numerically using a single kinked crack under pure shear. The results stated that the maximum change in crack angle propagation for a bi-layered material including kinked crack can be obtained when $E_1/E_2 = 0.1$ and $\sigma_{fs}/\sigma_{fb} = 0.75$. Therefore, for this architecture, the optimized value can be obtained by selecting $\theta = 45°$, $E_1/E_2 = 0.1$, and $\sigma_{fs}/\sigma_{fb} = 0.75$.

As mentioned in Chapters 5 and 6, Ironclad beetle cuticle contains alpha-chitin fibers embedded within a proteinaceous matrix that provides both strength and toughness. The top part of the cuticle (elytra) consists of separated parts connected using dovetail joints (ellipse-like blades). This microstructure inside the cuticle extended inside the blades as well. Both FE simulation and experiments of Ironclad beetle under compression reveals that the areas containing blades experience higher stress concentration. Also, Ironclad beetle develops only two blades to connect the separate parts in the elytra. Therefore, the role of blades size and number also investigated in this study. The parametric study on the role of the size and number of blades revealed that, when the size of the blade is constant, by increasing the number of blades, all the mechanical properties of the system increases. In contrast, when the width of the sample is constant, the sample with two blades shows higher values of toughness, while the samples with four blades contain higher values for stiffness and peak load. This can be explained by the fact that as the number of the blades increases, a higher compression load is observed across the width of the center part of the blades as well as higher vertical tensile stress inside the neck area. The compressive stress provides confinement as the number of the blades increases and, therefore, higher values of stiffness can be expected for the sample with five blades. As the confinement increases, the tensile stress in the neck region increases. This leads to energy dissipation due to inelastic deformation to a point where brittle fracture at the neck becomes a competing mechanism. As such, the sample with two blades exhibits the highest toughness.

The results indicated that by including microstructure inside the blade, one could increase energy dissipation due to delamination and avoid fracture or damage inside the blades. Adding layers into the blades microstructure can provide another competing mechanism to the system which is different from two other expected mechanisms (i.e., pull out or fracture). Also, a comparison between blades with and without puzzle-like layers reveal that existing of microstructure inside blade geometry can increase the energy dissipation up to four times with respect to the homogenous blades (depends on the puzzle-like layers number and angle θ). Finally, the study of a single blade consisting of a multilayered puzzle-like structure can be used as a guideline for designing the composite material in order to avoid localization. Based on the results of a single multi-layered puzzle-like blade, two types of stress-strain curves can be observed. The first type of stress-strain curve can be obtained for low angle θ (for $\theta < 30$), where the stress increases by increasing the stain up to the peak and then decreases until the pullout happened. While in the second type of stress-strain curves (for high angle θ, $\theta > 30$), the first peak occurs at lower strain follows by the second peak. Based on the comparison between these two cases, the multilayered blade with a high angle (is more desirable for the composite material since it avoids localization in the composites.

REFERENCES

ABAQUS 2017Abaqus Analysis User's Manual (RI, USA: SIMULIA Inc.).

Aboudi, Jacob. "Micromechanical prediction of initial and subsequent yield surfaces of metal matrix composites." International Journal of Plasticity 6, no. 4 (1990): 471-484.

Achrai, Ben, and H. Daniel Wagner. "The red-eared slider turtle carapace under fatigue loading: The effect of rib–suture arrangement." Materials Science and Engineering: C 53 (2015): 128-133.

Achrai, Ben, and H. Daniel Wagner. "The turtle carapace as an optimized multi-scale biological composite armor–A review." Journal of the Mechanical Behavior of Biomedical Materials (2017).

Ali, Majid, Ronald Jansen Gultom, and Nawawi Chouw. "Capacity of innovative interlocking blocks under monotonic loading." Construction and Building Materials 37 (2012): 812-821.

Anderson, G. P., K. L. DeVries, and M. L. Williams. "The influence of loading direction upon the character of adhesive debonding." Journal of Colloid and Interface Science 47, no. 3 (1974): 600-609.

Anderson, T. L. "Mathematical equations of linear elastic fracture mechanics." In Fracture mechanics fundamentals and applications, pp. 101-116. CRC Press Texas, 1995.

Anderson, Ted L., and T. L. Anderson. Fracture mechanics: fundamentals and applications. CRC press, 2005.

Ashby, Michael Farries, L. J. Gibson, U. Wegst, and R. Olive. "The mechanical properties of natural materials. I. Material property charts." Proceedings of the Royal Society of London. Series A: Mathematical and Physical Sciences 450, no. 1938 (1995): 123-140.

Askarinejad, Sina, Habibeh Ashouri Choshali, Christina Flavin, and Nima Rahbar. "Effects of tablet waviness on the mechanical response of architected multilayered materials: Modeling and experiment." Composite Structures 195 (2018): 118-125.

Bailleul, Alida M., John B. Scannella, John R. Horner, and David C. Evans. "Fusion patterns in the skulls of modern archosaurs reveal that sutures are ambiguous maturity indicators for the Dinosauria." PLoS One 11, no. 2 (2016): e0147687.

Barenblatt, Grigory I. "The formation of equilibrium cracks during brittle fracture. General ideas and hypotheses. Axially-symmetric cracks." Journal of Applied Mathematics and Mechanics 23, no. 3 (1959): 622-636.

Barsoum, Roshdy S. "Application of quadratic isoparametric finite elements in linear fracture mechanics." International Journal of Fracture 10, no. 4 (1974): 603-605.

Barthelat, F., H. Tang, P. D. Zavattieri, C-M. Li, and H. D. Espinosa. "On the mechanics of mother-of-pearl: a key feature in the material hierarchical structure." Journal of the Mechanics and Physics of Solids 55, no. 2 (2007): 306-337.

Bartol, Ian K., Morteza Gharib, Paul W. Webb, Daniel Weihs, and Malcolm S. Gordon. "Body-induced vortical flows: a common mechanism for self-corrective trimming control in boxfishes." Journal of Experimental Biology 208, no. 2 (2005): 327-344.

Bazant, Zdenek P., and Jaime Planas. Fracture and size effect in concrete and other quasibrittle materials. Vol. 16. CRC press, 1997.

Belytschko, Ted, and Tom Black. "Elastic crack growth in finite elements with minimal remeshing." International journal for numerical methods in engineering 45, no. 5 (1999): 601-620.

Bilby, B. A., and G. E. Cardew. "The crack with a kinked tip." International Journal of Fracture 11, no. 4 (1975): 708-712.

Besseau, L., and Y. Bouligand. "The twisted collagen network of the box-fish scutes." Tissue and Cell 30, no. 2 (1998): 251-260.

Bilby, B. A., and G. E. Cardew. "The crack with a kinked tip." International Journal of Fracture 11, no. 4 (1975): 708-712.

Bruet, Benjamin JF, Juha Song, Mary C. Boyce, and Christine Ortiz. "Materials design principles of ancient fish armour." Nature materials 7, no. 9 (2008): 748-756.

Buckingham, Edgar. "On physically similar systems; illustrations of the use of dimensional Eqn. s." Physical review 4, no. 4 (1914): 345.

Budyn, E., G. Zi, Nicolas Moλs, and Ted Belytschko. "A method for multiple crack growth in brittle materials without remeshing." International journal for numerical methods in engineering 61, no. 10 (2004): 1741-1770.

Camacho, Godofredo T., and M. Ortiz. "Computational modelling of impact damage in brittle materials." International Journal of solids and structures 33, no. 20-22 (1996): 2899-2938.

Cavalli, M. N., and M. D. Thouless. "The effect of damage nucleation on the toughness of an adhesive joint." The Journal of Adhesion 76, no. 1 (2001): 75-92.

Chai, Herz, Brian Lawn, and Sataporn Wuttiphan. "Fracture modes in brittle coatings with large interlayer modulus mismatch." Journal of materials research 14, no. 9 (1999): 3805-3817.

Chen, Irene H., James H. Kiang, Victor Correa, Maria I. Lopez, Po-Yu Chen, Joanna McKittrick, and Marc A. Meyers. "Armadillo armor: mechanical testing and micro-structural evaluation." Journal of the mechanical behavior of biomedical materials 4, no. 5 (2011): 713-722.

Chen, Irene H., Wen Yang, and Marc A. Meyers. "Alligator osteoderms: mechanical behavior and hierarchical structure." Materials Science and Engineering: C 35 (2014): 441-448.

Chen, Irene H., Wen Yang, and Marc A. Meyers. "Leatherback sea turtle shell: A tough and flexible biological design." Acta biomaterialia 28 (2015): 2-12.

Cheng, Liang, Liyun Wang, and Anette M. Karlsson. "Image analyses of two crustacean exoskeletons and implications of the exoskeletal microstructure on the mechanical behavior." Journal of Materials Research 23, no. 11 (2008): 2854-2872.

Cordisco, Fernando A., Pablo D. Zavattieri, Louis G. Hector, and Allan F. Bower. "Toughness of a patterned interface between two elastically dissimilar solids." Engineering Fracture Mechanics 96 (2012): 192-208.

Cordisco, Fernando, Pablo D. Zavattieri, Louis G. Hector, and Allan F. Bower. "On the mechanics of sinusoidal interfaces between dissimilar elastic–plastic solids subject to dominant mode I." Engineering Fracture Mechanics 131 (2014): 38-57.

Cordisco, Fernando A., Pablo D. Zavattieri, Louis G. Hector, and Blair E. Carlson. "Mode I fracture along adhesively bonded sinusoidal interfaces." International Journal of Solids and Structures 83 (2016): 45-64.

Cotterell, B., and JRf Rice. "Slightly curved or kinked cracks." International Journal of Fracture 16, no. 2 (1980): 155-169.

Dai, Zhendong, and Zhixiang Yang. "Macro-/micro-structures of elytra, mechanical properties of the biomaterial and the coupling strength between elytra in beetles." Journal of Bionic Engineering 7, no. 1 (2010): 6-12.

Dastjerdi, A.K. Pagano, M.,.Kaartinen, M.T, M.D.McKee, M.D., Barthelat, F. Cohesive behavior of soft biological adhesives: Experiments and modeling, Acta Biomateiralia, 8(9), (2012): 3349-3359.

Dastjerdi, A.K., Rabiei, R., Barthelat, F., 2013. The weak interfaces within tough natural composites: experiments on three types of nacre. J. Mech. Behav. Biomed. Mater. 19, (2013): 50–60

Dastjerdi, A. Khayer, and F. Barthelat. "Teleost fish scales amongst the toughest collagenous materials." journal of the mechanical behavior of biomedical materials 52 (2015): 95-107.

Deng, Yan, Brian R. Lawn, and Isabel K. Lloyd. "Characterization of damage modes in dental ceramic bilayer structures." Journal of Biomedical Materials Research: An Official Journal of The Society for Biomaterials, The Japanese Society for Biomaterials, and The Australian Society for Biomaterials and the Korean Society for Biomaterials 63, no. 2 (2002): 137-145.

Dizon, John Ryan C., Alejandro H. Espera Jr, Qiyi Chen, and Rigoberto C. Advincula. "Mechanical characterization of 3D-printed polymers." Additive Manufacturing 20 (2018): 44-67.

Dugdale, Donald S. "Yielding of steel sheets containing slits." Journal of the Mechanics and Physics of Solids 8, no. 2 (1960): 100-104.

Dunlop, John WC, and Peter Fratzl. "Biological composites." Annual Review of Materials Research 40 (2010): 1-24.

Dunlop, John WC, Richard Weinkamer, and Peter Fratzl. "Artful interfaces within biological materials." Materials Today 14, no. 3 (2011): 70-78.

Gentleman, Eileen, Andrea N. Lay, Darryl A. Dickerson, Eric A. Nauman, Glen A. Livesay, and Kay C. Dee. "Mechanical characterization of collagen fibers and scaffolds for tissue engineering." Biomaterials 24, no. 21 (2003): 3805-3813.

Elices, M. G. G. V., G. V. Guinea, J. Gomez, and J. Planas. "The cohesive zone model: advantages, limitations and challenges." Engineering fracture mechanics 69, no. 2 (2002): 137-163.

Escobar de Obaldia, Enrique, Chanhue Jeong, Lessa Kay Grunenfelder, David Kisailus, and Pablo Zavattieri. "Analysis of the mechanical response of biomimetic materials with highly oriented microstructures through 3D printing, mechanical testing and modeling." Journal of the mechanical behavior of biomedical materials 48 (2015): 70-85.

Espinosa, Horacio D., and Pablo D. Zavattieri. "A grain level model for the study of failure initiation and evolution in polycrystalline brittle materials. Part I: Theory and numerical implementation." Mechanics of Materials 35, no. 3 (2003): 333-364.

Espinosa, Horacio D., Allison L. Juster, Felix J. Latourte, Owen Y. Loh, David Gregoire, and Pablo D. Zavattieri. "Tablet-level origin of toughening in abalone shells and translation to synthetic composite materials." Nature communications 2 (2011): 173.

Evans, Anthony G., and John W. Hutchinson. "Effects of non-planarity on the mixed mode fracture resistance of bimaterial interfaces." Acta Metallurgica 37, no. 3 (1989): 909-916.

Fratzl, Peter, H. S. Gupta, E. P. Paschalis, and P. Roschger. "Structure and mechanical quality of the collagen–mineral nano-composite in bone." Journal of materials chemistry 14, no. 14 (2004): 2115-2123.

Freed, Alan D., and Todd C. Doehring. "Elastic model for crimped collagen fibrils." Journal of biomechanical engineering 127, no. 4 (2005): 587-593.

Gao, Y. F., and A. F. Bower. "A simple technique for avoiding convergence problems in finite element simulations of crack nucleation and growth on cohesive interfaces." Modelling and Simulation in Materials Science and Engineering 12, no. 3 (2004): 453.

Ghaffary, Azin, and Reza Karami Mohammadi. "Framework for virtual hybrid simulation of TADAS frames using opensees and abaqus." Journal of Vibration and Control 24, no. 11 (2018): 2165-2179.

Ghaffary, Azin, and Reza Karami Mohammadi. "Comprehensive nonlinear seismic performance assessment of MR damper controlled systems using virtual real-time hybrid simulation." The Structural Design of Tall and Special Buildings 28, no. 8 (2019): e1606.

Gharib, Mory, Francisco Pereira, Dana Dabiri, Jay R. Hove, and Darius Modarress. "Quantitative flow visualization: Toward a comprehensive flow diagnostic tool." Integrative and comparative biology 42, no. 5 (2002): 964-970.

Garner, San., Naleway, S., Hosseini, Maryam., Acevedo, Clair., Gludovatz, Bernd., Schaible, Eric., Jung, Jae-Young., Mckittrick, Joanna., Zavattieri, Pablo. "The role of collagen in dermal armor of boxfish". Acta biomaterialia, (2019).

Ghavami, M. S. M., Hosseini, M. S., Zavattieri, P. D., & Haddock, J. E. (2019). Investigating the need for drainage layers in flexible pavements (Joint Transportation Research Program Publication No. FHWA/IN/JTRP-2019/04). West Lafayette, IN: Purdue University. https://doi.org/10.5703/1288284316881

Ghavami, Masoud Seyed Mohammad, Maryam Sadat Hosseini, Pablo D. Zavattieri, and John E. Haddock. "Flexible pavement drainage system effectiveness." Construction and Building Materials 218 (2019): 99-107.

Ghavami, Masoud, Maryam Sadat Hosseini, Pablo D. Zavattieri, and John E. Haddock. Evaluation of Flexible Pavement Drainage. No. 18-01537. 2018.

Ghavami, Masoud Seyed Mohammad. Evaluation of asphalt pavements construction practice in West Virginia. West Virginia University, 2014.

Gdoutos, Emmanuel E., Chris A. Rodopoulos, and John R. Yates, eds. Problems of fracture mechanics and fatigue: a solution guide. Springer Science & Business Media, 2013.

Gibson, L. J. "Woodpecker pecking: how woodpeckers avoid brain injury." Journal of Zoology 270, no. 3 (2006): 462-465.

Guiberteau, Fernando, Nitin P. Padture, and Brian R. Lawn. "Effect of grain size on Hertzian contact damage in alumina." Journal of the American Ceramic Society 77, no. 7 (1994): 1825-1831.

Halouani, R., D. Bernache-Assolant, E. Champion, and A. Ababou. "Microstructure and related mechanical properties of hot pressed hydroxyapatite ceramics." Journal of Materials Science: Materials in Medicine 5, no. 8 (1994): 563-568.

Haut, Roger C. "The influence of specimen length on the tensile failure properties of tendon collagen." Journal of biomechanics 19, no. 11 (1986): 951-955.

He M.-Y., Hutchinson, J.W., "Crack deflection at an interface between dissimilar elastic materials", Int. J. Solids Structures, 25(9), pp. 1053-1067, 1989.

Henshell, R. D., and K. G. Shaw. "Crack tip finite elements are unnecessary." International journal for numerical methods in engineering 9, no. 3 (1975): 495-507.

Herring, S. W., and P. Ochareon. "Bone–special problems of the craniofacial region." Orthodontics & craniofacial research 8, no. 3 (2005): 174-182.

Hirsch, Franz, and Markus Kästner. "Microscale simulation of adhesive and cohesive failure in rough interfaces." Engineering Fracture Mechanics 178 (2017): 416-432.failure in rough interfaces. Eng. Fract. Mech. 178, 416–432.

Holmquist, Timothy J., and Gordon R. Johnson. "Characterization and evaluation of silicon carbide for high-velocity impact." Journal of applied physics 97, no. 9 (2005): 093502.

Hosseini, Maryam Sadat. "Parametric Study of Fatigue in Light Pole Structures." PhD diss., University of Akron, 2013.

Hosseini, M., Garner, S., Naleway, S., McKittrick, J. Zavattieri, P. (2018). Role of Architecture in Controlling Crack Propagation Direction Bio- Inspired From Box sh Scute. In T. Siegmund & F. Barthelat (Eds.) Proceedings of the IUTAM Symposium Architectured Materials Mechanics, September 17-19, 2018 , Chicago, IL: Purdue University Libraries Scholarly Publishing Services, 2018. h ps://docs.lib.purdue.edu/iutam/presentations/abstracts/31

Hosseini, Maryam S., Fernando A. Cordisco, and Pablo D. Zavattieri. "Analysis of bioinspired non-interlocking geometrically patterned interfaces under predominant mode I loading." Journal of the mechanical behavior of biomedical materials 96 (2019): 244-260.

Hosseini, Maryam S., Garner., Sean, McKittrick., Joanna, and Zavattieri., Pablo. "Role of architecture in controlling crack propagation direction Inspired by Boxfish Scute". Acta biomaterialia (2020).

Hedayat, Ahmadreza. "Mechanical and geophysical characterization of damage in rocks." PhD diss., Dissertation, Purdue University, 2013.

Huang W., Restrepo D., Jung J.-Y., Su, F.Y., Liu Z., Ritchie R.O., J. McKittrick, Zavattieri P., D. Kisailus, "Multiscale toughening mechanisms in biological materials and bioinspired designs, to appear in Advanced Materials, 2019.

Jack, C. Yu, James L. Borke, and Guigen Zhang. "Brief synopsis of cranial sutures: optimization by adaptation." In Seminars in pediatric neurology, vol. 11, no. 4, pp. 249-255. WB Saunders, 2004.

Jewell, Sharon A., Peter Vukusic, and N. W. Roberts. "Circularly polarized colour reflection from helicoidal structures in the beetle Plusiotis boucardi." New Journal of Physics 9, no. 4 (2007): 99.

Jung, J.-Y., Pissarenko, A., Trikanad, A.A., Restrepo, D., Su F.Y., Marquez A., Gonzalez D., Naleway S. E., Zavattieri P., McKittrick J., "A Natural Stress Deflector on the Head? Mechanical and Functional Evaluation of the Woodpecker Skull Bones", Advanced Theory and Simulations, 2, 1800152 , 2019

Jasinoski, S. C., B. D. Reddy, K. K. Louw, and A. Chinsamy. "Mechanics of cranial sutures using the finite element method." Journal of biomechanics 43, no. 16 (2010): 3104-3111.

Jaslow, C. R., and A. A. Biewener. "Strain patterns in the horncores, cranial bones and sutures of goats (Capra hircus) during impact loading." Journal of Zoology 235, no. 2 (1995): 193-210.

Kato, Y. Pedro, David L. Christiansen, Rita A. Hahn, Sheu-Jane Shieh, Jack D. Goldstein, and Frederick H. Silver. "Mechanical properties of collagen fibres: a comparison of reconstituted and rat tail tendon fibres." Biomaterials 10, no. 1 (1989): 38-42.

Kim, Jong Ho, Pedro Miranda, Do Kyung Kim, and Brian R. Lawn. "Effect of an adhesive interlayer on the fracture of a brittle coating on a supporting substrate." Journal of Materials Research 18, no. 1 (2003): 222-227.

Kim, Won-Seock, Il-Han Yun, Jung-Ju Lee, and Hee-Tae Jung. "Evaluation of mechanical interlock effect on adhesion strength of polymer–metal interfaces using micro-patterned surface topography." International Journal of Adhesion and Adhesives 30, no. 6 (2010): 408-417.

Kopp, R., and P. M. Dohmen, "Simulation und Planung von Walzprozessen mit Hilfe der Finite-Elemente-Methode (FEM)," Stahl U. Eisen, no.7, pp. 131–136, 1990.

Kotousov, A., and C. H. Wang. "Three-dimensional stress constraint in an elastic plate with a notch." International Journal of Solids and Structures 39, no. 16 (2002): 4311-4326.

Kotousov, A., P. Lazzarin, F. Berto, and L. P. Pook. "Three-dimensional stress states at crack tip induced by shear and anti-plane loading." Engineering Fracture Mechanics 108 (2013): 65-74.

Krauss, Stefanie, Efrat Monsonego-Ornan, Elazar Zelzer, Peter Fratzl, and Ron Shahar. "Mechanical function of a complex three-dimensional suture joining the bony elements in the shell of the red-eared slider turtle." Advanced Materials 21, no. 4 (2009): 407-412.

Kupczik, Kornelius, C. A. Dobson, M. J. Fagan, R. H. Crompton, C. E. Oxnard, and Paul O'Higgins. "Assessing mechanical function of the zygomatic region in macaques: validation and sensitivity testing of finite element models." Journal of Anatomy 210, no. 1 (2007): 41-53.

Lawn, Brian R. "Indentation of ceramics with spheres: a century after Hertz." Journal of the American Ceramic Society 81, no. 8 (1998): 1977-1994.

Lawn, Brian R., Yan Deng, Pedro Miranda, Antonia Pajares, Herzl Chai, and Do Kyung Kim. "Overview: damage in brittle layer structures from concentrated loads." Journal of Materials Research 17, no. 12 (2002): 3019-3036.

Lawn, Brian R., Antonia Pajares, Yu Zhang, Yan Deng, Mariano A. Polack, Isabel K. Lloyd, E. Dianne Rekow, and Van P. Thompson. "Materials design in the performance of all-ceramic crowns." Biomaterials 25, no. 14 (2004): 2885-2892.

Le Nguyen, Vina. Structure-Property Relations of the Exoskeleton of the Ironclad Beetle (Zopherus nodulosus haldemani). Mississippi State University, 2017.

Lee, Nayeon, M. F. Horstemeyer, Hongjoo Rhee, Ben Nabors, Jun Liao, and Lakiesha N. Williams. "Hierarchical multiscale structure–property relationships of the red-bellied woodpecker (Melanerpes carolinus) beak." Journal of The Royal Society Interface 11, no. 96 (2014): 20140274

Li, S., J. Wang, and M. D. Thouless. "The effects of shear on delamination in layered materials." Journal of the Mechanics and Physics of Solids 52, no. 1 (2004): 193-214.

Li, Yaning, Christine Ortiz, and Mary C. Boyce. "Bioinspired, mechanical, deterministic fractal model for hierarchical suture joints." Physical Review E 85, no. 3 (2012): 031901.

Li, Yaning, Christine Ortiz, and Mary C. Boyce. "A generalized mechanical model for suture interfaces of arbitrary geometry." Journal of the Mechanics and Physics of Solids 61, no. 4 (2013): 1144-1167.

Li, S., M. D. Thouless, A. M. Waas, J. A. Schroeder, and P. D. Zavattieri. "Mixed-mode cohesive-zone models for fracture of an adhesively bonded polymer–matrix composite." Engineering fracture mechanics 73, no. 1 (2006): 64-78.

Libby, E., D. E. Azofeifa, M. Hernández-Jiménez, C. Barboza-Aguilar, A. Solís, I. García-Aguilar, L. Arce-Marenco, A. Hernández, and W. E. Vargas. "Light reflection by the cuticle of C. aurigans scarabs: a biological broadband reflector of left handed circularly polarized light." Journal of Optics 16, no. 8 (2014): 082001.

Lin, Y. S., C. T. Wei, E. A. Olevsky, and Marc A. Meyers. "Mechanical properties and the laminate structure of Arapaima gigas scales." Journal of the mechanical behavior of biomedical materials 4, no. 7 (2011): 1145-1156

Lin, Erica, Yaning Li, James C. Weaver, Christine Ortiz, and Mary C. Boyce. "Tunability and enhancement of mechanical behavior with additively manufactured bio-inspired hierarchical suture interfaces." Journal of Materials Research 29, no. 17 (2014): 1867-1875.

Liu, Lei, and Yaning Li. "Failure Mechanism Transition of 3D-Printed Biomimetic Sutures." Engineering Fracture Mechanics (2018).

Liu, Zengqian, Zhefeng Zhang, and Robert O. Ritchie. "On the materials science of nature's arms race." Advanced Materials 30, no. 32 (2018): 1705220.

Malik, Idris A., and Francois Barthelat. "Toughening of thin ceramic plates using bioinspired surface patterns." International Journal of Solids and Structures 97 (2016): 389-399.

Malik, Idris A., and Francois Barthelat. "Bioinspired sutured materials for strength and toughness: pullout mechanisms and geometric enrichments." International Journal of Solids and Structures 138 (2018): 118-133.

Meyers, Marc André, Y. S. Lin, E. A. Olevsky, and P-Y. Chen. "Battle in the Amazon: arapaima versus piranha." Advanced Engineering Materials 14, no. 5 (2012): B279-B288.

Mirkhalaf, M., A. Khayer Dastjerdi, and F. Barthelat. "Overcoming the brittleness of glass through bio-inspiration and micro-architecture." Nature communications 5 (2014).

Mirkhalaf, Mohammad, and Francois Barthelat. "Design, 3D printing and testing of architectured materials with bistable interlocks." Extreme Mechanics Letters 11 (2017): 1-7.

Miura, Takashi, Chad A. Perlyn, Masato Kinboshi, Naomichi Ogihara, Mikiko Kobayashi-Miura, Gillian M. Morriss-Kay, and Kohei Shiota. "Mechanism of skull suture maintenance and interdigitation." Journal of anatomy 215, no. 6 (2009): 642-655.

Miyazaki, Hiroshi, and Kozaburo Hayashi. "Tensile tests of collagen fibers obtained from the rabbit patellar tendon." Biomedical Microdevices 2, no. 2 (1999): 151-157.

Moazen, Mehran, Neil Curtis, Paul O'Higgins, Marc EH Jones, Susan E. Evans, and Michael J. Fagan. "Assessment of the role of sutures in a lizard skull: a computer modeling study." Proceedings of the Royal Society of London B: Biological Sciences 276, no. 1654 (2009): 39-46.

Mobasherpour, Iman, M. Solati Hashjin, SS Razavi Toosi, and R. Darvishi Kamachali. "Effect of the addition ZrO2–Al2O3 on nanocrystalline hydroxyapatite bending strength and fracture toughness." Ceramics International 35, no. 4 (2009): 1569-1574.

Moes, Nicolas, and Ted Belytschko. "Extended finite element method for cohesive crack growth." Engineering fracture mechanics 69, no. 7 (2002): 813-833.

Nalla, Ravi K., John H. Kinney, and Robert O. Ritchie. "Mechanistic fracture criteria for the failure of human cortical bone." Nature materials 2, no. 3 (2003): 164.

Naleway, Steven E., Michael M. Porter, Joanna McKittrick, and Marc A. Meyers. "Structural design elements in biological materials: application to bioinspiration." Advanced Materials 27, no. 37 (2015): 5455-5476.

Noijen, S. P. M., O. Van der Sluis, P. H. M. Timmermans, and G. Q. Zhang. "A semi-analytic method for crack kinking analysis at isotropic bi-material interfaces." Engineering Fracture Mechanics 83 (2012): 8-25.

Oh, Tae-Sung, Jürgen Rödel, R. M. Cannon, and R. O. Ritchie. "Ceramic/metal interfacial crack growth: Toughening by controlled microcracks and interfacial geometries." Acta metallurgica 36, no. 8 (1988): 2083-2093.

Olvera, Diana, Elizabeth A. Zimmermann, and Robert O. Ritchie. "Mixed-mode toughness of human cortical bone containing a longitudinal crack in far-field compression." Bone 50, no. 1 (2012): 331-336.

Parks, D. M. "The virtual crack extension method for nonlinear material behavior." Computer Methods in Applied Mechanics and Engineering 12, no. 3 (1977): 353-364.

Popowics, Tracy E., and Susan W. Herring. "Load transmission in the nasofrontal suture of the pig, Sus scrofa." Journal of biomechanics 40, no. 4 (2007): 837-844.

Porter, Michael M., Nakul Ravikumar, Francois Barthelat, and Roberto Martini. "3D-printing and mechanics of bio-inspired articulated and multi-material structures." Journal of the mechanical behavior of biomedical materials 73 (2017): 114-126

Qi, Yue, and Louis G. Hector Jr. "Adhesion and adhesive transfer at aluminum/diamond interfaces: a first-principles study." Physical Review B 69, no. 23 (2004): 235401.

Qu, Jianmin. "Interfacial versus cohesive failure on polymer-metal interfaces in electronic packaging—effects of interface roughness." (2002).

Rayfield, Emily J. "Cranial mechanics and feeding in Tyrannosaurus rex." Proceedings of the Royal Society of London B: Biological Sciences 271, no. 1547 (2004): 1451-1459.

Rayfield, Emily J. "Finite element analysis and understanding the biomechanics and evolution of living and fossil organisms." Annu. Rev. Earth Planet. Sci. 35 (2007): 541-576.

Rice, J. R. "The mechanics of earthquake rupture, Physics of the Earth's Interior AM Dziewonski, E. Boschi, 555–649." (1980).

Rigby, Bernard J., Nishio Hirai, John D. Spikes, and Henry Eyring. "The mechanical properties of rat tail tendon." The Journal of general physiology 43, no. 2 (1959): 265-283.

Rim, Jee E., Pablo Zavattieri, Allison Juster, and Horacio D. Espinosa. "Dimensional analysis and parametric studies for designing artificial nacre." Journal of the mechanical behavior of biomedical materials 4, no. 2 (2011): 190-211.

Ritchie, R. O. "Mechanisms of fatigue crack propagation in metals, ceramics and composites: role of crack tip shielding." Materials Science and Engineering: A, 103, no. 1 (1988): 15-28.

Ritchie, Robert O. "Mechanisms of fatigue-crack propagation in ductile and brittle solids" International journal of Fracture, 100, no. 1 (1999): 55-83.

Rivera, J., Hosseini, MS., Restrepo D., Murata, S., Parkinson, D., Barnard, H., Arakaki, A., Zavattieri, P., Kisailus, D. " The Diabolical Ironclad elytra: a multifunctional crush resistance armor". Science (2019).

Roth, Sébastien, Jean-Sébastien Raul, Bertrand Ludes, and Rémy Willinger. "Finite element analysis of impact and shaking inflicted to a child." International journal of legal medicine 121, no. 3 (2007): 223-228.

Ruiz, C., P. H. B. Boddington, and K. C. Chen. "An investigation of fatigue and fretting in a dovetail joint." Experimental mechanics 24, no. 3 (1984): 208-217.

Salinas, Christopher L., Enrique Escobar de Obaldia, Chanhue Jeong, Jessica Hernandez, Pablo Zavattieri, and David Kisailus. "Enhanced toughening of the crossed lamellar structure revealed by nanoindentation." Journal of the mechanical behavior of biomedical materials 76 (2017): 58-68.

Santini, Francesco, Laurie Sorenson, Tina Marcroft, Alex Dornburg, and Michael E. Alfaro. "A multilocus molecular phylogeny of boxfishes (Aracanidae, Ostraciidae; Tetraodontiformes)." Molecular phylogenetics and evolution 66, no. 1 (2013): 153-160.

Saunders, W. Bruce, David M. Work, and Svetlana V. Nikolaeva. "The evolutionary history of shell geometry in Paleozoic ammonoids." Paleobiology 30, no. 1 (2004): 19-43.

Shih, C. F., B. Moran, and T. Nakamura. "Energy release rate along a three-dimensional crack front in a thermally stressed body." International Journal of fracture 30, no. 2 (1986): 79-102.

Suksangpanya, Nobphadon, Nicholas A. Yaraghi, David Kisailus, and Pablo Zavattieri. "Twisting cracks in Bouligand structures." Journal of the mechanical behavior of biomedical materials 76 (2017): 38-57.

Suksangpanya, N., Yaraghi N., Pipes, B., Kisailus D. , and Zavattieri P.D. "Crack twisting and toughening strategies in Bouligand architectures", International Journal of Solids and Structures, 150, pp. 83-106, 2018.

Sun, Zongyang, Eugenia Lee, and Susan W. Herring. "Cranial sutures and bones: growth and fusion in relation to masticatory strain." The Anatomical Record 276, no. 2 (2004): 150-161.

Sun, C., M. D. Thouless, A. M. Waas, J. A. Schroeder, and P. D. Zavattieri. "Rate effects for mixed-mode fracture of plastically-deforming, adhesively-bonded structures." International Journal of Adhesion and Adhesives 29, no. 4 (2009): 434-443.

Sun, Chang-Yu, and Po-Yu Chen. "Structural design and mechanical behavior of alligator (Alligator mississippiensis) osteoderms." Acta biomaterialia 9, no. 11 (2013): 9049-9064.

Suresh, S. "Crack deflection: implications for the growth of long and short fatigue cracks." Metallurgical Transactions A 14, no. 11 (1983): 2375-2385.

Timoshenko, Stephen P., and Sergius Woinowsky-Krieger. Theory of plates and shells. McGraw-hill, 1959.

Tvergaard, Viggo, and John W. Hutchinson. "The influence of plasticity on mixed mode Interface toughness." Journal of the Mechanics and Physics of Solids 41, no. 6 (1993): 1119-1135.

Van Dijk, H. J. A., N. Hattu, and K. Prijs. "Preparation, microstructure and mechanical properties of dense polycrystalline hydroxy apatite." Journal of materials science 16, no. 6 (1981): 1592-1598.

Van Wassenbergh, Sam, Klaas van Manen, Tina A. Marcroft, Michael E. Alfaro, and Eize J. Stamhuis. "Boxfish swimming paradox resolved: forces by the flow of water around the body promote manoeuvrability." Journal of the Royal Society Interface 12, no. 103 (2015): 20141146.

Vernerey, Franck J., and Francois Barthelat. "Skin and scales of teleost fish: Simple structure but high performance and multiple functions." Journal of the Mechanics and Physics of Solids 68 (2014): 66-76.

Weaver, James C., Garrett W. Milliron, Ali Miserez, Kenneth Evans-Lutterodt, Steven Herrera, Isaias Gallana, William J. Mershon et al. "The stomatopod dactyl club: a formidable damage-tolerant biological hammer." Science 336, no. 6086 (2012): 1275-1280.

Wang, Qian, Amanda L. Smith, David S. Strait, Barth W. Wright, Brian G. Richmond, Ian R. Grosse, Craig D. Byron, and Uriel Zapata. "The global impact of sutures assessed in a finite element model of a macaque cranium." The Anatomical Record 293, no. 9 (2010): 1477-1491.

Wigglesworth, V. B. "Digestion and nutrition." In the Principles of Insect Physiology, pp. 476-552. Springer, Dordrecht, 1972.

Witek, Lucjan. "Failure analysis of turbine disc of an aero engine." Engineering failure analysis 13, no. 1 (2006): 9-17.

Woodard, Joseph R., Amanda J. Hilldore, Sheeny K. Lan, C. J. Park, Abby W. Morgan, Jo Ann C. Eurell, Sherrie G. Clark, Matthew B. Wheeler, Russell D. Jamison, and Amy J. Wagoner Johnson. "The mechanical properties and osteoconductivity of hydroxyapatite bone scaffolds with multi-scale porosity." Biomaterials 28, no. 1 (2007): 45-54.

Xu, X-P., and Alan Needleman. "Numerical simulations of fast crack growth in brittle solids." Journal of the Mechanics and Physics of Solids 42, no. 9 (1994): 1397-1434.gjpp

Yang, Wen, Irene H. Chen, Bernd Gludovatz, Elizabeth A. Zimmermann, Robert O. Ritchie, and Marc A. Meyers. "Natural flexible dermal armor." Advanced Materials 25, no. 1 (2013): 31-48.

Yang, Wen, Steven E. Naleway, Michael M. Porter, Marc A. Meyers, and Joanna McKittrick. "The armored carapace of the boxfish." Acta biomaterialia 23 (2015): 1-10.

Yang, Shuang, Jiaqi Mi, Zhihao Liu, Baolian Wang, Xuejun Xia, Renyun Wang, Yuling Liu, and Yan Li. "Pharmacokinetics, Tissue Distribution, and Elimination of Three Active Alkaloids in Rats after Oral Administration of the Effective Fraction of Alkaloids from Ramulus Mori, an Innovative Hypoglycemic Agent." Molecules 22, no. 10 (2017): 1616.

Zavattieri, P. D. "Modeling of crack propagation in thin-walled structures using a cohesive model for shell elements." Journal of applied mechanics 73, no. 6 (2006): 948-958.

Zavattieri, Pablo D., Louis G. Hector, and Allan F. Bower. "Determination of the effective mode I toughness of a sinusoidal interface between two elastic solids." International Journal of Fracture 145, no. 3 (2007): 167-180.

Zavattieri, Pablo D., Louis G. Hector, and Allan F. Bower. "Cohesive zone simulations of crack growth along a rough interface between two elastic–plastic solids." Engineering Fracture Mechanics 75, no. 15 (2008): 4309-4332.

Zimmermann, Elizabeth A., Bernd Gludovatz, Eric Schaible, Neil KN Dave, Wen Yang, Marc A. Meyers, and Robert O. Ritchie. "Mechanical adaptability of the Bouligand-type structure in natural dermal armour." Nature communications 4 (2013): 2634.